Advancements in electron pulse compression technology applied to ultrafast electron scattering

Martin R. Otto

Doctor of Philosophy

Department of Physics

McGill University

Montreal, Québec, Canada

September 18, 2019

A thesis submitted to McGill University in partial fulfillment of the requirements of the degree of Doctor of Philosophy

ACKNOWLEDGMENTS

I would like to thank my supervisor Dr. Bradley Siwick for his commitment to excellent science and the consistent academic and personal support he was able to provide throughout my Ph.D. studies in his group at McGill. Your guidance and insistence on letting me chart my own research course formed a true path to understanding which I now realise to be precisely the reason I embarked upon a Ph.D. I would also like to deeply thank my colleagues and friends Laurent René de Cotret, Mark Stern and Dr. Jan-Hendrik Pöhls and members of the Kambhampati research team for their sustained support and [constructive] criticism. The work I was able to accomplish during my Ph.D. studies would not have been possible without the free and collaborative environment all of you helped foster and nurture. I would like to thank the various technicians in the McGill physics and chemistry departments for their kind and professional help over the years. Electronics technicians Rick Rossi and Weihua Wang, machinists Pascal Brourseguin and Jean-Phillipe Guay, technicians John Smeros and Robert Gagnon; you help form the backbone of an environment in which the success of all graduate students can take place. I would like to thank all friends and colleagues in the physics department with whom I enjoyed many professional and recreational experiences. I would like to specifically thank professors David Cooke and Mark Sutton, I learned much from you both when our research paths overlapped. I would like to thank my partner Alison and my family for their enduring love and support.

ABSTRACT

Ultrafast electron scattering with radio-frequency pulse compression is a laboratory scale technique capable of interrogating the time-dependent structure of matter with sub-picosecond temporal resolution. In this thesis, a novel approach to achieve high-quality laser-microwave synchronization is devised and implemented. The technique involves the direct generation of the compression field signal from a phase-locked frequency comb. The frequency comb is produced through direct photo-detection of an ultrafast laser pulse train and the appropriate signal is filtered and conditioned in an ultra-low phase noise microwave system. This synchronization system, combined with an active phase stabilization system integrated into the electron pulse compressor, is demonstrated to yield robust timing synchronization into the sub-50 fs level for electron pulse arrival time stability. The enhanced performance of the ultrafast electron diffraction instrument enabled by the new synchronization system is applied in the study of the photo-induced phase transitions in vanadium dioxide. The photo-induced monoclinic metallic phase is studied in detail and found the consist of an anti-ferroelectric charge-ordering along the c-axis of the material. In conjunction with complementary time-resolved terahertz spectroscopy measurements, the fluence-dependent non-equilibrium volume phase fractions are determined, and the formation times of the monoclinic metallic phase are found to have an energy activated character consistent with recent theoretical calculations. Titanium diselenide, a layered transition metal dichalcogenide compound is also studied in the high-temperature phase. Measurements of the time-resolved diffuse intensity reveal photo-induced phonon hardening on a 100 fs timescale at specific points of the Brillouin zone where a soft-mode lattice instability

and Kohn anomaly are found. This novel observation is understood in terms of a divergent electronic susceptibility and the relative magnitudes of the wave-vector dependent electron-phonon coupling are determined at various points in the Brillouin zone.

ABRÉGÉ

La diffraction ultrarapide par électrons avec compression radio-fréquence est une technique expérimentale capable dintérroger la structure évolutive de la matière, avec une résolution temporelle sous une picoseconde. Cette thèse décrit une approche nouvelle de synchronisation haute-performance entre laser et système électronique radiofréquence. Cette technique enjoint la génération directe du signal de compression à partir dun peigne de fréquence avec phase stabilisée. Le peigne de fréquence est produit par photo-détection directe dun train dimpulsions laser ultrarapides et le signal approprié est filtré puis conditionné dans un système radiofréquence à niveau de bruit ultra-faible. Ce système de synchronisation, combiné à un système de stabilisation active de phase intégré au compresseur radiofréquence, démontre une synchronisation robuste avec au plus 50 femtosecondes de variation darrivée. L'amélioration de la performance du diffractomètre ultrarapide par électron de au nouveau système de synchronisation est exploitée lors dune étude sur la transition de phase par induction optique du dioxide de vanadium. La phase métallique monoclinique induite de manière optique est étudiée en détail et est trouvée à supporter un ordre de charge anti-ferroélectrique le long de laxe c du matériau. En tandem avec la spectroscopie ultrarapide par térahertz résolue dans le temps, les fractions de phases dépendentes de la fluence ont sont déterminées, et le temps de formation de la phase métallique monoclinique est trouvée à avoir une énergie dactivation qui coincide avec de récents calculs théoriques. Le séléniure de titanium, une dichalcogènure de métal de transition stratifié, est aussi étudié dans sa phase de haute-température. Des mesures résolues dans le temps de lintensité diffuse révèlent un durcissement phononique par induction optique à léchelle de 100 fs à certain points spécifiques de la zone de Brillouin, là où une instabilité par adoucissement du mode phononique et une anomalie de Kohn se trouvent.

Ces nouvelles observations sont analysées en terme de divergences dans la susceptibilité électronique et lampleur relative du couplage électron-phonon est déterminés à plusieurs points de la zone de Brillouin.

TABLE OF CONTENTS

LIST OF TABLES

Table page

LIST OF FIGURES

PREFACE

The author, Martin R. Otto, affirms that the work presented in this thesis constitutes original scholarship and distinct contributions to the fields of ultrafast electron scattering instrumentation and condensed matter physics. Much of the work presented in thesis is centered around the design and implementation of an improved laser-microwave synchronization system for the ultrafast electron scattering instrument originally designed by former students in the Siwick laboratory Robert Chaterlain and Vance Morrison. Following the technical improvements to the instrument, experiments on two-different material systems, vanadium dioxide and titanium diselenide, were performed. The contributions of the author and various co-workers are summarize here. The new laser microwave synchronization system was designed and characterized by the author with data acquisition help provided by Laurent René de Cotret. The cavity modelling and RF electronics assembly was carried out by the author. The vanadium dioxide experiments involved a collaboration with the research group of David G. Cooke. His students, David Valverde-Chavez and Kunal L. Tiwari performed the time-resolved terahertz spectroscopy experiments. The author performed the data analysis presented in this thesis. The ultrafast electron scattering experiments where conducted by the author with help from Laurent René de Cotret. The titanium diselenide experiments and associated analysis of the results were conducted by the author. Acquisition and analysis of the ultrafast electron diffraction data was greatly aided by the software packages *faraday* and *iris* developed by Laurent René de Cotret.

CHAPTER 1
Introduction: material properties away from equilibrium

Time-dependent processes in nature play important roles in establishing the time-*independent*, or equilibrium character of matter. Despite our perception of existing in a universe which seems to be always "in-equilibrium", the way in which matter tends toward and ultimately reaches equilibrium is governed by the competition between fundamental excitations. Understanding the interactions and coupling strengths between such fundamental excitations is dramatically simplified in the time-domain because rates of change are often related to coupling terms. For well over a century, scientists have been developing techniques to capture the motion of objects which exceed the capabilities human perception. In time this conquest entered the domain of microscopic objects such as molecules, atoms and electrons. A central goal of science thus became recording physical and chemical processes in "real-time". There has been great excitement around this theme and its spans from single elements to massive macro-molecular systems existing in the gas, liquid and solid phases.

A related area of research is the use of external perturbations to control and even *create* novel states of matter [1, 2, 3, 4]. Ultrafast optical pulses provide a mechanism to selectively interact with electronic states on the femtosecond (10^{-15} s) timescale, rapidly displacing them from equilibrium with respect to the crystal lattice of the material. The competition between the interacting degrees of freedom (charge, spin, orbital and lattice) govern the response of the material and transitions into non-trivial states of matter with exotic properties can occur [5]. Understanding the microscopic processes which facilitate these events is a central focus of ultrafast science of solid-state materials.

1.1 The challenge of resolving fundamental atomic level dynamics

Measurements of dynamical processes in nature require both spatial resolution and temporal resolution often abbreviated as *spatio-temporal*. In basic terms, the apparatus used in the experiment must consist of components which actuate faster than the physical process to be measured. This condition is analogous to a conventional camera, for which the time-resolution is dictated by the exposure time and shutter speed. The time-dependent measurement of molecules and atoms is fundamentally constrained by the extreme scales of space and time associated with atomic and molecular motion. In condensed phases, atoms and molecules organize over length scales corresponding to roughly an Ångstrom (10^{-10} m) and their motion is governed by the energy and bandwidth of permitted processes along with their masses. Collective oscillations in solids typically have energies in the range of roughly 10–100 meV which translates to periods of picoseconds and below (1 ps = 10^{-12} s) within which an atom may oscillate back-and-forth about its equilibrium position. Larger molecular species, such as macro-molecules and proteins, are a thousand-fold more massive than single atoms, and have weak inter-molecular interactions which yield structural transformations transpiring on the order of microseconds (1 μs = 10^6 ps = 10^{-6} s).

1.1.1 Reversible pump-probe technique

Acquisition times of state of the art detectors remain orders of magnitude to slow for measuring atomic and molecular motion in a "continuous" manner. One way around this problem is to use "flashes" or pulses of radiation which measure the material over a short period of time established by the temporal duration of the pulse. Measuring time-dependent phenomena in this way requires initiating the relevant processes with respect to a timing reference or "clock" in the laboratory by means of an excitation or "pump" pulse. This clock is typically some type of electronic or optical oscillator which precisely produces

pulses at a well-defined repetition rate, or continuous signals at a stable frequency and phase. Second, the measurement or "probe" pulse measures the sample at a particular point during its temporal evolution following the pump excitation. This type of measurement is said to be *stroboscopic* and is called the pump-probe experiment. Experiments of this type are said to be *reversible* if the excited sample returns to its initial state (the state before excitation by the pump pulse) within the period of the timing reference, or before the next pump pulse. This concept is illustrated in Fig. 1–1. Physical processes which end up in different final states following excitation by the pump are said to be *irreversible*.

Stroboscopic experiments are often referred to as *equivalent time* methods. This means that the physical process undergoes an equivalent temporal evolution each time a pump pulse stimulates the sample. Each instance measured by the probe at time t following the pump is assumed to have behviour which is highly-correlated with the same time t for *any* other pump pulse during the total measurement interval.

1.1.2 Time-resolution of a pump-probe experiment

The overall time-resolution of a pump-probe experiment depends on many experimental parameters. In a typical pump-probe spectroscopy experiment, the pump and probe pulse widths dictate the total time resolution of the experiment. If the temporal envelope of the pump and probe pulses may be treated as Gaussian, with root-mean-squared (RMS) widths τ_{pump} and τ_{probe} respectively, the total time resolution is a quadrature sum $\tau_{\text{pump}}^2 + \tau_{\text{probe}}^2$. In general, there can be temporal fluctuations affecting synchronization between the pump and probe pulses, thus affecting the time-delay between the pulses, $\Delta\tau$. This is called *jitter* and is described by τ_{jitter}. Finally, there can be geometric temporal factor τ_{geom} which depends on the velocity mismatch of the pump and probe pulses at the sample position. The total time-resolution is thus given by

$$\tau_{\text{tot}} = \sqrt{\tau_{\text{pump}}^2 + \tau_{\text{probe}}^2 + \tau_{\text{jitter}}^2 + \tau_{\text{geom}}^2}. \tag{1.1}$$

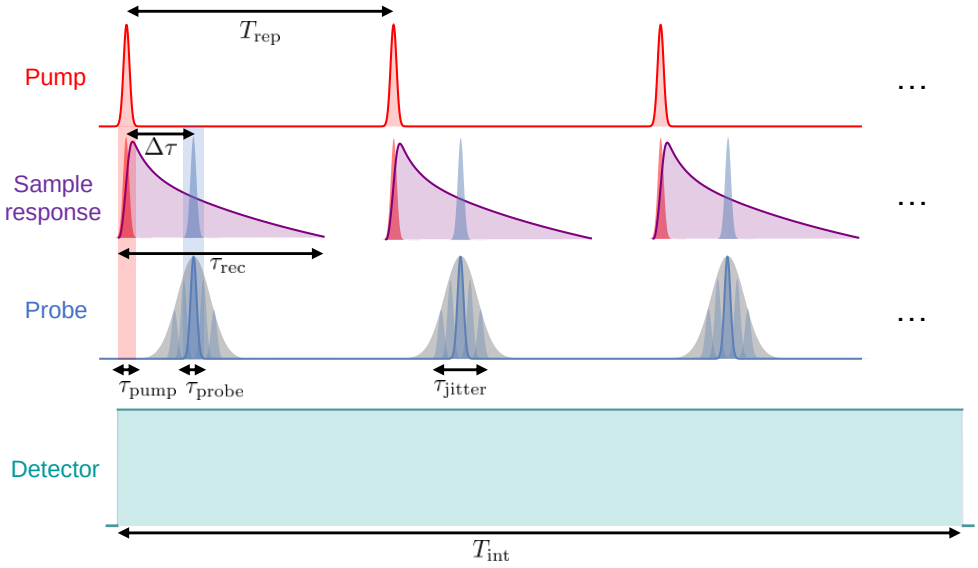

Figure 1–1: Illustration of a reversible pump-probe experiment.
A pump pulse having a temporal duration τ_{pump} excites a time-dependent sample response, which lasts for some duration τ_{rec}. The probe pulse measures the sample response after a precisely controlled time-delay $\Delta\tau$ and captures a "snapshot" of the dynamics occurring within a time interval established by the temporal duration of the probe pulse τ_{probe}. The pump and probe pulses are produced at a specific time interval $T_{\text{rep}} = 1/f_{\text{rep}}$ where f_{rep} defines the repetition rate of the experiment. Temporal jitter is described by τ_{jitter} and leads to a statistical broadening of the probe pulse. The condition for a reversible pump-probe experiment is that $\tau_{\text{rec}} < T_{\text{rep}}$, so that the sample returns to its initial state. This criteria allows for integration or averaging of many identical measurements within a time interval $T_{\text{int}} \gg T_{\text{rep}}$, elimating the constraint of using a relatively slow detector.

1.2 Ultrafast laser sources

It is no exaggeration to say that the development of ultrafast laser systems revolutionized both fundamental science and technology [6, 7]. The technique of mode-locking [8, 9] has proven itself capable of producing very short pulses into the sub-picosecond regime in *oscillator* lasers. These lasers and the work culminating to their optimization advanced our understanding of opto-electronics and photonics, key research areas of the telecommunications industry [10]. Oscillators also gathered considerable interest as ultrastable frequency

sources [11], and had the advantage of being highly tunable and broadband compared to conventional atomic clocks and solid-state oscillators. Oscillators can generate high-quality radio-frequency and microwave signals at the repetition rate of the laser f_{r} defined by the length of the laser cavity L_{c} and the speed of light c as $f_{\mathrm{r}} = c/2L_{\mathrm{c}}$. Harmonics are also produced at nf_{r} up to frequencies limited by the bandwidth of the opto-electronic device which converts the laser beam to the electrical signal forming a stable, broadband, phase-locked frequency comb. The opto-electronic device is typically a photo-detector, which consists of a semiconducting photo-diode shunted to an RC integrated circuit. The electron-hole carriers generated in the diode drive a current response in the time-domain at an interval established by f_{r}. In chapter 2 of this thesis, a synchronization system based on an ultra-stable frequency comb synthesized by a mode-locked oscillator is developed and applied to pump-probe measurements of atomically resolved dynamics in materials.

Oscillators were also implemented in pump-probe spectroscopy applications. The range of possible experiments were however limited, in part due to high repetitions rates of the oscillators but mostly due to the low pulse energies which limited the exploration of strongly driven light-matter interactions and non-linear optics [12]. This was overcome in the 1980's due to the invention of *chirped-pulse amplification* by Nobel laureates Donna Strickland and Gérard Mourou [13] which delivered roughly a factor of one-million increase in the pulse energy of ultra-short laser pulses. This step forward transformed the discipline, opening up many new avenues in fundamental science and industry. The field of optics flourished and advances in non-linear optics lead to further development of laser sources spanning from the ultraviolet to the far infrared. Strickland and Mourou stretched out the ultrashort optical pulse in time using diffraction gratings before amplifying it in a laser cavity. Only with this added dispersion was the peak power of the pulse low enough to efficiently increase the pulse energy. Following amplification, the pulse was re-compressed

using essentially the same grating configuration but to the reverse effect. This advancement could reliably increase pulse energies into the milli-Joule range and peak powers well into the giga-Watt regime. In turn, amplified femtosecond laser sources have become essential instruments driving ultrafast science and research and are common-place in modern ultrafast science laboratories.

1.3 Basic properties of electron pulses

Ultrafast laser systems provide the required time resolution for resolving atomic motion in a pump-probe experiment. However, the wavelength of the light produced by or subsequently derived from such laser systems remains a limitation in terms of spatial resolution. A suitable radiation source which has a wavelength on the order of the atomic scale must be found. Electron pulses meet this requirement and have a DeBroglie wavelength $\lambda = 2\pi\hbar/p$, where p is the relativistic momentum given by

$$p = \gamma m_e v, \tag{1.2}$$

where m_e is the rest mass of the electron and $\gamma = 1/\sqrt{1 - v^2/c^2}$ is Lorentz factor for which c is the speed of light in vacuum and v is the speed of the electron. The relationship between energy and momentum is given by

$$E = \sqrt{p^2c^2 + (m_e c^2)^2}. \tag{1.3}$$

For non-relativistic ($\gamma \approx 1$) Eqn. 1.3 is well approximated by $E \approx \frac{p^2}{2m_e} + m_e c^2$ in which the first term corresponds to the classical kinetic energy $E_k = \frac{1}{2} m_e v^2$ and the second term is the rest mass energy. For 100 keV electrons, the DeBroglie wavelength is 3.7 picometers (pm).

Ultrashort pulses of electrons can be generated by the process of photo-emission using UV light generated by a non-linear optical process called third harmonic generation. To

first order, electrons of energy $\epsilon = \hbar\omega - \Phi$ are emitted if the energy of the incident photons $\hbar\omega$ exceeds the intrinsic work function Φ of the source material. Metals will typically have values of Φ around 5 eV ($\Phi_{\mathrm{Cu}} \simeq 4.16$ eV for example) [14]. For an ideal pristine emission surface, the initial energy distribution of photo-emitted electrons is governed by the bandwidth of the optical pulse $\Delta\epsilon = \hbar\Delta\omega$, which is typically $\sim$ 0.2 eV for femtosecond pulses. In practice however, surface effects such as multi-faceting yield a distribution of work-functions [15] contributing to an enhanced energy broadening. The process of photo-emission will generate a dense bunch of electrons which then require acceleration to sufficient energies such that they obtain a DeBroglie wavelength comparable to or shorter than atomic length scales. This can be achieved using static DC fields, radio-frequency fields and laser fields depending on the application and design of the electron source.

An important figure of merit for an electron beam is the *transverse coherence* $\xi_\perp$ defined as [16, 17, 18]

$$\xi_\perp \equiv \frac{\lambda}{2\pi\sigma_\theta}, \tag{1.4}$$

where $\sigma_\theta = \sigma_{v_x}/v_0$ is the statistical RMS angular spread of the beam, expressed in terms of the transverse velocity spread σ_{v_x}. Making use of the DeBroglie formula, Eqn. 1.4 can be expressed as

$$\xi_\perp = \frac{\hbar}{m_e\sigma_{v_x}} = \frac{\hbar}{\sigma_{p_x}}, \tag{1.5}$$

where p_x is the transverse momentum. The beam *emittance* is a related quantity commonly used when discussing charged particle beams and is defined as

$$\varepsilon_x \equiv \frac{1}{m_e c}\sqrt{\langle x^2\rangle\langle p_x^2\rangle - \langle xp_x\rangle^2}, \tag{1.6}$$

where $\langle\rangle$ represents a statistical average over particles. The first term in the square-root describes uncorrelated statistical quantities whereas the second describes correlated quantities. In a Gaussian beam waist, Eqn. 1.6 becomes $\varepsilon_x = \frac{1}{m_e c}\sigma_x\sigma_{p_x}$ where σ_x is the

RMS width of the beam [16]. Therefore, the emittance of a beam in this case can be simply understood as the product of a beam's width and divergence, described by the transverse velocity spread. It then follows that the transverse coherence can be expressed as

$$\xi_\perp = \frac{\hbar}{m_e c}\frac{\sigma_x}{\varepsilon_x}. \tag{1.7}$$

As a general rule, the emittance of the beam determines how well (tight) it can be focused.

1.4 Space-charge dispersion

Electron pulses generated via photo-emission by an ultrashort (∼40 fs) laser pulse initially have a high charge density. Space-charge effects [19, 16] (Coulomb repulsion) are significant in this regime and initiate dispersive velocity broadening in both the longitudinal (propagation axis) and transverse (radial) directions in the rest frame of the pulse. Photo-emission produces a distribution of "photo-electrons" which may be approximately described by a uniformly charged axially-symmetric ellipsoid with maximum radius R and half-length L. The charge density of this distribution is given by $\rho_0 = Q/\frac{4}{3}\pi R^2 L$ where $Q = Nq$ is the total charge consisting of N electrons. The electrostatic potential $\Phi(r, z)$ of this electron distribution in cylindrical coordinates is given by [16, 20, 21]

$$\Phi(r,z) = \frac{\rho_0}{2\epsilon_0}\left(\frac{\arctan(\Gamma)}{\Gamma}R^2 - \frac{1}{2}\left(1-\mathcal{M}\right)r^2 - \mathcal{M}z^2\right), \tag{1.8}$$

where $\Gamma = \sqrt{R^2/L^2 - 1}$ is the eccentricity of the ellipse and $\mathcal{M}$ is given by

$$\mathcal{M} = \frac{1+\Gamma^2}{\Gamma^3}\left(\Gamma - \arctan(\Gamma)\right). \tag{1.9}$$

The fields in the electron bunch are found using $\mathbf{E}(r,z) = -\boldsymbol{\nabla}\Phi(r,z)$, which are found to depend linearly on the coordinates r and z as given by

$$\mathbf{E}(r,z) = \frac{\rho_0}{\epsilon_0}\left(\frac{1}{2}\left(1-\mathcal{M}\right)r\hat{\mathbf{r}} + \mathcal{M}z\hat{\mathbf{z}}\right). \tag{1.10}$$

The transverse and longitudinal linear space-charge fields in the bunch yield a linear expansion in both the longitudinal (ℓ) and transverse (t) directions during acceleration and propagation. In the rest frame of the pulse, potential energy is converted into kinetic energy as the pulse disperses. The potential energy of the bunch can be evaluated in closed form and is found by integration of $\Phi(\mathbf{r})$

$$U_p = \frac{1}{2}\rho_0 \int \Phi(\mathbf{r}) d\mathbf{r} = \frac{1}{2}\rho_0 \int_0^{2\pi} d\theta \int_{-L}^{L} dz \int_0^{R\sqrt{1-z^2/L^2}} \Phi(r,z) r dr, \tag{1.11}$$

$$U_p = \frac{3Q^2}{20\pi\epsilon_0 L} \frac{\arctan(\Gamma)}{\Gamma}. \tag{1.12}$$

In the limit where $R \gg L$, $U_p \to 3Q^2/40\epsilon_0 R$ remains finite. The particles in the bunch develop a linear spatial correlation for which the velocity vector describing an electron is $\mathbf{v}(r,z) = \frac{r}{R} v_t \hat{\mathbf{r}} + \frac{z}{L} v_\ell \hat{\mathbf{z}}$. The kinetic energy of the bunch is given by

$$U_k = \frac{1}{2} m_e \frac{\rho_0}{e} \int_0^{2\pi} d\theta \int_{-L}^{L} dz \int_0^{R\sqrt{1-z^2/L^2}} |\mathbf{v}(r,z)|^2 r dr \tag{1.13}$$

$$U_k = \frac{Q/e}{5} m_e v_t^2 + \frac{Q/e}{10} m_e v_\ell^2. \tag{1.14}$$

As an illustration of the effects of space-charge dispersion, the magnitude of the induced velocity chirp is estimated in the longitudinal direction by assuming that the potential energy U_p of the bunch at the instance of photo-emission gets completely converted to kinetic energy U_k after the pulse has dispersed in time during propagation. If the initial charge distribution is sufficiently uniform, the transverse and longitudinal velocities will be roughly equal. One then finds that $v_\ell = \sqrt{Ne^2/4\epsilon_0 m_e R}$, where $N = Q/e$ is the number of electrons in the bunch. For $N = 10^6$ electrons, the maximum longitudinal velocity gain is on the order or $v_\ell \approx 10^6$ m/s for an initial transverse pulse radius of 50 μm, corresponding to a maximum energy gain (loss) of $U_k \approx 20$ eV for particles at the front (back) of the electron pulse as indicated in figure 1–2. The $p_z - z$ phase space representation

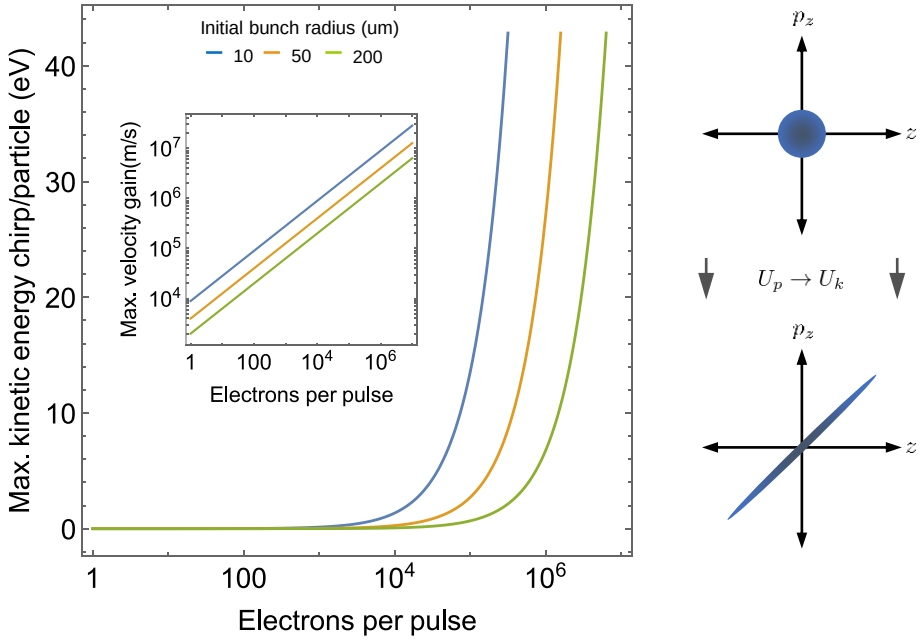

Figure 1–2: Space-charge effects in ultrashort electron pulses
Right) Magnitude of kinetic energy chirp acquired by an ultrashort electro pulse produced by photoemission for various initial radii as a function of the bunch charge (electrons per pulse). The maximum velocity gain is shown in the inset. Left) illustration of the $p_z - z$ phase space evolution of the electron pulse distribution. Initially there are no $p_z - z$ correlations and the bunch energy in the rest frame of the pulse is mostly potential energy due to a high charge density. Over time the potential energy is converted to kinetic energy resulting in a roughly linear $p_z - z$ correlation.

of this process is the following: Immediately following photo-emission, momentum in the longitudinal direction (p_z) is uncorrelated with the spatial coordinate (z); $p_z(z)$ is initially homogeneous. Over time the space-charge forces induce a strengthening linear correlation in the bunch distribution; $p_z(z) \propto z$ is linearly correlated along the longitudinal direction.

1.4.1 Momentum modulation with time-dependent fields

The dominant first order effect of space-charge broadening is the deterioration of the temporal resolution by lengthening the electron pulse in time. As shown in Fig. 1–2,

this effect is strongly dependent on the pulse-charge Q, conforming with a basic intuition from electrostatics. After roughly 1 nanosecond ($\sim$ 20 cm propagation length at 100 keV) an electron pulse containing $Q = 10^6$ electrons initially with temporal duration $\tau_0 \approx 100$ femtoseconds stretches to ~ 10 picoseconds due to space-charge dispersion. Fortunately, the linear correlation in $p_z - z$ occurring in phase space of the electron pulse distribution enables a solution. The solution is to re-compress the pulse with a time-dependent field so as to invert the linear $p_z - z$ correlation [16, 22].

Consider a harmonic time-varying electric field $E_z(t) = E_{0z}\sin(\omega t+\varphi)$ along the z axis of propagation of the electron pulse. Electrons interacting with the field will experience a net change in momentum Δp_z according to

$$\Delta p_z(t_i) = -e\int_{t_i}^{t_i+T} E_z(t)dt, \tag{1.15}$$

where T is the interaction time of the electrons injected into the field $E_z(t)$ at time t_i. Positively chirped electrons will interact with the field earlier in time and will thus sample a different portion of the oscillating field than the negatively chirped electrons. This difference in arrival time at the field position results in a difference in the momentum gained (or lost) by the electrons depending on their position within the pulse. This results in an energy/momentum dependent velocity modulation which can be used to "invert" space-charge induced dispersion. Since the space-charge induced energy gain is much less than the total kinetic energy ($v_\ell \ll v$) of each electron, it can be assumed that each electron spends the same amount of time $T = d/v$ interacting with $E_z(t)$. Furthermore, the phase of the field oscillation can be set to $\varphi \to -\omega d/2v + \phi$ such that electrons at the center of the pulse (*i.e.* those for which $v_\ell = 0$) experience on average $E_z(t) = 0$ when $t_i = 0$. Appropriate selection of the phase yields a deceleration (acceleration) of positively (negatively) chirped electrons. An overall field phase shift of π results in precisely the

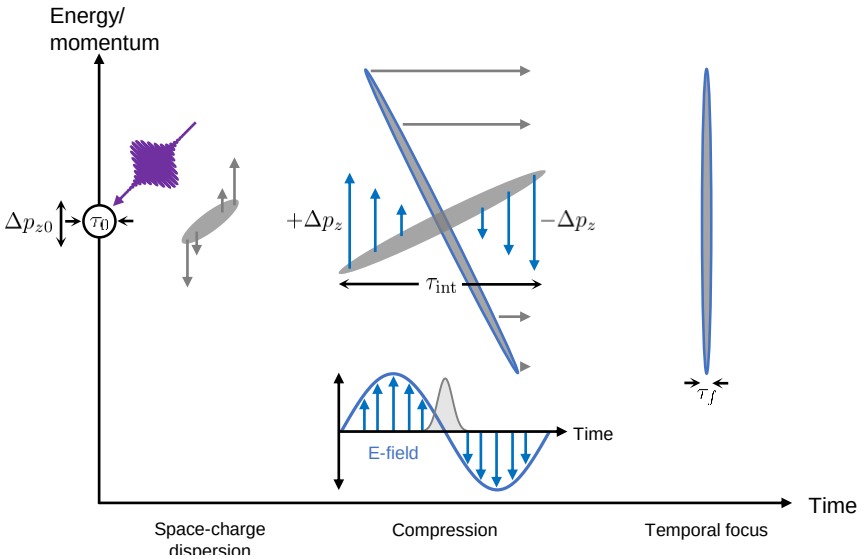

Figure 1–3: Concept of pulse compression with time-dependent electric fields
Electron pulses produced by photo-emission have an initial momentum spread Δp_{z0} and pulse duration τ_0 roughly equivalent to the optical pulse. Space-charge effects lead to the uniform broadening of the momentum distribution by Δp_z along the longitudinal $z-$axis resulting in an elongated pulse with duration $\tau_{\rm int}$. A linearly-varying electric field introduced a momentum dependent modulation of the pulse which reverses the space-charge evolution resulting in the re-compression of the pulse to a duration τ_f at the temporal focus position further down the propagation axis.

opposite effect: further temporal stretching of the pulse. In order to have a linear $\Delta p_z(t_i)$, necessary for the inversion of space-charge effects, the pulse duration upon injection into the field is much less than the period of the field cycle, $\tau \ll 1/\omega$ so that the electrons will sample the linearly varying segment of the field. The maximum momentum gain difference between the fastest electrons which interact with the electric field first and the slowest electrons which interact at the latest times can be estimated as follows. The duration of the electron pulse upon injection into the field region is $\tau = 2L/v$. This is found by evaluating $\Delta\Delta p_z^{\rm max} = \Delta p_z(t_i = \tau/2 = L/v) - \Delta p_z(t_i = -\tau/2 = -L/v)$ which yields

$$\Delta\Delta p_z^{\rm max} = \frac{eE_{0z}\omega\tau d}{v}\cos(\phi). \tag{1.16}$$

The details of the physics of electron pulse compression will be described further in chapter 2. The required compression fields can be reliably produced using 3-dimensional radio-frequency cavities operating in the gigahertz frequency range. In this thesis the compression of electron pulses to the ∼100 fs regime has been demonstrated for pulse charges of 0.1 pC ($\sim 10^6 e^-$) using a 3 GHz cavity. These pulses form a suitable probe of atomic scale dynamics in condensed matter.

1.5 Laser-microwave synchronization

Equation (1.15), along with our strict phase conditions lead to a pronounced sensitivity to the phase stability of the harmonic electric field performing the compression operation. In essence, phase fluctuations $\Delta\phi$ in the cycle of $E_z(t)$ result in either a gain or reduction in the average kinetic energy of the pulse depending on the sign of $\Delta\phi$. This translates to a change in the time-of-flight from the compression cavity to the sample position in an experiment and gives rise to a timing discrepancy with respect to a reference (for example, an optical laser pulse). This effect is extreme for typical cavity structures used for electron diffraction and is on the order of 100 fs/mrad depending on details of the beamline and cavity geometry. This complication arises predominantly from two sources: 1) the quality of synchronization between the laser system driving the electron pulse generation and the RF signal driving the cavity compressor and 2) the frequency detuning between the RF drive signal and the compression cavity resonance. Important concepts related to quantifying the quality of synchronization and the overall phase/frequency stability of a harmonic signal will be presented in Sec. 2.4.1.

1.6 Theory of electron scattering from crystalline materials

Scattering is a very general tool in physics and it can be applied with unprecedented precision in a host of systems. The basic idea is to determine information about a system

by analyzing the difference between incident and outgoing waves. This includes measuring the *momentum transfer* and *energy transfer* between the incident and outgoing waves. Scattering patterns are formed through the interference of the scattered waves. The resulting interference pattern results from phase modulations imparted on the scattered waves through the interaction of the wave with the scattering source. In large periodic systems such as crystals, this interference process culminates in a diffraction pattern which maps the crystal structure in momentum space. In this section the key results of scattering theory are presented when considering electrons as the radiation source. There are many excellent resources available on scattering [23, 24, 25, 26, 27].

1.6.1 Quantum description of single particle scattering due to a potential

Electrons moving in free-space satisfy the time-dependent Schrödinger equation [28]

$$\frac{\hbar^2}{2m_e}\nabla^2\Psi(\mathbf{r},t) - i\hbar\frac{\partial}{\partial t}\Psi(\mathbf{r},t) = 0, \tag{1.17}$$

and are described by plane-wave solutions of the form $\Psi(\mathbf{r},t) \propto \exp\left(2\pi i\mathbf{k}\cdot\mathbf{r} + i\omega t\right)$. The energy eigenvalue E is related to the wavevector $\mathbf{k}$ according to $E = \hbar\omega = \frac{\hbar^2|\mathbf{k}|^2}{2m_e}$, where $|\mathbf{k}| = 2\pi/\lambda$ is the electron wavelength. The evolution of this simple plane-wave solution upon the interaction with an electrostatic potential $V(\mathbf{r})$ is of primary interest. The influence of $V(\mathbf{r})$ on $\Psi(\mathbf{r},t)$ determines the amplitude of the scattered wave and transfers a specific phase relationship with respect to the incident wave. For an incident electron with energy $E = 100$ keV, $\lambda = 3.7$ pm, which yields an angular frequency of $\omega = \hbar/2m_e\lambda^2 = 4.23 \times 10^{18}$ Hz. The magnitude of this frequency establishes that the scattering sites (atoms for example) appear completely static during the temporal period of electron wave oscillation. From this it can be assumed that the scattering from the

potential $V(\mathbf{r})$ is a time-independent process and that the $i\omega t$ phase component may be ignored[1] .

It follows that the scattered electron wave is a solution of the time independent Schrödinger equation

$$-\frac{\hbar^2}{2m_e}\nabla^2\psi(\mathbf{r}) + V(\mathbf{r})\psi(\mathbf{r}) = E\psi(\mathbf{r}). \tag{1.18}$$

This can be re-written in the form of the Helmholtz equation given by

$$\left(\nabla^2 + k^2\right)\psi(\mathbf{r}) = \mathcal{V}\left(\mathbf{r}, \psi(\mathbf{r})\right), \tag{1.19}$$

where $\mathcal{V}\left(\mathbf{r}, \psi(\mathbf{r})\right) = \frac{2m_e}{\hbar^2}V(\mathbf{r})\psi(\mathbf{r})$ [29]. A solution can be found using the Green's function method, where the Green's function $\mathcal{G}(\mathbf{r})$ satisfies $\left(\nabla^2 + k^2\right)\mathcal{G}(\mathbf{r}) = \delta^3(\mathbf{r})$ [29]. It follows that $\psi(\mathbf{r}) = \int d\mathbf{r}_0 \mathcal{G}(\mathbf{r} - \mathbf{r}_0)\mathcal{V}(\mathbf{r}_0, \psi(\mathbf{r}_0))$ is a solution to Eqns. (1.18) and (1.19). A Green's function of the form $\mathcal{G}(\mathbf{r} - \mathbf{r}_0) = \exp\left(ik|\mathbf{r} - \mathbf{r}_0|\right)/4\pi|\mathbf{r} - \mathbf{r}_0|$ may be used which yields the following integral solution for Eqn. (1.19)

$$\psi(\mathbf{r}) = \psi_0(\mathbf{r}) - \frac{m_e}{2\pi\hbar^2}\int d\mathbf{r}_0 \frac{\exp\left(ik|\mathbf{r} - \mathbf{r}_0|\right)}{|\mathbf{r} - \mathbf{r}_0|}V(\mathbf{r}_0)\psi(\mathbf{r}_0), \tag{1.20}$$

where $\psi_0(\mathbf{r})$ satisfies the Schrödinger equation in free-space and describes the incoming wave before scattering.

The *first Born approximation* [30] is made by assuming that the interaction of $\psi(\mathbf{r})$ with $V(\mathbf{r})$ is spatially centered around $\mathbf{r}_0 = 0$. Furthermore, our interest in the behavior of the wave-function at large distances from the scattering location, *i.e.* for $|\mathbf{r}| \gg |\mathbf{r}_0|$. From this it can be said that $|\mathbf{r} - \mathbf{r}_0| \approx r - \hat{\mathbf{r}} \cdot \mathbf{r}_0$ and the Green's function simplifies to

[1] One might point out that the topic of this thesis is in fact *time-dependent* electron scattering. The experiments presented hereafter in this thesis measure time-dependent scattering through the assembly of scattering measurements each of which are assumed to be static ("snapshot") in time over a prescribed time sequence.

$\mathcal{G}(\mathbf{r},\mathbf{r}_0) = \exp\left(ik|\mathbf{r}-\mathbf{r}_0|\right)/4\pi|\mathbf{r}-\mathbf{r}_0| \approx r^{-1}\exp(ikr)\exp(-ik\hat{\mathbf{r}}\cdot\mathbf{r}_0)$, allowing for Eqn. (1.20) to take the form

$$\psi(\mathbf{r}) = \psi_0(\mathbf{r}) + \frac{\exp(ikr)}{r}\left[\frac{-m_e}{2\pi\hbar^2}\int d\mathbf{r}_0 \exp\left(-ik\hat{\mathbf{r}}\cdot\mathbf{r}_0\right) V(\mathbf{r}_0)\psi(\mathbf{r}_0)\right]. \tag{1.21}$$

Equation (1.21) represents the sum of a plane wave given by $\psi_0(\mathbf{r})$ and a *spherical wave* with a profile given by the $\exp(ikr)/r$ term. The term in the square brackets is the scattering amplitude f, which has units of distance. The qualitative features of Eqn. (1.21) are consistent with the scattering of light from a point source described by Huygen's principle, *i.e.* in the form of spherical waves. The amplitude, however, depends on the quantum mechanical interaction with of the wave-function ψ with the potential V at $\mathbf{r} \approx \mathbf{r}_0$.

Another approximation, called the *second Born approximation*, where the potential is assumed to be weak such that the $\psi_0(\mathbf{r}) \approx \psi_0(\mathbf{r}_0)$ can now be made. Specifically, the incident plane wave $\psi_0(\mathbf{r})\exp\left(i\mathbf{k}_0\cdot\mathbf{r}\right)$ and the scattered wave is only altered in its direction determined by $\mathbf{k}$. It follows that $\psi(\mathbf{r}_0) = \exp\left(i\mathbf{k}\cdot\mathbf{r}_0\right)$. Now the scattering amplitude f takes the following form

$$f = -\frac{m_e}{2\pi\hbar^2}\int d\mathbf{r}_0 V(\mathbf{r}_0)\exp\left(-i(\mathbf{k}-\mathbf{k}_0)\cdot\mathbf{r}_0\right). \tag{1.22}$$

The integrand above in Eqn. (1.22) can be understood as the Fourier transform of the real-space potential $V(\mathbf{r})$ with the Fourier variable $\mathbf{q} = \mathbf{k} - \mathbf{k}_0$. Moreover, it can also be seen as a matrix element describing the transition from $|\mathbf{k}_0\rangle$ to $|\mathbf{k}\rangle$ plane wave states through the interaction with $V(\mathbf{r})$ according to

$$V_{\mathbf{k}_0,\mathbf{k}} = \langle\mathbf{k}_0|V(\mathbf{r})|\mathbf{k}\rangle. \tag{1.23}$$

The scattering amplitude f is related to the differential scattering cross section $d\sigma/d\Omega = |f(\theta,\phi)|^2$, where $d\Omega = \sin\theta d\theta' d\phi'$ is the solid angle in the lab-frame.

In the case of a spherically-symmetric potential, *i.e.* $V(\mathbf{r}) = V(r)$, the angular integration may be carried out and the scattering amplitude may be expressed as

$$f(\theta) = -\frac{2m_e}{\hbar q(\theta)} \int_0^\infty dr_0 r_0 V(r_0) \sin(qr_0), \tag{1.24}$$

where the θ dependence is contained in $q(\theta) = |\mathbf{q}| = 2|\mathbf{k}| \sin(\theta/2)$. Equation (1.24) generally holds for spherical atoms (low energy orbitals, s and p, and ionically bonded materials) but becomes less accurate when the electrostatic potential involves bonding electrons. By convention, the scattering amplitude for electrons is expressed in terms of the scattering vector $\mathbf{q} = \mathbf{k} - \mathbf{k}_0$ and expressed as

$$f^e(\mathbf{q}) = \int d\mathbf{r}_0 \exp(-i\mathbf{q} \cdot \mathbf{r}_0) V(\mathbf{r}_0). \tag{1.25}$$

1.6.2 Scattering from a crystal at zero temperature

Scattering becomes a very powerful tool when the symmetry of a physical system imparts specific phase criteria for constructive and destructive or interference of the scattered waves. This allows for large scattered intensity to be measured at specific values of $\mathbf{q}$. In a crystalline solid, atoms are arranged in a periodic manner resulting in translational symmetry. A crystal consists of *unit cells* which are defined as the smallest repeating microscopic unit of the material. They can be single atoms or collections of many. In remaining completely general, the potential of the crystal is written as a sum over α atoms in the unit cell, and an infinite sum over unit cells n. The position of atom α in unit cell

n is located at $\mathbf{R}_n + \mathbf{r}_\alpha$, and the potential is written as[2] [25, 26, 23]

$$V(\mathbf{r}) = \sum_n \sum_\alpha V_\alpha \left(\mathbf{r} - \mathbf{R}_n - \mathbf{r}_\alpha\right), \tag{1.26}$$

where V_α is the potential of atom α in unit-cell n. The periodicity of $V(\mathbf{r})$ ensures that the form of $V_\alpha(\mathbf{r} - \mathbf{R}_n - \mathbf{r}_\alpha)$ is identical for a given pair of n and α values, thus the Fourier transform of $V(\mathbf{r})$, $V(\mathbf{q})$ can take the form

$$\begin{aligned} V(\mathbf{q}) &= \sum_n \sum_\alpha \int d\mathbf{r} V_\alpha(\mathbf{r} - \mathbf{R}_n - \mathbf{r}_\alpha) \exp\left(-i\mathbf{q}\cdot\mathbf{r}\right), & (1.27)\\ &= \sum_n \exp(-i\mathbf{q}\cdot\mathbf{R}_n) \sum_\alpha \int d\mathbf{r} V_\alpha(\mathbf{r}) \exp(-i\mathbf{q}\cdot\mathbf{r}) \exp(-i\mathbf{q}\cdot\mathbf{r}_\alpha), & (1.28)\\ &= \sum_{\{\mathbf{G}\}} \delta(\mathbf{q} - \mathbf{G}) \sum_\alpha V_\alpha(\mathbf{q}) \exp(-i\mathbf{q}\cdot\mathbf{r}_\alpha). & (1.29) \end{aligned}$$

In arriving at Eqn. (1.29), the mathematical identity $\sum_n \exp(-i\mathbf{q}\cdot\mathbf{R}_n) = \sum_{\{\mathbf{G}\}} \delta(\mathbf{q} - \mathbf{G})$ has been applied, and the set of vectors $\mathbf{G}$ satisfies

$$\mathbf{G}\cdot\mathbf{R}_n = 2\pi \times \text{Integer}. \tag{1.30}$$

The real-space vectors $\mathbf{R}_n = n_1\mathbf{a} + n_2\mathbf{b} + n_3\mathbf{c}$ form the basis of the crystal lattice. Equation (1.30) is a representation of the Bragg condition [31] and defines the *reciprocal* lattice vectors $\mathbf{G} = h\mathbf{a}^* + k\mathbf{b}^* + \ell\mathbf{c}^*$ which must be of the form

$$\mathbf{a}^* = 2\pi\frac{\mathbf{b}\times\mathbf{c}}{\Sigma_{\text{cell}}}, \qquad \mathbf{b}^* = 2\pi\frac{\mathbf{c}\times\mathbf{a}}{\Sigma_{\text{cell}}}, \qquad \mathbf{c}^* = 2\pi\frac{\mathbf{a}\times\mathbf{b}}{\Sigma_{\text{cell}}}, \tag{1.31}$$

where $\Sigma_{\text{cell}} = (\mathbf{a}\times\mathbf{b})\cdot\mathbf{c}$ is the volume of the unit cell and the vectors shown in Eqn. (1.31) satisfy orthogonality with their real-space counterparts, *i.e.* $\mathbf{a}^*\cdot\mathbf{a} = \mathbf{b}^*\cdot\mathbf{b} = \mathbf{c}^*\cdot\mathbf{c} = 1$.

[2] In practice, the crystal potential is multiplied by the so-called shape function $\mathcal{S}(\mathbf{r})$ which describes the finite spatial extent of the macroscopic material.

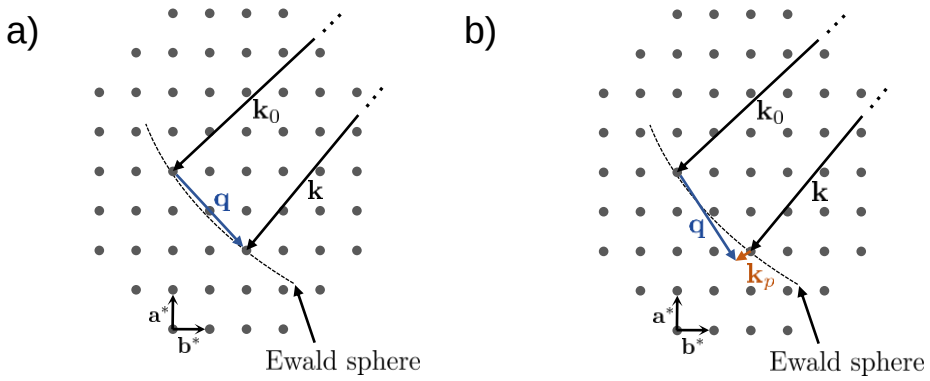

Figure 1–4: Illustration of scattering by a crystal in reciprocal space
a) Zeroth order elastic scattering where the Bragg and Laue conditions are met, $\mathbf{k} - \mathbf{k}_0 = \mathbf{q} = \mathbf{G}$, where $\mathbf{k}$ and $\mathbf{k}_0$ are the outgoing and incidient electron wavevectors, and $\mathbf{G}$ is a reciprocal lattice vector. b) First order thermal diffuse scattering where $\mathbf{q} = \mathbf{G} + \mathbf{k}_p$ with $\mathbf{k}_p$ describes a momentum contribution from phonons. The Ewald sphere is defined with a radius of $|\mathbf{k}| = |\mathbf{k}_0|$. The small electron wavelength yields a nearly flat Ewald sphere surface on the scale of the reciprocal lattice thus allowing for many instances where the Bragg and Laue conditions are satisfied.

The indices $hk\ell$ are the *Miller indices* of crystallography and define points in reciprocal space. Equation (1.30) is technically the *Laue condition* which explicitly states $\mathbf{k} - \mathbf{k}_0 = \mathbf{q} = \mathbf{G}$ and is illustrated in Fig. 1–4 a). For elastic scattering, $|\mathbf{k}| = |\mathbf{k}_0|$ and by taking the square modulus of the Laue condition one arrives at

$$\begin{aligned} 2\mathbf{k}\cdot\mathbf{G} &= |\mathbf{G}|^2, \\ 2|\mathbf{k}|\cdot|\mathbf{G}|\sin\theta &= |\mathbf{G}|^2, \\ 2\left(\frac{2\pi}{\lambda}\right)\left(\frac{2\pi n}{d}\right)\sin\theta &= \left(\frac{2\pi n}{d}\right)^2, \\ 2d\sin\theta &= n\lambda, \end{aligned} \tag{1.32}$$

where Eqn. (1.32) is the well-known Bragg Law. Above the parameter d was introduced as a lattice plane spacing distance and λ is the electron wavelength. In reciprocal space, $|\mathbf{k}| \propto \lambda^{-1}$ establishes the radius of the so-called Ewald sphere [32]. The number of reciprocal

lattice points which are intersected by the surface of the Ewald sphere determines where the Bragg and Laue conditions are met thereby yielding elastic scattering. One of the main differences between electrons and X-rays as scattering probes is that for electrons the radius of the Ewald sphere is much larger. For example, electrons at 100 keV have a wavelength on the order of picometers, which is roughly 100 times smaller than the wavelengths of hard X-rays used for diffraction (on the order of Ångstroms). This translates to a nearly flat Ewald surface of the scale of reciprocal lattice points since the radius of the Ewald sphere is ∼100 times larger. This allows for many more Bragg reflections to be observed in electron diffraction versus X-ray diffraction for a given crystal orientation.

In Equation (1.29), $V_\alpha(\mathbf{q})$ is defined for each atom labelled by α and determined through Eqn. (1.25). The term following the delta function in Eqn. (1.29), is defined as the *structure factor* $F_0(\mathbf{q} = \mathbf{G})$ [27]

$$F_0(\mathbf{G}) = \sum_\alpha V_\alpha(\mathbf{G}) \exp(-i\mathbf{G} \cdot \mathbf{r}_\alpha), \tag{1.33}$$

$$= \frac{1}{\Sigma_{\text{cell}}} \sum_\alpha f^e_\alpha(\mathbf{G}) \exp(-i\mathbf{G} \cdot \mathbf{r}_\alpha). \tag{1.34}$$

The structure factor $F_0(\mathbf{G})$ describes the amplitude of the scattering at regions of momentum space established by $\mathbf{q} = \mathbf{G}$ through the sum of contributions from all the atoms in the unit cell multiplied by a geometric phase $\mathbf{G} \cdot \mathbf{r}_\alpha$. This factor can yield extinction rules for certain $\mathbf{G}$ vectors where $F_0(\mathbf{G}) = 0$ and it generally describes the interference effects between waves scattered by different atoms in the unit cell.

As shown above, the amplitude of the wavefunction for the scattered electrons is proportional to the crystal potential, and therefore also the Fourier transform of the potential. The intensity, which is measured as some distance after the scattering, is determined by

probability amplitude of the scattered wavefunction[26]

$$I(\mathbf{q}) = \psi(\mathbf{q})^*\psi(\mathbf{q}) \propto |F_0(\mathbf{q})|^2 = \sum_\alpha \sum_\beta f_\alpha^e(\mathbf{q}) f_\beta^e(\mathbf{q}) \exp\left(-i\mathbf{q}\cdot(\mathbf{r}_\alpha - \mathbf{r}_\beta)\right). \tag{1.35}$$

1.6.3 Effect of lattice vibrations: phonons

The treatment of scattering presented in the previous section assumed a temperature of $T = 0$. This assumption fixes atoms perfectly at their equilibrium lattice positions and ensures that the distance between any pair of atoms in the material is perfectly equal to a lattice vector $\mathbf{R}_n = n_1\mathbf{a} + n_2\mathbf{b} + n_3\mathbf{c}$. Lattice vibrations and thermal effects complicate this picture, but do not in any way detract from the power of scattering as a tool for accurate structural determination of material properties. At finite temperatures, the lattice system of atoms contains thermal energy which is stored in the time-dependent displacement of the atoms about their equilibrium positions ($\mathbf{r}_\alpha$). The geometric structure factor must be re-written under the transformation of $\mathbf{r}_\alpha \rightarrow \mathbf{r}_\alpha + \mathbf{u}_\alpha$ where $\mathbf{u}_\alpha$ is the instantaneous displacement of atom α and a time average over the motion given by $\langle \mathbf{u}_\alpha(t) \rangle$ must be taken. Mathematically, this reads [23, 33, 26]

$$F_0(\mathbf{q}) = \sum_\alpha V_\alpha(\mathbf{q}) \left\langle \exp(-i\mathbf{q}\cdot(\mathbf{r}_\alpha - \mathbf{u}_\alpha)) \right\rangle = \sum_\alpha f_\alpha(\mathbf{q}) \exp(-M_\alpha(q)) \exp(-i\mathbf{q}\cdot\mathbf{r}_\alpha). \tag{1.36}$$

The factor $M_\alpha(q) = 2\pi^2\langle u_\alpha^2 \rangle q^2$ is the isotropic Debye-Waller factor and characterizes the weakening of the scattering amplitude of the atoms due to thermal motion. This suppression can also be thought of as resulting from the Bragg condition not being met as often during a time-averaging interval.

More generally, in order to understand the full effect of lattice vibrations on the scattering intensity $I(\mathbf{q})$, the ensemble time-averaged form of Eqn. (1.35) must be calculated. In fact, more specifically the ensemble average of the square of Eqn. (1.27) is required and

is given by

$$I(\mathbf{q}) = \left\langle \left| \sum_m \sum_\alpha f_\alpha \exp\left(-i\mathbf{q}\cdot(\mathbf{R}_m - \mathbf{r}_\alpha - \mathbf{u}_\alpha)\right) \right|^2 \right\rangle, \tag{1.37}$$

$$= \sum_{m,n} \sum_{\alpha,\beta} f_\alpha f_\beta \exp\left(-i\mathbf{q}\cdot(\mathbf{R}_{m,n} - \mathbf{r}_{\alpha,\beta})\right) \left\langle \exp\left(i\mathbf{q}\cdot(\mathbf{u}_{m,\alpha} - \mathbf{u}_{n,\beta})\right) \right\rangle, \tag{1.38}$$

$$= \sum_{m,n} \sum_{\alpha,\beta} f_\alpha f_\beta \exp\left(-i\mathbf{q}\cdot(\mathbf{R}_{m,n} - \mathbf{r}_{\alpha,\beta})\right) \exp\left(-\frac{1}{2}\left\langle \left[\mathbf{q}\cdot(\mathbf{u}_{m,\alpha} - \mathbf{u}_{n,\beta})\right]^2 \right\rangle\right) \tag{1.39}$$

In Eqn. (1.39) the double sums arise from squaring the sum, the vector abbreviations $\mathbf{z}_{i,j} = \mathbf{z}_i - \mathbf{z}_j$ have been introduced to simplify the equation and the identity $\langle \exp(-ix) \rangle = \exp(-\frac{1}{2}\langle x^2 \rangle)$ has been applied.

The motion of atoms in solids described by the displacement vectors $\mathbf{u}$ is not arbitrary, they consist of specific terms involving specific momenta and frequencies determined by the symmetries and material constants of the crystal lattice. In the harmonic approximation, valid when $|\mathbf{r}_\alpha| \gg |\mathbf{u}_\alpha|$, atoms move according to the phonon modes supported by the material. These modes are found by finding normal mode solutions to the *dynamical matrix* [34, 26, 35] which yields a set of phonon Eigenvectors $\hat{\mathbf{e}}_{j,\alpha,\mathbf{k}}$ and Eigenenergies $\omega_{j,\mathbf{k}}$ where the index j specifies the phonon branch which labels the symmetry properties of the phonon mode. Making use of this, the displacement of atom α in unit cell m may be written as a sum over phonon modes in the following manner

$$\mathbf{u}_{m,\alpha} = \Re\left\{ \frac{1}{m_\alpha} \sum_{j,\mathbf{k}} a_{j,\mathbf{k}} \hat{\mathbf{e}}_{j,\alpha,\mathbf{k}} \exp\left(-i\mathbf{k}\cdot\mathbf{R}_m - i\omega_{j,\mathbf{k}} t + i\varphi_{j,\mathbf{k}}\right) \right\}, \tag{1.40}$$

where m_α is the mass of atom α and $\varphi_{j,\mathbf{k}}$ is a phase factor. The phonon amplitude is $a_{j,\mathbf{k}}$ is related to the quantum number $n_{j,\mathbf{k}}$ of phonons in the phonon field $|a_{j,\mathbf{k}}|^2 = \frac{\hbar}{m_\alpha \omega_{j,\mathbf{k}}}\left(n_{j,\mathbf{k}} + \frac{1}{2}\right)$. Equation (1.40) is substituted into Eqn. (1.39) and expanded in the small displacement limit in a Taylor series $I(\mathbf{q}) \approx I_0(\mathbf{q}) + I_1(\mathbf{q}) + \ldots$. The derivation can be found in several references [33, 23]. The zeroth-order term reduces to the $T = 0$

expression shown in Eqn. (1.29) and describes the Bragg peak reflections. The first-order term is called the *thermal diffuse scattering* intensity and simplifies to

$$I_1(\mathbf{q}) \propto \sum_j \frac{n_{j,\mathbf{k}} + \frac{1}{2}}{\omega_{j,\mathbf{k}}} \left|F_{1j}(\mathbf{q})\right|^2, \tag{1.41}$$

where $F_{1j}(\mathbf{q})$ is called the *one-phonon structure factor* and is given by

$$F_{1j}(\mathbf{q}) = \sum_\alpha \frac{f_\alpha(\mathbf{q})}{\sqrt{m_\alpha}} \exp\left(-M_\alpha\right) \left(\mathbf{q} \cdot \hat{\mathbf{e}}_{j,\alpha,\mathbf{k}}\right) \exp\left(-i\mathbf{q} \cdot \mathbf{r}_\alpha\right). \tag{1.42}$$

The form of $F_{1j}(\mathbf{q})$ is very similar to Eqn. (1.36) except for an additional factor of $\mathbf{q} \cdot \hat{\mathbf{e}}_{j,\alpha,\mathbf{k}}$. This factor gives distinct structure to $F_{1j}(\mathbf{q})$ (and therefore also $I_1(\mathbf{q})$) through the set of phonon Eigenvectors, $\{\hat{\mathbf{e}}_{j,\alpha,\mathbf{k}}\}$ leading to regions of reciprocal space where $F_{1j}(\mathbf{q})$ vanishes if $\mathbf{q} \perp \hat{\mathbf{e}}_{j,\alpha,\mathbf{k}}$. The $\mathbf{q}$ dependence is contained through its relation to $\mathbf{k}$ and $\mathbf{G}$ which is $\mathbf{q} = \mathbf{G} + \mathbf{k}$. The thermal diffuse intensity also is proportional to the *mode occupancy* $n_{j,\mathbf{k}}$ which yields a linear dependence of the scattering intensity on the number of phonons in the branches j appearing at a given $\mathbf{q}$. Futhermore, the intensity depends inversely on the frequency of the phonons $\omega_{j,\mathbf{k}}$.

1.6.4 Time-resolved electron scattering

Ultrafast electron scattering in a pump-probe setup involves collecting diffraction intensity at a particular time delay value Δt, $I(\mathbf{q}, \Delta t)$. Each image of $I(\mathbf{q}, \Delta t)$ is formed by the scattering of an ultrashort electron pulse with a temporal duration of $\sim$ 100 fs. Thus $I_0(\mathbf{q}, \Delta t)$ is a measure of the average crystalline structure and $I_1(\mathbf{q}, \Delta t)$ is a measure of phonon properties within a 100 fs time-interval. In practice, the time-dependent intensity changes as the time-delay is varied in a controlled manner are of interest. It is also convenient to normalize the intensity by its value before laser excitation (which marks $\Delta t = 0$) which reads

$$\Delta I(\mathbf{q}, \Delta t) = \frac{I(\mathbf{q}, \Delta t) - I(\mathbf{q}, 0)}{I(\mathbf{q}, 0)}. \tag{1.43}$$

This convention is useful for our measurements as the relative changes which arise from effects such as lattice heating, changes in crystal symmetry during a phase transition and changes in atomic form factors are of primary interest. The relative change in thermal diffuse scattering $\Delta I_1(\mathbf{q}, \Delta t)$ reports on the number of phonons $n_{j,\mathbf{k}}$ along with their energies $\omega_{j,\mathbf{k}}$ as a function of Δt.

1.7 Optical excitation of solids

Light interacts with the electronic degrees of freedom of the material. There are many excellent texts about this diverse topic [36, 37, 38, 39], in this section the relevant physics for the experiments presented in later chapters are presented. Electrons are described by wavevector states $|\varphi_{\mathbf{k}_e}(\mathbf{r})\rangle$ with $\mathbf{k}_e$ being the electronic wavevector. In crystals, the electronic states are modulated by the periodicity of the lattice and their wavefunctions are given by Bloch states

$$|\varphi_{\mathbf{k}_e}(\mathbf{r})\rangle = v_{\mathbf{k}_e}(\mathbf{r}) \exp\left(i(\mathbf{G} - \mathbf{k}_e) \cdot \mathbf{r}\right). \tag{1.44}$$

The energy Eigenstates for the system described by a Hamiltonian is given by the dispersion $\epsilon(\mathbf{k}_e)$ which maps energy-momentum relationship for the electronic states in the form of continuous bands. For simple materials well-described by Bloch theory, if the Fermi energy ϵ_{F} falls within an electronic band, that band becomes the conduction band. Within the conduction band there are many un-occupied states into and out of which the electrons can collectively flow and the material is said to be metallic. In this situation electronic wavefunctions in the conduction band are delocalized throughout the material. Energy regions between bands are sometimes called forbidden bands, since electronic states with such energies are not supported in the material. When the Fermi energy falls in forbidden bands, the material is an insulator since electrons fill up all available valence band states below the Fermi level. The *band gap* is the energy difference between the valence band

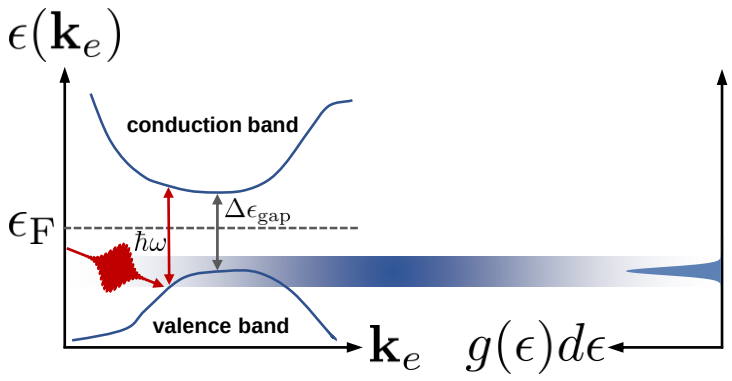

Figure 1–5: Illustration of optical excitation of electrons in solids in the form of an interband transition.
An interband transition occurs between valence and condution band states if the energy difference is matched by the photon energy $\hbar\omega$. The number of available states in a energy range $g(\epsilon)d\epsilon$ is largest for parallel bands, which typically occurs in the vicinity of the band gap $\Delta\epsilon_{\mathrm{gap}}$ for a direct band gap semiconductor.

maximum and conduction band minimum. A *direct* band gap is the situation where these points occur at the same point in momentum space, and an *indirect* band gap is where they do not.

Optical light fields drive electronic transitions defined by the band structure of the material. The process creates electrons in the conduction band and holes in the valence band. In general many types of transitions are possible, and they all reduce to evaluating the appropriate transition probabilities in terms of quantum mechanical Hamiltonian describing the light-matter interaction. Such a Hamiltonian for one electron in an optical field is given by

$$\mathcal{H}(\mathbf{r},\mathbf{k}_e) = \frac{\hbar^2}{2m}k_e^2 + V(\mathbf{r}) - \frac{e\hbar}{mc}\mathbf{A}\cdot\mathbf{k}_e + \frac{e^2}{2mc^2}A^2, \tag{1.45}$$

where $\mathbf{A}$ is the vector potential of the optical field. The procedure of second quantization transforms (1.45) into the *Jaynes-Cummings Hamiltonian* [40] of quantum optics which treat the optical field as a quantized photon field and the classical limit recovers Maxwell's

equations in a medium [41]. The strength of the optical field is generally weak, and the transition rates associated with Eqn. (1.45) can be treated within the framework of perturbation theory. The energy dispersion curves $\epsilon(\mathbf{k}_e)$ describing the electronic states form though the overlap of all the discrete atomic states of all the individual atoms comprising the material. Although a continuum of electronic states form, the bands still impose energy conditions which must be satisfied for an optical transition to occur. In semiconductors and insulators, electronic transitions from valence to conduction band can occur when the photon energy of the optical light field is equal to or greater than the energy of the band gap. Photons carry very little momentum ($k_{\text{photon}} = 2\pi/\lambda \approx 10^5$ cm^{-1}) compared to the dimensions of the Brillouin zone ($\pi/a \approx 10^8$ cm^{-1}, with a being a lattice constant). Given this, momentum conservation insists that the wavevectors of the valence and conduction band electronic states involved in an optical transition must be equal.

1.7.1 Interband transitions

An *interband transition* is considered first. In this case the photon energy equals the energy difference between the valence and conduction bands, $\epsilon_v(\mathbf{k})$ and $\epsilon_c(\mathbf{k})$, respectively. The transition probability per unit volume $\mathcal{W}(\mathbf{k})/d\mathbf{k}$ in momentum space is found using Fermi's Golden Rule (FGR) and depends on the matrix element $\langle\varphi_{\mathbf{k}_v}|\mathcal{H}'|\varphi_{\mathbf{k}_c}\rangle$ of the interaction Hamiltonian $\mathcal{H}' = -\frac{e\hbar}{mc}\mathbf{A}\cdot\mathbf{k}_e$ [39, 36].

$$\mathcal{W}(\mathbf{k}) = \frac{2\pi}{\hbar}\left|\langle\varphi_{\mathbf{k}_v}|\mathcal{H}'|\varphi_{\mathbf{k}_c}\rangle\right|^2 \delta\left(\epsilon_c(\mathbf{k}) - \epsilon_v(\mathbf{k}) - \hbar\omega\right) d\mathbf{k}. \tag{1.46}$$

The coupling between the two states is determined by $\langle\varphi_{\mathbf{k}_v}|\mathcal{H}'|\varphi_{\mathbf{k}_c}\rangle$ and can be taken as independent of $\mathbf{k}$ since $\mathbf{A}$ is approximately constant throughout the Brillouin zone. Integration of Eqn. (1.7.1) determined the total transition rate

$$W = \frac{2\pi}{\hbar}\left|\langle\varphi_{\mathbf{k}_v}|\mathcal{H}'|\varphi_{\mathbf{k}_c}\rangle\right|^2 g(\hbar\omega). \tag{1.47}$$

where $g(\hbar\omega)$ is called the joint density of states and describes the number of states per unit volume in momentum space between valence and conduction bands separated in energy by $\hbar\omega$. The joint density of states depends on the curvature of the valence and conduction bands. It is given by

$$g(\hbar\omega) = \frac{2}{(2\pi)^3}\int d\mathbf{k}\delta(\epsilon_c(\mathbf{k}) - \epsilon_v(\mathbf{k}) - \hbar\omega), \tag{1.48}$$

where the volume element can be written as $d\mathbf{k} = dSdk_n$ where S is an energy surface where $\epsilon_c - \epsilon_v = \hbar\omega$ and to which k_n is normal. Using the definition of the gradient $|\boldsymbol{\nabla}(\epsilon_c - \epsilon_v)|dk_n = d(\epsilon_c - \epsilon_v)$. The joint density of states then reads

$$g(\hbar\omega) = \frac{2}{(2\pi)^3}\iiint \frac{dSd(\epsilon_c - \epsilon_v)\delta(\epsilon_c - \epsilon_v - \hbar\omega)}{|\boldsymbol{\nabla}(\epsilon_c - \epsilon_v)|}, \tag{1.49}$$

$$g(\hbar\omega) = \frac{2}{(2\pi)^3}\iint \frac{dS}{|\boldsymbol{\nabla}(\epsilon_c - \epsilon_v)|_{\hbar\omega}}. \tag{1.50}$$

Equation (1.50) describes the number of states lying on the surface element dS of the energy difference between bands $\epsilon_c - \epsilon_v$. The dependence of g on the gradient of the bands translates to a large number of states available to undergo interband transitions in regions where energy surfaces are parallel. From this, the density of states is expected to be large near the band gap. For transitions where $\hbar\omega > \Delta\epsilon_{\text{gap}}$, transitions occur, but are carried out by fewer electron-hole carrier pairs. With ultrashort laser pulses, this can be overcome to some extent because the high energy bandwidth offered by ultrafast laser pulses covers more electronic states. Transitions for $\hbar\omega > \Delta\epsilon_{\text{gap}}$ inevitably leave the electrons and holes away from the band minimum and maximum respectively with excess energy roughly equal to $\hbar\omega/2 - \Delta\epsilon_{\text{gap}}/2$ depending on the curvature of the bands. In a typical semiconductor, the electrons and holes may then undergo scattering and/or phonon emission processes to relax back to the band minima/maxima before carrier recombination accross the gap.

For direct interband transitions discussed above, momentum conservation requires that the initial and final electronic wavevectors be equal. This means the electron remains at the same point in the Brillouin zone. Another possible interband transition is an indirect transition where the final electronic state has a different crystal momentum. Because the photons carry very little momentum, the transition must be mediated by a relatively large momentum quasiparticle such as a phonon. The interband transition becomes a second-order process where the matrix element can be expanded in terms of the coupling of the conduction and valence electronic states to phonon states of energy $\hbar\omega_p$ and wavevector $\mathbf{k}_p$. The transition rates are calculated by determining appropriate composite wavefunctions for the coupled electron-phonon system and evaluating a new joint density of states which involves the phonon system. A complete treatment of indirect transitions is beyond the scope of this thesis, so they are only mentioned here briefly for completeness. A deeper discussion can be found in various textbooks [39, 38].

1.7.2 Intraband transitions

The type of optical transitions most important for metals are *intraband* transitions. In this case, electrons are delocalized throughout a partially filled conduction band. In the steady-state regime, the collective electronic response is typically well described by the Drude model of conduction and other variants. Optical intraband transitions are governed by the availability of states s' with an energy difference given by the photon energy $\hbar\omega$ in the conduction band, the density of which are given by Fermi distribution functions $f(\epsilon_{s'})$. The transition probability per unit volume in momentum space from state $s \to s'$ is given by by the Golden Rule:

$$\mathcal{W}_{s\to s'} = \frac{2\pi}{\hbar} \left|\langle s'|\mathcal{H}'_{\text{int}}|s\rangle\right|^2 f(\epsilon_{s'}) \left[1 - f(\epsilon_s)\right] \delta\left(\hbar\omega - (\epsilon_{s'} - \epsilon_s)\right). \tag{1.51}$$

The states $|s\rangle$ and $|s'\rangle$ could be Bloch states, but are often considered free electron (Fermi gas) states. Ultrafast laser excitation of metals transfers energy to the electrons via the transitions described by Eqn. (1.51). This creates a non-thermal (non-Fermi-Dirac) electron distribution which thermalizes through electron–electron scattering and electron phonon-coupling processes. This process yields behavior such as screening dynamics and phonon emission.

1.8 Electron-phonon coupling

Electron-phonon interactions are very important in a variety of materials as they can have a significant impact of their bulk properties. A general picture and discussion of electron-phonon interactions insofar as they relate to experimental observables in an ultrafast electron diffraction experiment in presented in this section. The Hamiltonian for a system of phonons with wavevector $\mathbf{k}_p$ (in a lattice) and electrons with momentum p_i can be written as [42, 43, 25]

$$\begin{aligned} \mathcal{H} &= H_p + H_e + H_{ei}, \\ &= \sum_{\mathbf{k}_p n} \omega_{\mathbf{k}_p n} a^\dagger_{\mathbf{k}_p n} a_{\mathbf{k}_p n} + \sum_i \left[\frac{p_i^2}{2m} + \frac{e^2}{2} \sum_{j \neq i} \frac{1}{r_{ij}} \right] + \sum_{ij} V_{ei}(\mathbf{r}_i - \mathbf{R}_j), \end{aligned} \tag{1.52}$$

where the first term counts the numbers of phonons n at each wavevector $\mathbf{k}_p$, the second describes the total energy of the electrons and the third generally represents the interaction potential between between electrons at position $\mathbf{r}_i$ and atoms at position $\mathbf{R}_j$. As described in Sec.1.6.3 phonons create displacements $\mathbf{u}_j$ in the atomic coordinates, and it is reasonable to make the harmonic approximation for small $\mathbf{u}_j$ and take terms below $\mathcal{O}(u^2)$. Following this H_{ei} can be written as

$$H_{ei} \approx \sum_{ij} \left[V_{ei}(\mathbf{r}_i - \mathbf{R}_j^{(0)}) - \mathbf{u}_j \cdot \boldsymbol{\nabla} V_{ei}(\mathbf{r}_i - \mathbf{R}_j^{(0)}) \right]. \tag{1.53}$$

The first term in Eqn. (1.53) describes the periodic potential which determines the Bloch Eigenstates. The second term describes the modulation of this potential arising from atomic displacements and is denoted by $V_{ep}(\mathbf{r})$. By representing $V_{ei}(\mathbf{r})$ and $\boldsymbol{\nabla} V_{ei}(\mathbf{r})$ in terms of their Fourier transforms and the displacement $\mathbf{u}$ in terms of raising and lowering operators ($a_{\mathbf{k}_p}, a^{\dagger}_{\mathbf{k}_p}$ respectively) of the phonon modes, the electron-phonon interaction Hamiltonian is given by $H_{ep} = \int d\mathbf{r} \rho(\mathbf{r}) V_{ep}(\mathbf{r})$ where

$$V_{ep}(\mathbf{r}) = -\sum_{\mathbf{k}_p \mathbf{G}} \exp(i\mathbf{k}_p \cdot \mathbf{r}) \left\{ V_{ei}(\mathbf{k}_p + \mathbf{G})(\mathbf{k}_p + \mathbf{G}) \cdot \hat{\mathbf{e}}_{\mathbf{k}_p} \sqrt{\frac{\hbar}{2\rho V \omega_{\mathbf{k}_p}}} \right\} \left(a_{\mathbf{k}_p} + a^{\dagger}_{-\mathbf{k}_p} \right). \quad (1.54)$$

The term in curly brackets is the electron-phonon coupling matrix element $M_{\mathbf{k}_p+\mathbf{G}}$, with $\hat{\mathbf{e}}_{\mathbf{k}_p}$ and $\omega_{\mathbf{k}_p}$ being the polarization and frequency of phonon $\mathbf{k}_p$. Carrying out the integration, the following is obtained

$$H_{ep} = \sum_{\mathbf{k}_p \mathbf{G}} M_{\mathbf{k}_p+\mathbf{G}} \rho(\mathbf{k}_p + \mathbf{G}) \left(a_{\mathbf{k}_p} + a^{\dagger}_{-\mathbf{k}_p} \right), \quad (1.55)$$

where $\rho(\mathbf{k}_p+\mathbf{G})$ is a particle density operator. Equation (1.55) determines the rate at which electronic states couple to phonons in a material. In general the electron-phonon coupling matrix is difficult to evaluate theoretically and is often calculated using computational methods.

Consider the following simple situation to illustrate the effects of electron-phonon coupling. A metal initially at equilibrium is photoexcited by an ultrafast laser pulse. The carriers are initially described by a Fermi-Dirac distribution of temperature T_{e1}. Following photo-excitation, the carrier distribution achieves an elevated temperature T_{e2} extremely rapidly (typically within $\sim$ 100 fs) which then finds itself out-of-equilibrium relative to the phonon system of the lattice. In other words, the distribution of electron momenta p_i corresponds to a larger temperature compared to the lattice temperature. The H_{ep} coupling term lowers the energetic electronic states by creating phonons, *i.e.* by increasing

the number of phonons per branch $a^{\dagger}_{\mathbf{k}_p n} a_{\mathbf{k}_p n}$ contained in the first term of Eqn. (1.52). The momentum-averaged effect of electron-phonon coupling is to increase Debye-Waller term (M_α) appearing in the scattering intensity I_0 given by Eqn (1.36). This is proportional to the average atomic displacement due to the distribution of phonon modes. In a time-resolved measurement which examines the difference between scattering intensity before and after laser excitation, a transient suppression of the Bragg peak intensities measures these effects with a time-scale governed by the electron-phonon coupling term. Furthermore, if sufficient intensity can be measured off the Bragg peaks ($\mathbf{q} \neq \mathbf{G}$), the thermal diffuse intensity I_1 (Eqn. (1.6.3)) contains information about the occupancies of the various phonon branches visible at a particular $\mathbf{q}$.

1.9 Ultrafast electron scattering: a concise historical perspective

In this chapter the essential physics behind the technique of ultrafast electron scattering have been demonstrated. The technique is made possible by ultrafast laser technology and developments in ultrafast high-brightness electron sources. In this section, the experimental setup used in this work is described in detail, leaving out specifics which are discussed to a deeper extend in later chapters. Before this however, a brief historical account of where the technique of ultrafast electron scattering began and how it has evolved in recent years is presented.

The first demonstration of time-resolved electron diffraction was performed by Mourou and Williamson in 1982 [44]. They generated electrons through photo-emission from a thin-film cathode and accelerated them to an energy of 20 keV. Using this apparatus they where able to observe photo-induced melting in aluminum [45]. The time resolution of the apparatus was limited to 100 ps due to strong space-charge effects. The measurements were thus unable to capture in any detail the rate at which the transition from crystalline to amorphous occurred; they only saw an “ON–OFF” transition. These early results founded

the idea of the *space-charge problem*, and instilled within many the idea that Coulomb repulsion effects would inevitably be the bane of the technique. Many efforts which followed this sought improved time-resolution by working in the single electron regime [46, 47]. While this provided time-resolution in the femtosecond regime, the limited signal-to-noise of low brightness single electron sources severely limited the range of experiments which could be performed. A few years later, Siwick and co-workers [48] demonstrated a new type of compact high-brightness electron source which offered sub-picosecond temporal resolution and sufficient electron flux to enable irreversible laser-excited melting experiments. With this improvement the experiment of Williamson nearly 20 years before was finally resolved with sub-picosecond resolution, mapping out the details of how a laser excited metal film undergoes melting.

Despite this achievement, there remained a fundamental trade-off between beam intensity and time-resolution [19]; *i.e.* the space-charge problem endured. Compression techniques based on radio-frequency fields were proposed in 2007 by van Oudheusden [16]. As described in sec. 1.4.1, they offered a solution to the space-charge problem through the inversion of space-charge driven temporal broadening. Pulse compression of this type was demonstrated in the single-shot regime in 2010 [49] and later in 2012 by Chatelain [50] and Gao [51] in two different laboratories focussing on multi-shot reversible experiments. The resulting performance of ultrafast electron scattering instruments featuring pulse compression was strongly limited by synchronization jitter between the master laser source driving electron emission and the microwave cavity field oscillation performing the pulse compression. In chapter 2 of this thesis, a synchronization methodology is devised and demonstrates significant improvement in this area.

Over the past decade and a half, ultrafast electron diffraction has demonstrate powerful insight into the non-equilibrium behavior of laser-excited materials [48, 52, 53, 54, 55, 5, 56,

57]. The technique is capable of tracking with femtosecond time-resolution the structural response of a material following laser excitation as well as the nature of phonon excitations coupled to the photo-excited electron system. Some reviews of the field can be found in Refs. [58, 59, 60, 61].

1.10 The experimental apparatus at McGill University

An overview of the experimental setup used throughout this thesis is shown in Fig. 1–6. Earlier versions of the experimental setup are described in refs. [50, 62]. The system begins with a mode-locked Titanium:Sapphire oscillator (Spectra-Physics Tsunami) which produces 35 fs pulses at a repetition rate of $\sim$ 75 MHz. The central wavelength is 800 nm, and the pulse energy is roughly 5 nJ. The oscillator beam is split, with 5% supplying the RF system for synchronization and electron pulse compression and 95% providing the input seed pulse for a regenerative Titanium:Sapphire laser amplifier (Spectra-physics Spitfire XP pro). The laser amplifier cavity is synchronized to the oscillator laser by dividing the 75 MHz oscillator repetition rate and generating a 1 kHz signal. This 1 kHz signal triggers a set of Pockels cells which select a laser pulse to be amplified and allow for the pulse to spend a specific amount of time in the cavity in order to be optimally amplified. The amplified pulse is then released from the cavity, re-compressed and the output energy is roughly 3 mJ/pulse. The pulse is split 50%/50% on the optical table for the pump and probe beams respectively. The pump beam is used for photo-excitation of the sample and passes through a variable retro-reflector delay stage to tune the time-delay between pump and probe pulses. The pump pulse is then focused and coupling into the sample chamber which is maintained to a high-vacuum level ($\sim 10^{-7}$ Torr).

The probe laser beam is frequency tripled using a non-linear optical process called third harmonic generation [12]. This is achieved by sending the beam through a sequence of three crystals, beta-barium borate (BBO), calcite, BBO in that order. The excess 800

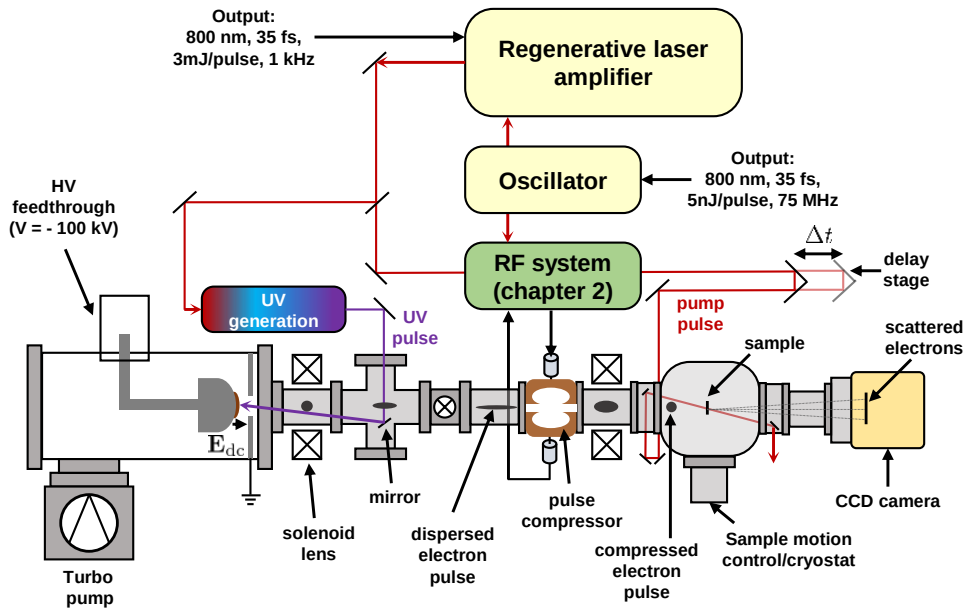

Figure 1–6: Schematic of an ultrafast electron scattering experiment with RF pulse compression.
An ultrafast laser system produces ultrashort pulses which are converted to UV light for the generation of electron pulses through a photo-emission process. The pulses are accelerated and recompressed using a radio-frequency cavity synchronized to the laser system. Compressed pulses are scattered by the sample (following photoexcitation) and the scattered intensity of the electron beam is collected by a CCD camera.

nm and 400 nm light is removed from the beam path using either prisms or filters. The remaining ultraviolet light (267 nm) is focused and coupled into the high-vacuum beam line at the end opposite the sample chamber reflects of an aluminum mirror and is aligned onto a copper DC photo-cathode which is at a voltage of -100 kV. The focusing lens is positioned such that the beam diameter of the UV pulse is roughly 50 µm. A photo-emitted electron bunch is accelerated to 100 keV energy. The electron beam collimated (transverse focusing) by a solenoid lens. Further down the beamline the electron pulse undergoes longitudinal space-charge broadening as described in Sec. 1.4. This dispersion is counteracted by a 3 GHz microwave cavity supporting a uniformly time-varying E field

mode along the axis of propagation (longitudinal). This re-compresses the electron pulse and it achieves a minimum temporal duration at the temporal focus of the microwave cavity some distance (roughly 20 cm) further down the beamline. The pulse is also focused further by a second solenoid lens which establishes a spatial focus at the position of a transmission electron microscope CCD camera roughly 26 cm behind the sample.

In a reversible pump-probe ultrafast electron diffraction experiment, (refer to Fig. 1–1) the dynamics initiated in the sample via pump pulse excitation occur within the time-interval between set by the laser repetition rate (1/1 kHz = 1 ms by default) and the sample returns to its "initial-state" before the next pulse arrives. When this condition is met, the slow acquisition times of typical CCD cameras (seconds) is not a limitation. An image formed by a 10 second exposure of the CCD camera, collects 10^4 scattered electron pulses each of which form a 100 femtosecond snapshot of the sample dynamics at time Δt following laser excitation.

1.10.1 Example: photo-excited chromium film

In this section a basic ultrafast electron diffraction measurement is presented to illustrate Bragg peak dynamics and how to interpret them for a laser-excited chromium film. The Cr film is a 50 nm thick polycrystalline sample grown by electron beam deposition. The texture of the sample is one consisting of vary small crystallites, (below 10 nm according to SEM images of the sample). Given this, Debye-Scherrer rings are expected in the scattering pattern rather than Bragg peaks, and their widths will be relatively broad due to the shape functions of the small crystallites. The diffraction pattern is shown in Fig. 1–7 a). The intensity of the diffraction rings is given by

$$\begin{aligned} I_0(\mathbf{q}) &= \delta\left(\mathbf{q}-\mathbf{G}_{hkl}\right) * \left|\mathcal{S}(\mathbf{q})F_0(\mathbf{q})\right|^2, \\ &= \delta\left(\mathbf{q}-\mathbf{G}_{hkl}\right) * \left|\mathcal{S}(\mathbf{q})f^e_{\mathrm{Cr}}(\mathbf{q})\exp\left(-M(q)\right)\right|^2, \end{aligned} \tag{1.56}$$

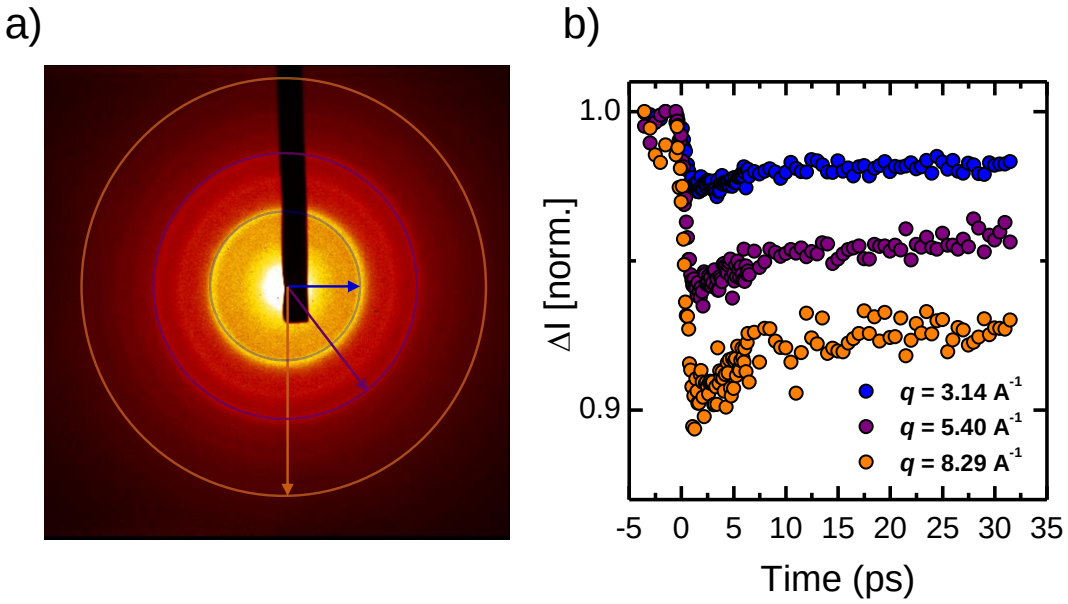

Figure 1–7: Ultrafast electron diffraction measurement of a photo-excited chromium film a) Electron scattering pattern of polycrystalline 50 nm thick chromium. Three Debye-Scherrer rings are indicated with blue, purple and orange arrows at reduced scattering lengths of $S = 0.25$, 0.43 and 0.66 Å respectively. The solid rectangle is a beam block which stops the intense beam at $S = 0$ of unscattered electrons. b) Time-resolved peak intensities for the azimuthally-averaged rings in a).

where $\mathcal{S}(\mathbf{q})$ is the shape or texture function of the film which broadens the delta function pertaining to the Bragg condition, $f^e_{\mathrm{Cr}}(\mathbf{q})$ is the electron scattering form factor for elemental chromium and M is the isotropic Debye-Waller factor given by $M(q) = 2\pi^2\langle u^2\rangle|\mathbf{q}|^2$ with $\langle u\rangle$ being the RMS thermal displacement of the Cr atoms. By taking the logarithm of the time-dependent intensity $I_0(\mathbf{q}, \Delta t)$ divided by the intensity of the sample before photo-excitation $I_0(\mathbf{q}, \Delta t = 0)$ is obtained [63]

$$-\ln\left(\frac{I_0(\mathbf{q},\Delta t)}{I_0(\mathbf{q},\Delta t=0)}\right) = 2\pi^2\left(\langle u(\Delta t)^2\rangle - \langle u(0)^2\rangle\right)q^2 = 2\pi^2\left(\langle \Delta u(\Delta t)^2\rangle\right)q^2. \qquad (1.57)$$

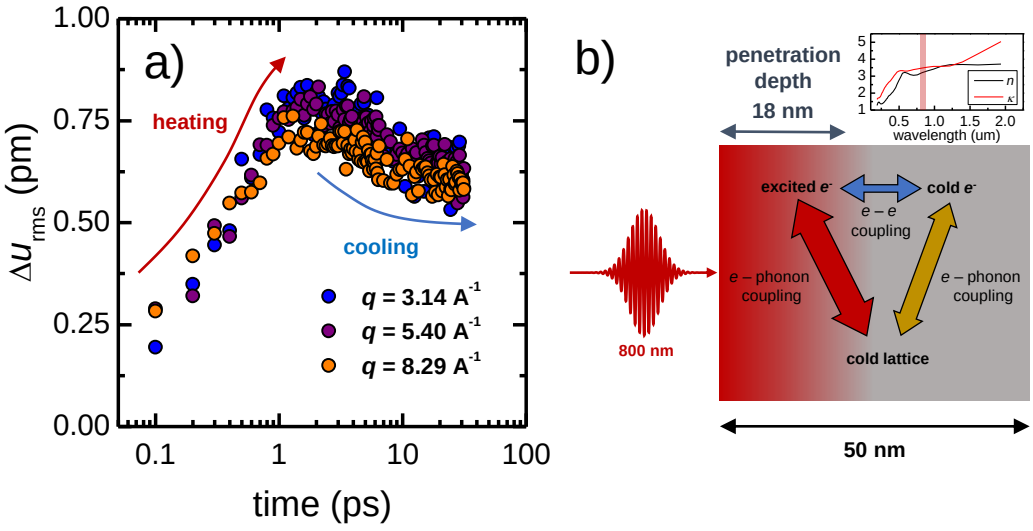

Figure 1–8: Electron and lattice relaxation dynamics is photo-excited chromium a) RMS change in atomic displacement Δu_{RMS} calculated from the diffraction peak dynamics. Heating is observed within the first 500 fs, due to strong electron-phonon coupling, followed by a relaxation in the average vibrational amplitude of the lattice. b) Top: complex index of refraction of chromium. Bottom: Schematic representation of partial photo-excitation of a chromium film illustrating the various coupling mechanism.

The data shown in Fig. 1–7 b) is transformed using Eqn. (1.57) and plotted in Fig. 1–8 a). As expected from Debye-Waller type effects, the q–scaling of the relative peak intensities apparent in Fig. 1–7 b) no longer appears once the change in the RMS atomic displacement Δu_{RMS} is calculated.

The behavior of a photoexcited Cr film is presented at a qualitative level to understand the importance of various coupling terms at play in the material with the goal of furnishing some basic intuition for undertanding ultrafast electron diffraction results. The electron pulses which form the diffraction pattern probe the full sample volume and therefore the Debye-Waller factor represents an ensemble average of $\langle u^2_{\mathrm{RMS}} \rangle$ and consequently the average lattice temperature. Clearly the data shown in Fig. 1–7 a) and Fig. 1–8 a) shows a rapid

increase occurring with a time constant of roughly 400 fs indicative of strong lattice heating through a large electron-phonon coupling term known to exist in chromium [64]. What is unexpected however is the subsequent cooling of the lattice which overtakes the heating after 1 ps and is characteristically slower. This effect arises because of the fact that the optical depth of Cr is only about 18 nm at a wavelength of 800 nm [65] (the complex index of refraction as a function of wavelength is shown in Fig. 1–7 b)), which produces an inhomogeneous sample excitation; only electrons in roughly 40% of the film are excited. The question now becomes how does the lattice lose heat? There are a few possibilities for this and they are illustrated in Fig. 1–7 b). First, the excited electrons may cool through interaction with the cold electrons which were not photoexcited with a rate determined by electron–electron coupling. The second mechanism is that the phonons couple to the cold electrons with a weaker electron–phonon coupling term, which is possible since the coupling can be dependent on the electron temperature. In general the answer is probably a combination of the two effects and without further experiments it would be difficult to determine. Another possibility is that certain phonons initially are excited and yield a particular Δu_{RMS} for the average sample. Over time, phonon-phonon coupling can redistribute the energy into lower frequency acoustic modes, which have a lower Δu_{RMS}. This could be a mechanism which conserves energy in the phonon system (average temperature).

Phenomenological models such as the two-temperature model [66, 64] and generalizations [67] can be used to interpret ultrafast electron diffraction results my modeling the system of electrons with temperature T_e and heat capacity $c_e(T_e)$ coupled to any number of phonon subsystems with temperature T_{pj} and heat capacity $c_{pj}(T_{pj})$. The electronic system is driven out of equilibrium by a laser pulse providing an energy input described by an impulsive function $f(t - t_0)$ which serves essentially as an initial condition for the

system of equations

$$c_e(T_e)\frac{\partial T_e}{\partial t} = \sum_j g_{e-p,j}(T_e)(T_e - T_{pj}) + f(t - t_0), \quad (1.58)$$

$$c_{pj}(T_{pj})\frac{\partial T_{pj}}{\partial t} = g_{e-p,j}(T_e)(T_e - T_{pj}) + \sum_{k\neq j} g_{p-p,jk}(T_{pj}, T_{pk})(T_{pj} - T_{pk}), \quad (1.59)$$

where $g_{e-p,j}(T_e)$ is a version of the electron-phonon coupling term in units of W K^{-1} m^{-3} and a phonon-phonon coupling term has been included $g_{p-p,jk}(T_{pj}, T_{pk})$ with the same units to remain general. A common approach for analyzing ultrafast electron diffraction results is to assign some heat capacities for the electrons and phonons using approximate models or direct computations. Using such results the RMS atomic displacement $\Delta\langle u^2_{\mathrm{RMS}}\rangle$ can be converted to a lattice temperature. Equations (1.58) and (1.59) are then numerically minimized to the data and the coupling terms may be extracted.

1.11 Thesis organization and statement of contributions

This thesis is arranged as follows; Chapter 2 focuses on the physics of electron pulse compression and laser-microwave synchronization. It is related but by no means limited to published work in ref. [68]. Chapter 3 presents ultrafast electron diffraction results in the strongly correlated material vanadium dioxide most of which is published in ref. [69]. Chapter 4 presents ultrafast electron scattering results on the 2-dimensional material titanium diselenide, and focuses on phonon hardening effects observed in the time-resolved diffuse scattering intensity.

CHAPTER 2
The machine physics of electron pulse compression

The use of radio-frequency (RF) electromagnetic fields to compress electron pulses is an extension of the core physics driving particle accelerator technology [70, 71]. For over half a century, resonant electromagnetic structures such as linear accelerators, bunchers and injectors have been integral in the operation of large scale particle colliders and radiation sources. In all forms of these technologies, energy is transferred to the particle beam from an RF field. The RF field must be thus accurately synchronized for consistent energy gain in the particle beam. Electron pulse compressors, similar to more advanced accelerator structures are based on RF cavity structures, are engineered to yield localized harmonic electromagnetic fields over specific spatial regions depending on the desired interaction with the electron pulses. RF electron pulse compressors have extreme synchronization requirements which must be properly addressed in order to achieve consistent, high time-resolution performance when applied to ultrafast electron scattering [50, 51, 55, 72, 22, 73, 74, 75]. This challenge depends on both the details of the RF cavity response and also the synchronization of the cavity field to the laser system driving the ultrafast electron scattering experiment.

This chapter will present the physics of charged particle acceleration and its application to a single-cell microwave cavity for use as a pulse compressor in an ultrafast electron scattering instrument. A novel approach to synchronize the microwave cavity fields with a femtosecond laser system is developed and characterized. In this approach, a phase-locked frequency comb is directly synthesized by photo-detection of the laser pulse train and the appropriate resonant frequency tone is selected for driving the resonant mode of

the compression cavity. Furthermore an active phase feedback system is designed and implemented for the compensation of phase fluctuations induced through the detuning between the synchronized driving signal and the cavity resonance which result primarly from thermal effects. The final performance of the instrument is characterized in detail by temporal streaking measurements of the compressed electron pulses which is sensitive to all forms of temporal jitter affecting time-resolution of a pump-probe ultrafast electron scattering experiment. Some of the work presented in this chapter has been published in ref. [68].

2.1 Charged particle acceleration in an electromagnetic field

First, some general features of charged particle acceleration in electromagnetic fields are presented and discussed. The equation of motion for a charged particle with momentum $\mathbf{p}$ in an electric field $\mathbf{E}$ and magnetic field $\mathbf{B}$ is determined completely by the Lorentz force law [41]

$$\frac{d}{dt}\mathbf{p} = q\left[\mathbf{E} + \frac{1}{m_e}\mathbf{p}\times\mathbf{B}\right]. \tag{2.1}$$

In general the evaluation of Eqn. (2.1) is difficult for arbitrary fields, but it will be shown that it can be greatly simplified when the interactions between the $\mathbf{E}$ and $\mathbf{B}$ field can be separated in space and when symmetry considerations constrain the field profiles.

Consider a charged particle subject to an standing electromagnetic field in the z - direction. The field is given by $E_z(z,t) = E(z)\cos(\omega t(z) + \phi)$, where $\omega = 2\pi f$ is the angular frequency of the field and ϕ is conventionally referred to as the *synchronous phase* of the field. The field acting on a particle of charge q, velocity v at position z is obtained by using $t(z) = \int_0^z dz/v(z)$ to describe the velocity dependence of the time spent in the field by the charged particle. This yields

$$E_z(z,t) = E(z)\cos\left(\omega\int_0^z \frac{dz}{v(z)} + \phi\right). \tag{2.2}$$

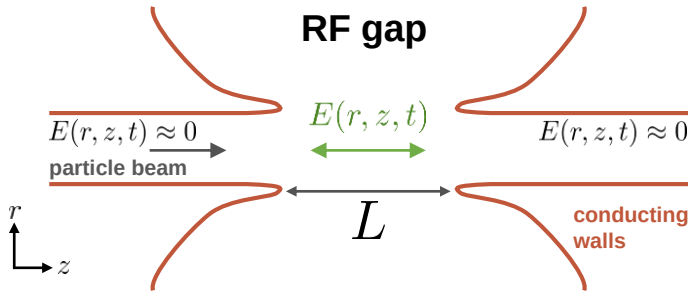

Figure 2–1: Particle acceleration across an RF gap
A particle travelled along the z direction in a field-free region then enters a gap of length L where it interacts with a field $E(r = 0, z, t)$ where it can be accelerated or deccelerated. This is a good approximation for the cavity used in this work as will be shown in sec. 2.2.

The simplest electromagnetic modes in accelerator structures are TM_{0n0} modes for which there are generally non-zero E_z, E_r and B_θ fields (working in cylindrical coordinated for simplicity). It follows from Eqn. (2.1) that the equations of motion for the particles in the fields are

$$\frac{dp_z}{dt} = q\left[E_z(r,z)\cos(\omega t+\phi) + v_r B_\theta(r,z)\sin(\omega t+\phi)\right], \tag{2.3}$$

$$\frac{dp_r}{dt} = q\left[E_r(r,z)\cos(\omega t+\phi) - v_z B_\theta(r,z)\sin(\omega t+\phi)\right], \tag{2.4}$$

where $\mathbf{v} = (v_r, v_\theta, v_z)$ is the velocity vector of the charged particle.

Consider now the case of on-axis ($r = 0$) acceleration occurring in a region of length L within which the fields are non-zero as illustrated in Fig. 2–1. In this situation $E_z(r = 0, z, t) = E(0, z)\cos(\omega t + \phi)$ and the momentum gain Δp is calculating by evaluating an integral over time

$$\Delta p(t_1, t_2) = q\int_{t_1}^{t_2} E_z(0, z(t), t)dt, \tag{2.5}$$

where $t_2 - t_1$ is the time-of-flight or transit-time through the field region. Similarly, the energy gain $\Delta\varepsilon$ is given by an integral over the spatial coordinate

$$\Delta\varepsilon = q \int_{-L/2}^{L/2} E(0, z, t(z)) dz. \tag{2.6}$$

In equations (2.5) and (2.6) position and time are related by $dz = dt v_z(z)$. Making use of a trigonometric identity, (2.6) can be written as

$$\Delta\varepsilon = q \int_{-L/2}^{L/2} E(0, z) \left[\cos(\omega t) \cos\phi - \sin(\omega t) \sin\phi\right] dz. \tag{2.7}$$

It is conventional to define an effective axial RF voltage as $V_0 = \int_{-L/2}^{L/2} E(0, z) dz$. This should be understood as the effective DC field experienced by the particle in the center of the gap (*i.e.* $z = 0, t = 0$). It follows that equation (2.7) can now be written as $\Delta\varepsilon = qV_0 T \cos\phi$ for which the *transit time factor* T is defined as [71, 76]

$$T \equiv \frac{1}{V_0} \left[\int_{-L/2}^{L/2} E(0, z) \cos(\omega t(z)) dz - \tan\phi \int_{-L/2}^{L/2} E(0, z) \sin(\omega t(z)) dz \right]. \tag{2.8}$$

An average RF axial field $E_0 = V_0/L$ can be defined which results in the famous Panofsky equation for the energy gain of a charged particle

$$\Delta\varepsilon = qE_0 TL \cos\phi. \tag{2.9}$$

Equations (2.8) and (2.9) describe the *transit time effect* which indicates that the energy gain of a particle in a sinusoidal time-varying field is always less than that for a particle in a DC field equal to that experienced by the particle in the center of the gap. Equation (2.8) thus represents the reduction in energy gain induced by the time dependence of the field. Most resonant accelerator structures yield fields which are symmetric functions with respect to the center of the gap. By maintaining this point as the origin, the dependence on ϕ can be removed since the second term of equation (2.8) vanishes and simplifies to the

cosine weighted average of the field

$$T = \frac{1}{V_0}\int_{-L/2}^{L/2} E(0,z)\cos(\omega t(z))dz. \tag{2.10}$$

2.2 The microwave pulse compression cavity

The character of the electromagnetic modes produced by a cylindrically symmetric pulse compression cavity will be considered next in greater detail. For our interests, it will be assumed that the relevant electromagnetic fields used for the acceleration of electrons exist in regions containing no free charges and can be well approximated as being surrounded by an equipotential surface. Making use of this, along with Maxwell's equations in the Lorentz gauge, it can be shown that the electric **E** and magnetic **B** fields depend only on the vector potential **A** according to the following

$$\mathbf{B} = \nabla \times \mathbf{A}, \qquad \mathbf{E} = -\frac{\partial}{\partial t}\mathbf{A}. \tag{2.11}$$

The vector potential is found by solving its wave equation which depends on a source current density **J** according to

$$\nabla^2\mathbf{A} - \frac{1}{c^2}\frac{\partial^2}{\partial t^2}\mathbf{A} = -\mu_0\mathbf{J} \tag{2.12}$$

The source term involving **J** is ideally confined to the conducting surfaces which defines the geometry to the electromagnetic structure.

The fields produces by a cylindrical resonator, historically referred to as the "pillbox" cavity, will now be considered. Such systems consist of two conducting boundaries located at $-L/2$ and $L/2$ and cross-sectional radius R_c. In practice the conducting boundaries have small holes to allow the electron beam to enter and exit the cavity, but these can be safely ignored as they produce a negligible perturbation to the overall electrodynamics of the resonant structure. Furthermore, the current density $\mathbf{j}_{\text{pulse}}$ contributed by the electron

pulse itself is negligible because it typically would be very small on average compared to the current density from the conducting surfaces of the cavity ($\mathbf{j}_{\text{pulse}} \ll \mathbf{J}$). The wave equation for $\mathbf{E}$ is determined in the usual manner from Gauss' law by taking $\nabla \times \nabla \times \mathbf{E} = -\nabla^2 \mathbf{E} = -\frac{\partial}{\partial t}(\nabla \times \mathbf{B}) = -\frac{1}{c^2}\frac{\partial^2}{\partial t^2}\mathbf{E}$. The component of the electric field in the z direction E_z must obey the wave equation which in cylindrical coordinates is given by

$$\frac{\partial^2 E_z}{\partial z^2} + \frac{\partial^2 E_z}{\partial r^2} + \frac{1}{r^2}\frac{\partial^2 E_z}{\partial \theta^2} + \frac{1}{r}\frac{\partial E_z}{\partial r} - \frac{1}{c^2}\frac{\partial E_z}{\partial t} = 0. \tag{2.13}$$

An azimuthally symmetric solution of the form $E_z(z, r, t) = R(r)e^{i\omega t}$ which is homogeneous along z is assumed for simplicity. It must be that $E_z(z, r = R_c, t) = 0$ in order to satisfy the continuity relation at the perpendicular conducting boundaries. First-order solutions are determined by separation of variables and expressed in terms of J_m Bessel functions [71, 77]

$$E_z(r,t) = E_{0z}(r)\cos(\omega_0 t + \phi) = E_0 J_0(k_r r)\cos(\omega_0 t + \phi), \tag{2.14}$$

$$B_\theta(r,t) = -\frac{E_{0z}(r)}{c}\sin(\omega_0 t + \phi) = -\frac{E_0}{c}J_1(k_r r)\sin(\omega_0 t + \phi), \tag{2.15}$$

where the boundary conditions are satisfied by the resonance frequency $\omega_0 = k_r c = 2.405c/R_c$.

2.2.1 TM modes of a cylindrical cavity

For most cavities used in particle acceleration applications, cylindrical symmetry is preserved, but the geometry of the structure is not a simple pillbox design. The reason for this is that the pillbox is not a power efficient design and would require RF power on the order of 10s of kW in order to perform the desired operations on the beam. Typical engineered accelerator cavity structures have "lobes" which create regions of high-field enhancement near the location of the particle beam and yield quality factors on the order of 10^3 times larger than a pillbox. A schematic comparison of a model pillbox and a power efficient cavity design is shown in Fig 2–2 c). The spatial profiles of the electromagnetic

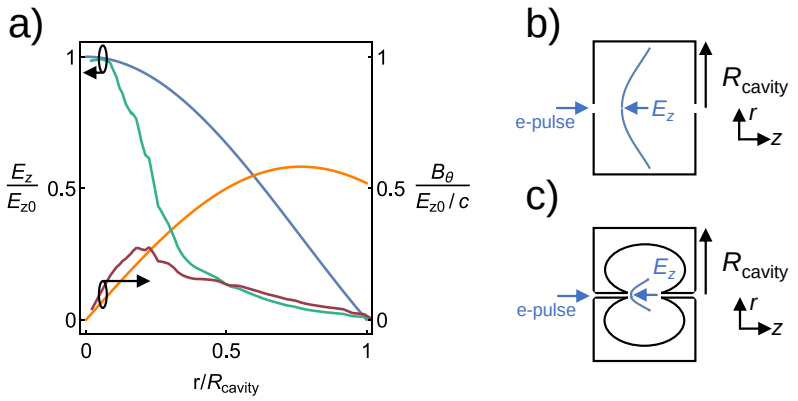

Figure 2–2: Electromagnetic fields of a cylindrical cavity.
a) Radial field profiles for the TM_{010} resonant mode. The blue and orange lines represent E_z and B_θ describe fields for an idealized pillbox cavity and the green and dark red lines are computed by a 3D finite element solver (ANSYS HFSS) of a power efficient design. Typical field enhancement factors are on the order of 10^3 near the axis of symmetry for engineered cavities. b) Geometry of an idealized pillbox cavity with radius R_{cavity}. c) Power efficient cavity design with lobed radial geometry. The power efficient design significantly enhances the E_z field along the longitudinal z axis at $r = 0$ where the electron pulse propagates.

fields described by Eqn. (2.14) and (2.15) remain accurate near the symmetry axis of the structure. In general a resonant cylindrical expansion of the fields may be carried out for the rotationally symmetric modes which gives the following for the relevant field components [77]

$$E_z(z,r,t) = \left(1+\frac{r^4}{2}\left(\frac{\partial^2}{\partial z^2}+\frac{\omega^2}{c^2}\right)+\cdots\right)E_z(r=0,z)\cos(\omega t+\phi), \tag{2.16}$$

$$\begin{aligned} E_r(z,r,t) &= -\frac{1}{r}\int_0^r r'\frac{\partial E_z(z,r,t)}{\partial z}dr', \\ &= \left(-\frac{r}{2}+\frac{r^3}{16}\left(\frac{\partial^2}{\partial z^2}+\frac{\omega^2}{c^2}\right)-\cdots\right)\frac{\partial E_z(r=0,z)}{\partial z}\cos(\omega t+\phi), \end{aligned} \tag{2.17}$$

$$\begin{aligned} B_\theta(z,r,t) &= \frac{1}{rc^2}\int_0^r r'\frac{\partial E_z(z,r,t)}{\partial t}dr', \\ &= \left(-\frac{r}{2}+\frac{r^3}{16}\left(\frac{\partial^2}{\partial z^2}+\frac{\omega^2}{c^2}\right)-\cdots\right)\frac{\omega}{c^2}E_z(z,r=0)\sin(\omega t+\phi). \end{aligned} \tag{2.18}$$

Using Eqns. (2.16), (2.17) and (2.18) with Eqns. (2.3) and (2.4) the longitudinal and transverse momentum components, p_z and p_r respectively, may be calculated.

2.2.2 Temporal focusing power of an RF cavity

In Sec. 1.4 it was illustrated how space-charge effects in the rest frame of the electron pulse produce a linear elongation in both the longitudinal and transverse directions of the electron pulse. These effects can by counteracted by the appropriate interaction with a linearly time-varying in time electric field. The longitudinal or temporal focusing power is determined by calculating the change in momentum p_z (Eqn. (2.3)) experienced by all of the electrons in the pulse. The following assumptions will be made in our case:

1. **The transverse width of the electron pulse is sufficiently small so that $E(r,t)$ only depends on z and $B_\theta(r \approx 0, t) \approx 0$.**
2. **The pulse duration $\tau = \xi/v_z \ll 1/\omega_0$ is much shorter than the oscillation period of the cavity field.**
3. **The positions of the electrons in the pulse are constant during propagation through the field. Compression doesn't occur until after the pulse exits the cavity fields.**
4. **The field-induced momentum change is small compared to the total momentum $\Delta p_z \ll p_z$ such that the time-of-flight in the cavity is constant for all electrons in the pulse. It follows from this that the spatial bunch duration $\xi = z - v_z t$.**

The following equation describes the momentum transfer due to interaction with the electric field

$$\begin{aligned}\Delta p_z &= -q\int_{-\infty}^{\infty} E_z(z,t)dt = -\frac{q}{v_z}\int_{-\infty}^{\infty} E_{0z}(z)\cos\left(\frac{\omega_0(z-\xi)}{v_z}+\phi\right)dz, \\ &= -\frac{q}{v_z}\int_{-\infty}^{\infty} E_{0z}(z)\left[\cos\left(\frac{\omega_0 z}{v_z}\right)\cos\left(-\frac{\omega_0\xi}{v_z}+\phi\right)-\sin\left(\frac{\omega_0 z}{v_z}\right)\sin\left(-\frac{\omega_0\xi}{v_z}+\phi\right)\right]dz,\end{aligned}$$

where the integral over t to z has been transformed using assumptions 3. & 4. The sin terms above are odd functions of z while $E_{0z}(z)$ is even, therefore the second term vanishes in the integral from $-\infty$ to ∞. Applying a trigonometric identity to the first term yields

$$\Delta p_z = -\frac{q}{v_z} E_0 d_{\text{cav}} \left[\cos\phi \cos\left(\frac{\omega_0 \xi}{v_z}\right) + \sin\phi \sin\left(\frac{\omega_0 \xi}{v_z}\right) \right], \tag{2.19}$$

$$\approx -\frac{q}{v_z} E_0 d_{\text{cav}} \left[\cos\phi + \frac{\omega \xi}{v_z} \sin\phi \right], \tag{2.20}$$

where a field weighted effective cavity length d_{cav} has been defined as

$$d_{\text{cav}} = \frac{1}{E_0(0)} \int_{-\infty}^{\infty} E_{0,z}(z) \cos\left(\frac{\omega_0 z}{v_z}\right) dz. \tag{2.21}$$

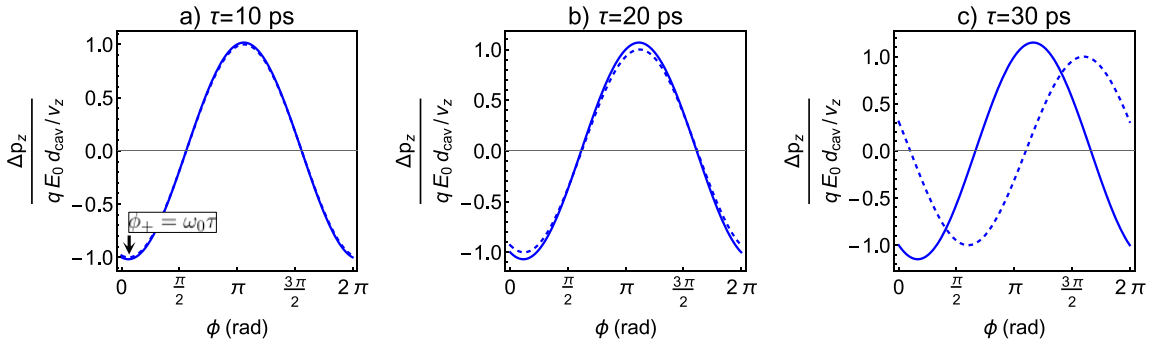

Figure 2–3: Transverse momentum (Δp_z) modulation for various input electron pulse durations.
The dashed blue line is Eqn. (2.19) and the solid blue line is the approximation valid for $\omega_0 \tau = \omega \xi / v_z \ll 1$ given by Eqn. (2.20). Ideal compression phase is offset from $\pi/2$ by $\phi_+ = \omega_0 \tau$. At a fixed field frequency the effect of increasing τ is to reduce the maximum amount of Δp_z which can be transferred to the electrons and also to shift the optimal compression phase. This reults from the breakdown of the linearly varying E_z over the time interval set by the pulse duration.

The temporal or longitudinal focusing power $\mathcal{P}_L$ of the compression cavity is related to the temporal focal length f_L and is defined according to the following [16, 77]

$$\mathcal{P}_L = f_L^{-1} \equiv -\frac{1}{p_z}\frac{\partial\left(\Delta p_z\right)}{\partial \xi} = \frac{qE_0 d_{\text{cav}}\omega_0}{m_e v_z^3}\sin\phi. \tag{2.22}$$

2.2.3 Phase sensitivity

An inspection of Eqn. (2.19) reveals that the momentum modulation $\Delta p_z = 0$ when the phase is $\phi_0 = \frac{\pi}{2} + \frac{\omega_0 \xi}{v_z} \approx \frac{\pi}{2}$. The phase of the RF field cycle must be synchronized such that electrons at the center of the dispersed pulse experience $\Delta p_z = 0$ during time-of-flight through the cavity. The effect of any phase departure from ϕ_0, to first order, is to give an overall momentum shift of the pulse depending on the phase shift $\Delta\phi$, translating to a change in the time-of-flight of the pulse from the cavity to the sample position. This yields a timing drift, or jitter, relative to the reference (an ultrashort laser pulse in pump-probe experiments which determined $t = 0$) and degrades the overall temporal resolution of the instrument. Differentiation of (2.19) with respect to ϕ yields

$$\frac{d\Delta p_z}{d\phi} = m_e\frac{dv_z}{d\phi} = -\frac{q}{v_z}E_0 d_{\text{cav}}\left[\cos\phi\sin\left(\frac{\omega_0\xi}{v_z}\right) - \sin\phi\cos\left(\frac{\omega_0\xi}{v_z}\right)\right].$$

The momentum is related to the time-of-flight over a distance L using $dt = d\left(L/v_z\right) = -L\left(dv_z/v_z^2\right)$ which gives the following when evaluating at $\phi_0 = \frac{\pi}{2} + \frac{\omega_0\xi}{v_z}$. The following expression is obtained and can be expanded in terms of the pulse duration $\tau = \xi/v_z$

$$\begin{aligned}\frac{dt}{d\phi} &\approx \frac{qE_0 d_{\text{cav}} L}{m_e v_z^3}\left[\frac{\omega_0\xi}{v_z}\sin\left(\frac{\omega_0\xi}{v_z}\right) + \cos\left(\frac{\omega_0\xi}{v_z}\right)\right] &(2.23)\\ &= \frac{L}{f_L\omega_0}\left(1 + \frac{3}{2}\left(\omega_0\tau\right)^2 + \frac{1}{6}\left(\omega_0\tau\right)^3 + \cdots\right). &(2.24)\end{aligned}$$

Equation (2.23) is a nice simple result. When positioned at the temporal focus ($L = f_L$), and assuming $\omega\xi/v_z \ll 1$ it can be seen that $|dt/d\phi| = \omega_0^{-1}$, which depends only on (and in fact is the definition of) the frequency of the field. Evaluating at a frequency of

$\omega_0 = 2\pi \times 3$ GHz, the resonance of the cavity used in this work, $|dt/d\phi| = 53$ fs/mrad is determined and describes the fundamental sensitivity of the compression fields to phase fluctuations. For uncompressed pulses with duration $\tau = 20$ ps the phase sensitivity for a 3 GHz cavity is 64 fs/mrad, this value is consistent with previous characterization measurements of the instrument [50]. It is interesting to note that for arbitrarily long pulses up to $\omega_0\tau = 1$, the fundamental sensitivity returns to $1/\omega_0$. In this regime however, pulses are not being compressed, since they sample the full range of E_z over time and Δp_z averages to zero for all electrons in the pulse interacting with the cavity field over 1 cycle.

2.3 Microwave network model

The compression of electron pulses using radio-frequency fields in a cavity depends fundamentally on the magnitude and phase of the electric field. However, it is often impractical to conduct measurements of the field directly. For ultrafast electron diffraction with pulse compression, the magnitude of the temporal shift Δt arising from all possible sources of phase fluctuations $\Delta\phi$ is of great interest. Fortunately, the cavity can be reasonably well described as an effective circuit consisting of impedance terms defined by the properties of the cavity in a *lumped element* approximation. Strictly speaking, the lumped element approximation assumes that the **E** and **B** fields are spatially separated, and that the energy stored within those fields form an effective capacitance C_c and inductance L_c respectively which are confined to spatial regions much smaller than the wavelength λ of the RF field. At 3 GHz, the wavelength is $\lambda \approx 10$ cm. In a typical pillbox cavity, most of the electric field energy is stored within a few mm along r near the z axis, and extends along z for less than 1 cm (d_{cav}). The magnetic field however, is homogeneous as a function r and angle θ about z. The field-weighted circumference of B_θ is

$$\mathcal{C}_{\mathrm{cav}} = \frac{2\pi}{B_\theta^{\max}} \int_0^{R_{\mathrm{cav}}} B_\theta(r) dr \approx 10 \text{ cm}. \tag{2.25}$$

The effect of this is that the inductance term becomes frequency dependent $L_c(\omega)$. In the steady-state regime near resonance, the inductance is roughly constant, so the lumped approximation may still be applied.

2.3.1 Driven RLC resonator

The cavity may be modeled as a parallel RLC circuit [78, 71] consisting of resistance R_c, inductance L_c and capacitance C_c. The current $I(t)$ and voltage $V(t)$ in the circuit governed by the following equation

$$I(t) = C_c \frac{dV(t)}{dt} + \frac{1}{L_c}\int V(t)dt + \frac{V(t)}{R_c}, \tag{2.26}$$

which, upon differentiation with respect to t yields

$$\frac{1}{C_c}\frac{dI}{dt} = \frac{d^2V}{dt^2} + \frac{\omega_0}{Q_0}\frac{dV}{dt} + \omega_0^2 V. \tag{2.27}$$

Equation (2.27) describes a samped harmonic oscillator with resonance frequency $\omega_0 = 1/\sqrt{L_c C_c}$. Steady state solutions of the form $V(t) = V_0 e^{i\omega t+\phi}$ and $I(t) = I_0 e^{i\omega t}$ are sought, where V_0 and I_0 are peak voltages and currents respectively. The energy stored in the cavity near resonance is given by $U_s = \frac{1}{2}C_c V_0^2$ and the energy dissipated is $U_d = V_0^2/2R_c\omega_0$, which defines an internal quality factor $Q_0 = U_s/U_d = \omega_0 R_c C_c$. The general steady state solution for $Q_0 \gg 1$ near resonance is given by

$$V(t) = \frac{R_c I_0 e^{i(\omega t+\phi)}}{\sqrt{1+\left(2Q_0\frac{\omega-\omega_0}{\omega_0}\right)^2}} = \frac{R_c e^{i\phi}}{\sqrt{1+\left(2Q_0\frac{\omega-\omega_0}{\omega_0}\right)^2}} I(t) = Z_c(\omega)I(t), \tag{2.28}$$

where $Z_c(\omega)$ is the shunt impedance response function of the cavity resonator, which can also be determined from the parallel addition of the circuit impedances

$$Z_c(\omega) = \left(\frac{1}{R_c} + \frac{1}{i\omega L_c} + i\omega C_c\right)^{-1} \approx R_c \frac{1 - i2Q_0\frac{\omega-\omega_0}{\omega_0}}{1+\left(2Q_0\frac{\omega-\omega_0}{\omega_0}\right)^2}. \tag{2.29}$$

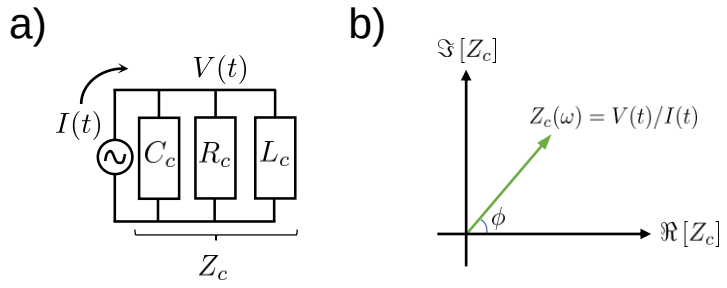

Figure 2–4: Driven RLC circuit.
a) Lumped element equivalent circuit model of a 3-dimensional RF cavity resonator. A current source $I(t)$ drives a voltage response $V(t) = Z_c(\omega)I(t)$ where $Z_c(\omega)$ is the impedance of the circuit which depends on the resistance R_c, inductance L_c and capacitance C_c. b) Phasor representation of Z_c in the complex plane indicating the phase angle ϕ between $I(t)$ and $V(t)$ in the circuit.

The phase ϕ of the voltage response $V(t)$ relative to the current response $I(t)$ is found by mapping $Z_c(\omega)$ in the complex plane and calculating the angle between the real and imaginary components

$$\phi = \arctan\left(\frac{\Im\left[Z_c\right]}{\Re\left[Z_c\right]}\right) = \arctan\left(2Q_0\frac{\omega-\omega_0}{\omega_0}\right). \tag{2.30}$$

Phase fluctuations $\Delta\phi$ produced by frequency detuning $\Delta\omega$ yield a timing shift of $\Delta t = \omega_0^{-1}\Delta\phi = 2Q_0\Delta\omega/\omega_0^2$, which is on the order of 50 fs/kHz for $Q_0 \approx 10^4$. This simple model illustrates the important features of the phase response of the cavity in the vicinity of resonance, in particular that the sensitivity as a function of detuning $\Delta\omega$ increases linearly with Q_0.

2.3.2 Microwave network response functions

In practice a microwave network consists of many impedance elements Z_i which have incident voltages V_i and currents I_i. Port i is some location within the network where the a wave excitation is defined or measured in terms of I_i and V_i. The relationship between

(V_i, I_i) at port i and (V_j, I_j) at port j is determined by the transmission matrix [78] (or $ABCD$ matrix) according to

$$\begin{pmatrix} V_i \\ I_i \end{pmatrix} = \prod_{i<j} \mathbf{T}_i \begin{pmatrix} V_j \\ I_j \end{pmatrix}. \tag{2.31}$$

For a parallel circuit element as shown in Figure 2–5 a), the transmission matrix is given in terms of the admittance $Y(\omega) = 1/Z(\omega)$ and reads

$$\mathbf{T}_i = \begin{pmatrix} 1 & 0 \\ Y_i & 1 \end{pmatrix} = \begin{pmatrix} A & B \\ C & D \end{pmatrix}$$

An accurate circuit model description of the microwave network comprising the compression cavity consists of a transmission line with characteristic impedance Z_0 coupled to the cavity resonator inductively by a transformer with power transfer coefficient n_1. The cavity is also coupled to second transformer (n_2) which allows for signal transmission out of the cavity to a second transmission line also with impedance Z_0. The total transmission matrix is given by the product of all transmission matrices

$$\begin{aligned} \mathbf{T} &= \mathbf{T}_{n_1}\mathbf{T}_{C_c}\mathbf{T}_{R_c}\mathbf{T}_{L_c}\mathbf{T}_{n_2} \\ &= \begin{pmatrix} 1/n_1 & 0 \\ 0 & n_1 \end{pmatrix} \cdot \begin{pmatrix} 1 & 0 \\ iC_c\omega & 1 \end{pmatrix} \cdot \begin{pmatrix} 1 & 0 \\ 1/iL_c\omega & 1 \end{pmatrix} \cdot \begin{pmatrix} 1 & 0 \\ 1/R_c & 1 \end{pmatrix} \cdot \begin{pmatrix} n_2 & 0 \\ 0 & 1/n_2 \end{pmatrix} \\ &= \begin{pmatrix} n_2/n_1 & 0 \\ n_2\left(iC_c\omega n_1 + n_1/R_c - in_1/L_c\omega\right) & n_1/n_2 \end{pmatrix}. \end{aligned} \tag{2.32}$$

The transmission function $S_{21}(\omega) = \left|V_2^-/V_1^+\right|$ is of interest, with $+$ and $-$ representing voltage waves entering or leaving the resonator circuit respectively. It can be shown that

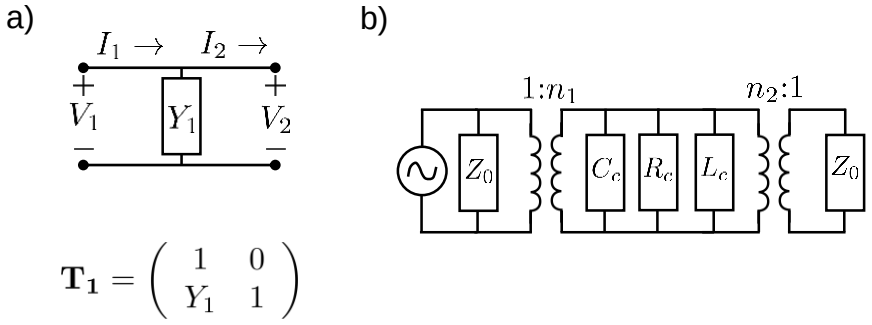

Figure 2–5: Network theory description of a lumped-model cavity.
a) Microwave network representation of a parallel admittance element Y_1. Port 1 has voltage and current V_1 and I_1 respectively and the element Y_1 transforms them to V_2 and I_2 at port 2 respectively. The transmission matrix $\mathbf{T_1}$ for Y_1 is shown below. b) Microwave network model of an RF generator connected to a transmission line with impedance Z_0 which couples to a parallel RLC resonator circuit via a transformer with transfer efficiency n_1. The resonator is output coupled via a second transformer (n_2) to a readout transmission line with impedance Z_0.

this function is related to the elements of $\mathbf{T}$ according to the following equation [78]

$$S_{21}(\omega) = \frac{2}{A + B/Z_0 + Z_0 C + D}, \tag{2.33}$$

$$= \frac{2}{n_1/n_2 + n_2/n_1 + n_1 n_2 Z_0/R_c - i n_1 n_2 Z_0 \left(C_c\omega - 1/L_c\omega\right).} \tag{2.34}$$

The above equation can be re-written in terms of the external quality factors $Q_{e1} = n_1\omega_0 Z_0 C_c$ and $Q_{e2} = n_2\omega_0 Z_0 C_c$ (one for each port), the internal quality factor Q_0 and one additional parameter $Q_z = \omega_0 Z_0 C_c$. In this representation the transmission function is

$$S_{21}(\omega) = \frac{2\left(Q_{e1}/Q_{e2}\right)}{1 + \frac{Q_{e1}^2}{Q_{e2}^2} + \frac{Q_{e1}^2}{Q_0 Q_z}\left(1 + i\frac{\omega_0}{\omega}Q_0\left(\frac{\omega^2 - \omega_0^2}{\omega_0^2}\right)\right)}. \tag{2.35}$$

Equation (2.35) is the true lineshape response function of the coupled RF cavity system and can be used as an exact fitting model for the cavity if measuring or simulating $S_{21}(\omega)$ using

a network analyzer or simulation package. By measuring the transmission S_{21} function,

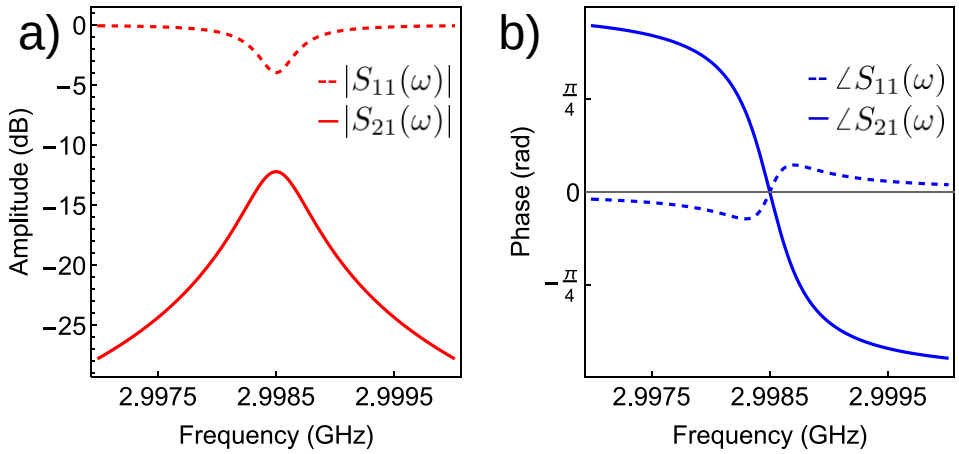

Figure 2–6: Response of the S_{21} transmission and S_{11} reflection functions. a) Magnitude of the transmission function $|S_{21}(\omega)|$ and $|S_{11}(\omega)|$ reflection function. b) Phase of the transmission funtion $\angle S_{21}(\omega)$. Circuit paramters used: $Z_0 = 50\ \Omega$, $R_c = 50\ \Omega$, $L_c = 0.26$ pH, $C_c = 10$ nF $Q_0 = 8 \times 10^3$, $\omega_0 = 2.9985$ GHz, $n_1 = 2$ and $n_2 = 3$.

information about the phase of the cavity field oscillation can be obtained. The amplitude and phase of the S_{21} are shown in Fig. 2–6. Another potentially useful microwave network parameter is the reflection function or the S_{11} parameter defined as $S_{21} = \left|V_1^-/V_1^+\right|$. In terms of the $ABCD$ matrix elements, the reflection function is given by

$$\begin{aligned} S_{11}(\omega) &= \frac{A + B/Z_0 - Z_0 C - D}{A + B/Z_0 + Z_0 C + D}, \\ &= \frac{-2iL_c n_2^2 R_c \omega}{n_1^2 n_2^2 R_c Z_0 + iL_c n_1^2 R_c \omega + iL_c n_2^2 R_c \omega + iL_c n_1^2 n_2^2 Z_0 \omega - C_c L_c n_1^2 n_2^2 R_c Z_0 \omega^2} - 1. \end{aligned} \tag{2.36}$$

The amplitude and phase of the S_{11} is shown in Fig. 2–6 for the purpose of comparing with the S_{21}. As seen in Fig. 2–6 b) in the vicinity of resonance, a linear phase-frequency relationship appears, thus indicating that a measurement of the reflected RF signal would contain information about the cavity phase. The slope (phase sensitivity) of the S_{21} phase

as a function of frequency for the cavity parameters considered here is less than that of the S_{21}. Furthermore, the general functional form of the phase of the S_{11} depends strongly on the details of the cavity coupling, whereas the overall $\arctan(x)$ character of the S_{21} is a robust feature, holds for arbitrary cavity coupling parameters and only depends on the internal Q_0. The origin of this is rooted in the linear response of a harmonic oscillator presented above. A detailed understanding of what constitutes the optimal cavity design in terms of yielding a useful S_{11} phase response would follow a detailed simulation analysis of the cavity as a function of coupling geometry. This analysis is beyond the scope of this thesis, but the general aspects described here provide a useful starting point.

2.4 Fundamental synchronization limits

Now that the physics of RF cavities has been presented, the focus shifts to understanding the synchronization requirements for ultrafast electron diffraction with RF pulse compression. There are fundamental processes in nature which establish limits to the maximum quality of synchronization which can be achieved. In the context of an ultrafast electron diffraction experiment, the temporal jitter Δt_s arising from the phase noise spectrum of the laser-microwave synchronization system is an important quantity to consider. This term contributes to the total time resolution $\mathcal{T}$ of the experiment/instrument given by Eqn. (1.1) which is given by

$$\mathcal{T} = \sqrt{\tau_{\text{laser}}^2 + \tau_{\text{electron}}^2 + \Delta t_s^2}, \tag{2.37}$$

where τ_{laser} and τ_{electron} are the optical and electron pulse durations respectively. The challenge of laser-microwave synchronization is to transfer the high-temporal resolution provided by stable ultrafast laser systems to the electron domain whilst introducing as little phase noise as possible. The main contributions to phase noise and therefore time resolution result from thermal noise, shot noise and amplitude-phase conversion processes [10, 79, 80,

81, 82, 83, 84]. These effects will be discussed in subsequent sections. In the next section the concept of phase noise is introduced as a general figure of merit for synchronization.

2.4.1 Phase noise

Consider an oscillating signal $A(t) = A_0(t)\sin(\omega(t)t + \phi(t))$ propagating in a transmission line, where $A(t)$ is a time-varying amplitude, $\omega(t)$ is a time-varying frequency and $\phi(t)$ is a time-varying phase. If the frequency fluctuations $\Delta\omega(t)$ are small relative to the time-averaged carrier frequency $\omega_0 = \langle\omega(t)\rangle$, such fluctuations yield an equivalent phase shift $\Delta\phi_\omega(t) = \Delta\omega(t)\ell/c$ which depends on the position ℓ along the transmission line where the phase difference relative to a reference phase defined by the carrier $\phi_{\text{ref}} = \omega_0\ell/c$ is measured. In this situation, phase fluctuations due to frequency fluctuations are indistinguishable from "pure" phase shifts characterized by $\Delta\phi(t)$ as illustrated in Figure 2–7. Phase fluctuations of this type produce *phase noise* [79, 80] which is characterized by a mean-squared power spectral density (PSD) of the phase fluctuations in a 1 Hz bandwidth

$$\mathcal{S}_\phi(\omega) = \langle\Delta\phi(\omega)\rangle^2. \qquad \left[\frac{\text{rad}^2}{\text{Hz}}\right] \tag{2.38}$$

Equation (2.38) is the double sided PSD, which is commonly taken as twice the single sided PSD, $\mathcal{S}_\phi(\omega) = 2\mathcal{L}_\phi(\omega)$, because fluctuations may be taken as symmetric about the carrier frequency ω_0. The timing jitter spectral density is related to $\mathcal{L}_\phi(\omega)$ according to

$$\mathcal{T}_\phi(\omega) = \frac{\Delta\phi(\omega)}{\omega_0} = \frac{1}{\omega_0}\sqrt{2\mathcal{L}_\phi(\omega)}. \qquad \left[\frac{\text{s}}{\sqrt{\text{Hz}}}\right] \tag{2.39}$$

For an application with bandwidth $\omega_2 - \omega_1$, the RMS timing jitter is found by integrating $\mathcal{L}_\phi(\omega)$ over that bandwidth.

$$t_{\text{RMS}} = \frac{1}{\omega_0}\sqrt{2\int_{\omega_1}^{\omega_2}\mathcal{L}_\phi(\omega)d\omega}. \qquad [\text{s}] \tag{2.40}$$

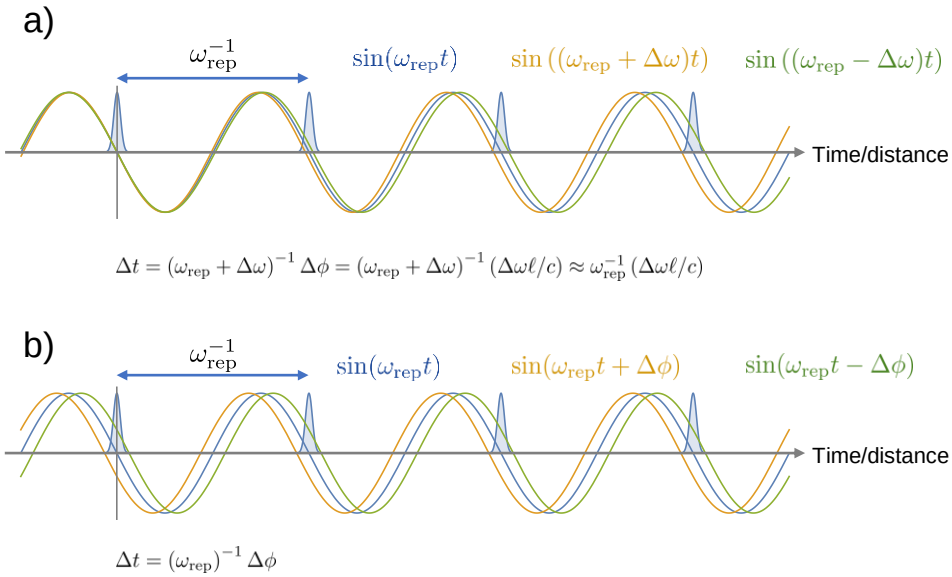

Figure 2–7: Illustation of frequency and phase fluctuations in the time domain. a) An optical pulse train with repetition rate ω_{rep} serves as a timing reference. Harmonic signals with frequency detuning $\Delta\omega$ yield an effective phase shifts at the time specified by a particular optical pulse. b) Pure phase shifts in the time domain produce delays relative to the optical pulse.

Inspection of Eqn. (2.40) indicates that the RMS timing jitter t_{RMS} can be reduced by minimizing the bandwidth of the application and the phase noise contributions within such a bandwidth. In typical situations involving phase noise, it is conventional to define the phase noise density relative to the power at the carrier frequency. In other words, the phase-modulated component of the total noise power spectrum normalized to the RF power of a carrier signal P_{rf} is of interest and is defined as [10]

$$\mathcal{L}_{\phi}(\omega) \equiv \frac{\text{Single-sideband noise PSD due to phase modulation } [\mathrm{W/Hz}]}{P_{\mathrm{rf}}(\omega_0)\,[\mathrm{W}]}, \qquad \left[\frac{\mathrm{dBc}}{\mathrm{Hz}}\right] \tag{2.41}$$

where the units of dBc/Hz represents decibels relative to the carrier signal. In practice there may be several sources contributing to $\mathcal{L}_\phi$ such as thermal noise, shot noise and amplitude-modulated phase noise. In Chapter 2, the relevant contributions will be discussed in detail with respect to the application of laser-microwave synchronization for electron pulse compression.

2.4.2 Optical-microwave timing transfer

In order to link the optical and electronic domains, an opto-electronic photonic device such as a photodetector is required. A photodetector consists of a PIN junction fabricated out of semiconducting material, the band-gap of which dictates roughly the wavelength around which the photodetector can sample light efficiently. The PIN junction is micro-fabricated in a circuit consisting of a shunt capacitance C_s and shunt resistance R_s which governs the response time $\tau_r = R_s C_S$ and correspondingly the bandwidth of the detector $\Delta\omega_{pd} \approx 1/\tau_r$. The circuit output coupled typically to a 50 Ω impedance. Applied to the PIN junction is typically some type of biasing voltage for optimal operation. A photodiode is characterized by its responsivity $\Re(\nu) = \eta(\nu)q/h\nu$, which has units of [A/W], where $\eta(\nu)$ is the quantum efficiency of the PIN junction and ν is the frequency of the optical light. When illuminated by an optical pulse train with repetition rate ω_r, typical of an ultrafast oscillator as described in sec. 1.2, the photo-diode will produce a current response of the general form

$$I(t) = I_0 \sum_{n=-\infty}^{+\infty} f\left(t - \frac{2\pi n}{\omega_r}\right) = \sum_{n=1}^{\infty} A_n \cos(\omega_n t) + \sum_{n=1}^{\infty} B_n \sin(\omega_n t), \tag{2.42}$$

where the RHS of Eqn. (2.42) is represented in general by a Fourier series with coefficients A_n and B_n. The form of f is governed by the response properties of the photo-detector. For the limiting case where the harmonic frequencies are perfectly defined, the current response in the Fourier domain at frequencies up to the bandwidth imposed by the response of the

detector is given by

$$I(\omega) = \sum_{n=1}^{\Delta\omega_{pd}/\omega_r} I_n \delta(\omega - n\omega_r), \tag{2.43}$$

which describes a frequency comb spanning up to the detector bandwidth in steps of the pulse train fundamental repetition rate. In practice, phase noise processes cause the delta functions to widen into Lorentzian functions, more representative of a signal measured using a typical spectrum analyzer.

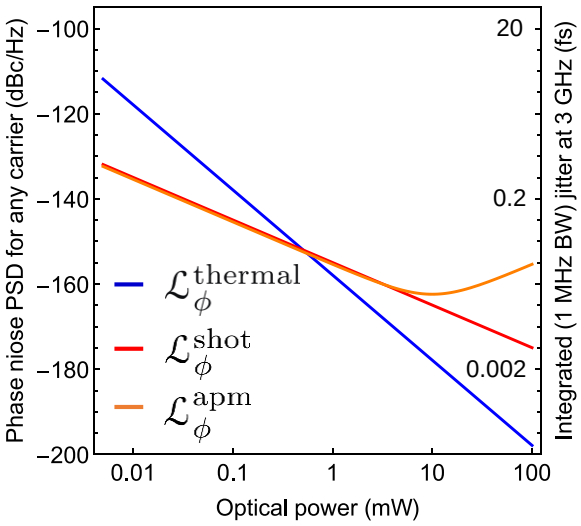

Figure 2–8: Fundamental phase noise power spectral densities as a function of optical power on a photodetector.
Thermal phase noise $\mathcal{L}_\phi^{\text{thermal}}$ and shot phase noise $\mathcal{L}_\phi^{\text{shot}}$ are independent of carrier frequency and exhibit P_{opt}^{-2} and P_{opt}^{-1} dependencies on optical power respectively. The jitter integrated over 1 MHz bandwidth represents a noise floor contribution. Amplitude phase modulation processes follow shot noise until the saturation point of the photodetector is achieved, beyond which the noise rapidly increases.

2.4.3 Thermal noise

Thermal agitation of charge carriers at a temperature T produce voltage fluctuations $\langle V \rangle$ which are approximately frequency independent when $\omega < k_B T/\hbar$. This process yields

a thermal noise power over a bandwidth $\Delta\omega$ given by

$$P_{\text{thermal}} = \frac{\langle V \rangle}{Z_0} = \frac{1}{2} k_B T \Delta\omega. \tag{2.44}$$

The thermal phase noise power spectrum for a signal with carrier frequency ω_c and power P_c in a 1 Hz bandwidth is $\mathcal{L}_\phi^{\text{thermal}} = \frac{1}{\Delta\omega} P_{\text{thermal}}/P_c(\omega_c) = k_B T/2P_c$. The magnitude of P_c produced by a photodiode in a 50 Ω system is $P_c = I^2 Z_0 = (\mathcal{R} P_{\text{opt}})^2 Z_0$ which allows us to express Eqn. (2.44) in terms of the optical power P_{opt} incident on a photodiode.

$$\mathcal{L}_\phi^{\text{thermal}} = \frac{k_B T}{2\mathcal{R}^2 Z_0 P_{\text{opt}}^2}. \tag{2.45}$$

The thermal phase noise as a function of optical power for any carrier frequency is shown in Fig. 2–8.

2.4.4 Shot noise

A second source of phase noise arises from shot noise of the optical pulse train which illuminates the photodetector. This type of noise yield fluctuations in the average photocurrent generated in the optical receiver circuit and is $\mathcal{L}_\phi^{\text{shot}} = qIZ_0/P_c$ which gives the following when expressed in terms of optical power

$$\mathcal{L}_\phi^{\text{shot}} = \frac{q}{\mathcal{R} P_{\text{opt}}}. \tag{2.46}$$

Equation (2.46) is also plotted in Fig. 2–8. Clearly $\mathcal{L}_\phi^{\text{shot}}$ demonstrates a weaker dependence on optical power and overtakes $\mathcal{L}_\phi^{\text{thermal}}$ at a power of $P_{\text{opt}} \approx 0.5$ mW in a 50 Ω system at T =295 K using a photodiode responsivity of 0.5 A/W.

Thermal noise and shot noise are both "white" processes which are frequency independent and essentially define the noise floor of a phase noise spectrum at large Fourier frequencies away from the carrier. Integration of $\mathcal{L}_\phi^{\text{thermal}}$ and $\mathcal{L}_\phi^{\text{shot}}$ over the bandwidth thus yield relatively small contributions to the total RMS timing jitter (see Fig. 2–8) as

per

$$t_{\mathrm{RMS}}^{\mathrm{thermal}} = \frac{1}{\omega_c}\sqrt{2\int_{\omega_1}^{\omega_2}\mathcal{L}_{\phi}^{\mathrm{thermal}}d\omega} = \frac{1}{\omega_c}\sqrt{\frac{k_B T\Delta\omega}{\mathcal{R}^2 Z_0 P_{\mathrm{opt}}^2}}, \tag{2.47}$$

$$t_{\mathrm{RMS}}^{\mathrm{shot}} = \frac{1}{\omega_c}\sqrt{2\int_{\omega_1}^{\omega_2}\mathcal{L}_{\phi}^{\mathrm{shot}}d\omega} = \frac{1}{\omega_c}\sqrt{2\frac{q\Delta\omega}{\mathcal{R}P_{\mathrm{opt}}}}. \tag{2.48}$$

The phase noise spectrum of a typical ultrafast oscillator pulse train incident on a photodetector will be dominated by phase/frequency fluctuations at small offset Fourier frequencies due to acoustic vibrations of the laser cavity, long term temperature drifts, electronic $1/f$ flicker noise and amplitude phase conversion. Electronic flicker noise can arises during subsequent amplification of the microwave signal generated by the photodetector and can be minimized through the use of *ultra-low phase noise* microwave components. Management of amplitude phase conversion processes in systems where low phase noise is required is of critical importance. In practice the phase noise of such processes can be challenging to measure and requires specialized frequency metrology techniques. Nonetheless accurate models based on differentials of statistical averages can be constructed and are useful in predicting the time-averaged effect of amplitude phase conversion.

2.4.5 Amplitude-phase conversion in photodetectors

The amplitude phase conversion process occuring in photodetectors may be modeled by looking at the fluctuations in the current response generated by the laser pulse train. Consider an ultrafast optical laser pulse with temporal duration τ_{laser} incident on a photodetector at $t = 0$. The time-domain response of the current generated in a photodetector $I_p(t)$ may be reasonably well-described by a product exponential function with rise-time τ_r and fall time τ_f given by

$$I_p(t) = \tilde{I}\left(1 - e^{-t/\tau_r}\right)e^{-t/\tau_f}, \tag{2.49}$$

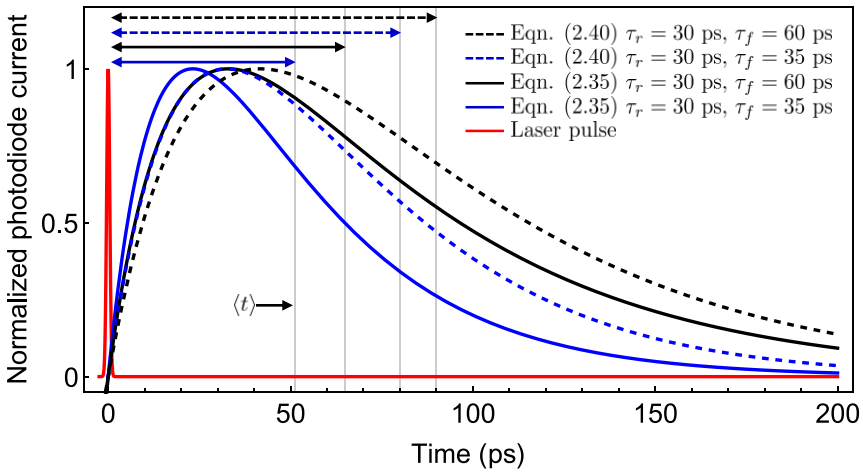

Figure 2–9: Amplitude phase modulation in photodetectors
The timing transfer of an ultrashort laser pulse (red) to a current response in a photodetector for various waveform models given by equations (2.49) and (2.54). The effect of saturation is to shift the first moment of the pulse $\langle t \rangle$ relative to the optical inpulse leading to a temporal phase shift.

where $\tilde{I}$ is a normalized current amplitude defined such that the maximum amplitude of $I_p(t)$ is the same for all values of τ_r and τ_f. $\tilde{I} = 1/I_p(t_{\max})$ where $t_{\max} = \tau_r \ln(1 + \tau_f/\tau_r)$ is found by minimizing dI_p/dt. The intrinsic *response delay* $\mathcal{D}$ of the photodetector relative to the optical pulse is found by calculating the first moment of the $I_p(t)$ in the time domain according to

$$\mathcal{D} \equiv \langle t \rangle = \lim_{t' \to \infty} \int_0^{t'} t I_p(t) dt \Big/ \int_0^{t'} I_p(t) dt, \tag{2.50}$$

$$= \frac{\tau_f(\tau_f + 2\tau_r)}{\tau_f + \tau_r}. \tag{2.51}$$

Saturation effects within the photodiode lead to the increase of τ_f which are strongly power dependent in the vicinity of and above the saturation power threshold P_{sat} of the photodetector. Such effects are of concern as they lead to changes in $\langle t \rangle$ relative to the

optical reference. Differentiation of Eqn. (2.51) with respect to τ_f yields

$$\frac{d\langle t\rangle}{d\tau_f} = \frac{\tau_f^2 + 2\tau_f\tau_r + 2\tau_r^2}{(\tau_f + \tau_r)^2}. \tag{2.52}$$

The fall time τ_f may be modeled as a function of incident optical power P_{opt} as $\tau_f(P_{\text{opt}}) = \tau_{f0}\left(1 + (P_{\text{opt}}/P_{\text{sat}})^{\beta}\right)$. Applying this transformation to Eqn. (2.52) yields the following expression

$$\frac{d\langle t\rangle}{dP_{\text{opt}}} = \frac{\beta\tau_{f0}}{P_{\text{sat}}}\left(\frac{P_{\text{opt}}}{P_{\text{sat}}}\right)^{\beta-1}\left[1 + \left(1 + \frac{\tau_{f0}}{\tau_r}\left(1 + \frac{P_{\text{opt}}}{P_{\text{sat}}}\right)^{\beta}\right)^{-2}\right]. \tag{2.53}$$

Equation (2.53) is the *amplitude phase coefficient* for the photodiode which can be converted to radians/pulse energy for a given laser system and carrier frequency. The phase noise spectrum of $\langle t\rangle$ would essentially be established by the amplitude noise spectrum of P_{opt}. For our purposes however it is useful to remain in the time domain.

An alternative representation of the current response of the photodiode could be taken as

$$I_p(t) = \tilde{I}\left(e^{-t/\tau_f} - e^{-t/\tau_r}\right), \qquad \tau_r < \tau_f \tag{2.54}$$

where $\tilde{I} = I_p(t_{\max})$, with $t_{\max} = \ln(\tau_f/\tau_r)\,/\left(\tau_r^{-1} - \tau_f^{-1}\right)$ is the normalization prefactor. In this model, the first moment is given simply by $\langle t\rangle = \tau_f + \tau_r$ which in turn yields the simple expression for the the amplitude phase coefficient

$$\frac{d\langle t\rangle}{dP_{\text{opt}}} = \frac{\beta\tau_{f0}}{P_{\text{sat}}}\left(\frac{P_{\text{opt}}}{P_{\text{sat}}}\right)^{\beta-1}, \tag{2.55}$$

which is roughly equivalent to Eqn. (2.53). The magnitude of Eqn. (2.55) may be easily estimated using typical photodiode parameters. In this work a commercial GaAs fast photodetector (Newport 818-BB-45) is used. This photodetector unit has an optical saturation power of $P_{\text{sat}} \approx 20$ mW, and an unsaturated fall time of $\tau_{f0} = 30$ ps. These are typical values for commercial products designed for ultrafast lasers. Using a non-linearity exponent

of $\beta = 2$, a value consistent with recent research in this area [85, 86, 87, 84, 88, 89] it is found that $\frac{d\langle t\rangle}{dP_{\rm opt}} = 1.5$ ps/mW for an input optical power of $P_{\rm opt} = 10$ mW. At saturation, this value doubles to 3 ps/mW. A typical Titanium:Sapphire mode-locked oscillator will have a power stability between $\Delta P_{\rm opt}/P_{\rm opt} \approx 0.1 - 1\%$ in terms of long-term stability and 0.2% at the shot-to-shot level. This translates to a time-averaged timing-transfer jitter of $15 - 150$ fs for an input power of $P_{\rm opt} = \frac{1}{2}P_{\rm sat}$. More elaborate solutions such as balanced optical-microwave phase detectors [90, 91, 92] exist but are based on Er-doped fiber laser technology [93] not transferable to Titanium:Sapphire technology.

2.4.6 Amplitude-phase conversion in microwave mixers

Amplitude phase conversion can occur in microwave mixers due to saturation effects in the diode ring array and power instability of the input signals. A microwave mixer combines two input signals typically referred to as the "local oscillator" (LO) and RF signals given by $V_{\rm LO}(t) = V^0_{\rm LO}\cos(\omega_{\rm LO}t + \phi_{\rm LO})$ and $V_{\rm RF}(t) = V^0_{\rm RF}\cos(\omega_{\rm RF}t + \phi_{\rm RF})$ respectively. The output signal is called the intermediate frequency signal (IF) and is ideally of the form [78]

$$V_{\rm IF}(V^0_{\rm LO}, V^0_{\rm RF}, \omega_{\rm LO}, \omega_{\rm RF}, t, \phi_{\rm LO}, \phi_{\rm IF}) = f(V^0_{\rm LO}, V^0_{\rm RF})\cos\left((\omega_{\rm LO} \pm \omega_{\rm RF})t + \phi_{\rm LO} \pm \phi_{\rm RF}\right). \tag{2.56}$$

In phase detection mode, the LO and RF frequencies are equivalent, and the IF output is low-pass filtered which results in a DC output which depends only on the relative phase between the LO and RF signals $\Delta\phi = \phi_{\rm LO} - \phi_{\rm RF}$. In practice, mixers have small, amplitude dependent, DC offset terms $\mathcal{A}(V^0_{\rm LO}, V^0_{\rm RF})$ which yields $V_{\rm IF} \neq 0$ for $\Delta\phi = \pi/2$. The phase detector is characterized by $dV_{\rm IF}/d\Delta\phi$ at $\Delta\phi = 0$, called the detector constant κ which is typically on the order of $\kappa \approx 0.1$ V/rad. When operating at near $\Delta\phi = \pi/2$, fluctuations in the offset yield a phase error given simply by $d\mathcal{A}/d\phi = \kappa$, which corresponds to the amplitude phase conversion coefficient of the mixer as illustrated in Fig. 2–10. The phase detector constant κ is also in principle sensitive to amplitude fluctuations, but these effects

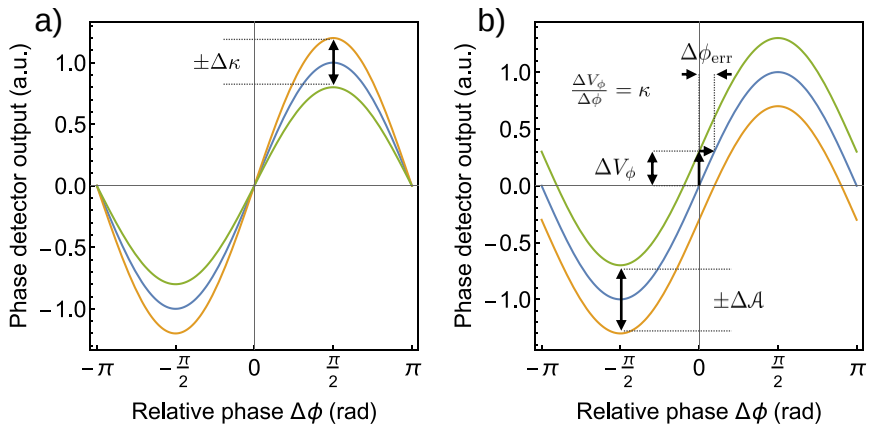

Figure 2–10: Microwave mixer amplitude phase conversion.
a) Amplitude-phase conversion yielding a scaling of the sinusoidal output. This process can be minimized by operating near the zero-crossing. Amplitude phase conversion by changes in detector offset. This process yields amplitude-modulated phase errors given according to the detector constant κ.

can be made negligible compared to offset fluctuations by operating as close as possible to $V_{\mathrm{IF}} = 0$. By converting to a timing error using a phase detector coefficient of $\kappa = 300$ mV/rad at a carrier frequency of $\omega_c = 2\pi \times 3$ GHz, $\Delta t/\Delta\mathcal{A}$ is roughly 180 fs/mV. So called *double-balanced* mixers do a reasonably good job in minimizing the amplitude sensitivity of the mixer, but for precise timing applications the detector offset can easily become a limitation in feedback systems such as phase locked loops [94] (PLLs). In general all measures should be taken to characterize the amplitude phase sensitivity of a detector and stabilize the microwave signals to below 1 mV. This can be very challenging at the microwave powers typically required for efficient operation of the mixer, which are usually above +10 dBm, meaning that power fluctuations of ±0.01 dBm correspond to a value of $\pm\Delta\mathcal{A} = \pm 0.8$ mV yielding roughly ±140 fs.

2.5 Robust high-performance synchronization for ultrafast electron diffraction with pulse compression

2.5.1 Issues with previous pulse compression systems

The first generation of ultrafast electron diffraction instruments with pulse compressors suffered from significant synchronization issues, which limited the overall temporal resolution to roughly 500 fs [50, 55]. As a result, the practical benefits from using microwave pulse compression were primarily enhanced signal and beam brightness rather than the expected significant improvement in time resolution compared to older generation compact ultrafast electron diffraction instruments. Most synchronization approaches employed a phase-locked-loop (PLL) to synchronize the laser to an external voltage-controlled-oscillator (VCO) which had a center frequency designed to be resonant with the compression cavity (2.9985 GHz). The system was a commercial product marketed for ultrafast electron diffraction with pulse compression provided by the company AccTec B.V. with a design based off of the work found in ref. [94]. The PLL worked in the following way: the 5th harmonic of the oscillator repetition rate ($5 \times f_{\text{rep}} \approx 375$ MHz) was synchronized to the 8th subharmonic of a ~ 3 GHz voltage controlled oscillator (VCO), obtained by frequency division. The locking was achieved by varying the VCO frequency until the mixing product of the two signals yielded a minimum DC term, which corresponded to the frequencies being equivalent thereby establishing a phase-lock. The PLL system worked reasonably well in the elimination of high-frequency jitter (i.e. the phase noise PSD was relatively low at larger carrier offset frequencies) but suffered significantly from low-frequency jitter (drift) components. These low frequency originated primarily from amplitude phase conversion intrinsic to the mixer of the PLL. Moreover the amplitude phase response properties of the cavity (as described in sec. 2.3.2) were not incorporated into the synchronization control loop.

2.5.2 Design considerations

In this section the synchronization system for ultrafast electron diffraction with pulse compression is presented. In our experiments the relative timing changes with respect to an optical pulse, not the absolute timing error error of a single clock, are important and of concern. Our approach thus elects to use the laser oscillator as the master clock as overall drift gets transferred to the entire system and does not impact the relative changes. This approach also has the advantage of eliminating amplitude phase conversion errors which arise inevitably when locking to an external oscillator in a phase-locked loop configuration. Furthermore, the phase noise power spectral density of the repetition rate is suppressed by a factor equal to the harmonic order extracted from the frequency comb which can be made far lower than standard voltage-controlled oscillators. The work presented hereafter is a detailed presentation and characterization of the new synchronization approach. At the end a comparison with the previous synchronization system will be made from the point of the view of amplitude-phase conversion effects.

The overall approach of the new synchronization system focuses on the minimization of all the phase/timing instability effects mentioned in the preceding sections. In summary the approach begins with synthesis of a phase-locked frequency comb from a mode-locked titanium:sapphire oscillator using a high-bandwidth photo-detector. The 40^{th} harmonic of the oscilliator repetition rate is isolated and passed through an ultra-low phase noise amplification and filtering chain. A reference portion of this signal is split prior to the high-power amplification step required for driving the electron pulse compression cavity. The reference signal is power stabilized and mixed with the transmitted cavity signal retreived by a pickup antenna integrated into the cavity. The mixing of the signals is performed in a low-phase noise detector and accurately measures phase fluctuations induced by cavity

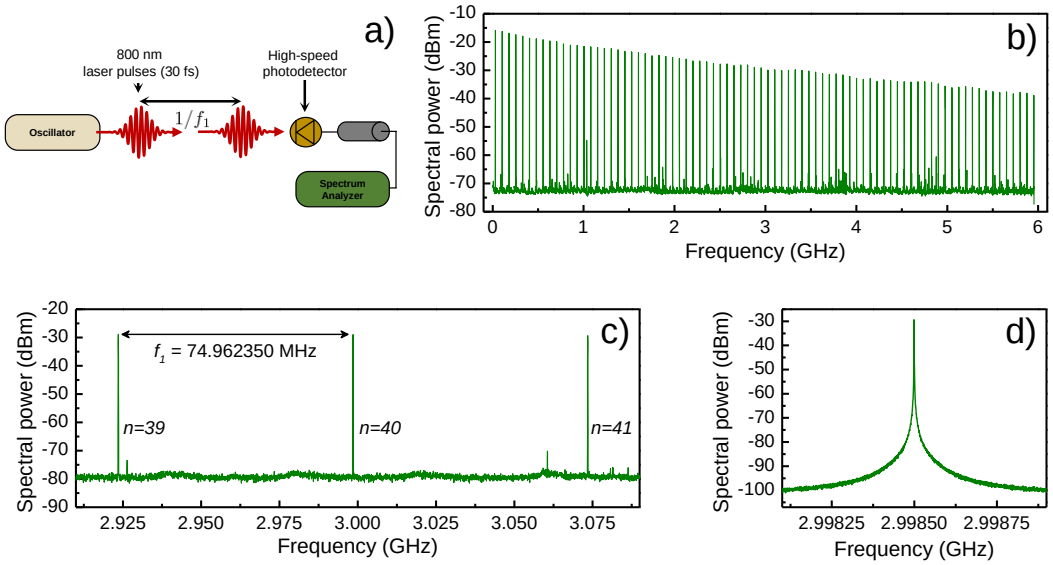

Figure 2–11: Photodetector spectrum of a 75 MHz mode-locked oscillator. a) Schematic of the measurement. b) Broadband output of a 12.5 GHz bandwidth high-speed photoectector illuminated by a 35 fs optical pulse produced by an ultrafast oscillator shown in a). c) 200 MHz spectrum centered on the 40^{th} harmonic of the laser repetition rate. d) 1 MHz spectrum.

resonance detuning processes. This output further serves in an active phase stabilization feedback system.

2.5.3 Microwave signal generation from a mode-locked laser

The first step in the synchronization system is the synthesis of the frequency comb by photodetection of the oscillator pulse train illustrated in Fig. 2–11. The photo-detector used in this work is a commercial product (Newport 818-BB-45) which has a PIN junction fabricated from GaAs, a bandwidth of 12.5 GHz and a responsivity at 800 nm of $\mathcal{R} = 0.475$ A/W. The saturation current is ~ 10 mA, corresponding to an optical saturation power of $P_{\text{opt}} \approx 20$ mW. The power incident on the photo-detector is set to 5 mW which translates to an amplitude phase modulation jitter of ~ 20 fs for oscillator power stability

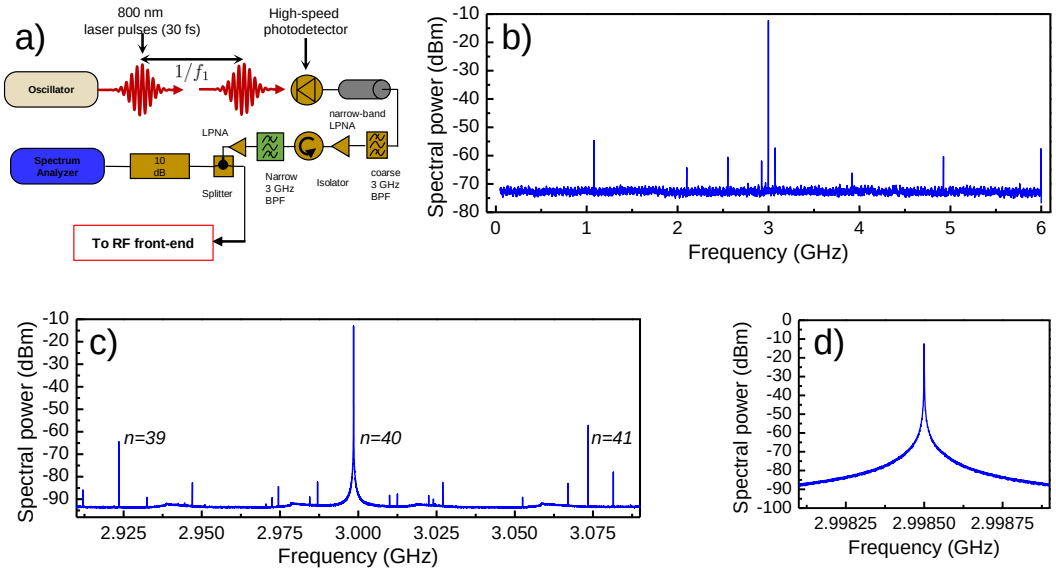

Figure 2–12: Low-level RF synchronization system.
a) Broadband spectrum analyzer trace of the filtered frequency comb showing the isoloation of the 40^{th} harmonic of the laser repetition rate. b) 200 MHz spectrum analyzer trace showing the harmonic signal along with some spurious signals. The spurious signals are insignificant as they fall outside the bandwith of the compression cavity. c) 1 MHz span of the drive signal. d) Schematic of the low-level RF system and measurement setup.

of 0.5% according to Eqn. (2.55). The oscillator-photodetector output spectrum is shown in Fig. 2–11 a) and consists of a broadband frequency comb with spacing given by the fundamental repetition rate of the ocillator which is $f_{\text{rep}} = 74.962350 \pm 0.5$ MHz measured using a nanosecond counter and confirmed by a second measurement with a calibrated spectrum analyzer. The amplitude of the comb signals demonstrate a inverse frequency dependence, and the power at the $n = 40$ harmonic of f_{rep} is measured to be -29.34 dBm in a 1 Hz bandwith.

2.5.4 Low-level RF system

The desired frequency for pulse compression is the $n = 40$ harmonic of f_{rep} which is resonant with the cavity frequency of $f_0 \sim 2.9985$ GHz (at 18 degrees Celsius). The

low-level signal requires amplification by nearly 80 dB before it can be used to drive the cavity. Before efficient amplification can occur however, the spectrum requires filtering to isolate the desired frequency, otherwise gain with be distributed across all harmonics which fall within the amplification band resulting is weaker spectral power at the harmonic of interest. The spectrum is coarsely filtered by a bandpass filter spanning $2.7 - 3.1$ GHz and then is amplified by an ultra-low phase noise amplifier (Miteq AMF-2F-02700310-04-10P-LPN) providing +28 dB of gain from $2.7 - 3.1$ GHz which has noise figure < 0.4 dB. The phase noise spectrum of this amplifier is specified at $\mathcal{L}_\phi = -123, -140, -148, -160$ dBc/Hz at 10 Hz, 1 kHz, 10 kHz and 1 MHz carrier offset frequencies respectively and contributes a negligible amount of jitter to the signal (< 1 fs RMS). The signal is then filtered by a custom designed K & L cavity bandpass filter which has bandwidth of 44.8 MHz centered at 2.9985 GHz and a lower and upper rejection of ~ 60 dB at 2.9 and 3.1 GHz. Between the first amplifier and filter is an isolator which protects the amplifier output from reflected signals which are rejected by the filter. Another low phase noise amplifier follows the filter (Holzworth HX2400) providing 14 dB of gain and has phase noise specified by $\mathcal{L}_\phi = -160, 172$ dBc/Hz at 100 Hz and 10 kHz carrier offset frequencies. The output spectrum after this stage is shown in Fig. 2–12. The magnitude of the synchronization signal is -2.56 dBm and is passed to the front-end of the RF-system.

2.5.5 Front-end RF system

The front-end of the RF synchronization system (see Fig. 2–13 a) and b)) consists of a high-power amplification stage and an active feedback system design to compensate for detuning of the cavity resonance frequency relative to the synchronized drive signal which is now referred to as f_d. The drive signal from the low-level RF system passes through a saturated low-noise amplifier to achieve optimal power stability which is crucial for the next step in the synchronization system. The drive signal is then split into two paths using

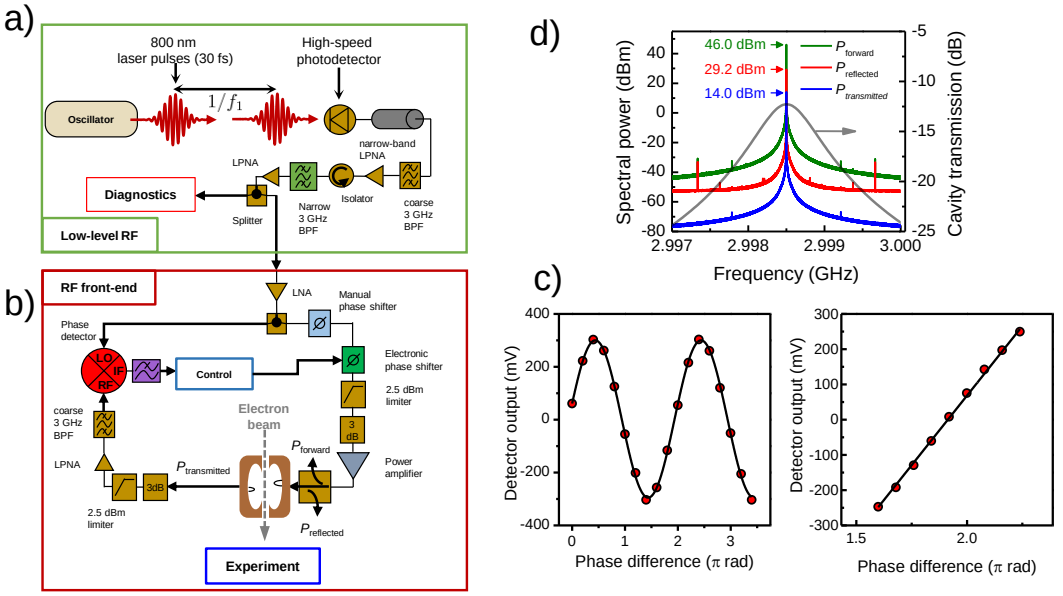

Figure 2–13: Front end of the synchronization system for electron pulse compression. a) The low-level RF system for the generation of the synchronization signal by photodetection of the oscillator pulse train. b) The low-level RF signal is split into two signals, the first being a stable reference (LO) and the second is used for pulse compression after high-power amplification using a solid state continuous wave amplifier. The signal transmitted (RF) through the cavity is amplitude stabilized and mixed in a homodyne configuration with the reference signal by a phase detector. The output of the phase detector measures the relative phase of the two signals which is used in a control loop. c) Phase detector output as a function of phase difference between the LO and RF signals the detector constant is 320 mV/rad. d) Measurement of the forward, reflected and transmitted compression cavity signals. The amplitude response (transmission function) of the cavity is shown as the gray line.

a low phase noise splitter (Holzworth HX3300) the first signal serves as the local oscillator reference of an ultralow phase noise mixer (Holzworth HX3100). The second signal passes through a manual phase-shifter which is used for manual tuning of the compression cavity phase, an electronic low-phase noise phase shifter (Holzworth HX5100), a power 2.5 dBm power limiter as an extra precaution to maxiumize power stability. High power amplification to the level of 50-100 W is achieved using a solid-state continuous-wave power

amplifier (Ophir RF 4022) which can provide up to 60 dB of gain from 2.7 to 3.2 GHz. The RMS power stability of the amplified signal was measured to be ±0.003 dBm. The amplified signal passed through a dual-directional coupler before coupling to the cavity for electron pulse compression. Measurements of the forward, reflected and transmitted power are shown in Fig. 2–13 d). The transmitted signal carries a phase shift given by equation (2.30) which is re-written here for completeness in terms of f_0 and f_d

$$\Delta\phi = \arctan\left(2Q_0\frac{f_d - f_0}{f_0}\right) \approx 2Q_0\frac{f_d - f_0}{f_0}, \qquad f_d/f_0 \approx 1. \tag{2.57}$$

The transmitted signal is amplitude stabilized by a low phase noise amplifier and power limiter before coupling to the RF port of the phase detector. The detector IF output yields a DC voltage depending on the phase difference between the LO and RF signals $\phi_{\mathrm{LO}} - \phi_{\mathrm{RF}}$ which is plotted in Fig. 2–13 c). The detector was calibrated and found to have a phase detector constant of $\kappa = 320$ mV/rad. The phase detector output voltage may be used to accurately follow fluctuations and drift of the cavity field phase. The fluctuations which yield phase changes according to equation (2.57) are primarily slow processes (longer than 1 s) associated with the drift in the cavity resonance f_0 and drive signal f_d. The cavity resonance is governed by cavity temperature changes ΔT and the thermal expansion coefficient according to $\Delta f_0/f_0(T_0) = -k\Delta T$ which is on the order of 300 kHz/K. This effect is minimized as much as possible using a recirculating chiller with a temperature stability of ±5 mK. This alone is insufficient for acheiving the required time resolution, but it is possible to make use of the measured phase changes and apply a correction to restore the cavity phase to an ideal operating point.

2.5.6 Active phase feedback for cavity resonance detuning

The phase detector signal can be further used to compensate phase changes induced by cavity detuning by integrating a feedback system which forms a closed loop around the

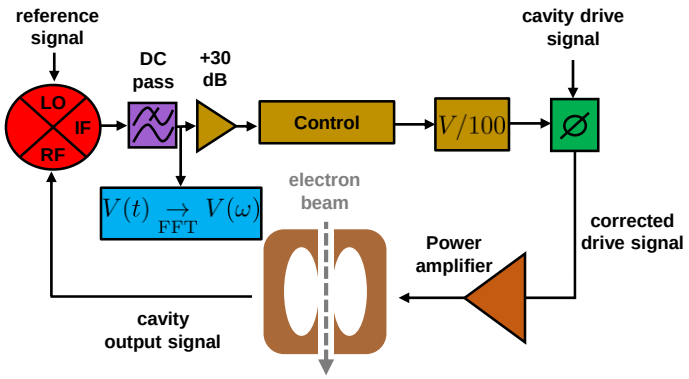

Figure 2–14: Schematic of the cavity active phase feedback system.
The transmitted cavity signal is mixed with a pre-amplification reference signal and the output is low pass filtered. Phase fluctuations relative to an initial point are detected and compensated for using an analog PID controller which drives a precise low phase noise phase shifter. The phase detector output can be analyzed in an FFT manner to yield the phase noise spectrum.

cavity and amplifier system as shown in Fig. 2–13 b) and 2–14. The phase detector signal establishes a reference phase which can be maintained over time by applying a corrective phase shift electronically to the cavity drive signal using low phase noise phase shifter. The feedback system is driven by a 100 kHz analog PID system (Stanford research systems SIM 960 module). The voltage resolution of the PID controller is (at maximum) ± 1 mV, which corresponds to a phase sensitivity given by 1 mV$\times/\kappa = 3.125$ mrad. This limit would mean that the minimum detectable phase difference occuring in the cavity would be $\sim$ 165 fs according to equation (2.23). The phase detection sensitivity is increased by a factor or $\sim$30 by amplifying the output voltage from the phase detector using a 30 dB scaling amplifier. This translates to an absolute phase/timing measurement resolution of roughly 5 fs assuming no amplitude-phase conversion occuring in the mixer (this will be treated later). The electronic phase shifter can perform a phase shift of 0 to 190 degrees over the voltage range of 0 to 10V, which translates to $\sim$ 330 mrad/V. The resolution of the control voltage is also 1 mV which would only correspond minimum phase correction

of 0.33 mrad, which is improved by division of the control voltage by 100 such that the correction resolution is 3.3 μrad/10μV, which lies in the sub-fs regime.

2.5.7 Feedback stabilization performance

The time dependent voltage output of the phase detector $V(t)$ represents phase fluctuations induced by the compression cavity system. The cavity phase noise spectrum is thus related to the Fourier transform of $V(t)$, $\tilde{V}(\omega)$ through the phase detector constant κ. This phase noise describes the *additive phase noise* on top of the reference LO signal since the phase detector operates as a homodyne receiver. Measurements of the cavity phase drift as a function of time measured over a period of time exceeding 16 hours is shown in Fig. 2–15 a) for both free-running and phase-stabilized modes of operation. The additive phase noise spectrum of the compression cavity system (represented as a timing noise power spectral density) is shown in Fig. 2–15 b). As a function of laboratory time, without active phase correction the cavity demontrates long term drift components on the order roughly 10 mrad, corresponding to a timing drift of roughly 500 fs at a carrier frequency of 2.9985 GHz. A histogram of the phase measurements reveals that the RMS timing drift is reduced from 100 to 5 fs. The phase noise spectra demonstrate the suppression by roughly 2 orders of magnitude of the low frequency drift components in the 10 μHz to above 100 mHz. The measurements shown in Fig. 2–15 are electronic measurements of the timing noise/jitter between two signals. In principle this translates 1-to-1 to the temporal arrival time drift of the compressed electron pulses in the limit where $\omega_0\tau \ll 1$ is well satisfied according to Eqn. (2.23). This considerable improvement in the synchronization of RF field cycles in a pulse compression cavity are entirely the product of accounting for the phase response function which is highly sensitive to the cavity resonance relative to the drive signal.

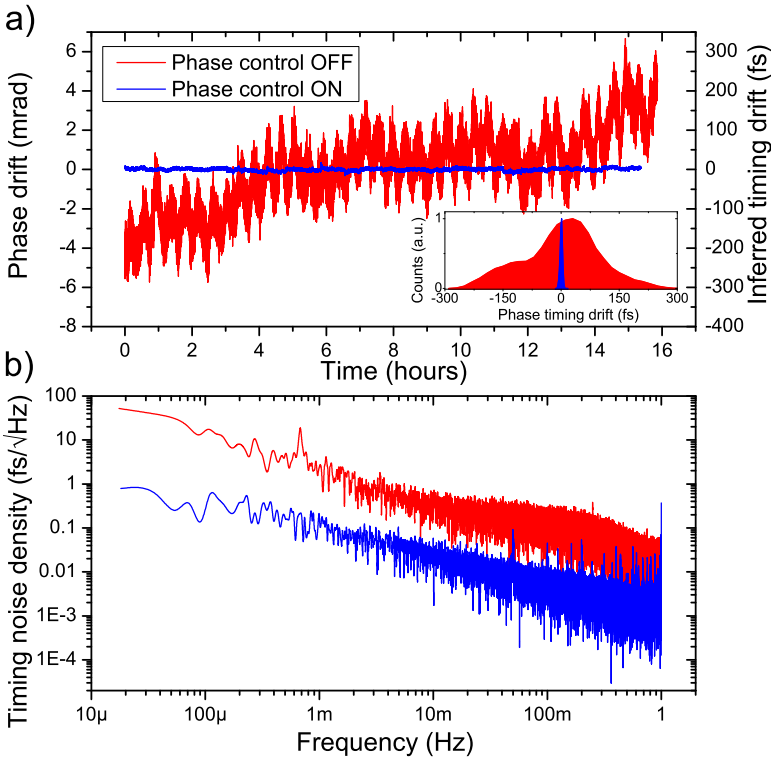

Figure 2–15: Electronic phase stabilization of the compression cavity system. a) Measurements of the cavity phase drift as a function of time with and without the phase correction system activated. b) Fourier tranforms of the traces shown in a) representing the additive phase noise contribution of the compression cavity system to the underlying synchronization signal. Frequencies represent offset frequencies with respect to the carrier frequency of the cavity drive $f_d \simeq 2.9985$ GHz.

2.5.8 Resolution and stabilization limits

Our ability to ultimately correct for phase fluctuations and drift resulting from the cavity detuning factor depend on the ability to detect the phase, or rather, to distinguish real phase changes from those induced by amplitude fluctuations which modulate the detector output as describes in section 2.4.6. All measures are taken to stabilize the power levels of both the reference LO signal and the RF signal feeding the phase detector. The LO signal is amplitude stabilized using the hardware illustrated in Fig. 2–13 to an RMS

stability of $\sigma_{\rm LO} = 0.001$ dBm at a power of 12.00 dBm which yields an amplitude-phase conversion timing error of $\Delta t_{\rm LO}^{\rm err} = \sigma_{\rm LO}/\omega_d\kappa = 16$ fs. The RF signal is more challenging to stabilize. The first challenge is that the signal is necessarily amplified to high power (~ 47.0 dBm) using a CW solid-state amplifier. The amplifier has an output-level control of 0.1 dBm an a stability of $\sigma_A = \pm 0.05$ dBm which would on its own yield timing fluctuations of ± 800 fs (assuming the signal is obviously attenuated down to the 12 dBm level required by the phase detector). Furthermore, the RF signal is amplitude modulated according to the cavity amplitude response (Eqn. (2.35)) unless precisely at resonance, which clearly cannot always be satisfied. As such, the cavity operation is always initiated as close to resonance as possible (found by temperature tuning an optimizing the transmitted power). Figure 2–16 show the arrangement for power stabilization of the RF signal. The transmitted cavity signal is first attenuated slightly by 3 dB then limited to 2.5 dBm using a precision limiter. The power level is then well within the input range which results in a saturated output of an ultra-low phase noise amplifier the output from which is filtered prior to coupling to the phase detector. The power stability of the resulting signal is measured to be $\sigma_{\rm LO} = \pm 0.0031$ dBm which results in an amplitude-phase conversion timing error of $\Delta t_{\rm RF}^{\rm err} = \sigma_{\rm RF}/\omega_d\kappa = 53$ fs. At present in this system, these fundamental limits associated with the power stability of the microwave signals prevents the phase/timing detection threshold from becoming comparable or ideally equal to the phase correction threshold which is established by the control loop. The phase shifter can apply a minimum correction of 3.3 μrad which at 2.9985 GHz translates to a timing shift of 175 attoseconds. The required amplitude stability in order to distinguish a phase shift of this magnitude is roughly 10^{-5} dBm, or 1μV. Achieving this would be technically quite challenging in this configuration, but could perhaps be achieved using complex interferometric stabilization

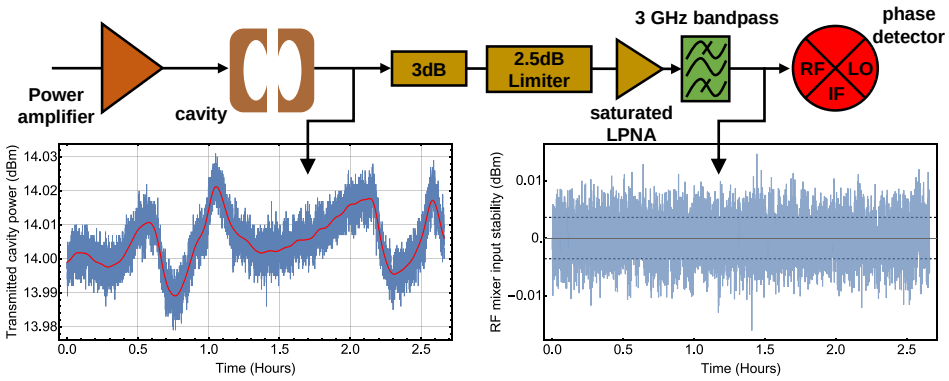

Figure 2–16: Power stability of the phase feedback system.
The raw transmitted cavity power demontrates amplitude noise which is stabilized using a microwave limiter and a low phase noise amplifier operating in saturation mode. This sequence of components smooths out the RF signal feeding the mixer to an RMS stability of 0.0031 dBm.

techniques, IQ quadrature demodulation prior to phase detection or perhaps a secondary power stabilization feedback loop.

2.6 Temporal characterization of compressed electron pulses

In order to be confident about the performance of the pulse compressor and to determine the overall time resolution of the instrument, direct temporal measurements of the electron pulses are required. In general this requires invoking some means of projecting the longitudinal (temporal) axis of the electron pulse onto the transverse axis, thereby linking the pulse duration to a measurable distance on a detector. A simple way to achieve this is to use a streaking electric field field orthogonal to the momentum vector $\mathbf{p}_z$. The electric field $E_x(t)$ (defined along the x axis) must be sufficiently time varying such that electrons within the compressed pulse experience a range of field strengths. This leads to the *streaking* of the pulse by imparting a range of transverse momenta $p_x(t)$ which depends on the interaction time of the pulse in the streaking field and by consequence the pulse duration τ. Figure 2–17 a) illustrates the principle of electron pulse streaking. Streaking can be accomplished using high-frequency fields ranging from microwaves to terahertz, in either resonant structures or free-space. Pulse duration measurements may also be performed using optical fields using the method of grating-enhance ponderomotive scattering.

The momentum transfer along the x direction is determined by the Lorentz force according to

$$p_x(t) = q \int_0^{d_s/v_z} E_x(t) dt, \tag{2.58}$$

where d_s/v_z is the time-of-flight of the electrons with speed v_z in the transverse streaking electric field which has a spatial extent d_s. Depending of the time-dependence of $E_x(t)$ the electrons in the pulse experience (ideally) a linearly-varying field such that electrons acquire a linearly varying transverse momentum p_x depending on their position within the pulse, and therefore the pulse duration. After interaction with the streaking field, the electrons propagate freely over a drift region and are then imaged by a detector. The streaked electron pulses are displaced by an average amount Δx and are streaked to a width

σ_S. The resolving power of a streak camera is characterized by its streaking rate (or streak velocity) v_S defined as $v_S = \Delta x/\Delta t$ where Δt is the time after which the streaking field is initiated. The pulse duration is determined by deconvolution of the streaked electron pulse with an unstreaked reference of width σ_R according to

$$\tau = \frac{1}{v_S}\sqrt{\sigma_S^2 - \sigma_R^2}. \tag{2.59}$$

A streak camera can be efficiently used for pulse duration measurements and also arrival time stability measurements by tracking the position of the streaked pulse Δx as a function of time in the laboratory.

2.6.1 Ultra-compact streak camera design

A compact (1×2 cm) streak camera device has been designed in this work and is implemented for simple and efficient characterization of the electron pulses. The design is based on using a GaAs photoswitch to optically trigger the streaking field using an 800 nm ultrafast laser pulse. The operation of the streak camera is nearly identical to a pump-probe measurement, and thus is a reliable method for characterizing the performance of an ultrafast electron scattering instrument. The streak camera is an RC circuit (see Fig. 2–17 b)) which is charged by a high-voltage (1 kV) square-wave pulse as shown in Fig. 2–17 c). Once the capacitor is charged, an ultrashort laser pulse impinges on a GaAs chip coupled to the circuit impulsively creating a short in the circuit, resulting in a discharge of the capacitor. The electron pulses pass through the capacitor plates during this discharge and thus samples a time-varying electric field as shown in Fig. 2–17 c). The discharge process in the streak camera results in a *ring-down* which has a frequency roughly determined by the resonant properties of the circuit.

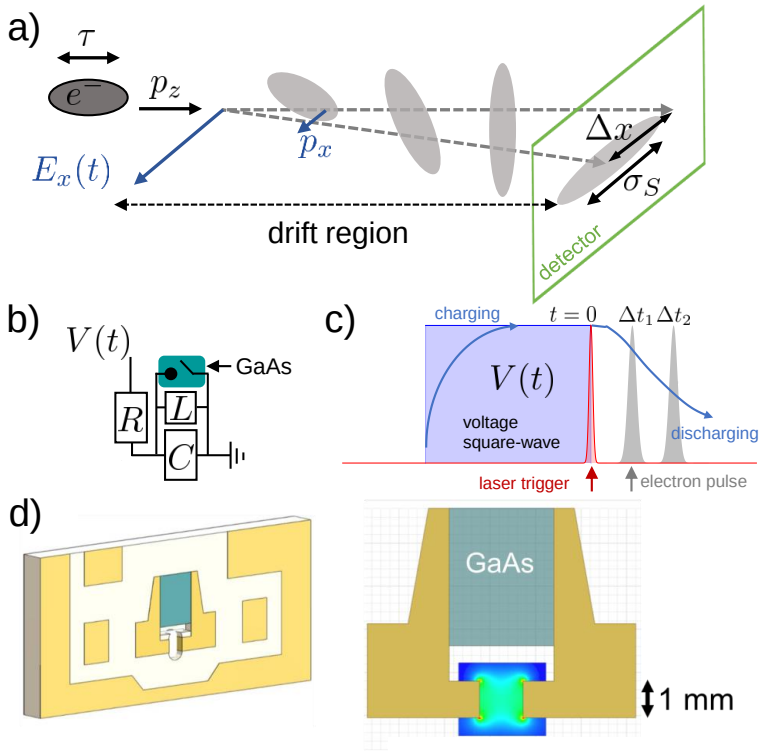

Figure 2–17: Streak camera principle of operation and design.
a) Electron pulses with momentum p_z interact with a transverse streaking field $E_x(t)$ and obtain a transverse momentum p_x via the Lorentz force. The effect is to streak and displace the pulse thereby mapping the temporal axis onto spatial axis at the position of the detector. The width of the streaked pulse is σ_S. b) Circuit model of a photo-triggered streak camera. A voltage $V(t)$ charges and RLC circuit coupling to a GaAs switch which "flips" when illuminated by a laser pulse causing the circuit to discharge and create a time varying electric field in the capacitor which streakes the electrons as described in c). d) Design of the streak camera fabricated on a printed circuit board. The GaAs photoswitch is located in the middle above a parallel plate capacitor structure. Bonding pads and ground planes are present for additional circuit elements. The electric field profile between the plates is shown to the right.

The streak camera is fabricated on a printed circuit board (pcb) (Rogers RO3003 laminate 1.52mm, 70µm electro-deposited copper foil). The material was chosen for its high-vacuum compatibility and also for its high-frequency properties such as low-dissipation

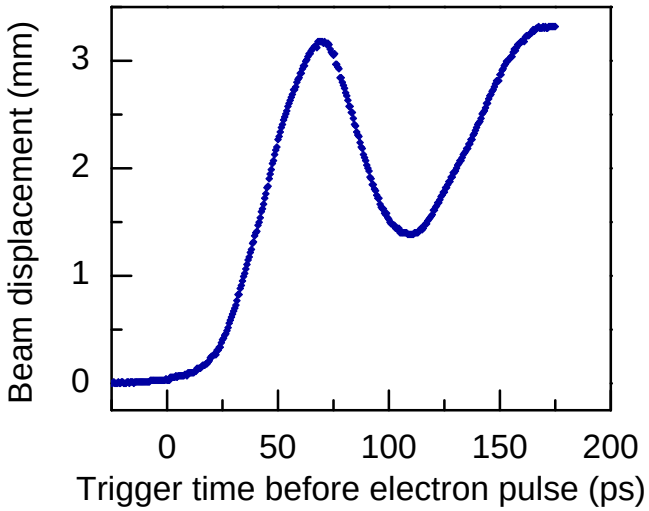

Figure 2–18: Streak camera calibration measurement.
Displacement of the electron pulse on the detector as a function of the time after the streak camera is triggered using 800 nm laser light. The streaking velocity of the device is given by the slope of the data in the first linearly varying region. It is determined to be $v_S = 87 \pm 2$ μm/ps.

above 10 GHz and high breakdown voltage characteristics. The design is shown in Fig. 2–17 d), and consists of various bonding pads for the soldering of resistors and ground connections. The GaAs chip is placed roughly in the middle of the device, in a pocket milled out to a depth of 500 μm. The GaAs chip has patterned Ohmic contacts deposited in a Ti-Ge-Au trilayer process which are connected to adjacent contact pads on the pcb by silver paint. The capacitor is a simple parallel plate structure located beneath the GaAs chip. The plate structures where fabricated by milling a slot, plating the sides extending into the board and then defining the plates by drilling out the top and bottom regions. The electric field profile is shown in the right of Fig. 2–17 d).

The performance of the streak camera is determined by streaking the electron pulse as a function of time after the streaking fields are initiating via the optical laser trigger.

The calibration data is shown in Fig. 2–18, which plots the center position of the streaked pulse as a function of time. The linearly-varying region of the streaking field is found in the vicinity of roughly 50 ps, where the slope is calculated to be 87 ± 2 μm/ps corresponding to the streak velocity v_S. The ring-down of the streak-camera roughly traces out a damped oscillation, with a frequency of approximately 10 GHz. The temporal resolution of the streak camera is directly proportional to the streak velocity and depends how well streaked pulsed can be differentiated from the reference pulse. For the geometry of the instrument studied in this work, the center of the pulse can be detected by fitting down to ±0.25 detector pixels which corresponds to $\Delta x_{\min} = \pm 4.0$μm and thus an RMS temporal resolution of $\Delta x_{\min}/v_S = 46 \pm 1$ fs (108 ± 3 full-width at half-maximum). This limit is also applies for distinguishing between streak and unstreaked pulsed for IRF measurements.

2.6.2 Temporal impulse response function

The time-averaged temporal impulse response function (IRF) defines the time-resolution of the instrument over a particular averaging time. Depending on the duration of this time interval, the IRF is determined by the electron pulse duration τ, the arrival time jitter Δt ranging from as fast as shot-to-shot ($1/f_{\text{exp}} = 1$ ms) up to the averaging time and also the optical pulse duration according to

$$\text{IRF} = \sqrt{\langle \tau \rangle^2 + \langle \tau_{\text{laser}} \rangle^2 + \langle \Delta t \rangle^2}, \tag{2.60}$$

where $\langle x \rangle$ denotes the time-average of x. The time-averaged pulse duration $\langle \tau \rangle$ is determined using (2.59), where σ_S and σ_R are determined over a period of 30 seconds (1 s per image, 30 images averaged together), with an electron pulse repetition rate of 1 kHz. Thus an image acquired by integrating the streaked electron pulse signal for 30 seconds intrinsically averages 30,000 individual pulses. This image is fit to a 2-dimensional Gaussian

function to determine the center position of the pulse along with the width σ_S. Measurements of the streaked electron pulse as a function of cavity phase are presented first to determine and characterize the cavity performance when the streak camera is positioned at the position of the sample for an ultrafast electron scattering experiment. The distance between the compression cavity to the streak camera (sample plane) is 23 cm and the IRF is measured for various cavity phase settings. For all phase settings, the streaked pulse is maintained in the center of the linearly varying streak field (Fig. 2–18) by varying the time delay of the optical trigger of the streak camera. Figure 2–19 shows IRF vs. phase for 3 different cavity driving strengths. This ensures that the resolving power of the streak camera is roughly equivalent for all measurements. Optimal power for compression is found to be 44.7 W for a cavity temperature of 18.0 degrees Celsius (measured using an external thermometer anchored to the copper) and a drive signal of 2.99849 GHz. In this regime, the measured IRF very near to optimal compression phase "levels-out" as the streak camera resolution is reached; the streaked and unstreaked pulses cannot be differentiated within the error established by fitting the images. At optimal phase for compression, the power dependence of the cavity may be characterized. Figure 2–20 shows the IRF for various powers relative to the optimal power of 44.7 W. The temporal focusing power demonstrates a sharp minimum and behaves asymmetrically as a function of power with respect to this minimum. The asymmetry at larger power results from over compression counteracted by space-charge repulsion effects. The smallest measurable IRF determined using our streak camera was 106 ± 2 fs FWHM.

2.6.3 Long-term arrival time stability

The long-term temporal stability of the compressed electron pulses over the typical time-scales necessary to perform ultrafast electron scattering experiments is of particular importance because of its direct detrimental impact on the data. The reason for this is

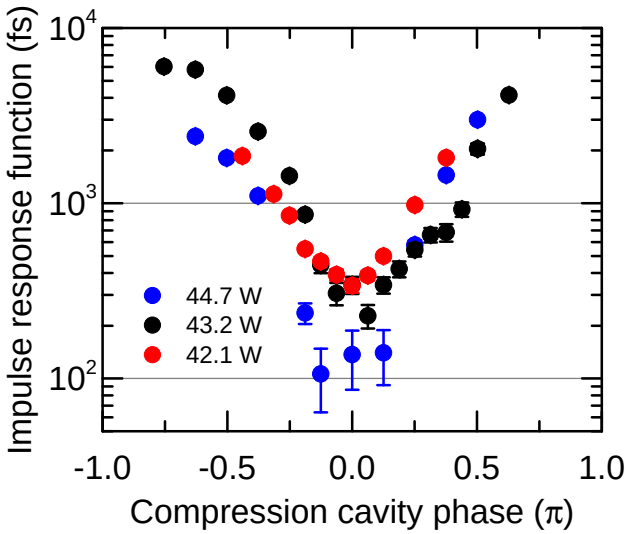

Figure 2–19: Electron pulse temporal impulse response function as a function of cavity phase.
The bunch charge of the electrons was 0.2 pC, the drive frequency was 2.99849 GHz and the cavity was temperature stabilized to 18 C. At the optimal power of 44.7 W, the measured IRF becomes resolution limited by the streak camera.

because typical measurements run for several hours and several tens of individual time-delay scans are carried out. At the end of the measurement, all of these individual scans are averaged together to improve signal to noise. Problems arise when "time-zero" drift occurs between subsequent scans resulting in a degradation of time-resolution following the averaging process. In certain cases, there may be sufficient time-resolved diffraction intensity signal such that the true value of time-zero can be determined for each scan and a post-processing correction procedure called "time-stamping" may be performed to eliminate the scan-to-scan drift. For many measurements however, this procedure is not possible. The long term drift of the electron pulse is tracked relative to the optical pulse in the following manner. The center of the streaked pulse is tracked over the course of 4 hours to measure the performance of the phase feedback system in compensating for

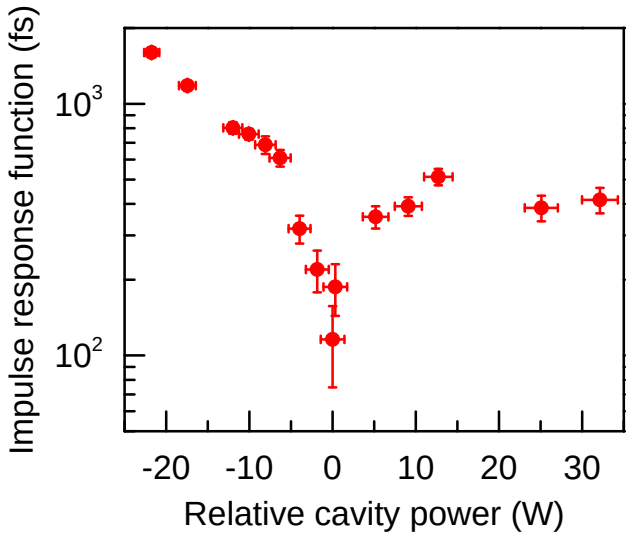

Figure 2–20: Electron pulse temporal impulse response function as a function of cavity power.
Cavity power is relative to 44.7 W and the paramters of the instrument are the same as those described in Fig. 2–19.

cavity induced phase changes, and thus time-of-flight drift between the cavity and the sample (streak camera) position. The results are displayed in Fig. 2–21 for both the phase feedback control ON and OFF. Without active phase correction, the arrival time drift demonstrates a long-term underlying drift on the order of 500 fs and also oscillation cycles on the order of hours. With phase stabilization activated, both of the long-term drift and oscillatory behaviour are eliminated. By examining the arrival time distribution in the form of a histogram, it can be seen that the statistical RMS arrival time drift is reduced from greater than 200 fs to below 50 fs RMS, roughly equivalent to the limit of the measurement due to the temporal resolution of the streak camera.

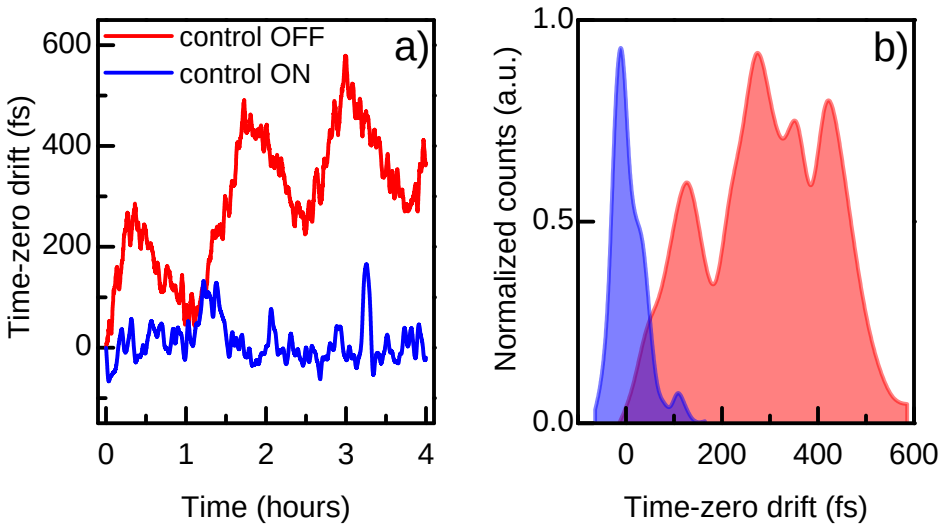

Figure 2–21: Long-term arrival time stability of compressed electron pulses. a) Arrival time drift converted from the streaked pulse position measured on the detector for both phase contol ON (blue) and OFF (red). b) Histograms of the data shown in a) depicting the statistical jitter contribution to the overall instrument resolution.

2.6.4 Correlation with microwave power stability

In this section, the impact of microwave power stability on the performance of the feedback system is quantified in detail. As described in sections 2.4.6 and 2.5.8, amplitude drift and instability in the microwave signals feeding the phase detector produces phase errors through amplitude-phase conversion processes. The feedback system is unable to differentiate such phase errors from true phase terms and will thus apply false corrections to the phase. This effect would not be observed in a electronic measurement of the phase, but would appear in the behaviour of the streaked electron pulses which are subject to the phase stabilization system. The amplitude phase conversion coefficient was measured to be 54 mV/dBm by varying the power of the compression cavity. This translates to 170 mrad/dBm using the detector constant and translates to a timing error of 9.0 ps/dBm.

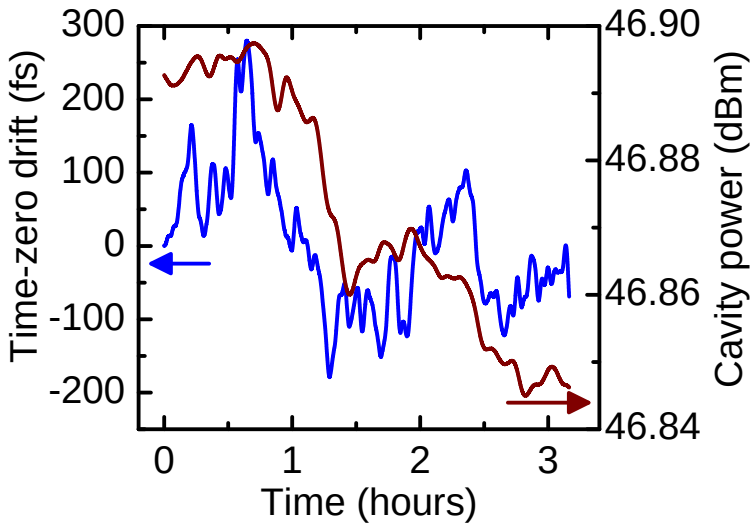

Figure 2–22: Long-term arrival time stability of compressed electron pulses. Measurement of the time-zero shift as a function of time plotted along-side the compression cavity drive power. Correlations between the arrival time and power drift are observed and correspond well to the measured amplitude phase conversion coefficient for the phase detector which was determined to be 9.0 ps/dBm.

This number is consistent with what is observed by comparing the cavity drive power and the temporal drift of the streaked electron pulse shown in Fig. 2–22. A drift in amplifier power of ~ 0.03 dB correlates well with an arrival time drift of ~ 300 fs observed in the measurements of the streaked pulse. Following these measurements, as described in 2.5.8, the RMS power stability of the cavity signal was improved by roughly a factor of 10 to 0.0031 dBm, yielding an improved amplitude-phase timing error term of 28 fs RMS.

2.6.5 Comparison of amplitude-phase conversion effects

Pulse streaking measurements may also be conducted to characterize the amplitude-phase-conversion processes ocurring in the synchronization system prior to the pulse compression cavity. Here we present a comparison between the new synchronization approach described in this chapter and the previous approach based on the used of a commercial

PLL. The measurements are carried out by varying the optical power incident on the fast photodetector used for synchronization and measuring the microwave power at the synchronization frequency of interest. As a function of this power the displacement of the streak is recorded and corresponds to an erroneous phase shift in the microwave signal relative to the optical pulse which triggers the streak field. For these measurements the phase feedback was left off as the measurements could be taken quickly and compensation for long-term drift was not required. Here we present an important comparison of the amplitude phase conversion processes between the new synchronization approach and the old approach involving the VCO-based phase-locked-loop (PLL). The measurement schematic and results are displayed in Fig. 2–23. For the current synchronization system (3 GHz direct generation) the amplitude phase conversion factor is determined to be 2.2 ps/dBm which reflects the amplitude phase conversion processes arising in the photodetector alone. The PLL based synchronization system is influenced amplitude phase conversion processes both in the photodetector and also in the double balanced mixer of the PLL. The PLL approach yields a value of 43 ps/dBm nearly 20 times larger than the current approach. This indicates a pronounced sensitivity to optical power fluctuations coming from the oscillator.

2.6.6 Summary and outlook

To conclude this chapter we have presented a new synchronization approach for ultrafast electron scattering featuring microwave pulse compression. The approach involved using the relevant oscillator repetition rate harmonic signal generated from a phase locked frequency comb. The comb is generated directly by photodetection using a high-bandwidth (12.5 GHz) photodetector. The signal is instrincally phase locked and is less sensitive to amplitude phase conversion effects than a PLL-based approach. The compression cavity phase response is actively stabilized by a phase correction system which accurately compensates for phase shifts arising from detuning between the cavity resonance and the

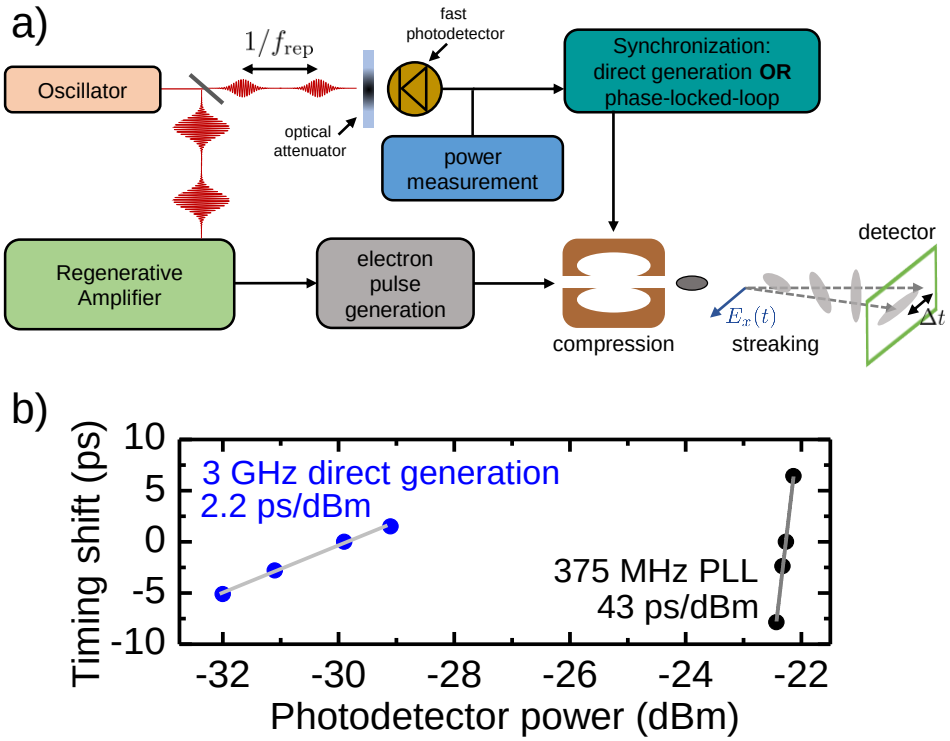

Figure 2–23: Comparison of amplitude phase conversion effects.
a) Measurement schematic. The power of the portion of the oscillator pulse train illuminating the synchronization diode is attenuated using a variable neutral density wheel. The microwave power at the synchronization frequency (3 GHz for the direct generation and 375 MHz for the phase-locked-loop) is measured using a calibrated power meter. As a function of the power, the position of the streaked electron pulse is tracked over the linear streaking range the amplidue phase conversion coefficient is determined.

synchronized microwave drive signal. The synchronization system presented here, along with long-term stability over time-periods exceeding measurement times (days), offers a 5-fold improvement in the overall temporal resolution of the instrument [68, 50]. Importantly, the performance of the instrument has now been pushed to a regime where the time resolution is limited by the pulse duration, not the arrival time jitter and drift. The impulse response function over the course of many hours is 131 ± 5 fs FWHM (56 ± 5 RMS)

and it essentially limited by the temporal resolution of the streak camera. With strong streaking fields, such as those generated by THz fields we would be able to determine the pulse duration more reliably, and possibly push the temporal resolution to the sub-50 fs regime with high-brightness pulses.

CHAPTER 3
Photo-induced phase transitions in vanadium dioxide

Revealing how the complex interplay between charge, spin, orbital and lattice-structural degrees of freedom gives rise to emergent properties is central to materials research. Using external perturbations to modify this interplay and control materials is at the forefront of these efforts. Vanadium dioxide, VO_2, is a prototypical material whose properties are strongly dependent on the correlations between the aforementioned degrees of freedom. A key feature of VO_2 is an insulator-to-metal transition (IMT) with a relatively low transition temperature of $T_c \simeq 340$ K [95]. Associated with the IMT is a crystallographic phase transition (CPT) where the lattice structure transforms from its low-symmetry monoclinic (M_1) phase to a high symmetry rutile (R, tetragonal) phase. The key difference between the M_1 and R phases is the existence of V–V dimers in the M_1 phase which produces a periodic lattice distortion (PLD) along the chains of V atoms yields a doubling of the lattice constant along the c axis of the R phase. The driving mechanism(s) for IMT and CPT transitions, along with an understanding of to what extent they depend on each other have been longstanding open questions.

Optical excitation pulses can be used to modify and control electronic correlation effects in materials [1, 96] and in turn provide insight into the basic interactions at play. For the case of VO_2, measurements have demonstrated a complicated structural response [97, 98, 5] to optical excitation which cannot be understood simply in terms of phases found on the equilibrium phase diagram. This has made reconciliation of the results obtained using various time-resolved spectroscopy techniques [99, 100, 101, 102, 103] difficult and often misleading. Not only can an IMT and CPT that are analogous to the equilibrium case be

driven by sufficiently intense laser excitation, but a metastable phase possessing metallic properties for which no equilibrium analog exists is also formed under certain excitation conditions [5, 104]. This non-equilibrium phase retains the crystal symmetry and atomic coordinates of its parent monoclinic M_1 (to a very good approximation) phase and is known as the *monoclinic metallic* or $\mathcal{M}$ phase. It has been established qualitatively that the $\mathcal{M}$ phase is characterized by a re-arrangement of valence charge density to a distribution demonstrating 1-dimensional anti-ferroelectric charge ordering [69]. Details concerning the nature of this $\mathcal{M}$ phase are challenging to obtain, mostly because of the complicated spectroscopic response of VO_2 due to the concurrency of multiple phase transitions.

In this chapter, UED and time-resolved terahertz spectroscopy (TRTS) are combined to perform a detailed structure-property correlative study of the photo-induced phase transitions in VO_2, with the primary aim of understanding in as much detail as possible the structural changes associated with the monoclinic metallic $\mathcal{M}$ phase. Time-dependent structural changes in VO_2 from the diffraction data as a function of photo-excitation strength are associated to conductivity changes in the low-frequency THz range and linked according to their temporal behaviour. The combination of these techniques allows for the various phase transitions to be separated and in turn the details of the monoclinic metallic phase can be extracted. We determine from the electron diffraction data the nature of the optically-induced charge ordering within the unit cell. We then determine the fluence dependent heterogeneous response of the material using a phase-fractional model based on diffraction peak intensities serving as order parameters for the various phases. Furthermore, we characterize the fluence-dependent formation time and kinetics of the $\mathcal{M}$ phase. Finally, we present a consistent picture of photo-induced phase transitions in VO_2.

3.1 Vanadium dioxide at equilibrium

Before we present the experimental results we will overview the equilibrium properties of VO_2 and also relevant time-resolved studies. Under equilibrium conditions, the various phases of VO_2 reside on a complicated phase diagram illustrated in Fig. 3–1 a). As a function of pressure P and temperature T, VO_2 has three structurally distinct low-symmetry insulating phases, namely, monoclinic M_1 and M_2 and triclinic T occuring at low temperature or higher pressure (or strain from doping). The high-symmetry metallic rutile R (tetragonal) phase lives above the IMT temperature of $T_c \approx$ 340 K. The IMT is the hallmark feature of this complicated phase diagram and yields a conductivity change of 5 orders of magnitude in addition to striking changes in optical properties [105]. The first measurements of the IMT were conducted by Morin [95] and are shown in Fig. 3–1 b) along with various other transition metal oxide compounds. The primary structural distortion is the V–V dimerization which occurs along the c–axis of the rutile phase depicted in Fig. 3–1 c). The dimers do not form in a perfect 1-dimensional manner, as they are tilted with respect to the c–axis in two different directions depending on which V–V pair within the unit cell is considered. In the M_1 phase, electrons are localized on the dimer pairs and this is generally thought to arise from the mixing of V–3d electrons. Interestingly, the low-temperature insulating M_1 phase exhibits no magnetic ordering (paramagnetic). This property differs from so-called *Mott insulators* which typically have insulating phases demonstrating anti-ferromagnetic ordering [106]. In the R phase electrons become delocalized across the unit cell volume. Although at first glance it seems clear that the structural distortions are responsible for the IMT, the role of Mott-Hubbard physics [106] and the interplay with the structural distortions must be considered.

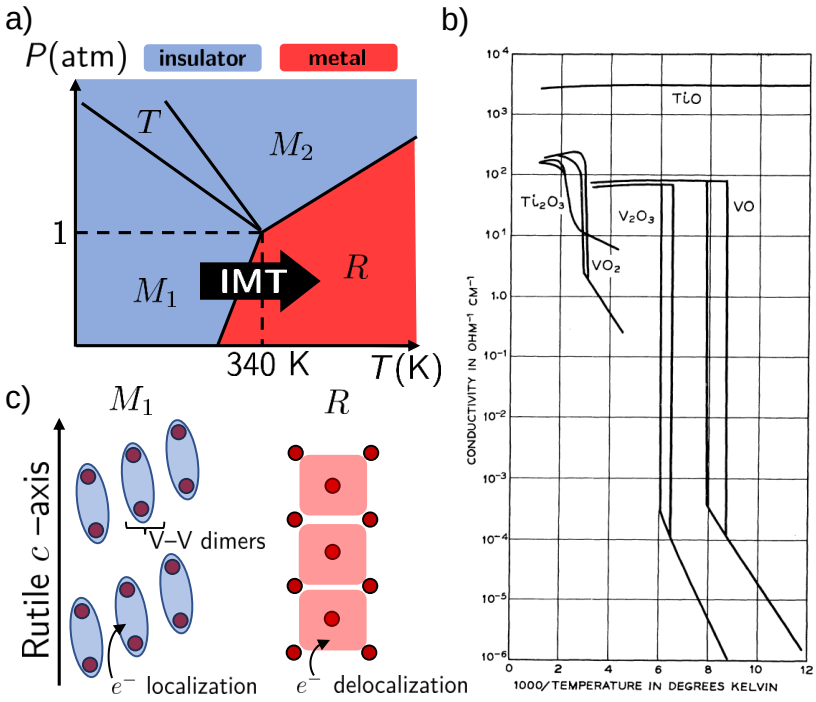

Figure 3–1: Equilibrium phase diagram and insulator metal transition in vanadium dioxide. a) $P-T$ phase diagram indicating the 3 structurally distinct low temperature insulating phases, M_1, M_2 and T and the high-symmetry rutile R phase at higher temperature. b) Data of the electrical conductivity for various transition metal oxides including VO_2 from Ref. [95] (with permission). c) Cartoon illustration of the effect of dimerization between M_1 and R VO_2. In this dimerized state electrons are localized on the dimers wheres in the R phase they become delocalized.

3.1.1 Crystal structures

The M_1 and R phases of VO_2 are the most common in nature and are the phases relevant to the content of this chapter. The space group of the M_1 phase is $P_{21/c}$ and the lattice constants are $a = 0.575$ nm, $b = 0.452$ nm and $c = 0.538$ nm [107]. The monoclinc angle of the unit cell is $\beta = 122.6°$. The R phase has a space group of $P_{42/nmn}$ and the lattice constants are $a = b = 0.455$ nm and $c = 0.286$ nm [108]. Figure 3–2 shows 3-dimensional atomic models of the M_1 and R VO_2 systems along with various projections

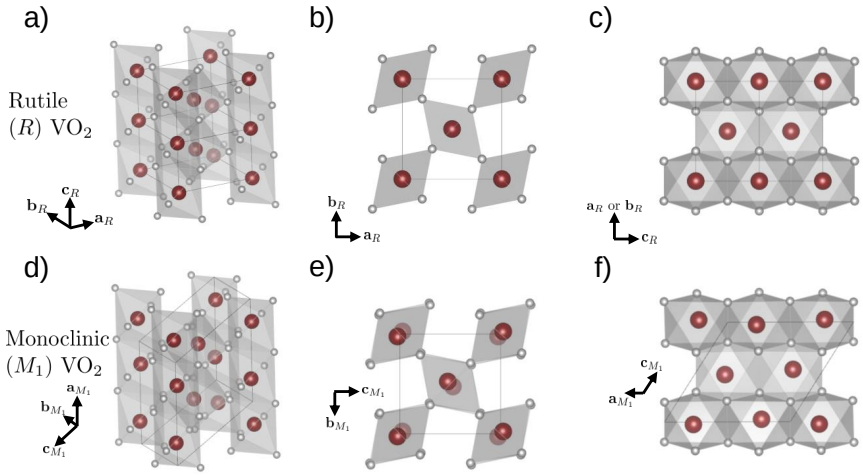

Figure 3–2: Equilibrium crystal structures of vanadium dioxide.
a) View of 2 units cells of R VO_2. b) view up the rutile $\mathbf{c}_R$ axis. c) View of equidistant V atoms. d) View of single unit cell of M_1 VO_2. e) View up the rutile $\mathbf{c}_R$ axis ($\mathbf{a}$ axis in the M_1 basis.) f) Dimerized V–V pairs.)

to illustrate the structural distortions. Figure 3–2 a) and d) show views of the VO_2 unit cells for the R and M_1 respectively. Figure 3–2 b) and e) show the unit cell looking down the $\mathbf{c}_R$–axis in both phases. In b) there are no dimer pairs (see c)) and in e) the tilt of the dimer pairs is clearly seen along the $\mathbf{a}_R + \mathbf{b}_R$ and $\mathbf{a}_R - \mathbf{b}_R$ directions for the V atom chain at the unit cell edge and center respectively. A secondary effect arising from this dimerization is the displacement of the V atoms to off-center coordinates with respect to the VO_6 octahedral units. Moreover, the two different dimer tilt directions are accommodated by a small rotation of the VO_6 octahedra in the $\mathbf{a}_R$–$\mathbf{b}_R$ plane. These effects are illustrated in Fig. 3–2 b) e) and f).

3.2 Insulator-metal transition

The first step in understanding the insulator-metal-transition in vanadium dioxide involves understanding the band structures of the equilibrium phases. There have been

many theoretical descriptions of VO_2 and the driving mechanism of the IMT over the years [109, 110, 111] which consider both the impact of structural distortions and electron-electron correlations. There have alse been many computational studies [112, 113, 114, 115, 116, 117] which in some cases re-affirm the earlier theoretical models, but often omit important interactions necessary for a complete and accurate account. Before this however, the Peierls and Mott insulator transition models will be introduced, as they form the essential building blocks for understanding the IMT in VO_2.

3.2.1 Peierls and Mott models

Many materials demonstrate dimerization of atoms along a particular direction at low temperatures. This fact came as quite a surprise; it was not expected that systems would favour a lower symmetry state in this way [118]. The argument and description of this fact in 1-dimension is quite straightforward and was calculated by Rudolf Peierls in 1930 [119]. Although 1-dimensional materials do not exist in nature, ordering or dimerization often occurs along a particular direction. This is approximately true for M_1 VO_2, where V–V pairs form along the rutile $\mathbf{c}_R$ axis, albeit with a tilt either in or out of the $\mathbf{a}_R, \mathbf{b}_R$ plane breaking the truly 1-dimensional character of the distortion.

Peierls considered the ground state energy of a 1-dimensional chain of atoms with equal spacing a and with 1 free electron per site. The electron wave-vector is $k_F = \pi/2a$ which falls halfway between the zone-boundary (π/a). The effect of displacing every other atom by $\delta < a$ (creating a structural distortion) is analyzed in terms of the energy gain to the lattice and energy loss of the electronic bands. The structural distortion lowers the symmetry of the system and doubles the unit cell to length to $2a$ and halving the crystal momentum to $\pi/2a$ in reciprocal space. When this happens the electronic states become "nested" at the new-zone boundary (since $k_F = \pi/2a$) and it is energetically preferable for the system to open up a band gap. The energy change of the electronic system was found

to be $\Delta E_e \propto -\delta^2 \log \delta$, whereas the energy of the lattice goes as $\Delta E_l \propto \delta^2$. Thus for small distortions electron energy changes dominates.

In their basic form, Mott insulators are described by the *Mott-Hubbard Hamiltonian* [106, 120] which is essentially a tight-binding model [25] with additional on-site Coulomb interactions. The Hamiltonian is given by

$$\begin{aligned} \mathcal{H}_H &= \mathcal{H}_t + \mathcal{H}_U - \mu N, \\ &= -t \sum_{\langle ij \rangle} \left(c^\dagger_{i\sigma} c_{j\sigma} + c_{i\sigma} c^\dagger_{j\sigma} \right) + U \sum_i^N \left(n_{i\uparrow} - \frac{1}{2} \right) \left(n_{i\downarrow} - \frac{1}{2} \right) - \mu \sum_i^N c^\dagger_{i\sigma} c_{i\sigma}, \quad (3.1) \end{aligned}$$

where, $\langle ij \rangle$ represents nearest-neighbour pairs and t is the tight-binding energy. This first term, $\mathcal{H}_t$, describes many conventional metals and insulators, the solutions of which are Bloch-like states. The μN term describes the self-energy or chemical potential of the electrons in the solid. The effect of $\mathcal{H}_U$, the Hubbard on-site interaction term is to localize the electronic states, split the conduction band and create a larger density of states below the Fermi level. A general feature of interacting systems is the lowering of the energies of the electronic states. The qualitative behaviour of a Mott-insulator is shown in Fig. 3–3.

3.2.2 Band structures of VO_2

We start with a molecular orbital picture which illustrates the relevant orbitals along with their symmetry properties [109, 113]. The vanadium atoms are typically assumed to have a $3d^1$ character, meaning each V-atom has one electron in the valence $3d$ orbital shell. In the high-symmetry rutile phase the vanadium atoms are situated at the center of a coordinated VO_6 octahedra (see Fig. 3–4 b)), and the symmetric crystal field of these O atoms split the five V-$3d$ orbitals shown in Fig. 3–4 a) into states of e_g ($d_{x^2-y^2}$, d_{xy}, d_{yx}) and t_{2g} (d_{xz}, d_{z^2}) symmetry. Hybridization of the V–$3d$ and O–$2p$ orbitals leads to the formation of σ and π type orbitals, with stronger overlap occurring in the σ and σ^* (with $*$ denoting anti-bonding) yielding a larger energy splitting. The bonding orbitals are mostly

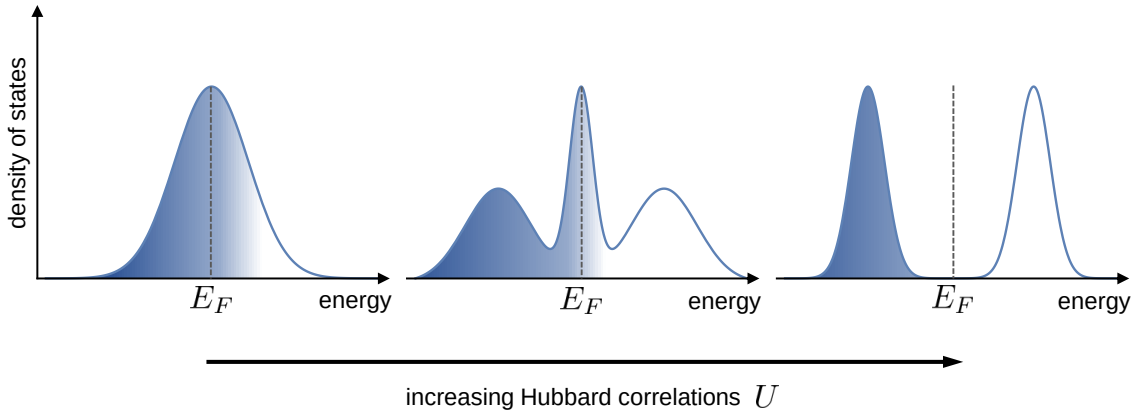

Figure 3–3: Mott-Hubbard metal insulator transition diagram.
For low on-site Coulomb interactions U, a conduction band forms at the Fermi level. As the interaction is increased, electron correlation effects open up a gap and push electronic states to lower energies, yielding a fully occupied valence band and insulating behavior at sufficiently larger U.

formed by fully occupied O–2p orbital states below the Fermi level. The anti-bonding orbitals are primarily formed by the V–3d orbital manifold within which the Fermi level falls because of the electron count. This manifold technically forms two overlapping bands, the so called $d_{\|}$ band and the π^* band. The metallic conductivity of the R phase is carried by the $d_{\|}$ and the π^* bands.

A robust feature of structural distortions is the lifting of degeneracies held by the orbital states forming conduction bands [119, 43]. In some cases this effect opens up an optical gap in the electronic structure. In monoclinic M_1–VO_2 for example, the degeneracy of the t_{2g} V–3d obitals is lifted by molecular orbital effects following the structural distortion. This process strongly influences band structure of the material. Most calculations indicated that these effects alone were insufficient to open up an optical band gap, suggesting that M_1 VO_2 should remain a metallic [113]. This was because despite the splitting of the $d_{\|}$ band the remaining π^* band was predicted to still cover the Fermi level. Initially this was

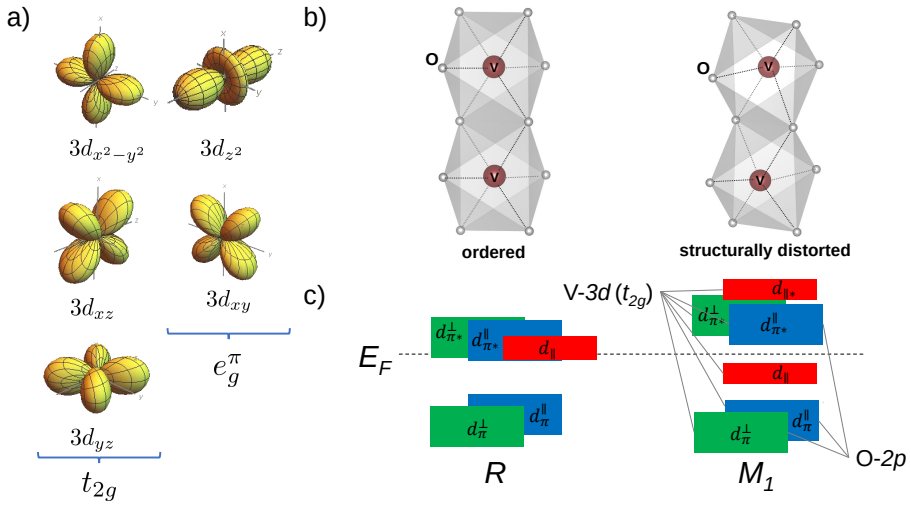

Figure 3–4: Vanadium orbitals involved in the electronic bands of VO_2. a) V-3d orbitals. b) V–V pairs in the rutile (R) and monoclinic (M_1). The V atoms are uniformly surrounded by 6 O atoms in the R phase and off center the O–cage octahedra in the M_1 phase. c) Electronic band of R (left) and M_1 (right).

interpreted as a failure of the local densiy approximation (LDA) of density function theory (DFT), which may be partially true, but it is now clear that electron-electron interactions and Mott-Hubbard physics play important roles in opening a band gap in M_1 VO_2. That is, there is a growing consensus that the M_1 phase must be accompanied by the localization of electrons on the V–V dimer pairs themselves through correlation effects in a manner which respects the structural distortion. Among the questions remaining are those concerning the relative importance of structural distortions, orbital degeneracy and electron-electron correlations. There was great hope that understanding these would pinpoint the driving mechanism behind the phase transition.

The work of Biermann *et al.* [114] made an important step in identifying that electron correlations effects are necessary in allowing for a Peierls-type transition to open up a gap. They achieve this by extending DFT calculations to include cluster-extended dynamical mean field theory (C-DMFT) to accurately include long-range correlation effects. They

perform the calculations within a multi-band Hubbard Hamiltonian [121] description of VO_2 so as to properly account for the electron-electron interaction terms. Their results establish that VO_2 is a not a conventional Mott-Hubbard insulator, as correlation effects alone cannot open up an insulating gap. Rather, the structural distortion of the M_1 phase allows for the formation of *dynamical singlets* through electron-electron and inter-dimer correlation effects, yielding the localization of electrons on the dimers. In this view, M_1 VO_2 is a "Mott-assisted" Peierls insulator; Mott-Hubbard (electronic correlations) physics renormalizes the Peierls gap in between the $d_{\|}$ and $d^*_{\|}$ and opens an optical gap. This was an important step in understanding how the M_1 is insulating, but did not focus on the driving mechanism of the IMT phase transition.

Later, Weber *et al.* [116], motivated by recent X-ray absorption measurements [122] proposed that the Peierls transition is assisted by orbital selection rather than electron correlations. They conduct *linear-scaling* DFT along with non-local DMFT corrections to determined the band structure of M_1. Within these calculations they established that Coulomb repulsion alone cannot drive the IMT, because a Hubbard–U energy of ~ 25 eV, roughly 10 times larger that typical values, would be required to de-stabilize the R phase. Moreover, the structural distortion lifts the degeneracy of the t_{2g} and drives orbital overlap of the V–$3d_{xy}$ and $3d_{xz}$ states along the rutile c–axis (rougly in the direction of the dimer bond). When this happens the $3d_{yz}$ orbital is nearly entirely depleted and it follows that 2 electrons rather than one become shared by the V–$3d_{xy}$ and $3d_{xz}$ states. This is what they refer to as orbital selectivity, and they claim this mechanism is responsible for enhanced dynamical singlet (dimer) correlations which drive a self-energy divergence in the form of a Mott transition. In Weber's view, VO_2 is well described as a " Peierls-assisted" Mott transition. They link their findings qualitatively to the anti-ferroelectric structural distortion mentioned in the pioneering work of Goodenough [109].

Recent work by Brito *et. al* [117] suggest that the best description of VO_2 is one in which the IMT is correlation driven (Mott transition), but only in conjunction with strong intersite exchange correlations between dimers. In other words, the structural distortion facilitates and enhances correlation effects. They indicate that the intersite exchange correlations are connected to a Peierls-like transition in the adiabatic limit. Furthermore, they present calculations inspired by time-resolved experiments of the IMT (see following section) which show that because the optical gap in VO_2 is temperature dependent, suppression of correlation effects alone can collapse the gap given reasonable interaction strengths.

3.3 Photo-excitation of vanadium dioxide

Photoexcitation using ultrafast laser pulses has provided another route to initiate the transition between the insulating and metallic phases of VO_2 since it was discovered that the IMT occurs very rapidly following femtosecond laser excitation with sufficient fluence [123]. Since this discovery, VO_2 has been the focus of many time-resolved experiments including X-ray [97, 124] and electron [98, 5, 125] diffraction, X-ray absorption [126, 122], photoemission [104] and optical spectroscopies [127, 99, 101, 102, 100, 103, 128, 129, 130] from terahertz to ultraviolet aimed at uncovering the connection between the photo-induced IMT and changes in lattice structure.

The band gap of insulating VO_2 is 0.6 eV, therefore photo-excitation with 1.55 eV (800 nm) photons drive direct interband transitions and shown in Fig. 3–5 b) (see section. 1.7) between the $d_{\|}$ and $d^*_{\|}$ bands creating photo-excited carriers (electrons and holes) with considerable excess energy. This mechanism in some basic sense provides an avenue for the control of electronic correlation effects and in the strong-driving (high-fluence) regime the ability to dissolve the lattice distortion and transform the crystal structure. Optical

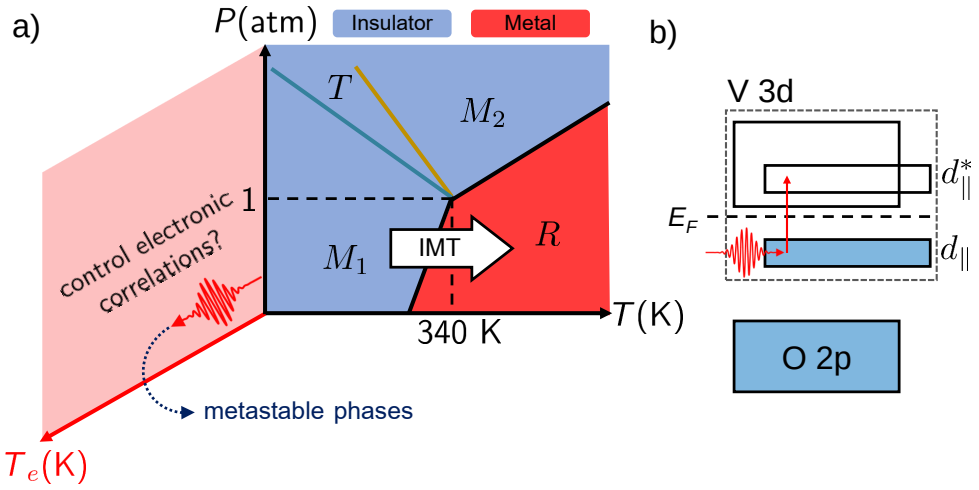

Figure 3–5: Non-equilibrium phase diagram of VO_2 and photo-excitation processes. a) Photo-excitation of vanadium dioxide provides a mechanism to control electron correlation effects which enables transitions into metastable phases of matter. b) Simplified VO_2 band structure showing $d-d$ interband transitions driven by 800 nm (1.55 eV) femtosecond laser pulses.

excitation creates another axis to the phase diagram (see Fig. 3–5 a)) along which electron correlations can be varied.

3.3.1 Summary of time-resolved measurements

The first time-resolved measurements of the IMT initiated using laser excitation were presented by Becker *et al.* in two publications [123, 131]. They determined the complex index of refraction of a polycrystalline VO_2 film excited by 780 nm laser light using optical transmission and reflection measurements. They find metallic behaviour in the film for fluences above 3.7 mJ/cm^2 occurring within roughly 500 fs, which was also the temporal resolution of their apparatus. Visible in their data is clearly the presence of two-timescales which they interpret in terms of a modified electron plasma model which relies on using different electronic parameters than the equilibrium metal. Given the known existence of the IMT in VO_2 the easy (and of course logical given the knowledge at hand!) explanation

for the results was that photoexcitation was driving the M_1 to R CPT transition, even though the spectroscopic response only measured the electronic character of the material *not* the crystal structure.

The evolving picture of VO_2 became more interesting when time resolved X-ray diffraction measurements of the photo-induced M_1 to R phase transition were carried out by Cavalleri *et al.* [97]. These results demonstrated that the photo-induced change in crystal structure occurred within 300 fs, and that this time-scale suggested it's character was *non-thermal* and occurring above a threshold fluence of 7 mJ/cm^2. The non-thermal character of the transition is defined as being driven solely through electronic excitation and with a rate faster that one expected from the equilibrium electron-phonon coupling. Furthermore they determined that the IMT is completely concurrent with the CPT. This motivated later work in which ultrafast spectroscopy tracked the IMT for various excitation pulse widths [127], and demonstrated that the onset of the IMT was limited to roughly 100 fs, governed by the intrinsic lattice response. Spectroscopic reflectivity measurements with high time resolution also revealed that below the structural threshold the metallic character induced by photoexcitation would not recover to the expected value of the M_1 phase prior to photo-excitation rather it would undertake a partial recovery on the picosecond timescale towards something neither M_1 or R in terms of its optical response.

A few years later, the first time-resolved multi-THz spectroscopy measurements were performed by Kubler *et al.* [99] which measured the photo-induced complex conductivity ($\sigma(\omega)$) of a VO_2 sample. They clearly identify two timescales of the IMT response, one roughly 60 fs due to transient metallization of the film by the photo-excited carriers and the second associated with a $\sim$ 1 ps recovery of the conductivity. The recovery of the conductivity was complete at fluences up to roughly 3 mJ/cm^2 and partial above a threshold fluence determined to be 4.6 mJ/cm^2. They approached understanding this exclusively in

terms of M_1 and R phases, as they were not directly sensitive to crystal structure, and provided a qualitative model in terms of the electron relaxation in the R phase. This work was extended by Pashkin [101] which pointing to a "long-lived metallic state" for which the electronic response is coupled to the V–V dimer phonons.

The detailed temperature dependent THz spectroscopy measurements performed by Cocker *et al.* mapped the IMT from 300 K to 17 K. They establish that the fluence threshold is strongly dependent on temperature and that both Mott and Peierls-like mechanisms play important roles. They confirm the non-thermal character of the IMT and model the transition as being triggered by a critical electron density on the V–V dimers which in turn couples to dimer modes. They also found some evidence that an intermediate metallic phase, one for which the Peierls distortion remains intact and Mott correlations are significantly suppressed, although they lacked direct structural evidence.

Recently, ultrafast electron diffraction and mid-infrared spectroscopy experiments perfomed by Morrison *et al.* [5] were combined to show that there are two distinct photo-induced IMTs in M_1 VO_2. The first, accessible at relatively high pump fluence, is an analog of the equilibrium IMT and is associated with the lattice-structural transition between M_1 and R crystallography expected from the equilibrium phase diagram. The second, accessible at lower pump fluence, has no equilibrium analog and yields a metastable, structurally distinct monoclinic metal phase ($\mathcal{M}$) that retains the crystallographic symmetry of its parent equilibrium monoclinic phase. These claims were deduced through the fact that the mid-infrared spectroscopy results demonstrated that the VO_2 sample exhibited a metallic response for fluences above 3.7 mJ/cm^2 while the electron diffraction measurements of the same sample at such a fluence indicated the crystal symmetry remained monoclinic. Furthermore the diffraction patterns in this regime showed that the intensity of specific low-index (low–q) Bragg reflections perpendicular to the c–axis of the rutile

structure (roughly perpendicular to the V–V dimers). Given the nature of this observed feature in the diffraction, the most robust explanation involved a re-organization of unit cell charge leading to a enhanced scattering amplitude while retaining the symmetry of the monoclinic structure (atomic coordinates). In summary this identifies a new IMT process, distinct from the equilibrium transition, which was observed to be metastable, lasting for 100s of picoseconds. This was the first clear observation of metallic monoclinic VO_2.

Around the same time, Wegkamp *et. al.* [104, 132] performed time-resolved photo-emission experiments which clearly showed that hole-doping of VO_2 through photo-excitation of electrons from localized V-3d states (M_1 phase) leads to an effectively instantaneous band-gap collapse above the threshold fluence of roughly 3 mJ/cm^2. At lower fluences, the response was Mott-Hubbard like in the sense that the band gap quickly reopened with-ing hundreds of femtoseconds. They propose that the effect of hole-doping alone through photo-excitation is sufficient to drive an iso-structural IMT (*i.e.* monoclinic metal). They support this claim with first-principles many-body perturbation theory calculations which reveal that the hole-doped state has a finite density of states at the Fermi-level, explaining its metallic nature.

The work mentioned above emphasizes the importance of multi-modal experimental approaches. The need to measure both the electronic and structural response of complex systems was crucial in reconciling the vast number of experiments on VO_2 demonstrating what initially seemed like profound disagreement. During the remainder of this chapter we present results obtained in commitment to a multi-modal approach to understanding VO_2. We seek to answer the following question using ultrafast electron diffraction and time-resolved terahertz spectroscopy (TRTS): 1) What specifically are the microscopic changes in unit cell charge arrangement occurring during the formation of the monoclinic metal phase? 2) What is the relative participation of the photo-induced monoclinic metal and rutile

metal phase as a function of excitation fluence? 3) What are the kinetics describing the formation of the monoclinic metal phase, and do our results agree with recent theoretical results? Most of the results presented hereafter are published in Ref. [69].

3.4 Ultrafast electron diffraction measurements

Ultrafast electron diffraction measurements are carried out at $\sim$ 300 K in transmission mode with 90 keV RF-compressed electron pulses which have a bunch charge of $\sim$ 0.1 pC [68, 50]. The compression technique and synchronization approach follows that outlined in chapter 2. The sample and the beam line are under high-vacuum ($\sim 10^{-7}$ mbar). The laser setup is based on a commercial Ti:Sapphire amplified system (Spectra-Physics Spitfire XP-Pro). The photo-induced transitions in VO_2 are reversible processes which require relatively long recovery times between measurements. Repetition rates of 50–200 Hz (depending on excitation fluence) were thus used to allow for sufficient sample recovery. The duration of the optical pump pulse is 40 fs (FWHM) with a spot size of 350 μm (FWHM). The 50 nm VO_2 samples were deposited by pulsed laser deposition on a 40 nm SiN_x substrate. The sample area is formed by a 250 μm by 250 μm silicon window. Details of the deposition process can be found in [133]. A schematic of the measurement and data acquisition procedure is shown in Fig. 3–6.

A single image acquired during the experiment is formed by a 10 second exposure of the CCD camera to the scattered electron beam which forms a diffraction pattern for VO_2 shown in Fig. 3–6 a). A single image therefore contains the accumulated signal from 2500 electron pulses, each of which captures a snapshot of the material structure at a particular time-delay value Δt following photo-excitation. A typical UED experiment consists of an array of images index by pump-probe delay value t. This array constitutes a *scan*. To achieve sufficient signal-to-noise, several scans are required. This is particularly important

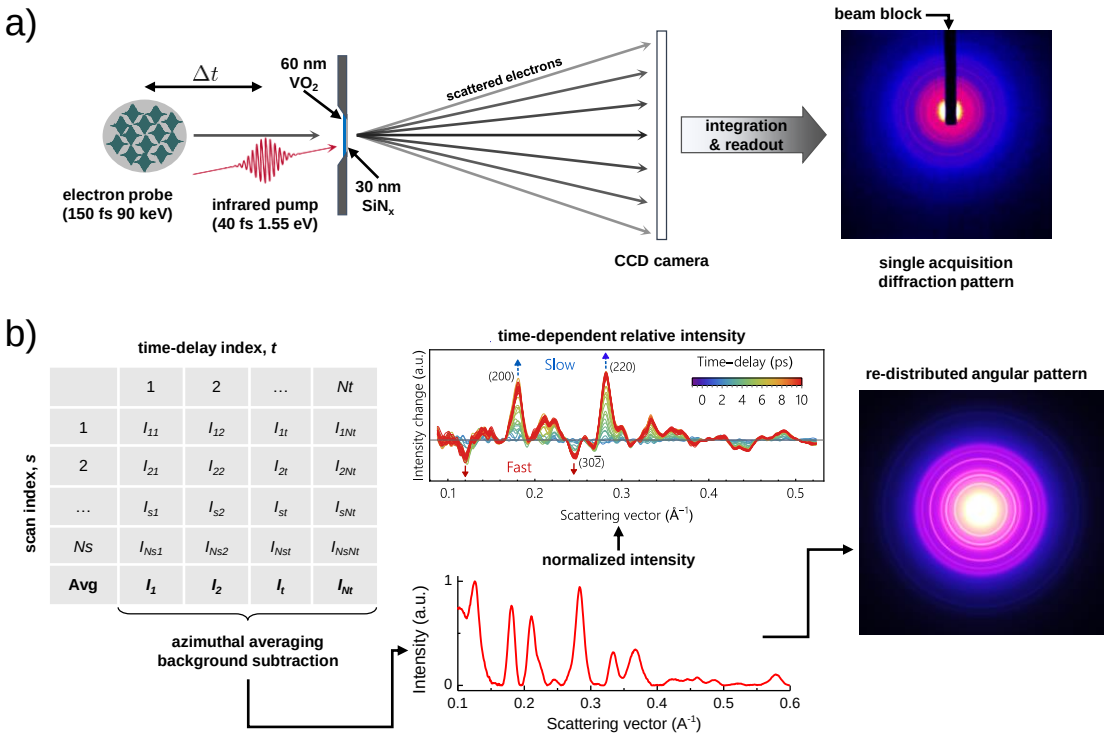

Figure 3–6: Ultrafast electron diffraction measurement and processeing of VO_2
a) Schematic illustration of an ultrafast electron diffraction measurement of VO_2. An 800 nm pump pulse (40 fs FWHM) illuminates the VO_2 sample which is deposited to a thickness of 60 nm on a 30 nm SiN_x substrate. Transmitted scattered electrons are collected by a CCD detector camera for various pump-probe time-delays Δt. A typical image formed by a 10 second exposure to the scattered electrons is shown in the top right. b) An experiment consists of a matrix of individual images I_{st} where s indexes the scan number and t indexes the time-delay. Scans are averaged together at the end of the experiment during the analysis procedure. For each average image $\langle I_t \rangle$, a dynamic background is removed, and a radial pattern is generated by azimuthal integration. Changes in $\langle I_t \rangle$ as a function of time yield the structural dynamics of the material.

for VO_2 because the necessarily low repetition rates of the experiments yield a trade-off in terms of scattering signal. We denote the scan index as s and the measurement becomes a matrix of images I_{st}, with dimension $N_s \times N_t$ where N_t and N_s are the size of

the time and scan arrays respectively as shown in Fig. 3–6 b). In post-processing steps, scans are averaged together and images are normalized. Averaged images are azimuthally integrated and the time-dependent background of the entire pattern is removed using an iterative algorithm based on the dual-tree complex wavelet transform [134, 135]. These post-processing steps are performed using a home-built open-source software package called *iris* which uses many functions and libraries from *scikit-ued*.

3.4.1 Bragg peak analysis

For detailed analysis of the Bragg peaks in the diffraction pattern, a local background is estimated similarly in the vicinity of the peak of interest in order to correct for skewness as shown in FIG. 3–7 b) for the (220) peak. Diffraction peaks of interest at a time-delay point t is fit to a Gaussian function given by

$$I(G - G_0, t) = I_{(hkl)}(t, t_0) e^{-(G-G_0)^2/2\Gamma^2}, \tag{3.2}$$

where $I_{(hkl)}(t, t_0)$ is the peak intensity, $|\mathbf{G}| = G$ is the scattering vector, G_0 is the peak center and Γ is the RMS peak width. The relative peak intensity is computed by finding the set of $I_{(hkl)}(t, t_0)$ for all pump probe time-delays. The parameter t_0 is "time-zero" and represents the initiation of the photo-induced dynamics (the moment when the pump pulse stimulates the sample) and is usually $t_0 \simeq 0$. Typically, prior to a measurement, t_0 is determined with a precision only to a picosecond level. Therefore we let t_0 float as a fitting parameter, and determine its value more precisely for each measurement. This data is then fit to $I_{(hkl)}(t, t_0) = \Theta(t - t_0)\Delta I_{(hkl)} \left(1 - e^{-(t-t_0)/\tau_{(hkl)}}\right)$ to extract the amplitude $\Delta I_{(hkl)}$ and time constants $\tau_{(hkl)}$ for each diffraction peak (hkl) used in the analysis. Appropriate error bars are determined from the standard error calculated by the fitting routine based on the χ^2 distribution. Hereafter we will refer to measurements of time-dependent Bragg peak intensities as normalized changes relative to the equilibrium intensity before $t = 0$,

$I_{(hkl)}(t<0)$. Explicitly this is given by

$$\Delta I_{(hkl)}(t) = \frac{I_{(hkl)}(t) - I_{(hkl)}(t<0)}{I_{(hkl)}(t<0)}. \tag{3.3}$$

3.4.2 Monoclinic insulator to Monoclinic metal dynamics

The photo-induced structural changes occuring in the VO_2 sample begin at a fluence level of $\sim$ 2 mJ/cm^2 and are characterized by a relatively slow *increase* in diffracted intensity of the low-index (200) and (220) peaks shown in Fig. 3–7 a). We interpret these signals in the following way: The intensity changes preserve the crystal symmetry of the equilibrium monoclinic insulator phase since none of the diffraction peaks vanish, nor do any new diffraction peaks appear. The changes in diffraction intensity on a Bragg peak are proportional to the geometric structure factor

$$I \propto |F_0(\mathbf{G})|^2 = \left| \sum_j \exp\left(-M_j(\mathbf{G})\right) f_j(\mathbf{G}) \exp\left(-i\mathbf{G}\cdot\mathbf{r}_j\right) \right|^2, \tag{3.4}$$

where M_j is the Debye-Waller factor, $f_j(\mathbf{G})$ is the atomic form factor and $\mathbf{r}_j$ is the co-ordinate of atom j in the unit cell. The atomic form factor is determined by the Fourier transform of the electrostatic potential of atom j, $V_j(\mathbf{r})$ according to

$$f_j(\mathbf{G}) = \int d\mathbf{r} V_j(\mathbf{r}) \exp\left(i\mathbf{G}\cdot\mathbf{r}\right). \tag{3.5}$$

Commonly observed in ultrafast electron diffraction, is the transient suppression of peak intensities due to an increase in $M_j(\mathbf{G})$ known as the *transient Debye-Waller effect*. This arises directly from the transfer of energy from the photo-excited electrons to the lattice, yielding an increase in the RMS atomic displacement due to the creation of phonons. This effect demonstrates a clear $|\mathbf{G}|^2$ dependence and always results in a peak-suppression with time following laser excitation. Neither of these traits are observed in our measurements. The only remaining explanation of our observations is a photo-induced change in the atomic

form factors f_j contributing to $I_{(200)}$ and I_{220}. Electron scattering is sensitive to valence charge distributions, and thus to a certain extent orbital order. Photo-excitation impulsively perturbs the carrier (and hole) densities of the valence band and can be detected by electron scattering if a significant change in $V_j(\mathbf{r})$ follows. The transient changes in I_{200} and I_{220} are thus attributed to changes in $f_j(\mathbf{G})$ (via changes in $V_j(\mathbf{r})$) at low $\mathbf{G}$ in reciprocal-space and correspondingly large $\mathbf{r}$ (valence) in real-space.

Now we will present in greater detail a dataset of VO_2 photo-excited at a fluence of 6 mJ/cm^2 to illustrate the important aspects of the results. The (200) and (220) peak intensity dynamics at low-fluence demonstrate a slow increase with time contants determined to be $\tau_{(200)} = 5.5 \pm 1.4$ ps and $\tau_{(220)} = 5.3 \pm 1.2$ ps determined by a single-exponential fit up for data up to +15 ps to capture the full extent of the rise. The data and the fitting results are shown in Fig. 3–8 a) and b). Visible at later times, is an even slower partial recovery of the scattering intensity signal. It was not possible to reliably fit this feature of the measurement occurring at longer time-scales and determine significant parameters for a single bi-exponential fitting function. A separate fit of data spanning from +15–60 ps revealed a time-constants of $\tau^*_{(200)} = 8.7 \pm 3.6$ ps and $\tau^*_{(220)} = 9.3 \pm 2.2$ ps. This recovery could be the result of a Debye-Waller-like effect transpiring in the $\mathcal{M}$ phase, due to the heating of the lattice following the formation of the $\mathcal{M}$ phase. This is difficult to determine definitively however, due to the limited number of diffraction peaks which demonstrate the signals illustrated in Fig. 3–8. limiting our ability verify the expected scaling of this effect as a function $|\mathbf{G}|^2$. Furthermore, the overall dynamics of the material become increasingly complicated as the fluence is increased (this will be discussed further in the following sections) and longer-term dynamics play important roles for timescales exceeding 100 ps. Our focus for this work is the time-window spanning the initial $\sim 10 - 15$ ps following photo-excitation with the goal of characterizing the initial formation of the $\mathcal{M}$ phase.

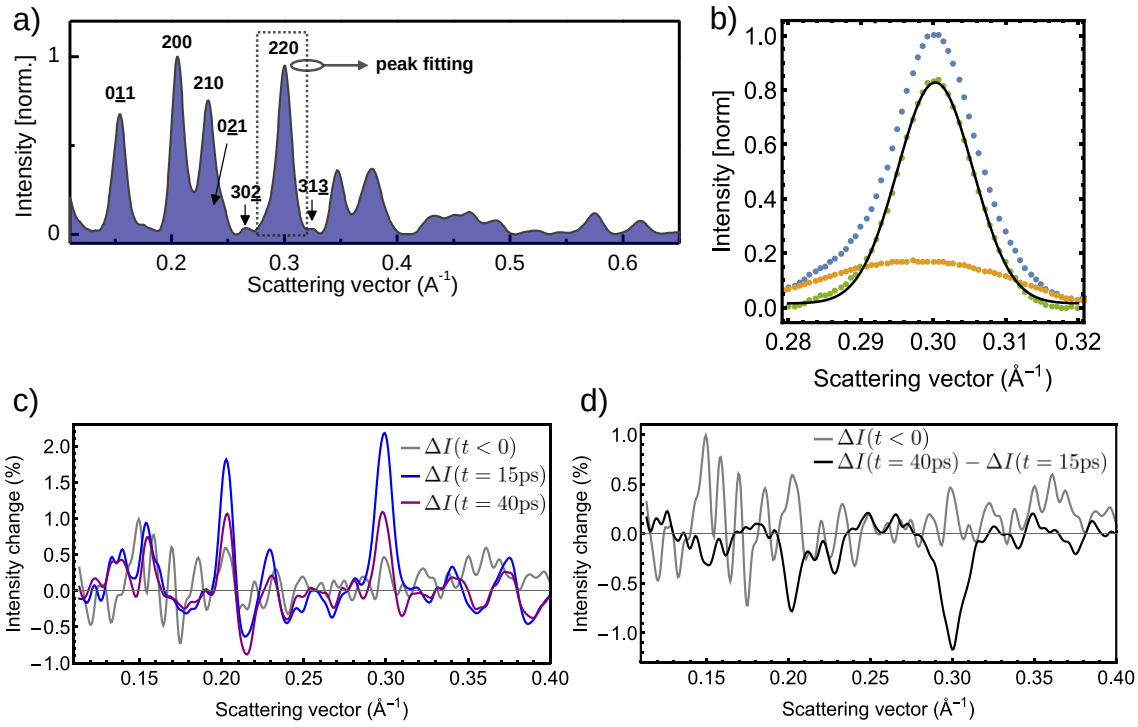

Figure 3–7: Low fluence dynamics in VO_2.
a) Diffraction pattern for monoclinic M_1 VO_2 with various diffraction peaks indexed with respect to the high-temperature rutile R phase. b) Example of peak-fitting with a local background refinement for the (220) diffraction peak. c) Normalized intensity change $\Delta I(t)$ as a function of scattering vector for a few relevant time-delay values. The grey curve is the average of all traces before photo-excitation ($t = 0$) and thus describes the noise level of the relative intensity change measurement as a function of scattering vector. d) The black curve is the relative intensity change between the blue and purple traces shown in c) along with the noise level.

3.4.3 Monoclinic insulator to Rutile metal dynamics

The dynamics which occur at higher fluences describe the M_1 to R phase transition. This transition occurs much faster that the M_1 to $\mathcal{M}$ phase transition and corresponds to a clear change in crystal symmetry. The $(30\bar{2})$ reflection shown in Fig. 3–9 a) is a forbidden peak (the geometric structure factor vanishes) in the high-symmetry R phase

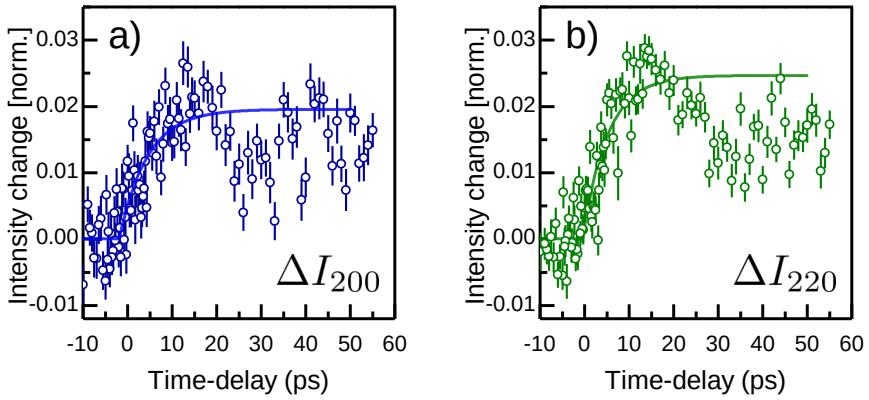

Figure 3–8: Low-fluence VO_2 integrated peak intensity dynamics
a) Peak intensity dynamics for the (200) Bragg peak. The rise is fit to an exponential function, and the time constant is 5.5±1.4 ps. a) Peak intensity dynamics for the (220) Bragg peak. The rise is fit to an exponential function, and the time constant is 5.3±1.2 ps. The rise in diffraction intensity is due to a transient atomic form factors, produced by charge re-distribution within the unit cell of the material.

and can its magnitude can be suppressed roughly linearly with photo-excitation fluence indicating partial conversion of the film. The time constant of this transition is roughly 300 fs and independent of fluence in our measurements. This transition occurs in the material alongside the M_1 to $\mathcal{M}$ transition described in the previous section and indicated in the plot of the relative intensity change show in Fig. 3–9 a) and c). Below a threshold fluence of roughly 8 mJ/cm^2 the suppression of the $(30\bar{2})$ peak is not visible in our measurements. At highest excitation fluences, the $(30\bar{2})$ peak is suppressed by greater than 75%. The fluence dependence will be discussed further in Sec. 3.7.

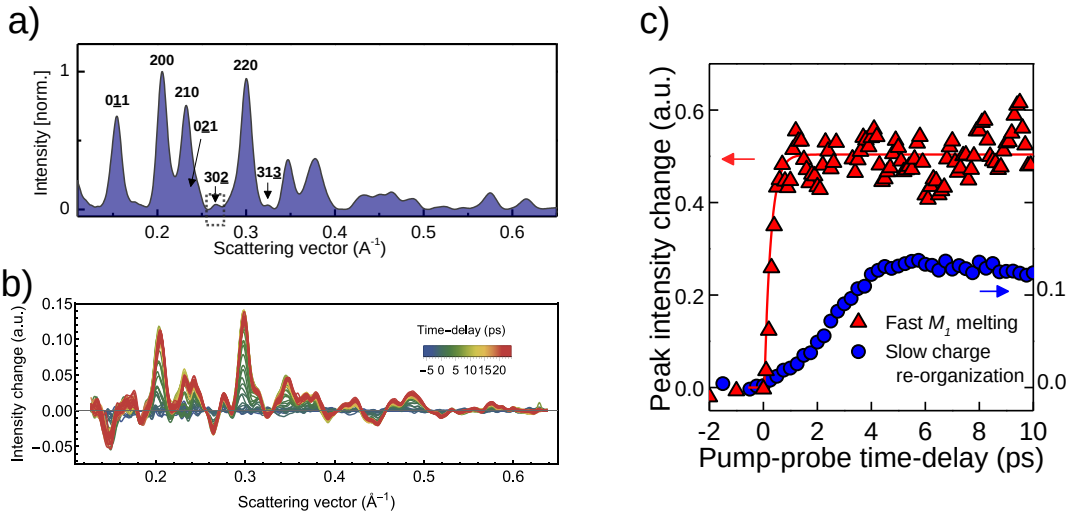

Figure 3–9: High-fluence VO_2 dynamics
a) Azimuthally averaged powder diffraction pattern of M_1 VO_2. The $30\bar{2}$ peak serves at an order parameter for the M_1 phase, as it vanishes in the R phase. b) Time-resolved differential scattering signal at high fluence (23 mJ/cm^2) indicated the presence of both fast and slow processed, M_1 to R melting and M_1 to $\mathcal{M}$ charge re-organization respectively. c) Time-traces of the normalized peak intensity dynamics for the $30\bar{2}$ (fast M_1 melting) and 220 peak (slow charge re-organization).

3.5 Real-space reconstruction

At fluences below the CPT threshold, there is no formation of R phase crystallites. This has been confirmed by several other works and out measurements show no significant change in the intensity of the $(30\bar{2})$ which is a forbidden reflection in R phase VO_2. Therefore, observed intensity changes in this regime pertain exclusively to structural changes in the material during the formation of the $\mathcal{M}$ phase. Since its discovery [5], the structure of the photoinduced $\mathcal{M}$ phase and its relationship to the parent M_1 phase has remained unclear as the subtle details of the material microstructure are difficult to discern through spectroscopic measures. Here we use measured UED intensities to determine the changes in the electrostatic crystal potential, $V(\mathbf{r})$, associated with the transformation between

M_1 and $\mathcal{M}$ phases. This is a Fourier inversion process which transforms the diffraction data back to a real-space representation. The centrosymmetry of the monoclinic and rutile phases provides a solution to the phase problem [136] and allows for the reconstruction of the full three-dimensional real-space electrostatic potential from each one-dimensional diffraction pattern obtained using UED. The analysis procedure and results are described below.

As mentioned in section 3.4.2, the M_1-to-$\mathcal{M}$ phase transition involves no lattice symmetry changes. Simply put, the atoms remain in their positions established by the M_1 phase. Moreover, the measured diffracted intensity changes associated with the M_1-to-$\mathcal{M}$ transition are only observed at low scattering vectors ($|\mathbf{G}| < 0.3$ Å^{-1}). This reinforces the claim of preserving lattice symmetry as there is no change in atomic coordinates ($\mathbf{r}_j$ in the geometric structure factor (Eqn. 3.4) which would not affect scattering vectors ($|\mathbf{G}| > 0.3$ Å^{-1}). Therefore, the changes in diffracted intensity must primarily be caused by changes in atomic form factors $f_j(\mathbf{G})$.

3.5.1 Fourier synthesis

The real-space electrostatic potential, $V(\mathbf{r})$, is given by an inverse Fourier-transform of the structure factors:

$$V(\mathbf{r}) = \sum_{\{\mathbf{G}\}} \sqrt{I_{\mathbf{G}}} \exp\left(i\varphi_{\mathbf{G}}\right) \cos(\mathbf{r} \cdot \mathbf{G}), \tag{3.6}$$

where the set $\{\mathbf{G}\}$ is understood to be the set of scattering vectors $\mathbf{G}_{hkl} = h\mathbf{b}_1 + k\mathbf{b}_2 + l\mathbf{b}_3$ lying within range of angles visible to the diffractometer. $I_{\mathbf{G}}$ is the diffraction intensity associated *only* with scattering vector $\mathbf{G}$, and $\varphi_{\mathbf{G}}$ is the diffraction phase. Diffraction measurements are not sensitive to the phases $\varphi_{\mathbf{G}}$; we must therefore infer them. We use the centrosymmetry of VO_2 rutile R and monoclinic M_1 phases (and by association the monoclinic metal $\mathcal{M}$ phase). This limits the phases to either 0 or π. It follows that we can

infer the phases from the well-known crystal structures. In this case, the diffraction phase $\varphi_{\mathbf{G}}$ is simply the complex phase of the structure factor $F_0(\mathbf{G})$:

$$\varphi_{\mathbf{G}} = \angle F_0(\mathbf{G}) \tag{3.7}$$

The assumption that the diffraction phases of the theoretical structure are the same as the observed structure is tested in section 3.5.4.

For the electrostatic potential maps shown for the M_1 and non-equilibrium $\mathcal{M}$ phases (Fig. 3), we distribute the measured intensity in a manner consistent with the expectation for the known equilibrium M_1 phase, rather than via Le Bail decomposition or other methods typically used when the initial crystallography is unknown. The extraction of diffraction intensity associated with a reflection $\mathbf{G} = (hkl)$ is arduous for the case of VO_2 because of many overlapping reflections. For an experimental diffraction pattern $I_{\text{exp}}(\mathbf{G})$, we extract the diffracted intensity associated *only* with the reflection $\mathbf{G}$, $I_{\mathbf{G}}$ like so:

$$I_{\mathbf{G}} = I_{\text{exp}}(|\mathbf{G}|) \times \frac{F_0(\mathbf{G})^2}{I_{\text{theo}}(|\mathbf{G}|)} = I_{\text{exp}}(|\mathbf{G}|) \times \frac{F_0(\mathbf{G})^2}{\sum_{\{\mathbf{K}\}} F_0(\mathbf{K})^2} \tag{3.8}$$

where $I_{\text{theo}}(\mathbf{G})$ is a simulated electron powder diffraction pattern computed according to Eqn. 3.4 using the $\mathbf{r}_j$ values for the equilibrium monoclinic M_1 phase, and $F_0(\mathbf{G})$ is the theoretical structure factor associated with reflection $\mathbf{G}$. The calculation of theoretical quantities are provided by the open-source package *scikit-ued* [135]

3.5.2 Reconstruction of the equilibrium phases

Although we are confident that the VO_2 samples are in the monoclinic M_1 phase prior to photo-excitation, it is useful to confirm that the real-space reconstruction algorithm involving the diffraction intensities reflects this fact. Equilibrium diffraction patterns of M_1 and R phase VO_2 are used in Eqn.(3.6) along with the known phases $\varphi_{\mathbf{G}}$ and the results are shown in Fig.3–10. It is conventional when comparing the phases of VO_2 to

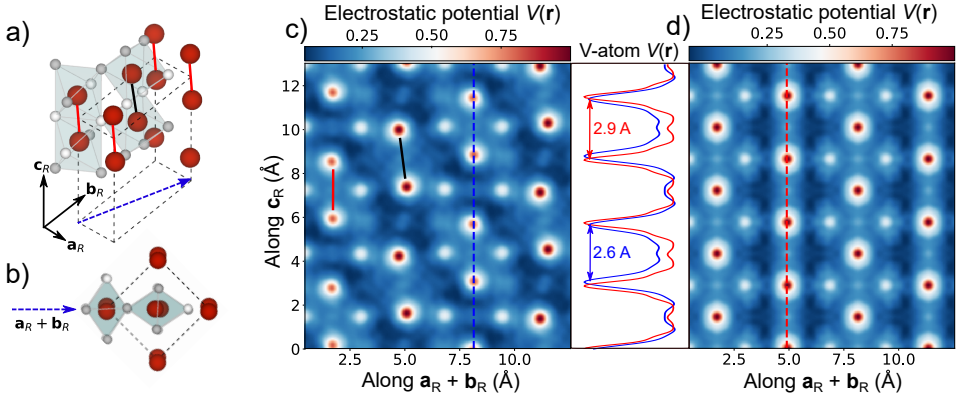

Figure 3–10: Real-space reconstruction of the equilibrium monoclinic M_1 and rutile R phases
a) View of the crystal structure of M_1 VO_2 using the basis vectors from the R phase $\mathbf{a}_R$, $\mathbf{b}_R$ and $\mathbf{c}_R$. Vanadium atoms are shown as red sphere while oxygen atoms appear as smaller gray spheres. V–V dimer pairs are shown by black and red lines where the former tilts in and the latter tilts out of the plane defined by $\mathbf{a}_R + \mathbf{b}_R$ and $\mathbf{c}_R$. b) Side view of the unit cell showing more clearly the in-plane and out-of-plane dimer tilting. c) Reconstructed $V(\mathbf{r})$ for M_1 VO_2. The dashed blue line marks a line-cut of $V(\mathbf{r})$ which is plotted to the right showning the V–V spacings along $\mathbf{c}_R$. d) Reconstructed $V(\mathbf{r})$ for R VO_2. The dashed red line marks a line-cut of $V(\mathbf{r})$ plotted to the left illustrating the uniform V–V spacings along $\mathbf{c}_R$.

remain in the basis for the R phase established by $\mathbf{a}_R$, $\mathbf{b}_R$ and $\mathbf{c}_R$. Figure 3–10 a) and b) shows the crystal arrangement of the M_1 system and illustrates the dimerization of the vanadium atoms. The important features of VO_2 are best captured by plotting the a slice of the 3-dimensional function $V(\mathbf{r})$ in the plane spanned by the vectors $\mathbf{a}_R + \mathbf{b}_R$ and $\mathbf{c}_R$ as shown in Fig. 3–10 c) and d). The dimerization occurs primarily along the $\mathbf{c}_R$ direction with certain dimers tilted in the plane and other out of the plane as depicted by the black and red lines in Fig. 3–10 c) and d). We observe clearly this structural distortion, and retrieve the expected V–V spacing of 2.6 Å and 3.1 Å in the M_1 phase and 2.9 Å in the R phase.

3.5.3 Reconstruction of the monoclinic metallic phase

Using the ultrafast electron diffraction data, we are in a position to directly determine the changes in the electrostatic potential $V(\mathbf{r})$ from the changes in the diffraction intensity. At low fluence, a small fraction of the material transforms to the monoclinic metal $\mathcal{M}$ phase and none transforms to rutile R as we are in the regime below the CPT threshold. Thus $\Delta I_{\mathbf{G}}$ relates directly and exclusively to $\Delta V(\mathbf{r})$ pertaining to charge re-arrangement leading to the $\mathcal{M}$ phase.

In Fig. 3–11 the changes in $V(\mathbf{r})$ associated with the M_1–$\mathcal{M}$ transition are revealed. This map is computed from the measured $\Delta I_{\mathbf{G}}$ between the $\mathcal{M}$ and M_1 phases 10 ps after photoexcitation at a fluence of 6 mJ/cm^2. The preservation of M_1 crystallography is clear; *i.e.* V–V dimerization and tilting along the $\mathbf{c}_R$ axis endures. Also evident is a transition to a novel 1-dimensional anti-ferroelectric charge order along $\mathbf{c}_R$. In the equilibrium phases all oxygen atoms are equivalent. The $\mathcal{M}$ phase however, exhibits a periodic modulation in $\Phi(\mathbf{r})$ at the oxygen sites along the $\mathbf{c}_R$ axis indicated by arrows in Fig. 3–11 (d). This charge modulation is commensurate with the lattice constant and mirrors the existing periodic lattice distortion established by the vanadium dimers. The oxygen atoms exhibiting the largest changes are those associated with the minimum V–O distance in the octahedra and, therefore, the V–V dimer tilt. This emphasizes a relationship between the lattice distortion (dimers) present in the parent M_1 phase and the emergence of the $\mathcal{M}$ phase. The anti-ferroelectric lattice distortion in M_1 was already emphasized by Goodenough [109] in his seminal work on VO_2. Significant changes in electrostatic potential are also visible between V atoms in the octahedrally-coordinated chains along $\mathbf{c}_R$ that is consistent with a delocalization or transfer of charge from the V–V dimers to the region between dimers. These findings revealed by the reconstruction of the transient electrostatic potential $\mathcal{M}$

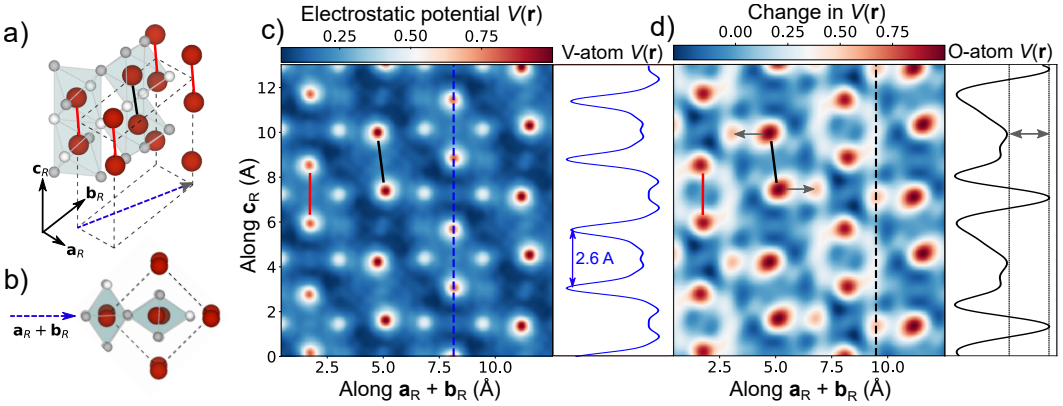

Figure 3–11: Real-space reconstruction of the change in the electrostatic potential during the monoclinic metal phase
a) Atomic model of the unit cell of M_1 VO_2 illustrating the V–V dimers up the $\mathbf{c}_R$ axis. Dimers tilting out of the plane define by $\mathbf{a}_R$ and $\mathbf{b}_R$ are depicted by red lines and those tilting in the plane are represented by black lines. b) View of the unit cell atoms looking up the $\mathbf{c}$-axis showing more clearly the dimer tilts. c) Reconstruction electrostatic potential $V(\mathbf{r})$ of M_1 VO_2 using illustrating the V–V dimer pairs. d) Change in electrostatic crystal potential 10 ps following photo-excitation at a fluence of 6 mJ/cm^2. Important features are the retention of dimerization, and increased in oxygen atom charge for those nearest V atoms in the O-cage octahedra.

phase clearly indicate that it arises from a collective reorganization of the valence charge distribution.

3.5.4 Patterson Pair-distribution Function

The reconstruction of real-space electrostatic potential from diffraction data requires the knowledge of diffraction phases as well, information that is not available to ultrafast electron diffraction measurements. We get around this by using the known crystal structures of monoclinic M_1 and rutile VO_2. It could be possible that there is a small (though not resolvable in experiment) relaxation in the lattice structure to accommodate the new charge order of the $\mathcal{M}$-phase.

To validate the use of theoretical diffraction phases in the reconstructed electrostatic potential maps, we calculate the radial pair-distribution function $\mathcal{G}(r,t)$ in two ways:

- Directly from the polycrystalline diffraction patterns; the Patterson function $\mathcal{G}_{\mathrm{P}}(r,t)$
- As the autocorrelation of the 3D electrostatic potential, $\mathcal{G}_{\mathrm{A}}(r,t)$

To calculate the Patterson radial pair-distribution function, the diffracted intensity $I(G,t)$ must be normalized to a per unit cell level. The normalized (or reduced) intensity $\mathcal{I}$ is defined for a general unit cell U of N atoms as follows:

$$\mathcal{I}(G,t) \equiv \frac{I(G,t) - \frac{1}{N}\sum\limits_{a\in U}^{N} |f_a(G)|^2}{\frac{1}{N}\sum\limits_{a\in U}^{N} |f_a(G)|^2} \tag{3.9}$$

where $f_a(G)$ is understood to be the atomic form factor for electrons for atom a. The Patterson radial pair-distribution function is then given by:

$$\mathcal{G}_{\mathrm{P}}(r,t) = \frac{1}{2\pi^2 r}\int_0^\infty dG\ \mathcal{I}(G,t)\sin(G\cdot r)G. \tag{3.10}$$

The radial pair-distribution function can also be computed as the radial auto-correlation of a 3D electrostatic potential $V(\mathbf{r},t)$:

$$\mathcal{G}_{\mathrm{A}}(r,t) = \int_0^\infty dS_{r'} V(\mathbf{r},t)V^*(\mathbf{r}-\mathbf{r}',t) \tag{3.11}$$

where dS_r is the spherical surface element.

The radial pair-distribution function of the unpumped monoclinic M_1 VO_2, $G(r, t < 0)$, is presented in fig. 3–12. It is contrasted with the radial autocorrelation of an electrostatic potential volume of $2 \times 2 \times 2$ unit cells of monoclinic M_1 VO_2. The agreement between the two curves is close to perfect, indicating that the use of theoretical diffraction phases in this work is fully consistent with other analyses based on the diffraction data.

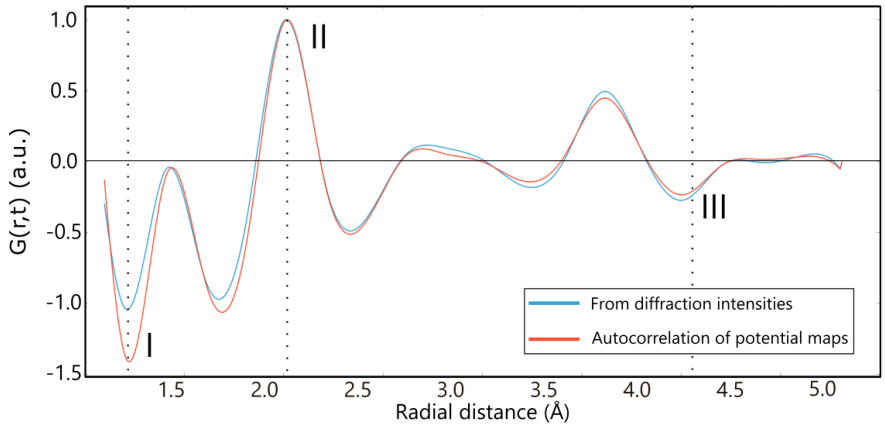

Figure 3–12: Comparison of the radial pair-distribution function computed in two separate ways from static diffraction of monoclinic M_1 VO_2.
The blue curve has been calculated directly from the polycrystalline diffraction intensity. The orange curve was calculated by reconstructing a large real-space electrostatic potential map ($2 \times 2 \times 2$ unit cells) and autocorrelating it. Negative feature at I is due to the average half V–V dimer length. Positive feature at II is due to the average V-O distance around the octahedron. Negative feature at III represents the sum of dimerized and undimerized average V-V distance.

3.6 Time-resolved terahertz spectroscopy

Complementary time-resolved terahertz spectroscopy (TRTS) measurements were performed on the same samples under identical excitation conditions to determine the associated changes in the time-dependent complex conductivity, $\tilde{\sigma}(\Delta t, \omega) = \sigma_1(\Delta t, \omega) + i\sigma_2(\Delta t, \omega)$. The conductivity is extracted by measuring the complex electric field waveforms directly by electro-optic sampling. The THz pulse is split in two parts, one which probes the conductivity response of the photo-excited sample and yields a transmitted waveform $\tilde{E}_{\mathrm{t}}(\Delta t, t)$ the profile of which depends of the time Δt following photo-excitation with 800 nm laser light. The second is a reference waveform $\tilde{E}_{\mathrm{ref}}(t)$ and is used calculate the pump-induced differential electric field $\Delta\tilde{E}(\Delta t, t) = \tilde{E}_{\mathrm{ref}}(t) - \tilde{E}_{\mathrm{t}}(\Delta t, t)$. The pump-induced photo-conductivity of the VO_2 sample of thickness $d = 50$ nm is analyzed in a thin-film model involving the index of refraction of the SiN_x substrate which is $n = 1.85$ in the THz

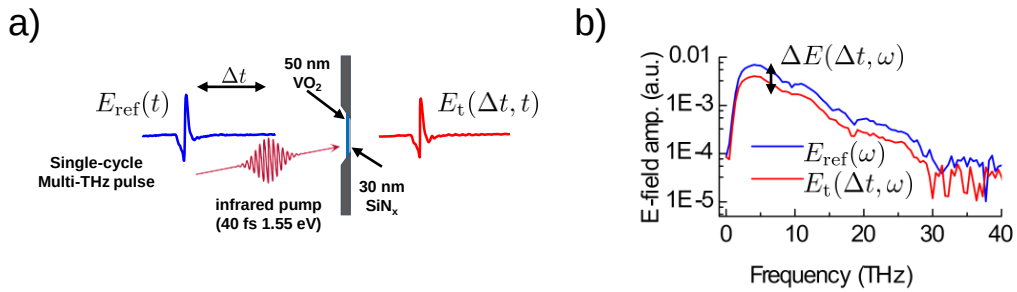

Figure 3–13: Time-resolved terahertz spectroscopy (TRTS) of thin-film VO_2. a) Experimental schematic of time-resolved terahertz transmission measurement of a VO_2 thin film photo-excited by 800nm laser light. THz waveforms E_{ref} (reference pulse) and E_{t} are determined by electro-optic sampling. b) Fourier transforms of the THz electric field waveforms shown in a). The differential conductivity is extracted from the difference between the two spectra.

range. In a transmission geometry as shown in Fig. 3–13 a). The Fourier transforms of the electric field waveforms $\tilde{E}_{\mathrm{ref}}(\omega)$ and $\tilde{E}_{\mathrm{ref}}(\Delta t, \omega)$ are shown Fig. 3–13 b) and related to $\tilde{\sigma_1}(\omega)$ according to the following analytic model [137, 138, 139]

$$1 + \frac{\Delta\tilde{E}(\Delta t, \omega)}{\tilde{E}_{\mathrm{ref}}(\omega)} = \left(\frac{1+n}{1-n}\right) \frac{1 - n - Z_0 d\tilde{\sigma_1}(\Delta t, \omega)}{1 + n + Z_0 d\tilde{\sigma_1}(\Delta t, \omega)}, \tag{3.12}$$

where $Z_0 = 377\ \Omega$ is the vacuum impedance of freespace.

The TRTS experiments performed to acquire the data presented in this thesis are based on two-color laser plasma generation of single cycle, broadband THz pulses and air-biased coherent detection providing a spectral range from 0.5–30 THz and temporal resolution of $\sim$ 40 fs [137]. The THz spectrometer is driven by 35 fs, 795 nm pulses from an amplified Ti:sapphire femtosecond laser operating at 250 Hz repetition rate to allow for sample recovery between shots. The pump spot size was $\sim$ 700 μm which was at least 4 times the size of the THz pulse for the lowest frequencies analyzed here (2 THz).

A typical TRTS experiment proceeds as follows: At a particular 800 nm pump excitation fluence, $\tilde{E}_{\mathrm{ref}}(\omega)$ and $\tilde{E}_{\mathrm{ref}}(\Delta t, \omega)$ waveforms are acquired by the electro-optic sampling spectrometer as a function of pump-probe time-delay Δt. The waveforms are Fourier transformed to the spectral domain and the complex conductivity $\tilde{\sigma_1}(\Delta t, \omega)$ is retreived using Eqn. 3.12. This process is carried out for all fluences of interest.

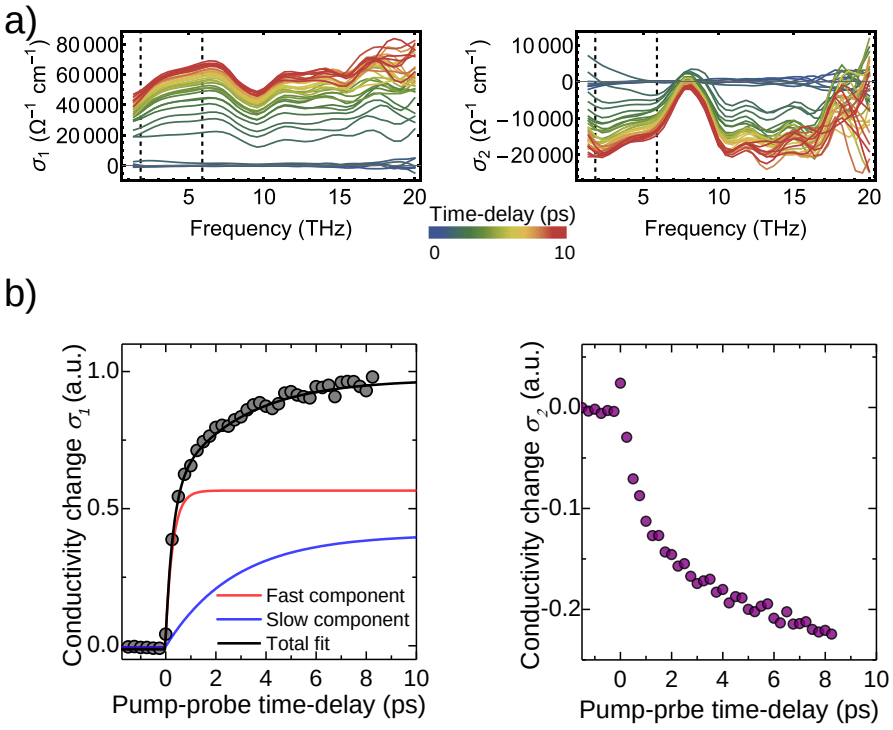

Figure 3–14: Time-resolved terahertz conductivity of VO_2.
a) Complex conductivity components σ_1 and σ_2 of photo-excited VO_2 at a fluence of 22 mJ/cm^2. The dashed lined represent the frequency bounds within which the conductivity response is integrated (2–6 THz) b) Normalized conductivity change (left:σ_1, right:σ_2) illustrating the bi-exponential time-dependence. The fast component matches the timescale for the M_1 to R transition and the slow matches the M_1 to $\mathcal{M}$ transition.

3.6.1 Time-dependent terahertz conductivity

The pump-induced changes in real conductivity, $\sigma_1(\Delta t, \omega)$, over the ∼2–20 THz frequency range (Fig. 3–14 (a)) also exhibit qualitatively distinct fast ($\Delta\sigma_1^{\text{fast}}$) and slow ($\Delta\sigma_1^{\text{slow}}$) dynamics, consistent in terms of timescales those described above for the structural transitions found in the UED measurements. These findings are similar measurements performed on sputtered VO_2 films in the 0.5–2 THz window [100]. Additional structure at higher frequencies is due to optically active phonons associated with O–cage vibrations around V atoms [99]. The total conductivity response is integrated across a spectral bandwidth of interest and the data is then fit to a bi-exponential function of the form

$$\int \sigma_1(\omega, t-t_0)d\omega = \Theta(t-t_0)\left(\Delta\sigma_1^{\text{fast}}\left(1-\exp\left(-\frac{t-t_0}{\tau_{\text{fast}}}\right)\right)+\Delta\sigma_1^{\text{slow}}\left(1-\exp\left(-\frac{t-t_0}{\tau_{\text{slow}}}\right)\right)\right). \tag{3.13}$$

An example of this fitting is shown for σ_1 in Fig. 3–14 b) at a fluence of 22 mJ/cm^2. Given the clear link established by the similar time-scales, we attribute the fast rise in conductivity to the M_1–R IMT (CPT) and the slower metallicity onset to the M_1–$\mathcal{M}$ IMT. The THz response is connected to the two structural transformations by focusing on the integrated spectral region from 2–6 THz, which includes exclusively electronic contributions to the conductivity (Drude-like) and omits phonon resonances [99, 101, 102]. Figure 3–14 (b) shows an example of the transient real conductivity measured at 22 mJ/cm^2 along with the fast and slow exponential components plotted individually. These time constants are in excellent agreement with those of the fast and slow processes determined from the UED measurements at similar fluences. This comparison will be made more thoroughly in the coming sections when the fluence dependence is examined in detail.

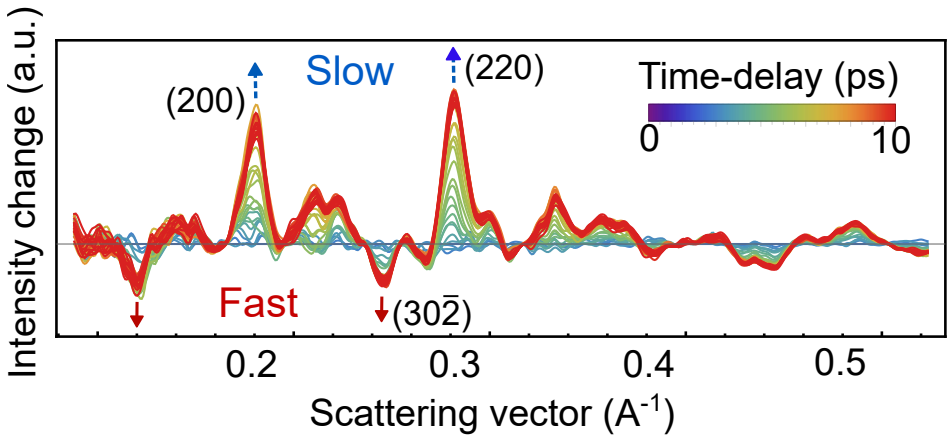

Figure 3–15: Differential ultrafast electron diffraction intensity at 21 mJ/cm^2. Both fast and slow structural processes are observed to occur in parallel according to the transient scattering.

3.7 Fluence dependence of the photo-induced transitions in VO_2

We return now to the ultrafast electron diffraction measurements and discuss the evolution of the photo-induced dynamics as the excitation fluence is increased. UED measurements of pulsed laser deposited 50 nm VO_2 films (optical depth is $\sim$ 130 nm at 800 nm wavelength) reveal rich pump-fluence dependent dynamics up to the damage threshold of $\sim$50 mJ/cm^2 (35 fs, 800 nm, $f_{\text{rep}} = 50 - 200$ Hz). The (30$\bar{2}$) peak serves as an order parameter for the $M_1 \rightarrow R$ transition, since it is forbidden by the symmetry of the R phase, while the (200) and (220) peaks remain present in all equilibrium phases albeit with slightly different amplitudes because of varying structure factor terms.

Consistent with previous work [5], as the excitation fluence increases, the pump-induced changes to diffracted intensity (Fig. 3–15) depict the two distinct and independent photo-induced structural transformations; the M_1–$\mathcal{M}$ phase transition and the M_1 to R phase transition. As mentioned previously, at low pump fluences ($\sim$4–8 mJ/cm^2) the M_1–$\mathcal{M}$ is exclusively observed, while at high pump fluences ($>$ 35 mJ/cm^2) the fast process

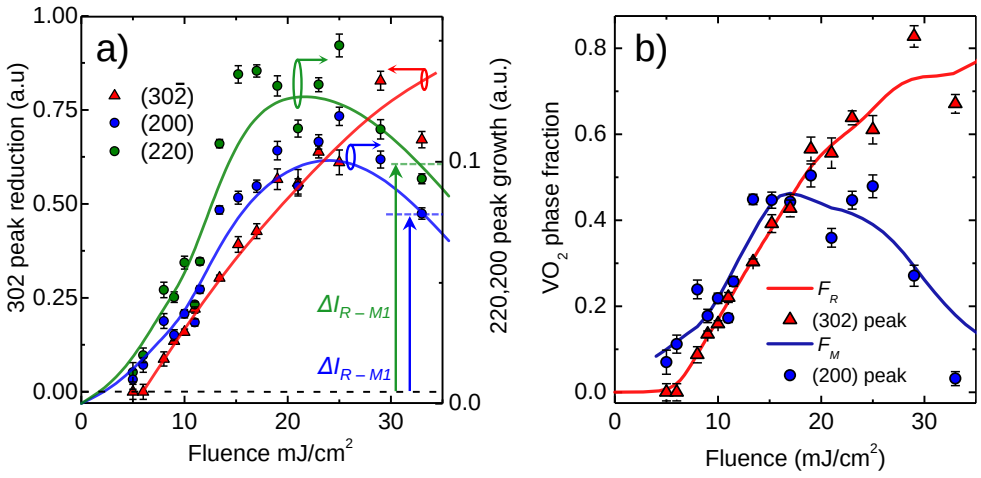

Figure 3–16: Fluence dependence of diffraction peak intensity dyanmics. a) Relavtive intesity changes of (200), (220) and (30$\bar{2}$) Bragg peaks. b) Phase volume fractions for the $\mathcal{M}$ (blue line) and R (red line) phases calculated using the ultrafast electron diffraction data shown in (a) via the volume phase fraction model. Red triangles are the (30$\bar{2}$) data points from (a) and blue circles are the (200) data points in (a) (scaled for clarity) with the $M_1 \rightarrow R$ phase transition contribution subtracted.

dominates. In the intermediate fluence range of 8–30 mJ/cm^2 both transitions occur in a concurrent manner and form a complex heterogeneous sample response. We emphasize again that these structural transitions are independent; the M_1–$\mathcal{M}$ transition is *not* a prerequisite for the eventual formation of the R phase.

The samples studied in this work are polycrystalline powder samples grown by pulsed laser deposition. The microscopic sctructure of the sample consists of crystallites on the order of 50 nm with a distribution width of 25 nm. In the following discussion of the heterogenous sample response of photo-excited VO_2, we assume that the various populations of R and $\mathcal{M}$ phases produced are restricted to a single phase per crystallite as supported by spatially resolved studies of the photo-induced IMT [140, 141, 142, 143]. The conclusions of our measurements do not rely on this claim, since the diffraction measurements report

fundamentally on the ensemble averaged content of the material, but a discussion of the physics is more clearly articulated by assuming each individual crystallite in the material is either photo-induced R or M.

Having established the fact that there are two qualitatively distinct ultrafast photo-induced phase transitions in VO_2. The pump-fluence dependence of the sample response, specifically the heterogeneous character of the film following photoexcitation (due to both $M_1 \rightarrow \mathcal{M}$ and $M_1 \rightarrow R$ transformations) is addressed in this section. UED intensities report on the fluence dependence of both structural phase transitions (Fig. 3–16 (a)). The change in the $(30\bar{2})$ peak intensity provides an order parameter exclusively for the $M_1 \rightarrow R$ transition, while the (200) and (220) peak intensities report on both $M_1 \rightarrow \mathcal{M}$ and $M_1 \rightarrow R$ transformations. Measurements of the $(30\bar{2})$ peak intensity (Fig. 3–16 (a) red triangles) clearly demonstrate a fluence threshold of ~ 8 mJ/cm^2 for the $M_1 \rightarrow R$ transformation that is consistent with previous work [5, 98, 97]. Above this threshold the suppression of the $(30\bar{2})$ peak increases approximately linearly with fluence up to a magnitude greater than 75% at ~ 30 mJ/cm^2. This result is inconsistent with a widely implemented"two-step" model [98] to describe the M_1–R transition in VO_2. This model involves fast V–V dimer dilation (elongation of V–V pairs to the distance corresponding to the R lattive constant) on the order of ~ 300 fs followed by a slow dimer rotation occurring within roughly 7 ps. This slower timescale is even slower that the M_1–$\mathcal{M}$ time constant reported in our work for comparable fluences. Structure factor simulations suggest that complete V–V dimer dilation can only yield maximum $(30\bar{2})$ peak suppression of 50%. Our results clearly show a greater magnitude which is consistent with a simplified picture of the M_1–R transition where the periodic lattice distortion of the M_1 phase simply melts in ~ 300 fs or perhaps less as suggested by recent ultrafast x-ray scattering work [144]. The photoinduced fraction

of R–phase VO_2 reaches $\sim 75\%$ of the film on this timescale at the highest pump fluences reported.

The (200) and (220) peaks (Fig. 3–16 (a)) show a more complicated fluence dependence, reaching a maximum change in intensity in the 20 mJ/cm^2 range. At the highest excitation fluences reported the intensity changes in the (200) and (220) peaks correspond to the relative increase expected for the R phase compared to the M_1 of VO_2. The maximum at ~ 20 mJ/cm^2 is entirely due to the presence of the $\mathcal{M}$ phase as we demonstrate next by converting the changes in UED intensities to phase volume fractions in a detailed model.

3.7.1 Phase fraction analysis

The normalized peak intensity changes measured using UED are shown in Fig. 3–16 a). This data provides the necessary inputs for our phase fractional model to determine the volume fractions. We denote F_R as the phase volume fraction for the R phase and $F_{\mathcal{M}}$ for the $\mathcal{M}$ phase. The normalized relative intensity change $\tilde{i}(\mathcal{F})$ as a function of fluence $\mathcal{F}$ for the $\chi = (200)$ and (220) peaks can be written as

$$\begin{aligned} \tilde{i}(\mathcal{F}) &= \frac{\Delta I_\chi(\mathcal{F})}{\bar{I}_\chi^{M_1}} \\ &= \frac{\bar{I}_\chi^{M_1} F_{M_1}(\mathcal{F}) + \bar{I}_\chi^{R} F_R(\mathcal{F}) + \bar{I}_\chi^{\mathcal{M}} F_{\mathcal{M}}(\mathcal{F}) - \bar{I}_\chi^{M_1}}{\bar{I}_\chi^{M_1}}. \end{aligned} \tag{3.14}$$

Equation (3.14) includes intensity contributions $\bar{I}_\chi^\phi F_\phi$ from the three phases $\phi = M_1, \mathcal{M}, R$ of VO_2, where F_ϕ is the fluence-dependent volume phase fraction, and $\bar{I}_\chi^\phi$ is the peak intensity when *completely* in phase ϕ. We may write it more compactly as

$$\tilde{i}(\mathcal{F}) = \frac{\Delta I_\chi}{\bar{I}_\chi^{M_1}} = \frac{1}{\bar{I}_\chi^{M_1}} \sum_{\phi = M_1, R, \mathcal{M}} \bar{I}_\chi^\phi F_\phi - 1. \tag{3.15}$$

Using the condition that $\sum_\phi F_\phi = 1$ (crystallites are conserved) to eliminate F_{M_1} we obtain

$$\frac{\Delta I_\chi}{\bar{I}_\chi^{M_1}} = (\Lambda_\chi - 1)\, F_R + (\Sigma_\chi - 1)\, F_{\mathcal{M}}, \tag{3.16}$$

where $\Lambda_\chi = \bar{I}_\chi^R / \bar{I}_\chi^{M_1}$ and $\Sigma_\chi = \bar{I}_\chi^{\mathcal{M}} / \bar{I}_\chi^{M_1}$. The model parameter Σ_χ can be determined in the high fluence limit by setting $F_{\mathcal{M}} \to 1 - F_R$ (*i.e.* there are no remaining M_1 crystallites in the sample at high fluences) and using $F_R = \Delta I_{(30\bar{2})}(\mathcal{F}) / \bar{I}_{(30\bar{2})}^{M_1}$ which is simply the normalized diffraction peak suppression for the $30\bar{2}$ peak. The results for this estimation are shown in Fig. 3–17. We will assume that $\Sigma_{(200)} = \Sigma_{(220)} = \Sigma$. Consistency of the model requires that $\sum_\phi F_\phi = 1$ be respected, yielding a lower bound of $\Sigma^{\min} = 1.125$. The maximum value we compute over the fluence range of 20 to 30 mJ/cm^2 is $\Sigma^{\max} = 1.175$. Taking the average of the (200) and (220) results gives a value of $\Sigma = 1.150 \pm 0.025$. This value in some sense describes the increase in scattering strength of $\mathcal{M}$–phase VO_2 compared to the M_1 phase since it is also describes a structure factor ratio. Consider the peak at (200), we then have

$$\Sigma_{(200)} = \frac{\bar{I}_{(200)}^{\mathcal{M}}}{\bar{I}_{(200)}^{M_1}} = \frac{|F_0^{\mathcal{M}}(\mathbf{G} = 2\mathbf{a}_1^* + 0\mathbf{b}_2^* + 0\mathbf{c}_3^*)|^2}{|F_0^{M_1}(\mathbf{G} = 2\mathbf{a}_1^* + 0\mathbf{a}_2^* + 0\mathbf{b}_3^*)|^2}. \tag{3.17}$$

Since the $\mathcal{M}$ phase has the same lattice symmetry (atomic unit cell coordinates) Eqn. 3.17 roughly describes the ratio of the average unit cell form factors, *i.e.* $\Sigma_{(200)} \approx \langle f^{\mathcal{M}} \rangle_{\text{unit-cell}} / \langle f^{M_1} \rangle_{\text{unit-cell}}$.

The results of the model calculation are shown in Fig. 3–16 b). For fluences below the CPT (M_1 to R) IMT fluence threshold of ~ 8 mJ/cm^2, we observe clearly that only a small percentage ($\sim 10\%$) of $\mathcal{M}$ crystallites have been formed by photoexcitation. As the fluence increases, the photoexcitation of R crystallites begins at the threshold and increases roughly linearly afterwards. The $\mathcal{M}$ phase, achieves a maximum in the vicinity of 20 mJ/cm^2 where we determine that $F_{\mathcal{M}} = 45 \pm 13\%$. At greater fluences, $F_{\mathcal{M}}$ decreases as the material becomes increasingly R phase due to stronger photoexcitation. The data

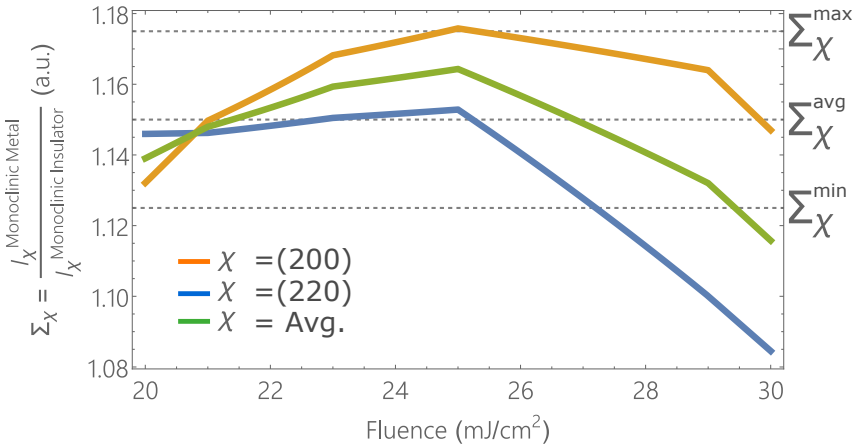

Figure 3–17: Phase fraction model paramters
Estimation of Σ_χ using ultrafast electron diffraction measurements and Eqn. 3.16. Peak intensity data $\Delta I(\mathcal{F})/\bar{I}_\chi^{M_1}$ for peaks $\chi = (200), (220)$ are used along with $\Delta I(\mathcal{F})/\bar{I}_{(30\bar{2})}^{M_1}$ in the high-fluence limit to solve for Σ. We assume that no M_1 crystallites remain ($1 = F_R + F_\mathcal{M}$). The orange (blue) curve is the calculation using the (200) ((220)) peak, and the green curve is the average, which is the final result we use under the assumption that $\Sigma_{(200)} = \Sigma_{(220)} = \Sigma$ is an intrinsic constant. $\Sigma_\chi^{\max}$ is the maximum value (upper bound) determined using the data and $\Sigma_\chi^{\min}$ is a lower bound enforced by the crystallite normalization condition $\sum_\phi F_\phi = 1$. Σ_χ^{avg} is the average of the green curve over the fluence range given by the bounds.

points shown in Fig. 3–16 b) as blue circles are an average of the (200) and (220) data points from (a) with the contribution from the $M_1 \to R$ phase transition subtracted.

We obtain quantitatively consistent results for the fluence dependence of the transient conductivity obtained by TRTS, firmly establishing a link between the differential structure and differential electronic response. The combination of the THz conductivity measurements and the structural dyanmics provided by the UED results, allow for the clear separation of the two photo-induced IMTs based on their temporal character. Figure 3–18 shows the fluence dependence of the fast ($\Delta\sigma_1^{\text{fast}}$) and slow ($\Delta\sigma_1^{\text{slow}}$) conductivity terms extracted from the TRTS measurements. The $\Delta\sigma_1^{\text{fast}}$ component corresponds to the

conductivity response associated with the transition from $M_1 \rightarrow R$ as it increases steadily with fluence in accordance with F_R shown in Fig. 3–16 a) and b). Furthermore, we clearly observe that $\Delta\sigma_1^{\text{slow}}$ achieves a maximum at a fluence of $\sim$20 mJ/cm^2 beyond which it decreases, consistent with the behavior of the (200) and (220) diffraction peaks and $F_{\mathcal{M}}$ shown in Fig. 3–16 b). The TRTS results indicate that the photo-induced conductivity of the VO_2 film at a fluence of 20-25 mJ/cm^2 is formed by roughly equal contributions from $\Delta\sigma_1^{\text{fast}}$ and $\Delta\sigma_1^{\text{slow}}$. Based on these results it is interesting to note that the total conductivity $\Delta\sigma_1^{\text{total}} = \Delta\sigma_1^{\text{slow}} + \Delta\sigma_1^{\text{fast}}$ is roughly equal to $\Delta\sigma_1^{\text{fast}}$ in the high fluence limit where only the M_1 to R process is occurring. This indicates that under our experimental conditions in order to achieve a THz conductivity comparable to the high-temperature R phase, sufficient photo-excitation is required such that the M_1 to R CPT occurs. This directly answers the question: is there a "structural bottleneck" in the IMT phase transition?

The TRTS measurements are analyzed in a similar manner using a Bruggeman effective medium model [145] in the limit where the material is mostly metallic ($F_{\mathcal{M}} + F_R \rightarrow 1$). The conductivities determined from the TRTS measurements presented in Fig. 3–18. $\Delta\sigma_1^{\text{fast}}$ and $\Delta\sigma_1^{\text{slow}}$ form two contributions to the an effective medium for which the Bruggeman model states

$$F_R \frac{\Delta\sigma_1^{\text{fast}} - \sigma_e}{\Delta\sigma_1^{\text{fast}} + 2\sigma_e} + F_{\mathcal{M}} \frac{\Delta\sigma_1^{\text{slow}} - \sigma_e}{\Delta\sigma_1^{\text{slow}} + 2\sigma_e} = 0, \tag{3.18}$$

where σ_e is an *effective* conductivity of the heterogeneous material. Due to the time-resolution provided by the TRTS data, we have access to all conductivity terms, since we temporally distinguish between σ_1^{fast} and σ_1^{slow}, and σ_e is simply the total measured conductivity (after 10 ps). In the high-fluence limit, we use (3.18) to compute $F_{\mathcal{M}}$ which is shown in FIG. 3–18 b). We find that this yields a result consistent with what was determined using the UED measurements in the high-fluence regime.

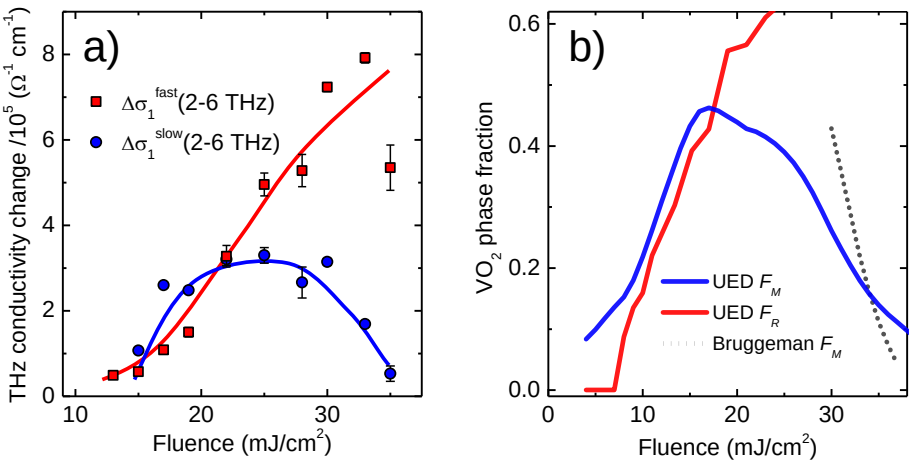

Figure 3–18: Terahertz conductivity fluence dependence
a) Fluence dependence of the fast $\Delta\sigma_1^{\text{fast}}$ and slow $\Delta\sigma_1^{\text{slow}}$ components of the transient terahertz optical conductivity (red and blue respectively). Solid lines serve as a guide to the eye. $\Delta\sigma_1^{\text{fast}}$ increased steadily and corresponds to the formation of R crystallites and $\Delta\sigma_1^{\text{slow}}$ attains a maximum at 25 mJ/cm^2 and corresponds to the formation of $\mathcal{M}$ crystallites. Error bars represent the error given by the fitting routine. b) Structural phase fraction model results determined from the ultrafast electron scattering data. The $\mathcal{M}$ phase fraction is maximal around 20-25 mJ/cm^2 in agreement with the THz conductivity shown in a).

The TRTS results can examined in another manner which nicely shows the temporal evolution of the IMTs as the fluence is increased. Figure 3–19 a) shows a high-temporal resolution measurements of the normalized conductivity change $\Delta\sigma_1/\Delta\sigma_1^{\text{max}}$. At the lowest fluence reported, 8.8 mJ/cm^2, the conductivity response is very fast, effectively time-resolution limited and a small recovery occurs within roughly 500 fs. This is consistent with previous THz studies in the low-fluence regime [99, 101, 100]. This corresponds primarily to the rapid transient metallization due to the promotion of electrons to the conduction band by photo-excitation and is well understood as a Mott-Hubbard like response. It should be notes that the magnitude of $\Delta\sigma_1^{\text{max}}$ at 8.8 mJ/cm^2 is roughly 10 times smaller than $\Delta\sigma_1^{\text{max}}$

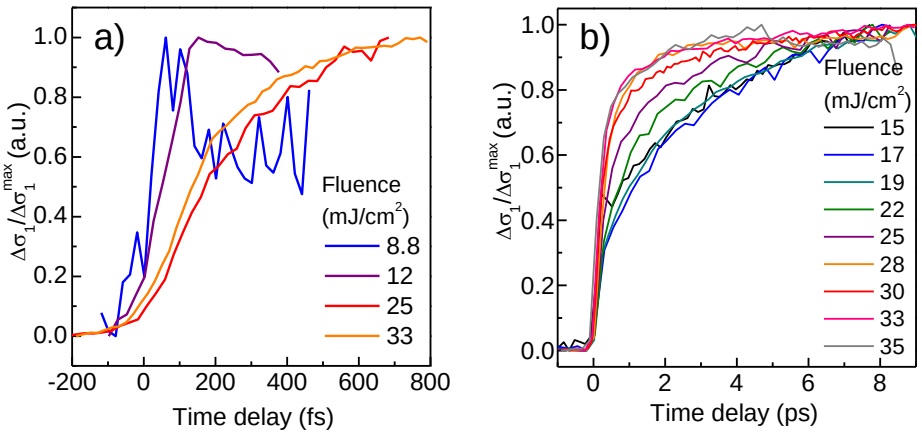

Figure 3–19: Normalized time-resolved terahertz spectroscopy time traces for various fluences
a) Photo-induced conductivity within a 1 ps window. At lowest fluences the transient conductivity is described by a resolution limited rise (much smaller in magnitude compared to the higher fluence measurements) followed by a small recovery. At higher fluences the photo-induced conductivity follows the M_1 to R CPT timescale. b) Photo-induced conductivity within a 10 ps window, with traces normalized to demonstrate the evolution of the bi-exponential character.

at 12 mJ/cm^2 which is above the CPT threshold fluence. The small recovery found in the 8.8 mJ/cm^2 trace shown in Fig. 3–19 a) is relaxation of the exited carriers in the $\mathcal{M}$ phase. At fluences well above the CPT threshold, (25 an 33 mJ/cm^2 in Fig. 3–19 a)) demonstrate a qualitatively slower time-scale indicating clearly that the onset of metallic behaviour is established by the M_1 to R CPT transition. In other words the electronic response follows the structural response of the material. Over a time interval spanning up to 10 ps, the role of the slower M_1 to R transition is evident. All fluences ranging up to 35 mJ/cm^2 the bi-exponential character of the THz conductivity response is clearly oberved. At lower fluences (15-22 mJ/cm^2 shown in Fig. 3–19 b)) the transition is dominate by the slow process and at high fluences the fast process is nearly exclusively observed in the measurement. In

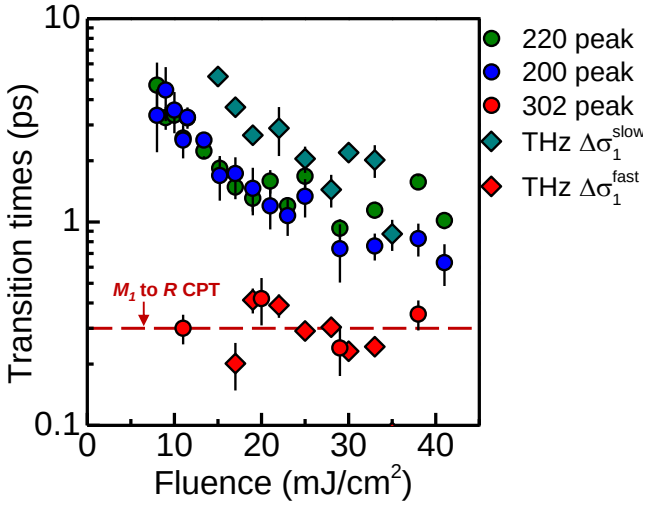

Figure 3–20: Time constants for the photoinduced phase transitions in VO_2. Shown as circles are the slow ((200) blue, (220) green) and fast ($30\bar{2}$, red) peak dynamics as determined from the UED measurements. Not all fluences were carried out with sufficient time resolution to resolve the fast dynamics, thus certain data points are not shown. TRTS measured time constants pertaining to the slow and fast components of σ_1 are depicted by turquoise and red diamonds respectively. The red dashed line represents the temporal region (300 ± 150 fs) associated with the photo-induced structural phase transition from $M_1 \rightarrow R$ which dominates at high pump fluence. The slow time constants general demonstrate an exponential dependence on fluence.

the following section we will investigate in greater detail the fluence dependent behaviour of the IMT times in terms of a kinetic model.

3.8 Structural transition kinetics

The $M_1 \rightarrow R$ and $M_1 \rightarrow \mathcal{M}$ transitions exhibit qualitatively different kinetic behavior as evidenced by the fluence dependence of the time constants τ_{fast} and τ_{slow} obtained from both UED and TRTS (Fig. 3–20). The time constant for the $M_1 \rightarrow R$ transition (τ_{fast}), captured by the dynamics of the ($30\bar{2}$) peak in the UED measurements and by τ_{fast} in the THz measurements, is 350 ± 100 fs *independent* of fluence. This demonstrates that photo-induced $M_1 \rightarrow R$ transition – the melting of the periodic lattice distortion and CPT

transition – is *non-thermal* and barrier free. This is inferred from the observed fact that the transition rate is independent from the driving excitation strength. The results for the R–phase volume fraction (Fig. 3–16) also show that the excitation threshold for this non-thermal phase transition is heterogeneous in the films since not all crystallites switch from M_1 to R at a fluence of 8 mJ/cm^2. The crystallites only start switching at this point and an increasing proportion of them convert as the fluence is augmented. What is consistent however is the rate and therefore time-constant extracted for this process. These facts are supported by previous observations of the inhomogeneous threshold using ultrafast electron microscopy [146] and others by nanoscopy [140, 141].

The $M_1 \rightarrow \mathcal{M}$ time constant, conversely, decreases significantly with pump fluence as seen in the (200) and (220) peak dynamics from UED and the τ_{slow} from TRTS. The exponential increase in the $M_1 \rightarrow \mathcal{M}$ rate with excitation energy deposited in the electron system strongly suggests that the $M_1 \rightarrow \mathcal{M}$ is an activated process, *i.e.* there exists an energy barrier which the system must overcome in order to realize the phase transition. We can extract the activation energy E_A from this data by determining the electronic excitation energy per unit cell E deposited in the sample as a function of pump fluence. We may apply the Eyring-Polanyi equation from transition state theory [147] which is given by

$$\ln\left(\frac{h\tau_{\text{slow}}^{-1}}{k_B T_e}\right) = -\frac{E_A}{k_B T_e} + \frac{\Delta S^{\ddagger}}{k_B}, \tag{3.19}$$

where $\Delta S^{\ddagger}$ is the entropy of activation and T_e is an effectice temperature of the source which receives the photo-excitation energy. We will treat this temperature as the electron temperature.

3.8.1 Optical energy absorption

We follow the prescription shown in [148] which uses the Fresnel equations to determine the energy deposited in a thin film resting on a substrate. The 50 nm thick VO_2 sample is

on top of a 40 nm SiN_x substrate which is illuminated by a beam with fluence $\mathcal{F}$ (normal incidence is assumed). The complex index of refraction for VO_2 is $\tilde{n} = 2.9 + i0.5$ [97, 149] and $n = 2.0$ for SiN_x. We determine the absorption to be $\mathcal{A} = 0.222$ at 800 nm. VO_2 has a unit cell volume of $V_{\text{unit-cell}} = 117$ Å^3 and the number of unit cells in the sample is $N = V_{\text{sample}}/V_{\text{unit-cell}}$. The energy deposited per unit cell is given by

$$\varepsilon(\mathcal{F}) = \frac{\mathcal{A}}{N}\mathcal{F}\ A_{\text{sample}}, \tag{3.20}$$

where A_{sample} is the area of the sample on the substrate (250 μm by 250 μm).

3.8.2 Calculation of electron temperature

We must now understand how the deposited energy translates to an increase in the electron temperature within VO_2 following photo-excitation. This involves applying some type of model involving the electronic heat capactiy. In general, information about the electronic heat capacity $c_e(T_e)$ is difficult to extract in the vicinity of room temperature using conventional techniques, since the total heat capacity of the material is dominated by the lattice heat capacity. For strongly correlated electron system, information about the electronic heat capacity is even more scarce and must be determined through computational techniques. To first order, it is reasonable to model the photo-excited electrons using a free electron model, as this roughly describes their character after photo-excitation drives them into the conduction band. Within 300 fs following photo-excitation interactions between the photo-excited electrons causes them to thermalize to a common temperature T_e. This is often described as a *pseudothermal* electronic state and recent theoretical work has established this state to be a necessary prerequisite for the formation of the monoclinic metallic phase [149]. Since our results indicated that the $\mathcal{M}$ phase constitudes electronic restructuring of the valence charge exclusively we are interest in the rate of this process as a function of the electron temperature T_e.

We begin with $dE = c_e dT_e$, where E is the internal energy from photo-excitation acquired by the electrons, c_e is the electronic heat capacity, and T_e is the electron temperature. In the free electron model, $c_e = \gamma T_e$ where

$$\gamma = \frac{\pi^2 N_A k_B^2}{2E_F}, \tag{3.21}$$

where $E_F = \frac{\hbar^2}{2m_e}\left(3\pi^2 \frac{N}{V}\right)^{2/3}$ is the Fermi energy, with m_e the mass of the electron, and $N/V = n$ is the carrier density. Integration of $dE = c_e dT_e$ yields $E = \frac{\gamma}{2} T_{e,f}^2$ from which a final temperature $T_{e,f}$ can be computed from an initial temperature $T_{e,i}$ given an energy increase ΔE (photo-excitation). We have for $T_{e,f}$

$$T_{e,f} = \sqrt{\frac{2\Delta E}{\gamma} + T_{e,i}^2}. \tag{3.22}$$

Using Eqn. (3.22) along with the Eqn. 3.20 as ΔU, we may calculate $T_{e,f}$ for a set of physically plausible γ values (and therefore photoexcited carrier densities N/V). Figure 3–21 shows temperatures computed for carrier densities n ranging from 0.1 to 10 electrons per unit cell. These temperatures are then used in the Eyring-Polanyi equation given by Eqn. (3.19). Figure 3–21 shows various plots of $\ln\left(\frac{h\tau_{slow}^{-1}}{k_B T_e}\right)$ vs. $1/k_B T_e$ for various values of γ along with fits to Eqn. (3.19). We take the values of τ_{slow} for the (200) peak shown in Fig. 3–20 and plot $\ln\left(h\tau_{\text{slow}}^{-1}/E\right)$ vs. $1/E$ which is shown in the inset of Fig. 3–21. The results are tabulated in Table 3–1. For the model where the deposited energy $E = k_B T_e$, we find a lower limit to the activation energy of $E_A = 304 \pm 109$ meV, which is similar to the value found for a photo-excited carrier density of $n = N/V = 0.1$ e^-/unit cell using Eqn. 3.22 in a free electron heat capacity model. For realistic photo-excited carrier densities up to $\sim$ 1 e^-/unit cell the value of the activation energy is roughly 700 meV (see Fig. 3–21 and Table 3–1).

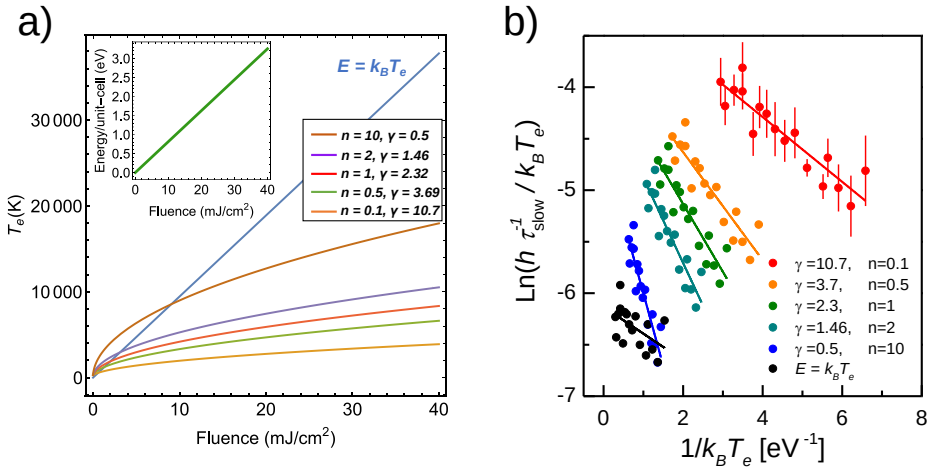

Figure 3–21: Kinetics of the $M_1 \rightarrow \mathcal{M}$ phase transition.
a) Calculations of the electron temperature created by photo-excitation using the absorption properties of VO_2 within a simple free-electron model. b) Various plots of $\ln\left(h\tau_{slow}^{-1}/k_B T_e\right)$ vs $1/k_B T_e$ for various electron temperatures T_e computed using a free electron heat capacity model and $E = k_B T_e$.

		E_A (meV)
$E = k_B T_e$		304 ± 109
N/V (e^-/ unit cell)	γ (mJ/mol K^2)	
0.1	10.7	315 ± 36
0.5	3.69	524 ± 61
1.0	2.32	659 ± 77
2.0	1.46	828 ± 97
10	0.50	1410 ± 165

Table 3–1: Results for the activation energy E_A determined using the Eyring-Polanyi equation for various electron temperatures T_e.

This analysis speaks to a fundamental property of the photo-induced $M_1 \rightarrow \mathcal{M}$ transition, namely, that it is an activated transition because the rate dependes on the energy drive. Furthermore we find that the fluence required to deposit E_A per unit cell is $\mathcal{F} \approx 3.7$ mJ/cm^2, which is the value previously attributed to the $M_1 \rightarrow R$ IMT threshold [123, 99]. This is also in agreement with the fluence threshold extracted from the low fluence data points in Fig. 3–6 a). This fact offers a clear explanation as to why metallic character what measured below the CPT threshold.

3.8.3 Comparison with theoretical work

Recent calculations performed by He and Millis [149] provide a convincing description of the photo-induced IMT and the metastable monoclinic metallic phase. Their computational approach begins by solving for the relaxation dynamics of the photo-excited electron distribution in a quantum-Boltzmann equation (QBE) methodology. They demonstrate that the electron distribution forms a *pseudothermal* state at an elevated temperature due to photo-excitation and that this is a precursor for a sequence of "soft-band" effects wherein the magnitude of the optical varies significantly. They demonstrate that the shifts in the various bands of VO_2 arise from pronounced changes to the Hartree-Fock interaction term which includes the onsite interaction U and intersite interaction V due to $d-d$ orbital exchange. They calculate the change in the free energy of the non-equilibrium VO_2 system and determine two minima as a function of the number of electrons in the V–3d_{xz} orbital. They show that this feature is robust for a range of realistic U and V interaction parameters.

He and Millis also compute the new valence band partial density of states (see Fig. 3–22) which reveals that bands formed by the V–3d_{xz} and O–2p orbital states fall over the Fermi level, eliminating the gap. They vary the magnitudes of the U and V parameters assumed in their calculations they show that the $\mathcal{M}$ phase can only arise for a U interaction

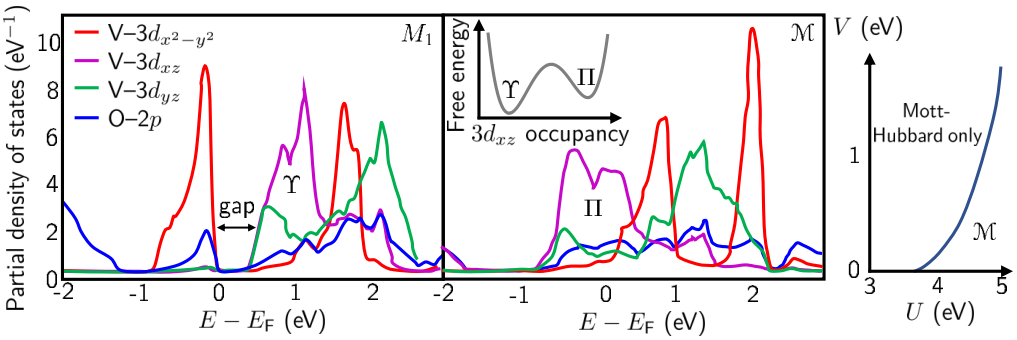

Figure 3–22: Calculated partial density of states for insulating monoclinic M_1 and monoclinic metal $\mathcal{M}$ phase adapted from He and Millis [149].
Band overlap at the Fermi level is driven by the occupancy of the V–3d_{xz} orbital which corresponds to a free energy minima. This minima is attainable for certain onsite (intradimer) U correlation energies and intersite ($d - d$ orbital) exchange energies (far right).

term above roughly 3.5 eV, and that V must be weaker. When the $\mathcal{M}$ phase cannot be formed because of these parameters, the behavior of the IMT falls into a Mott-Hubbard like response where transient screening collapses the gap, but it quickly recovers as the electrons cool. They focus on U and V values of 4.5 and 0.6 eV respectively and for this they show that the band closes (and stays closed) for a pseudothermal electron temperature of $\sim$ 220 meV and energy per unit cell of $\sim$ 700 meV. These numbers are in excellent qualitative agreement with our results in section 3.8.

3.8.4 Free energy landscape

We have demonstrated that photoexcitation of M_1 VO_2 yields a complex, heterogeneous, multi-phase film whose structure and properties are both time and fluence dependent. The character of the fluence dependent transformation is summarized in Fig. 3–23. At pump fluences below $\sim$ 4 mJ/cm^2 there is no long-lived ($>$ 1 ps) transformation of the M_1 structure, and VO_2 behaves like other Mott insulators insofar as optical excitation induces a relatively small, impulsive increase in conductivity followed by a complete

recovery of the insulating state [101, 100, 5, 104]. Above $\sim$ 4 mJ/cm^2, however, photoexcitation stimulates a phase transition in the electron system that stabilizes metallic properties through an orbitally selective charge re-organization: the $\mathcal{M}$ phase. Between $\sim$4-8 mJ/cm^2 photoexcitation exclusively yields the $\mathcal{M}$ phase, which populates 15–20% of the film by 8 mJ/cm^2. In this fluence range, time-resolved photoemission experiments show a complete collapse of the band gap [104], TRTS experiments show a dramatic increase in conductivity [101, 100] and optical studies show large changes in the dielectric function [97, 102, 129], all of which are persistent, long-lived and characteristic of a phase-transition. Given the nature of the equilibrium phase diagram, these observations were interpreted mostly as evidence of the $M_1 \rightarrow R$ transition. The $M_1 \rightarrow R$ transition, however, exhibits a minimum fluence threshold of $\sim$8–9 mJ/cm^2 consistent with surface sensitive experiments [98, 146] and coherent phonon investigations [102]. Above 8 mJ/cm^2 photoexcitation yields a heterogeneous response with both $\mathcal{M}$ and R phase fractions increasing with fluence to approximately 20 mJ/cm^2 where each phase occupies $\sim$ 50% of the film. At higher fluences $M_1 \rightarrow R$ dominates and the $\mathcal{M}$ phase occupies a decreasing proportion of the film. Our measurements are ensemble averaged over the probe volume, and are thus not sensitive to the spatial detail of this heterogeneity. Spatially resolved studies have indicated M_1 and R phase separation on length scales of 50–100 nm [146, 141, 140] which is on the order of the average crystallite size in our samples. Given this, and the fact that it would be energetically unfavorable to have a mixture of M_1 and R phases for reasons related to strain we believe that M_1 and R phase coexistence within a single crystallite to be unlikely. Phase coexistence between M_1 and $\mathcal{M}$ however, since they share the same crystal structure, could be occurring and would be interesting to investigate with sensitive spatially-resolved techniques.

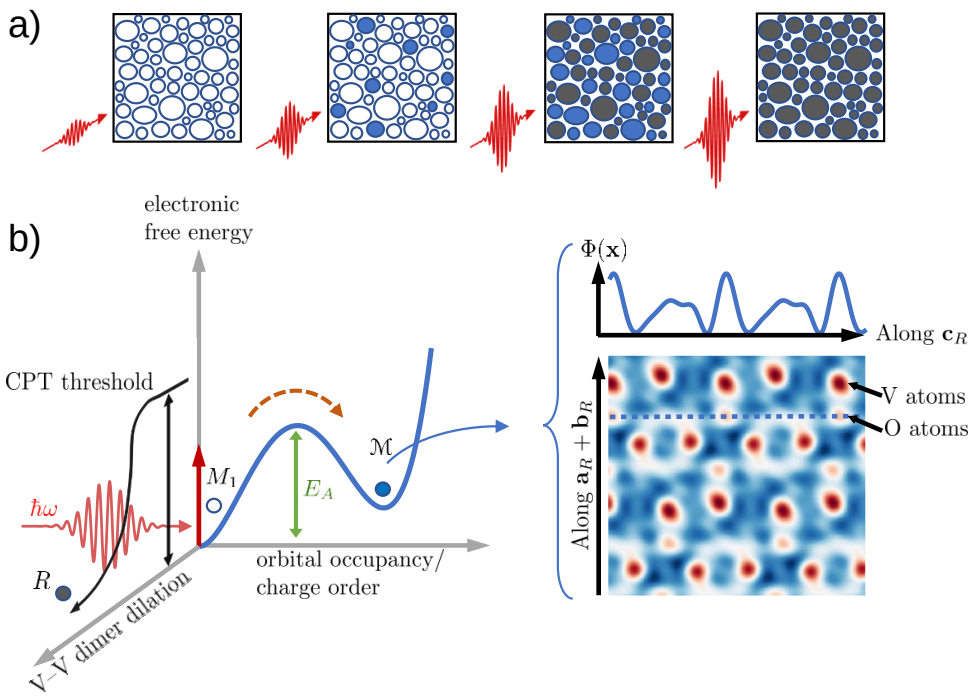

Figure 3–23: Illustration of photo-induced IMTs and the electronic free energy landscape a) Schematic illustration of the heterogeneous sample response of VO_2 as a function of fluence. At low-fluence the material undergoes neither IMT, the transient response of the metal is Mott-Hubbard like, rapid metallization from hot excited carriers, but followed by complete recovery within roughly 1 ps. At stronger fluences, above 4 mJ/cm^2 the monoclinic metal ($\mathcal{M}$) phase is formed. At intermediate fluences (roughly 8-30 mJ/cm^2) both the $\mathcal{M}$ and rutile R are formed among different crystallites in the material. In this high fluence limit (>30 mJ/cm^2) the R phase forms exclusively. b) Illustration of the electronic free energy landscape of photo-excited VO_2. The M_1 to $\mathcal{M}$ transition is thermally activated over an energy barrier E_A. The M_1 to R forms if a critical electron excitation density is reached, which leads to the CPT and rapid dimer dilation.

3.8.5 Discussion

Non-thermal melting as a route to the control of material structure and properties with femtosecond laser excitation has been known for some time and there are examples

in several material classes. Much more novel is the ($M_1 \rightarrow \mathcal{M}$) which has no equilibrium analog and represents a new direction for using optical excitation to control the properties of strongly correlated materials. The $M_1 \rightarrow \mathcal{M}$ is thermally activated and does not involve a significant lattice structural component, representing a phase transition in the electron (valence charge) system alone. Our results are consistent with the recent computations of He and Millis [149] which indicate that an orbital selective first-order transition can be driven in M_1 VO_2 through the increase in electron temperature following femtosecond laser excitation. This transition depletes the occupancy of the V–3$d_{x^2-y^2}$ band that is split by the V–V dimerization in favor of the V–3d_{xz} band that mixes strongly with the O–2p orbitals due to the anti-ferroelectric tilting of the V–V dimers (3–11 (d)). The M_1 band gap collapses along with this transition yielding a metallic phase. The three salient features of this picture are in agreement with our observations: thermal activation on the order of 100 meV, orbital selection and band gap collapse to a metallic phase. Of interest is the fact that depletion of the V–3$d_{x^2-y^2}$ band where states are expected to be localized on the V–V dimers does not seem to significantly lengthen the V–V dimer bond. The question arises whether this phenomena can be entirely understood inside a picture that treats M_1 VO_2 as a d^1 system, or whether more than a single V–3d electron is involved as DMFT calculations suggest [116]. Such DMFT results from Weber [116] suggest that M_1 VO_2 is a paramagnetic metal with anti-ferroelectric character, like that shown in Fig. 3–11 (d).

3.9 Conclusion

In this chapter, detailed time-resolved measurements of thin-film VO_2 were presented. Ultrafast electron diffraction measurements tracked the structural evolution of the sample at the atomic level during the 20 ps time interval following photo-excitation with 800 nm ultrafast laser pulses. During this period, the sample demonstrates a heterogeneous response as a function of photo-excitation comprising two distinct and independent phase

transitions. One of the transitions, is the expected and well-studied change in crystal symmetry (atomic lattice coordinates) where the low-temperature, structurally distorted (V–V dimers) M_1 phase transitions to the high-temperature R phase. This processes occurs at fluences above 8 mJ/cm^2 with an increasing proportion (phase fraction) of the sample undergoing the transition with increasing photo-excitation fluence. Furthermore, the time-constant for this transition is roughly 300 fs and independent of fluence. The second transition is more novel, and involves a redistribution of valence charge in the M_1 sample which maintains crystal symmetry but acquires metallic properties. This transition occurs at lower fluences ($\sim$3 mJ/cm^2) and transpires at a quantitatively slower timescale than the $M_1 \rightarrow R$ transition and is dependent on fluence. Analysis of the time-dependent diffraction patterns reveal an anti-ferroelectric charge order along Oxygen atoms situated closest to the Vanadium atoms. This picture and the nature of the transition to this monoclinic metallic $\mathcal{M}$ phase is consistent with theoretical results describing the transition in terms of a change in V–3d_{xz} orbital occupancy.

Complementary time-resolved terahertz spectroscopy measurements show excellent agreement with the ultrafast electron diffraction results. Time-dependent photo-conductivity measurements of the VO_2 sample show the onset of metallic behaviour with two distinct timescales. The timescales found here are in agreement with the $M_1 \rightarrow R$ and $M_1 \rightarrow \mathcal{M}$ time constants extracted from the diffraction measurements. From these measurements, the conductivity component of the $\mathcal{M}$ phase is determined and found to be roughly 1/3 that of the R phase conductivity. This is an important result, as it helps address a long-standing question about VO_2; is there a structral bottleneck to the photoinduced IMT? Our results indicate clearly that the extent to which the photo-excited film can be made metallic *without* changing the crystal symmetry is only 1/3 that of the equilibrium R phase. This fact will have consequences for ultrafast electronic devices based on VO_2.

The combination of ultrafast electron diffraction and time-resolved terahertz spectroscopy have yielding a consistent picture of photo-induced phase transitions in VO_2 and should be very informative for other strongly-correlated materials which demonstrate complex phenomena such as insulator-metal transitions.

CHAPTER 4
Photo-induced phonon hardening in titanium diselenide

Exotic phenomena and emergent material properties can arise in materials possessing reduced dimensionality. Such materials are often called "low-dimensional" and many of them exhibit enhanced interactions and symmetry breaking processes that drive novel phase transitions. Transition metal dichalcogenides (TMDCs) [150, 151, 152, 153], are layered compounds which have complex in-plane physics arising from their two-dimensional character, high-anisotropy and in some cases significantly weaker out-of-place forces. These materials are a very active research area because of their rich condensed matter physics [154] and broad range of applications in optoelectronric devices [150, 151]. Many TMDCs undergo *charge-density wave* (CDW) transitions [155], where the ground state of the system consists of a periodic modulation of charge density determined by the Fermi wavevector k_F. In a *commensurate* charge-density wave system, there is corresponding modulation of the lattice constant(s) with a matching period. For an *incommensurate* charge-density wave system, the periodicity of the associated lattice distortion does not match that of the charge density.

As a general rule, the CDW transition is a consequence of enhanced electron-phonon interactions enabled by the reduced dimensionality of the material. There are two mechanisms which can lead to the CDW phase. The first is *Fermi-surface nesting* where the Fermi-wavevector of conduction electrons connects many different points on the Fermi-surface. The second is more conventional electron-phonon coupling, which mediates a transition to a more stable phase through energy exchange to a CDW. Both the electronic and phononic spectra of the materials are strongly modified as the system tends toward and

passes into the CDW phase. The electron gas describing the conduction electrons in a 1-dimensional system acquires divergences its electronic susceptibility $\chi(\mathbf{q}, T)$ at a particular wave-vector $q = 2k_F$ [43]. This effect is also known as the Kohn anomaly [156]. As a result, electron screening effects at this point in momentum space lead to a re-normalization of the frequency of a phonon $\omega_{q,\mathrm{ren}}$ which tends to $\omega_{q,\mathrm{ren}} \to 0$ at a finite temperature corresponding to the CDW transition, T_{cdw}. This "frozen-phonon" component of a CDW transition is a common feature found in many CDW materials such as $NbSe_2$ [157], $ZrTe_3$ [158], $TbTe_3$ [159], $NbSe_3$ [160] and $TiSe_2$ [161]. In this picture the periodic lattice and charge modulations arise simulatenously when the phonon frequency becomes zero at the point in reciprocal space where the Kohn anomaly occurs. A specific question which remains in certain cases is: what are the microscopic processes contributing to the lattice ordering vector(s) associated with a CDW transition? In considering only the effect of $\chi(\mathbf{q}, T)$, complete phonon softening ($\omega_{q,\mathrm{ren}}(T = T_{\mathrm{cdw}}) = 0$) through electronic screening effects only occurs in the situation of so-called *perfect nesting*, which means all points on the Fermi-surface can be connected by the same wave-vector magnitude. This is only exactly true in 1-dimensional systems, roughly true in certain special 2-dimensional systems depending on the Fermi surface topology (graphite [162] for example), but seldom true in many TMDCs which demonstrate the CDW phase transition [163, 157]. An excellent discussion of Fermi surface nesting and its relations to CDW phase transitions can be found in the paper of Johannes and Mazin [164].

The TMDC material studied in this chapter is titanium diselenide ($TiSe_2$) which has a bulk CDW transition at $T_{\mathrm{cdw}} = 188$ K [165]. $TiSe_2$ has been extensively studied theoretically since the 1970s [166]. Accurate computation of the electronic and phononic band structures in both the high-temperature semi-metallic and low temperature insulating (CDW) phases is challenging. X-ray studies of the phonon system have clearly revealed

and characterized the soft phonon behaviour in $TiSe_2$ [161, 163] and strongly suggested the presence of a divergent electronic susceptibility and a Kohn anomaly. These results will be discussed further in sec. 4.4. $TiSe_2$ is an example of a CDW material whose Fermi surface does not exhibit nesting [167]. Therefore, the divergent character of χ must depend on other aspects of the interacting electron and phonon systems. Time-resolved and angle-resolved photo-electron spectroscopy (ARPES) experiments have been conducted to learn about the behaviour of the electron system [168, 169, 170], by examining in detail the behavior of the valence and conduction bands with momentum resolution within the Brillouin zone. These results motivated a description of $TiSe_2$ as an *excitonic insulator* [171, 172, 173] which emerges from an indirect bandgap combined with electron-phonon coupling across the narrow gap yielding bound excitonic states which sustain insulating character throughout the material. However, other mechanisms for the CDW transition such as a band Jahn-Teller effect [174] have been proposed and remain plausible. Time-resolved measurements have examined non-thermal melting and recovery of the CDW phase using various spectroscopic techniques to glean information about electron-phonon and electron-hole coupling [175, 176, 177, 178]. These ARPES measurements, however, lack direct sensitivity to the phonon system, which is a necessary ingredient for a complete understanding of χ and the CDW transition in $TiSe_2$.

In this chapter, ultrafast electron diffuse scattering of single crystal 70 nm $TiSe_2$ are presented. Ultrafast electron scattering provides a direct time and momentum resolved view of the phonon system. The measurements are carried out at room temperature so that the sample is well away from the CDW transition temperature. The sample is photo-excited with 800 nm laser pulse which drives interband transitions in the $M - L - M$ region of reciprocal space where hole-pockets in the band-structure are found. Unexpectedly, measurements of the time-dependent diffuse scattering intensity reveal, for

the first time in the time-domain, the instantaneous hardening of the transverse optical phonon at the expected region of the Brillouin zone. The wave-vector of this phonon matches the ordering vector of the CDW phase. This novel effect indicates the presence of an electronic susceptibility divergence responsible for soft-mode behaviour in $TiSe_2$ and manifests as a rapid reduction in diffuse intensity occurring over an impulse-response-limited ∼150 fs timescale. Following this effect, is a recovery and increase of diffuse signal due to expected overall lattice heating. This slower, secondary effect, is consistent in terms of time-scale with the suppression of the Bragg peaks due to the Debye-Waller effect. The results presented in this chapter are an important new account of how ultrafast electron diffuse scattering quantities can be used to measure not only changes in phonon occupancy but also changes in phonon frequency. It is demonstrated that ultrafast electron diffuse scattering reports on the re-normalization of phonon frequencies resulting from optical modulation of $\chi(\mathbf{q})$ due to electron screening in addition to energy transfer between the electron and phonon systems.

4.1 Electronic susceptibility

Before proceeding with the discussion of the experimental results, some basic notions pertaining to the electronic susceptibility in a low-dimensional material are presented. Consider the microscopic electrostatic potential of the material given as

$$\phi(\mathbf{r}) = \int d\mathbf{q}\ \phi(\mathbf{q}) \exp\left(i\mathbf{q}\cdot\mathbf{r}\right), \tag{4.1}$$

where the Fourier transform of the microscopic potential in momentum space is $\phi(\mathbf{q})$ [43]. Consider now a homogeneous electron gas (*i.e.* a Fermi gas, which is an accurate approximation for conduction band electrons in this case) subject to the potential $\phi(\mathbf{q})$. A corresponding induced charge density given as $\rho^i(\mathbf{q})$ will be determined in the static linear

response regime by the electronic susceptibility $\chi(\mathbf{q})$ according to

$$\rho^i(\mathbf{q}) = \chi(\mathbf{q})\phi(\mathbf{q}). \tag{4.2}$$

Equation (4.2) describes the response of the conduction electron system to the presence of the lattice ions (and bound valence electrons). $\chi(\mathbf{q})$ thus strongly influenced by the microscopic bonding environment of the material. In general, the quantities can be easily recast to include a time-dependence (or frequency dependence), but this is not necessary in our situation, since within the temporal resolution of the instrument ($\sim$ 100 fs) the evolution of the quantities in Eqn. (4.2) may be treated as static.

4.1.1 Lindhard susceptibility function

For metals, the complete form of the electronic susceptibility was established in the 1950s by Lindhard [179, 180, 181, 42, 43] and is given in d dimensions by

$$\chi_d(\mathbf{q}, \omega, T) = \int \frac{d\mathbf{k}}{(2\pi)^d} \frac{f(\epsilon_{\mathbf{k}+\mathbf{q}}, T) - f(\epsilon_{\mathbf{k}}, T)}{\hbar\omega + \epsilon_{\mathbf{k}+\mathbf{q}} - \epsilon_{\mathbf{k}}}, \tag{4.3}$$

where $f(\epsilon_{\mathbf{k}}, T)$ is the Fermi-Dirac distribution function, $\epsilon_{\mathbf{k}}$ are the electronic energies for states with wavevector $\mathbf{k}$, and T is the absolute temperature. The frequency ω is important in the dynamic case, when the potential is time-dependent ($\phi(\mathbf{q}, \omega)$). In the static limit, $\omega \to 0$, and for the integration only values up to k_F are required, since the distribution functions vanish shortly above. Following some algebra, the following expression is obtained [181]

$$\chi_d(\mathbf{q}, T) = -\frac{2k_F^2}{\epsilon_F} \int_{k \le k_F} \frac{d\mathbf{k}}{(2\pi)^d} \frac{2q^2}{q^4 - 4\left(\mathbf{k}\cdot\mathbf{q}\right)^2}. \tag{4.4}$$

For the case of $d = 2$ dimensions the expression becomes

$$\chi_2(q, T) = -\frac{k_F^2}{\pi^2\epsilon_F} \int_0^{k_F} dk k \int_0^{2\pi} \frac{d\varphi}{q^2 - 4k^2\cos^2\varphi}, \tag{4.5}$$

$$= -\frac{2k_F^2}{\pi^2\epsilon_F} \left[1 - \Theta\left(q - 2k_F\right)\sqrt{1 - \left(2k_F/q\right)^2}\right], \tag{4.6}$$

where Θ is the Heaviside step function. The character of the step function imposes a discontinuity in χ which can be a precursor to a divergence depending on other interactions in the material. The behaviour of the electrons in the vicinity of $2k_F$ are strongly affected by χ as is in turn the relation between $\rho^i(\mathbf{q})$ and $\phi(\mathbf{q})$.

4.2 Soft modes and the charge density wave transition: the Fröhlich model

As mentioned above, highly anisotropic materials often have CDW transitions which emerge through extreme instances of electron-phonon coupling. This strong coupling plays a role in conjuction with the electronic susceptibility and other material properties which vary considerably along different crystal axes. In a material, a fully second-quantized Hamiltonian of free electrons with wavevector states k and phonons of momentum k' coupled by an anisotropic (wave-vector dependent) coupling $g_{k'}$ is described by the Fröhlich Hamiltonian [43, 182]

$$\mathcal{H} = \sum_k \epsilon_k a_k^\dagger a_k + \hbar \sum_{k'} \omega_{k'} b_{k'}^\dagger b_{k'} + \sum_{k,k'} g_{k'} a_{k+k'}^\dagger a_k \left(b_{-k'}^\dagger + b_{k'} \right). \tag{4.7}$$

In Eqn. 4.7 above, $a_k^\dagger$ ($b_{k'}^\dagger$) and a_k ($b_{k'}$) are the creation and anhilliation operators for the electrons (phonons). In a Heisenberg picture, the equations of motion for the atoms described by normal coordinates $\mathcal{Q}_{k'}$ are determined by solving $\hbar^2 \ddot{\mathcal{Q}}_{k'} = -\left[\left[\mathcal{Q}_{k'}, \mathcal{H} \right], \mathcal{H} \right]$. This is achieved by using the definition of momenta $P_k = \sqrt{\hbar M \omega_q / 2} \left(b_{k'}^\dagger - b_{-k'} \right)$ along with the commutation relation $[\mathcal{Q}_i, P_j] = i\hbar\delta_{ij}$, which gives

$$\ddot{\mathcal{Q}}_{k'} = -\omega_{k'}^2 \mathcal{Q}_{k'} - g_{k'} \sqrt{\frac{2\omega_{k'}}{M\hbar}} \sum_k a_{k+k'}^\dagger a_k, \tag{4.8}$$

where the sum term $\sum_k a_{k+k'}^\dagger a_k$ is in fact charge density in the volume element k' which we denote as $\rho_{k'}$. It follows from Eqn. (4.2) that this is related to $\chi(k', T)$ through the potential $\phi_{k'}$. In a quasi-mean field approach the potential can be written as $\phi_{k'} = g_{k'} \sqrt{2M\omega_{k'}/\hbar} \mathcal{Q}_{k'}$ [155], because it describes a relative displacement amplitude, and scales

with the coupling strength. Using these notions, Eqn. 4.8 becomes

$$\ddot{\mathrm{Q}}_{k'} = -\left[\omega_{k'}^2 + g_{k'}^2 \frac{2\omega_{k'}}{\hbar}\chi(k',T)\right] \mathrm{Q}_{k'}, \tag{4.9}$$

where the term in the square brackets describes the re-normalization (r) of the phonon frequency $\omega_{k'}$ due to electron screening ($\chi(k')$) and electron-phonon coupling $g_{k'}$. Equation (4.9) describes harmonic motion of the atoms due to the phonon with re-normalized frequency given by

$$\frac{\omega_{k',\mathrm{r}}^2(T)}{\omega_{k',0}^2} = 1 + \frac{2g_{k'}^2}{\hbar\omega_{k',0}}\chi(k',T). \tag{4.10}$$

As the system is cooled toward the CDW transition temperature T_{cdw}, the phonon frequency is reduced (softening) and achieves a minimum at T_{cdw} where the lattice symmetry changes and the charge density wave forms. It will be shown later, that the behaviour of Eqn. (4.10) directly impacts the time-resolved electron scattering intensity.

4.3 Properties of $TiSe_2$

In this section, the essential properties of titanium diselenide will be presented. The type of crystalline $TiSe_2$ which are measured in this work is $1T-TiSe_2$, where $1T$ refers to the stacking order of 1 layer per trigonal unit cell. The lattice parameters are $a = b =$ 3.536 Å and $c = 6.004$ Å with a symmetry group of $P\bar{3}m1$. The real-space unit cell is shown in Fig. 4–1 a) along with the lattice vectors. The Brillouin zone of $TiSe_2$ is shown in Fig. 4–1 b) illustrating the zone center at Γ along with various other high-symmetry points.

The phonon and electronic band structures of TiSe2 are shown in Fig. 4–2. In general detailed and accurate calculations of the band structures are tedious and computationally intensive [183, 184, 185, 186, 187]. The semi-metallic character of high-temperature $TiSe_2$ has been established for some time [166]. Photo-excitation with 800 nm (1.55 eV) drives interband transitions at the M and L regions of the Brillouin zone, where electron pockets

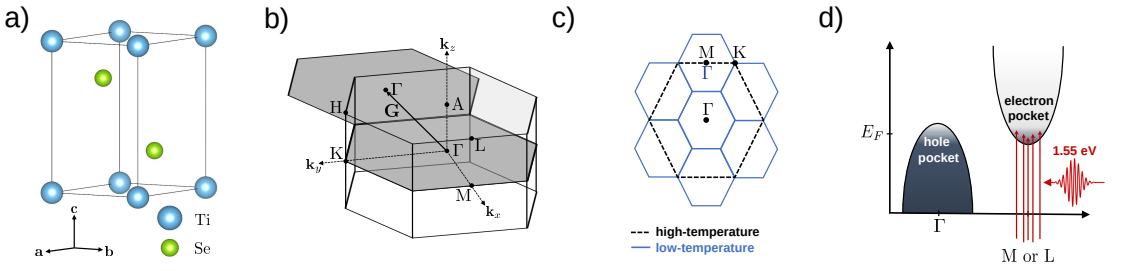

Figure 4–1: Structural properties of 1T-$TiSe_2$.
a) Unit cell of layered 1T-$TiSe_2$ showing the Ti and Se atoms and basis crystal lattice vectors. b) Brillouin zone of $TiSe_2$ in reciprocal space. A reciprocal lattice vector **G** connects different zone centers (Γ points). High-symmetry points are indicated by M, K, H, A and L. c) Hexagonal Brillouin zones of the high and low-temperature phases indicating the reduction of zone by one-half (in the Γ–M plane). d) Schematic illustration of photo-excitation of $TiSe_2$ at room temperature. Interband transitions are driven at the M and L points of reciprocal space to regions of a partially filled conduction band.

exists below the Fermi-level. These high-symmetry points of the Brillouin zone are of particular interest because they correspond to momenta of the CDW ordering vector and are where phonon softening is expected to occur.

When $TiSe_2$ undergoes the transition to the CDW phase, the lattice parameters double in all three directions, *i.e.* the unit cell transforms from $a \times a \times c \rightarrow 2a \times 2a \times 2c$. This differs from most other TMDCs where the CDW phase forms only in the plane perpendicular to c. In reciprocal space, the unit cell volume reduces as shown in Fig. 4–1 c). The hexagonal Brillouin zone boundary reduces to half its size, transforming the M points of the high-temperature phase into zone-center Γ points in the low-temperature CDW phase. This picture can be understood in terms of the soft phonon picture discussed previously. When the phonon frequency goes to zero, the symmetry of the high-temperature phase is broken yielding a modulation of charge density corresponding to the wavelength of the phonon. Figure 4–1 d) shows the photo-excitation mechanism. 1.55 eV photons undergo transitions into a partially occupied conduction band at M and L points of reciprocal space. At

the Γ-point, an unoccupied region of the band exists above the Fermi level and forms a hole-pocket.

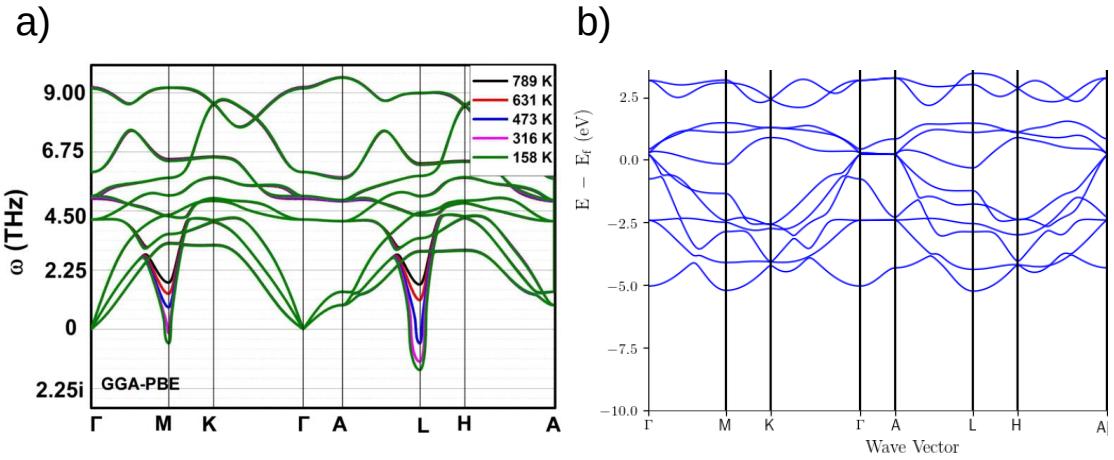

Figure 4–2: Phononic and electronic band structures of 1T-$TiSe_2$.
a) Phonon band structure computed by Duong *et al.* [186], used with permission. b) Electronic band determined from the Materials Project database [188].

4.4 X-ray thermal diffuse scattering of titanium diselenide

Static X-ray diffuse and inelastic scattering measurements have characterized in detail the behaviour of the soft phonon mode which varies strongly with temperature [161, 163]. These measurements will be summarized here as they are relevant in understanding the ultrafast electron scattering results which follow.

In 2001, Holt and co-workers reported the first observation of the soft phonon mode in $TiSe_2$ [161]. The existence of a such a soft mode was expected and the presence of a Kohn anomaly had been suggested by neutron scattering measurements carried out the M and L points of reciprocal space [165], but the limited scattering cross-section of the neutrons limited the ability to identify the behaviour of the phonon energy. Holt used the latest

generation of X-ray synchrotron radiation with a beam flux sufficient to resolve thermal diffuse intensity off the Bragg peaks, and thus was able to resolve the phonon energy as a function of temperature. The soft-mode phonon has a symmetry of L_1^- and they find that the temperature dependence of the phonon can be described by the following empirical relation

$$\omega(T) = \sqrt{T - T_c}\left[a + b(T - T_c) + c(T - T_c)^2\right], \tag{4.11}$$

where $a = 7.92 \times 10^{-2}$ THz/$\sqrt{\text{K}}$, $b = 2.40 \times 10^{-4}$ THz/K$^{3/2}$ and $c = 1.91 \times 10^{-6}$ THz/K$^{5/2}$ are fitting parameters. They identify a critical temperature of $T_c = 188$ K and the minimum energy of the phonon they are able to determine is roughly 0.1 THz. Their results provided the first important evidence of the soft mode CDW behaviour in $TiSe_2$.

A decade later, Weber and colleagues [163] performed new inelastic X-ray measurments of the L_1^- phonon. They combine their results with *ab-initio* calculations of the electronic structure. In their analysis, they suggest that electron-phonon coupling along with a strongly divergent electronic susceptibility is sufficient to yield a stable CDW phase. They verify the relation for a stable CDW phase predicted in Ref. [189]

$$\frac{4g_{k'}^2}{\hbar\omega_0} \geq \frac{1}{\chi(k', T)} + 2U_{k'} - V_{k'}, \tag{4.12}$$

where ω_0 is the bare (not-renormalized) frequency, $U_{k'}$ is the Coulomb interaction and $V_{k'}$ is the correlation-exchange interaction. The energy resolution provided by their experiment indicates that both a strongly divergent $\chi_{k'}$ and strong electron-phonon coupling terms must exist in $TiSe_2$.

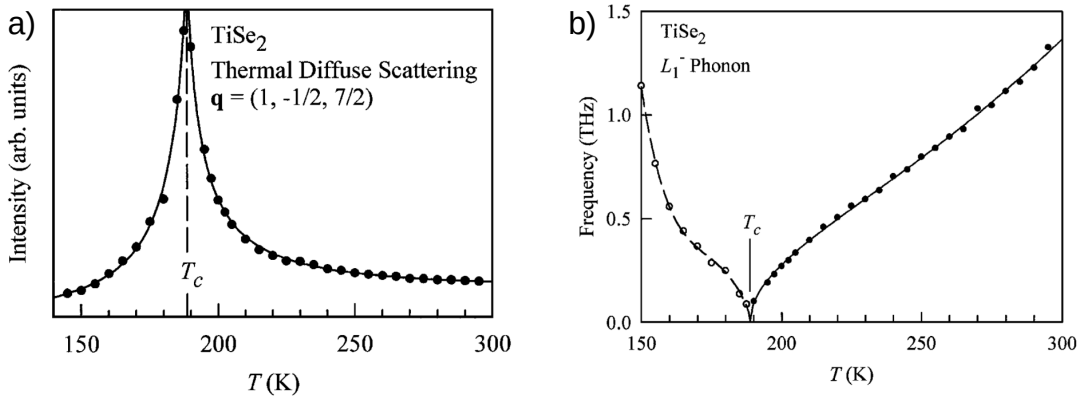

Figure 4–3: Soft phonon in $TiSe_2$ observed by X-ray thermal diffuse scattering [161]. a) Thermal diffuse intensity at $\mathbf{q} = (1, -1/2, 7/2)$ (L-point) in reciprocal lattice units. b) Phonon frequency vs. temperature of the L_1^- phonon indicating a T_c of 188 K corresponding to the CDW phase transition. Figures used with permission.

4.5 Contribution of χ to time-resolved diffuse intensity

Given the intriguing nature of $TiSe_2$ revealed by ARPES and X-ray thermal diffuse scattering measurements, ultrafast electron scattering is expected to be a powerful technique capable of revealing insights into the qualitatively distinct electron-lattice interactions in the material from the perspective of the phonon system directly. To understand how the relevant physical quantities of $TiSe_2$ may be determined by ultrafast electron diffuse scattering, consider the first-order thermal diffuse intensity given by Eqn. (1.6.3)

$$I_1(\mathbf{q}) \propto \sum_j \frac{|F_{1j}(\mathbf{q})|^2}{\omega_{\mathbf{q},j}} \coth\left(\frac{\hbar\omega_{\mathbf{q},j}}{2k_B T_j}\right), \tag{4.13}$$

where j labels the phonon modes $\omega_{\mathbf{q},j}$ at wavevector $\mathbf{q}$ and $F_{1j}(\mathbf{q})$ is the one-phonon structure factor. In the thermal limit we have $\hbar\omega_{\mathbf{q},j} \ll k_B T_j$ which is a very good approximation for low-frequency phonons such as the one which softens at the M-point in the Brillouin zone of $TiSe_2$ (this approximation in fact holds holds for most other phonons in $TiSe_2$ as

well). It follows that Eqn. (4.13) can be approximated as

$$I_1(\mathbf{q}) \approx \frac{2k_B}{\hbar} \sum_j \frac{T_j}{\omega^2_{\mathbf{q},j}} |F_{1j}(\mathbf{q})|^2. \tag{4.14}$$

For the moment both $\omega_{\mathbf{q},j}$ and T_j will be treated and time-dependent. In a charge density wave system, there is usually only 1 phonon which has a strongly temperature-dependent frequency, we label this phonon s and separate it from the "normal" phonons (those which do not have temperature-dependent frequencies) indexed by $j \neq s$. Then the above expression has two components is written as

$$I_1(\mathbf{q}) \approx \frac{2k_B}{\hbar} \frac{T_s}{\omega^2_{s0}\left(1 + \frac{2g^2_{\mathbf{q}}}{\hbar\omega_{\mathbf{q},0}}\chi(\mathbf{q}, T_e)\right)} |F_{1s}(\mathbf{q})|^2 + \frac{2k_B}{\hbar} \sum_{j \neq s} \frac{T_j}{\omega^2_{\mathbf{q},j}} |F_{1j}(\mathbf{q})|^2, \tag{4.15}$$

where Eqn. (4.10) has been used to described the temperature (χ) dependence of the phonon frequency. As described earlier, the electronic susceptibility $\chi(\mathbf{q}, T_e)$ depends on the electronic temperature T_e, which can be modulated much more rapidly than the phonon temperature T_s (and T_j for the normal phonons) when the material is laser-excited. The separation of the electronic temperature from the phonon temperatures is valid when the system is laser-excited to a non-equilibrium state in which interband transitions have been driven by the optical excitation field. From this, Eqn. (4.15) naturally separates into fast and slow terms. Furthermore, increasing T_e via photo-excitation yields an increase in χ which actually corresponds to phonon *hardening*. The effect of this is in fact a reduction of the diffuse intensity, which would be measurable only while the changes in χ are faster than changes in the phonon temperatures T_s and T_j. This effect can be understood in the following manner: photo-excitation modifies the electronic environment via the susceptibility χ. In turn this directly influences the electronic screening of atomic vibrations at particular wavevectors and therefore the effective force-constants between the atoms. A phonon mode with momentum vector falling at the point where χ diverges is

strongly influcenced by this efffect. In this remainder of this chapter, this femtosecond process is measured for the first time using ultrafast electron diffuse scattering and allows for the relative magnitude of the electron-phonon coupling constant to be determined at various points in the Brillouin zone.

4.6 Ultrafast electron scattering of $TiSe_2$

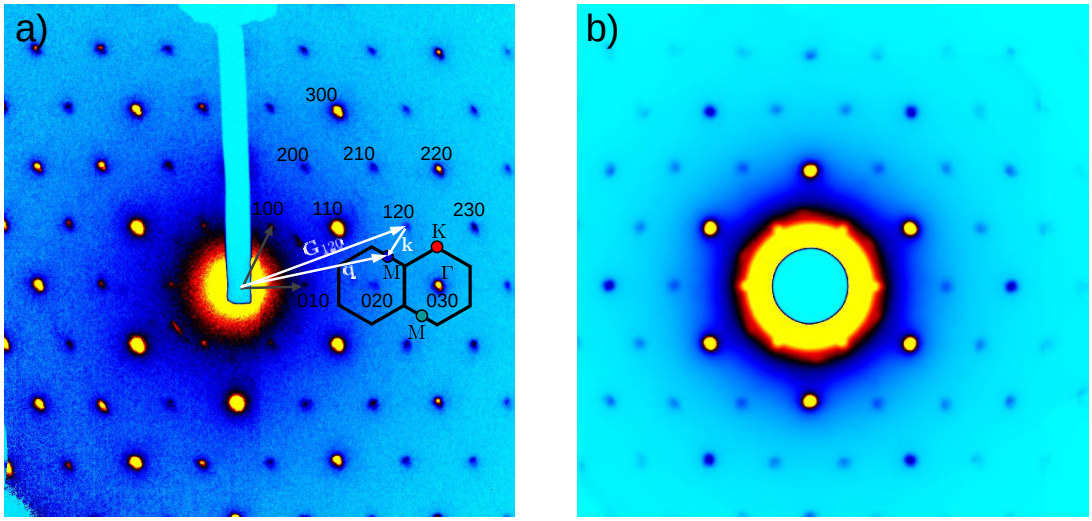

Figure 4–4: Diffraction pattern formed by a 70 nm single crystal $TiSe_2$ sample. a) Raw diffraction image formed by 60 images of each having a 10 second exposure time of the CCD detector. Various Bragg reflections are indicated to show the reciprocal lattice and points of interest in various Brillouin zones are shown in blue (M), green (M) and red circles (K). $\mathbf{G}_{120}$ is a reciprocal lattice vector, $\mathbf{q}$ is the scattering vector, and $\mathbf{k}$ is the phonon wavevector. b) 6-fold symmetrical version of the image in a), generated for improved signal to noise since the diffraction pattern is 6-fold redundant due to its symmetry.

Thin flakes of $TiSe_2$ are sliced by ultra-microtomy at the McGill facility for electron microscopy research by Jeannie Mui who is an electron microscopy technician. Suitable flakes are transferred to a transmission electron microscopy substrates which have a 200µm diameter hold and aligned for optimal diffraction illumination conditions. The sample is

mounted in the ultrafast electron diffraction instrument for experiments involving laser-excitation. Normal incidence of the electron beam is found by fine tuning the angle using a UHV motorized sample holder. An example diffraction pattern of $TiSe_2$ obtained using the instrument is shown in Fig. 4–4 a). The sample area is roughly 10000 μm^2 (80% coverage of the substrate aperture) and the spot size of the 800 nm excitation laser pulse is 450 μm in diameter ensuring a uniform excitation across the probed volume of the sample.

The ultrafast electron scattering measurements of $TiSe_2$ which are presented exhibit very small diffuse intensity changes on the order of a few percent. In order to obtain sufficient signal to noise for the experiments, measurements spanning 24-48 hours where conducted. Temporal stability throughout the measurements was crucial in order to reliably resolve the scattering intensity changes. The timing and synchronization system for pulse compression presented in Chapter 2 was critical in achieving sufficient time resolution and stability for the following experiments.

4.6.1 Bragg peak dynamics

The Bragg peak dynamics of photo-excited $TiSe_2$ are shown by examining the time-dependent behavior of the (030) reflection at the Γ point. The results are shown in Fig. 4–5. Consistent with previous UED measurements [190], is the bi-exponential time-dependence of the Debye-Waller effect which demonstrates a 833 ± 188 fs initial decrease followed by a slower 2.09 ± 1.08 ps decrease. An explanation of this in terms of strongly-coupled optical phonons has been given [191, 190]. The Debye-Waller effect is observed in all reflections and demonstrated the expected q^2–scaling. The time-scales found in this data report on the average heating of the lattice, and will thus form a useful reference time-constant when comparing to time-scales found in the diffuse intensity signals.

Ultrafast diffuse scattering strives to determine where the scattering intensity which leaves the Γ points is distributed throughout the rest of the Brillouin zone [192]. In general,

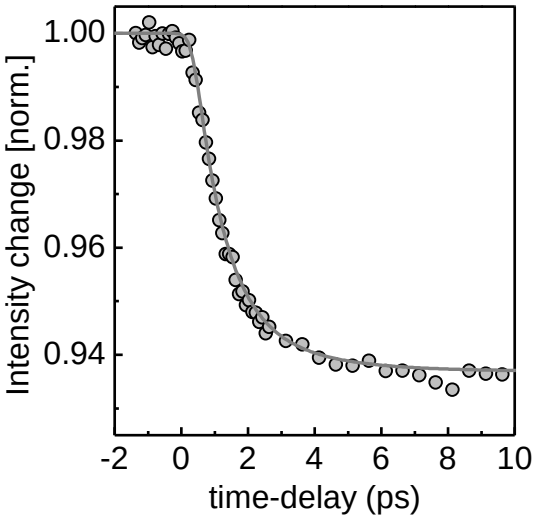

Figure 4–5: Transient Debye-Waller effect in $TiSe_2$.
a) Time-dependent intensity of the (030) Bragg peak. A bi-exponential time-dependence is observed, with an 833 ± 188 fs fast component and 2.09 ± 1.08 ps slow component. The solid line is a fit to such a model.

the intensity will be distributed among specific modes in time according to the magnitude of the wave-vector dependent electron-phonon coupling $\mathbf{g}_k$, followed by phonon-phonon coupling between optical and acoustic modes in a manner which respects momentum and energy conservation. This results in an energy flow into the phonon system, yielding non-equilibrium mode populations. In this work however, changes in intensity corresponding to modulation of the soft phonon are also observed in addition to changes in phonon mode populations.

The fluence range of 2–6 mJ/cm^2 was investigated in this work. Measurements at higher-fluences were found to cause damage to the sample. Differential changes in scattering intensity of roughly 1% are detectable given the signal to noise which can be achieved in the instrument. This is because a typical $TiSe_2$ single crystal flake has relatively small area limiting the possible electron flux for the measurement and it is not practical to run

measurements much longer that a few days to collect statistics. Changes in intensity of this magnitude are only found to occur for fluences at or above 2 mJ/cm^2 because of the limited response of the sample. For fluences above 7 mJ/cm^2 the sample doesn't survive a measurement run.

4.6.2 Diffuse intensity dynamics

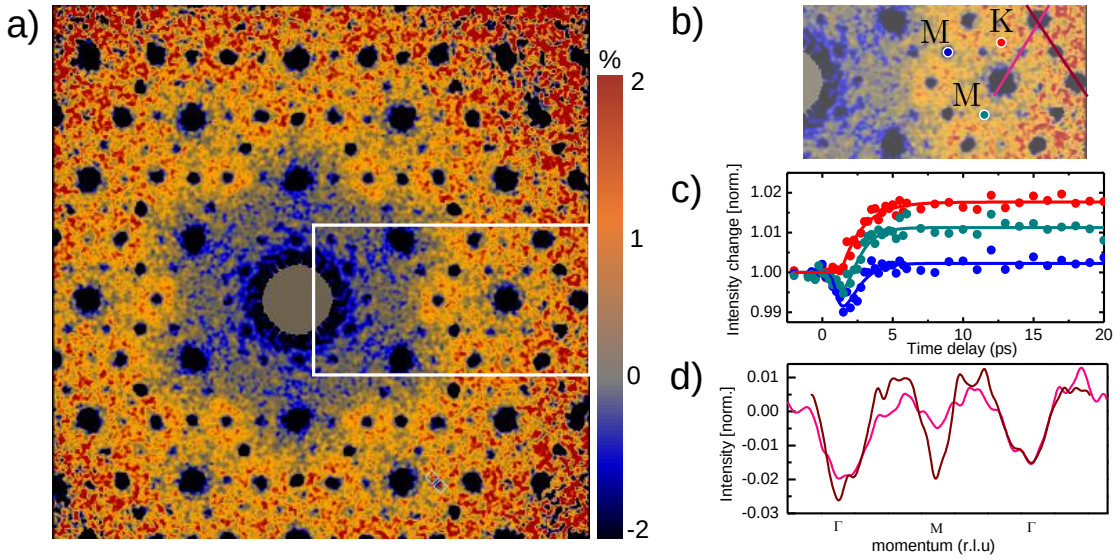

Figure 4–6: Ultrafast electron diffuse scattering of $TiSe_2$.
a) Normalized intensity change 1 ps after photo-excitation with a fluence of 4 mJ/cm^2. b) Selected region of reciprocal space shown in the white rectangle of a). The green circle identifies the M-point around the (030) Bragg, the blue circle identifies the M-point around the (020) peak and the red circle identifies the K point around the (030) peak. c) Time traces at the points shown in b) showing the rapid decrease and slower increase found at the M-points and only the slower increase at the K-points. d) Intensity line-cuts along the lines shown in b).

The diffuse intensity dynamics are analyzed by comparing the normalized relative intensity change (*i.e.* the change normalized to pattern shown in Fig. 4–4 b)) in regions of reciprocal space which fall off the Bragg peaks (regions off of the Γ points of the Brillouin zone). The change in intensity at a pump-probe time delay of 1 ps is shown in Fig. 4–6 a).

What is striking, and unique compared to other diffuse scattering measurements [192, 193, 194], is the fact that a *decrease* in intensity is found not only on the Bragg peaks but also effectively instantaneously at the M-points of reciprocal space. In Fig 4–6 a) and b) black regions depicting a negative change occur at all Γ and M-points. Unlike the Bragg dynamics however, the time-resolved dynamics at the M-points demonstrate a rapid recovery after 1 picosecond which is qualitatively consistent with other points in the Brillouin zone (such as the K-point) which corresponds to the expected increase in phonon mode occupancy due to lattice heating by energy transfer from the photoexcited carriers through electron-phonon coupling. A comparison of the time-traces is shown in Fig. 4–6 c). The decreasing intensity is of particular interest because it occurs where phonon softening/hardening is expected in $TiSe_2$. Line-cuts of the intensity change are shown in Fig 4–6 d) along two different Γ–M–Γ paths which are shown in b). At a time-delay of 1 ps, the decrease in intensity at the M-points is a few percent, comparable with that of the Bragg peaks.

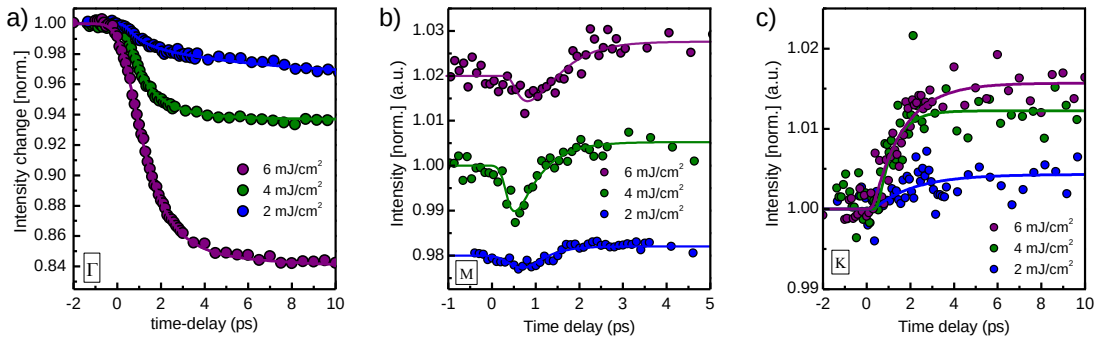

Figure 4–7: Fluence dependent dynamics in $TiSe_2$.
Photo-induced scattering intensity dynamics at the Γ (a)), M (b)) and K (c)) points of the Brillouin zone for various fluences.

The sample was measured at fluences of 2, 4 and 6 mJ/cm^2. The fluence dependence of the intensity dynamics are shown in Fig. 4–7. The Bragg peaks show the expect scaling of peak suppression with fluence, as more energy from the laser excitation translates in an

increased average lattice heating through the transient Debye-Waller effect. The dynamics of the M-point, interestingly do not demonstrate a clear dependence on fluence. The two components of the time-domain response remain present, but the magnitude doesn't demonstrate a clear scaling or dependence on fluence up to 6 mJ/cm^2, which is approaching the maximum excitation which can be applied to the sample. Between 2 and 4 mJ/cm^2 the intensity change at the M-point roughly scales in a manner proportional to the incident fluence. Further determination of this at lower fluences is limited by realistic signal to noise considerations. A similar scaling is found to occur at the K points shown in Fig. 4–7 c).

At a fluence of 4 mJ/cm^2, the M-points dynamics are fit to a bi-exponential function, which yields a time constant of 137 ± 29 fs for the fast decrease in intensity and a 508 ± 66 fs increase. Based on these time-constants, the fast component is most likely instrument resolution limited, since the total instrument response function is roughly 100 fs as determined previously (see Chapter 2.) The fast rise which follows, interestingly, is slightly faster than the reduction of the Bragg peak intensities (833 ± 188 fs). These values should be in agreement if they report on the same mechanism of lattice heating. A possible explanation is that the phonon hardens impulsively but "kicks-back" and softens quickly thereafter, with a time-constant slightly faster that the heating of the other phonons in the material. More detailed measurements of this are expected to clarify this point, as the modeling of this data is limited by the fitting analysis procedure. The time-constant of the dynamics at the K-point is found to be 724 ± 176 fs which is in better agreement with the Bragg peak dynamics.

4.7 Analysis of phonon hardening

The rapid decrease in diffuse scattering intensity at the M-points is of primary interest because it represents novel physics of CDW materials which can be probed by ultrafast electron diffuse scattering. The first term of Equation (4.15) describes the diffuse scattering

intensity due exclusively to the soft phonon of $TiSe_2$ at the M-point. It reads

$$I_1(\mathbf{q}) \approx \frac{2k_B}{\hbar}\frac{T_s}{\omega_s^2}|F_{1s}(\mathbf{q})|^2.$$

An rapid decrease in I_1 can be described by an increase in the phonon frequency ω_s which is related to the electronic susceptibility χ according to $\omega_{s0}^2\left(1+\frac{2g_{\mathbf{q}}^2}{\hbar\omega_{s,0}}\chi(\mathbf{q},T_e)\right)$. Photo-excitation impulsively increases χ by excitation of carriers into the electron pocket at the M and L points yielding an increase in the effective electron temperature T_e. The frequency of the phonon before photo-excitation is found by examining Fig. 4–3 b) to be $\omega_{s0} = 1.3$ THz [161]. Fitting the data shown in Fig. 4–7 b) at a fluence of 4 mJ/cm^2 reveals that the decreasing component has an amplitude of $3.4 \pm 0.5\%$ which directly corresponds to an equivalent percent increase in χ of 3.4% and an $\omega_s - \omega_{s0}$ of 24 GHz.

The line-cuts of the time-resolved intensity change after 1 ps shown in Fig. 4–6 d) also reveal the momentum range over which the phonon hardening occurs. This is determined to be $0.26 \pm 0.03 \times G$ centered at the M-points where G is the magnitude of a reciprocal lattice vector. Within this range about the M, ω_s^2 has hardened by 1–3% with the maximum hardening occurring exactly at the M-point, consistent with the computations shown in Fig. 4–2 a) and expected features of soft-phonon CDW materials.

The existence of the rapid decrease in diffuse intensity at the M-points occurs because of the character of χ for a soft-phonon system. The rate at which this process occurs however, is governed by the electron-phonon coupling term g_{M} at M in the Brillouin zone. Changes in electron screening and χ resulting from photo-excitation are the precursor the phonon hardening observed, but the coupling of the electrons to the soft mode at this wavevector must be very strong in order to rapidly change the frequency of the phonon. The magnitude of this term at M relative to other points in the zone is in fact what truly allows for separation of changes in phonon frequency from changes in phonon occupancy in

the time domain. Given the time-constants determined in this work we find that $\frac{g_{\mathrm{M}}^2}{g_{\mathrm{K},\Gamma}^2} \approx 5.7$ indicating that both strong electron phonon coupling and a divergent χ exist in the high-temperature phase of $TiSe_2$.

It is particularly interesting to note that the differential scattering shown in Fig. 4–6 a) demonstrates the symmetry of the the expected scattering pattern of $TiSe_2$ in the low-temperature charge density wave phase. All of the regions with decreasing diffuse intensity are areas which either remain or become Γ points after the CDW transition (see Fig. 4–1 c)). Thus, this new type of time-resolved measurement identifies directly the signature of a lattice instability (Kohn anomaly) and its wave-vector far away from charge-density wave transition through phonon re-normalization.

4.8 Outlook and conclusion

In this chapter, ultrafast electron diffuse scattering measurements of 1T-$TiSe_2$ have been presented at 300 K. The measurements reveal transient phonon hardening of the L_1^- optical phonon that plays a critical role during the charge density wave transition. A change in the electronic susceptibility χ of $3.4 \pm 0.5\%$ is inferred from the changes in diffuse scattering at the M-point of the Brillouin zone corresponding to a frequency shift of ~ 24 GHz of the phonon. Furthermore it is determined that the electron-phonon coupling at the M-point must be roughly 6 times stronger that elsewhere in the Brillouin zone.

Temperature-dependent measurements of $TiSe_2$ down to and through the CDW transition are expected to reveal more information related to the effects observed in this chapter. This is experimentally challenging because of the nature of the sample which is mounted in the instrument for the scattering measurements. The thin flake of $TiSe_2$ is placed on a TEM grid substrate with poor thermal contact. This makes cooling the flake challenging and highly sample-dependent (each flake has a different contact area). When thermal contact is sufficient, the vacuum conditions of the chamber (10^{-7} torr) are insufficient because

the formation of ice layers on the order of 10 nm occurs since the monolayer growth rates are on the order of Å/min [195]. This result of this is that there is insuffient time to perform an experiment before the ice layers completely attenuated the electron beam and the scattering signal. This is expected to be overcome in the near future with improved UHV conditions and sample mounting capacity.

Measurements at fluences below 2 mJ/cm^2 would be interesting to conduct if improved instrument signal to noise can be obtained. This is because the strength of the photo-excitation remains quite a strong perturbation to the electron system. Finding strategies to produce larger area $TiSe_2$ flakes would be the quickest avenue to increasing the signal to noise, as the scattering intensity scales with the area of the flake.

Excitation of the $TiSe_2$ sample with different photon energies would also be interesting to investigate. The 1.55 eV excitation drives transitions at the M points, which impact directly the electron environment which strongly influences the soft phonon in $TiSe_2$. It would be interesting to investigate whether phonon hardening occurs when photo-excitation drives transitions elsewhere in the Brillouin zone, creating either band-edge excited carriers (1 eV, 1200 nm, laser light) or carriers with significant excess energy (3 eV, 400 nm).

In conclusion, the observation of ultrafast phonon hardening in $TiSe_2$ using ultrafast electron diffuse scattering establishes that the technique is able to detect changes in phonon frequency which are directly related to the momentum dependent electronic susceptibility. The technique is thus capabable of probing phenomena reliant on the Kohn anomaly, a feature of condensed matter systems difficult to access experimentally.

REFERENCES

[1] D. Basov, R. Averitt, and D. Hsieh, "Towards properties on demand in quantum materials," *Nature materials*, vol. 16, no. 11, p. 1077, 2017.

[2] T. Kampfrath, K. Tanaka, and K. A. Nelson, "Resonant and nonresonant control over matter and light by intense terahertz transients," *Nature Photonics*, vol. 7, no. 9, p. 680, 2013.

[3] J. Zhang and R. Averitt, "Dynamics and control in complex transition metal oxides," *Annual Review of Materials Research*, vol. 44, pp. 19–43, 2014.

[4] D. Fausti, R. Tobey, N. Dean, S. Kaiser, A. Dienst, M. C. Hoffmann, S. Pyon, T. Takayama, H. Takagi, and A. Cavalleri, "Light-induced superconductivity in a stripe-ordered cuprate," *Science*, vol. 331, no. 6014, pp. 189–191, 2011.

[5] V. R. Morrison, R. P. Chatelain, K. L. Tiwari, A. Hendaoui, A. Bruhacs, M. Chaker, and B. J. Siwick, "A photoinduced metal-like phase of monoclinic VO_2 revealed by ultrafast electron diffraction," *Science*, vol. 346, pp. 445–448, 10 2014.

[6] C. Rulliere *et al.*, *Femtosecond laser pulses*. Springer, 2005.

[7] F. Krausz, M. E. Fermann, T. Brabec, P. F. Curley, M. Hofer, M. H. Ober, C. Spielmann, E. Wintner, and A. J. Schmidt, "Femtosecond solid-state lasers," *IEEE Journal of Quantum Electronics*, vol. 28, pp. 2097–2122, Oct 1992.

[8] W. E. Lamb, "Theory of an optical maser," *Phys. Rev.*, vol. 134, pp. A1429–A1450, Jun 1964.

[9] H. A. Haus, "Mode-locking of lasers," *IEEE Journal of Selected Topics in Quantum Electronics*, vol. 6, pp. 1173–1185, Nov 2000.

[10] V. J. Urick, K. J. Williams, and J. D. McKinney, *Fundamentals of microwave photonics*. John Wiley & Sons, 2015.

[11] D. J. Jones, S. A. Diddams, J. K. Ranka, A. Stentz, R. S. Windeler, J. L. Hall, and S. T. Cundiff, "Carrier-envelope phase control of femtosecond mode-locked lasers and direct optical frequency synthesis," *Science*, vol. 288, no. 5466, pp. 635–639, 2000.

[12] R. W. Boyd, "Nonlinear optics: Third edition.," 2008.

[13] D. Strickland and G. Mourou, "Compression of amplified chirped optical pulses," *Optics Communications*, vol. 55, no. 6, pp. 447 – 449, 1985.

[14] H. J. Qian, C. Li, Y. C. Du, L. X. Yan, J. F. Hua, W. H. Huang, and C. X. Tang, "Experimental investigation of thermal emittance components of copper photocathode," *Phys. Rev. ST Accel. Beams*, vol. 15, p. 040102, Apr 2012.

[15] T. Munakata, T. Sugiyama, T. Masuda, and N. Ueno, "Photoemission microspectroscopy of occupied and unoccupied surface states of crystalline facets formed on polycrystalline copper," *Phys. Rev. B*, vol. 68, p. 165404, Oct 2003.

[16] T. van Oudheusden, E. F. de Jong, S. B. van der Geer, W. P. E. M. O. t Root, O. J. Luiten, and B. J. Siwick, "Electron source concept for single-shot sub-100 fs electron diffraction in the 100 kev range," *Journal of Applied Physics*, vol. 102, no. 9, p. 093501, 2007.

[17] M. Reiser, *Theory and design of charged particle beams*. John Wiley & Sons, 2008.

[18] F. O. Kirchner, S. Lahme, F. Krausz, and P. Baum, "Coherence of femtosecond single electrons exceeds biomolecular dimensions," *New Journal of Physics*, vol. 15, p. 063021, June 2013.

[19] B. J. Siwick, J. R. Dwyer, R. E. Jordan, and R. J. D. M. Miller, "Ultrafast electron optics : Propagation dynamics of femtosecond electron packets Ultrafast electron optics : Propagation dynamics of femtosecond electron packets," 2002.

[20] É. Durand, *Électrostatique: Les distributions*. MASSON et Cie, 1964.

[21] O. D. Kellogg, *Foundations of potential theory*, vol. 31. Courier Corporation, 1953.

[22] A. Gliserin, M. Walbran, and P. Baum, "Passive optical enhancement of laser-microwave synchronization," *Applied Physics Letters*, vol. 103, no. 3, pp. 1–5, 2013.

[23] B. E. Warren, *X-ray Diffraction*. Courier Corporation, 1990.

[24] P. M. Chaikin, T. C. Lubensky, and T. A. Witten, *Principles of condensed matter physics*, vol. 1. Cambridge university press Cambridge, 1995.

[25] N. Ashcroft and N. Mermin, *Solid State Physics*. Holt, Rinehart and Winston, 1976.

[26] Z.-l. Wang, *Elastic and inelastic scattering in electron diffraction and imaging*. Springer Science & Business Media, 2013.

[27] B. Fultz and J. M. Howe, *Transmission electron microscopy and diffractometry of materials*. Springer Science & Business Media, 2012.

[28] L. D. Landau and E. M. Lifshitz, *Quantum mechanics: non-relativistic theory*, vol. 3. Elsevier, 2013.

[29] E. N. Economou, *Green's functions in quantum physics*, vol. 3. Springer, 1983.

[30] M. Born, "Quantenmechanik der Stoßvorgänge," *Zeitschrift für Physik*, vol. 38, pp. 803–827, Nov 1926.

[31] W. H. Bragg and W. L. Bragg, "The reflection of x-rays by crystals," *Proceedings of the Royal Society of London. Series A, Containing Papers of a Mathematical and Physical Character*, vol. 88, no. 605, pp. 428–438, 1913.

[32] P. P. Ewald, "Die berechnung optischer und elektrostatischer gitterpotentiale," *Annalen der Physik*, vol. 369, no. 3, pp. 253–287, 1921.

[33] R. Xu and T. C. Chiang, "Determination of phonon dispersion relations by X-ray thermal diffuse scattering," *Zeitschrift fur Kristallographie*, vol. 220, pp. 1009–1016, 2005.

[34] M. Born, "über schwingungen in raumgittern," *Phys. Z*, vol. 13, p. 287, 1912.

[35] G. P. Srivastava, *The physics of phonons*. CRC press, 1990.

[36] M. Fox, *Optical properties of solids*. Oxford University Press, 2001.

[37] P. Parravicini, *G. Electronic States and Optical Transitions in Solids*. Pergamon press, 1975.

[38] M. Dressel and G. Grüner, *Electrodynamics of solids: optical properties of electrons in matter*. Cambridge University Press, 2002.

[39] P. Y. Yu and M. Cardona, *Fundamentals of semiconductors: physics and materials properties*. Springer, 2010.

[40] E. T. Jaynes and F. W. Cummings, "Comparison of quantum and semiclassical radiation theories with application to the beam maser," *Proceedings of the IEEE*, vol. 51, pp. 89–109, Jan 1963.

[41] J. D. Jackson, *Classical Electrodynamics*. John Wiley & Sons, 2007.

[42] G. D. Mahan, *Many-particle physics*. Springer Science & Business Media, 2013.

[43] G. Grüner, *Density waves in solids*. CRC Press, 2018.

[44] G. Mourou and S. Williamson, "Picosecond electron diffraction," *Applied Physics Letters*, vol. 41, no. 1, pp. 44–45, 1982.

[45] S. Williamson, G. Mourou, and J. Li, "Time-Resolved Laser-Induced Phase Transformation in Aluminum," *Physical Review Letters*, vol. 52, pp. 2364–2367, 6 1984.

[46] J. C. Williamson, J. Cao, H. Ihee, H. Frey, and A. H. Zewail, "Clocking transient chemical changes by ultrafast electron diffraction," *Nature*, vol. 386, no. 6621, p. 159, 1997.

[47] H. Ihee, V. A. Lobastov, U. M. Gomez, B. M. Goodson, R. Srinivasan, C.-Y. Ruan, and A. H. Zewail, "Direct imaging of transient molecular structures with ultrafast diffraction," *Science*, vol. 291, no. 5503, pp. 458–462, 2001.

[48] B. J. Siwick, J. R. Dwyer, R. E. Jordan, and R. J. D. Miller, "An atomic-level view of melting using femtosecond electron diffraction.," *Science*, vol. 302, pp. 1382–5, 11 2003.

[49] T. van Oudheusden, P. L. E. M. Pasmans, S. B. van der Geer, M. J. de Loos, M. J. van der Wiel, and O. J. Luiten, "Compression of subrelativistic space-charge-dominated electron bunches for single-shot femtosecond electron diffraction," *Phys. Rev. Lett.*, vol. 105, p. 264801, Dec 2010.

[50] R. P. Chatelain, V. R. Morrison, C. Godbout, and B. J. Siwick, "Ultrafast electron diffraction with radio-frequency compressed electron pulses," *Applied Physics Letters*, vol. 101, no. 8, p. 081901, 2012.

[51] M. Gao, H. Jean-Ruel, R. R. Cooney, J. Stampe, M. de Jong, M. Harb, G. Sciaini, G. Moriena, and R. J. D. Miller, "Full characterization of rf compressed femtosecond electron pulses using ponderomotive scattering," *Opt. Express*, vol. 20, pp. 12048–12058, May 2012.

[52] G. Sciaini, M. Harb, S. G. Kruglik, T. Payer, C. T. Hebeisen, F.-J. M. zu Heringdorf, M. Yamaguchi, M. Horn-von Hoegen, R. Ernstorfer, and R. D. Miller, "Electronic acceleration of atomic motions and disordering in bismuth," *Nature*, vol. 458, no. 7234, p. 56, 2009.

[53] R. Ernstorfer, M. Harb, C. T. Hebeisen, G. Sciaini, T. Dartigalongue, and R. D. Miller, "The formation of warm dense matter: experimental evidence for electronic bond hardening in gold," *Science*, vol. 323, no. 5917, pp. 1033–1037, 2009.

[54] M. Eichberger, H. Schäfer, M. Krumova, M. Beyer, J. Demsar, H. Berger, G. Moriena, G. Sciaini, and R. D. Miller, "Snapshots of cooperative atomic motions in the optical suppression of charge density waves," *Nature*, vol. 468, no. 7325, p. 799, 2010.

[55] M. Gao, C. Lu, H. Jean-Ruel, L. C. Liu, A. Marx, K. Onda, S.-y. Koshihara, Y. Nakano, X. Shao, T. Hiramatsu, *et al.*, "Mapping molecular motions leading to

charge delocalization with ultrabright electrons," *Nature*, vol. 496, no. 7445, p. 343, 2013.

[56] S. Vogelgesang, G. Storeck, J. Horstmann, T. Diekmann, M. Sivis, S. Schramm, K. Rossnagel, S. Schäfer, and C. Ropers, "Phase ordering of charge density waves traced by ultrafast low-energy electron diffraction," *Nature Physics*, vol. 14, no. 2, p. 184, 2018.

[57] E. J. Sie, C. M. Nyby, C. Pemmaraju, S. J. Park, X. Shen, J. Yang, M. C. Hoffmann, B. Ofori-Okai, R. Li, A. H. Reid, *et al.*, "An ultrafast symmetry switch in a weyl semimetal," *Nature*, vol. 565, no. 7737, p. 61, 2019.

[58] A. H. Zewail, "4d ultrafast electron diffraction, crystallography, and microscopy," *Annu. Rev. Phys. Chem.*, vol. 57, pp. 65–103, 2006.

[59] G. Sciaini and R. D. Miller, "Femtosecond electron diffraction: heralding the era of atomically resolved dynamics," *Reports on Progress in Physics*, vol. 74, no. 9, p. 096101, 2011.

[60] R. D. Miller, "Femtosecond crystallography with ultrabright electrons and x-rays: Capturing chemistry in action," *Science*, vol. 343, no. 6175, pp. 1108–1116, 2014.

[61] G. Sciaini, "Recent advances in ultrafast structural techniques," *Applied Sciences*, vol. 9, no. 7, 2019.

[62] V. R. Morrison, R. P. Chatelain, C. Godbout, and B. J. Siwick, "Direct optical measurements of the evolving spatio-temporal charge density in ultrashort electron pulses," *Optics Express*, vol. 21, p. 21, 1 2013.

[63] K. Sokolowski-Tinten, R. K. Li, A. H. Reid, S. P. Weathersby, F. Quirin, T. Chase, R. Coffee, J. Corbett, A. Fry, N. Hartmann, C. Hast, R. Hettel, M. H. von Hoegen, D. Janoschka, J. R. Lewandowski, M. Ligges, F. M. zu Heringdorf, X. Shen, T. Vecchione, C. Witt, J. Wu, H. A. Drr, and X. J. Wang, "Thickness-dependent electron–lattice equilibration in laser-excited thin bismuth films," *New Journal of Physics*, vol. 17, p. 113047, nov 2015.

[64] S. D. Brorson, A. Kazeroonian, J. S. Moodera, D. W. Face, T. K. Cheng, E. P. Ippen, M. S. Dresselhaus, and G. Dresselhaus, "Femtosecond room-temperature measurement of the electron-phonon coupling constant γ in metallic superconductors," *Phys. Rev. Lett.*, vol. 64, pp. 2172–2175, Apr 1990.

[65] P. B. Johnson and R. W. Christy, "Optical constants of transition metals: Ti, V, Cr, Mn, Fe, Co, Ni, and Pd," *Phys. Rev. B*, vol. 9, pp. 5056–5070, Jun 1974.

[66] P. B. Allen, "Theory of thermal relaxation of electrons in metals," *Phys. Rev. Lett.*, vol. 59, pp. 1460–1463, Sep 1987.

[67] L. Waldecker, R. Bertoni, R. Ernstorfer, and J. Vorberger, "Electron-phonon coupling and energy flow in a simple metal beyond the two-temperature approximation," *Phys. Rev. X*, vol. 6, p. 021003, Apr 2016.

[68] M. R. Otto, L. P. René de Cotret, M. J. Stern, and B. J. Siwick, "Solving the jitter problem in microwave compressed ultrafast electron diffraction instruments: Robust sub-50 fs cavity-laser phase stabilization," *Structural Dynamics*, vol. 4, no. 5, p. 051101, 2017.

[69] M. R. Otto, L. P. René de Cotret, D. A. Valverde-Chavez, K. L. Tiwari, N. Émond, M. Chaker, D. G. Cooke, and B. J. Siwick, "How optical excitation controls the structure and properties of vanadium dioxide," *Proceedings of the National Academy of Sciences*, vol. 116, no. 2, pp. 450–455, 2019.

[70] A. W. Chao, K. H. Mess, *et al.*, *Handbook of accelerator physics and engineering*. World scientific, 2013.

[71] T. P. Wangler, *RF Linear accelerators*. John Wiley & Sons, 2008.

[72] A. Gliserin, A. Apolonski, F. Krausz, and P. Baum, "Compression of single-electron pulses with a microwave cavity," *New Journal of Physics*, vol. 14, p. 073055, jul 2012.

[73] A. Gliserin, M. Walbran, F. Krausz, and P. Baum, "Sub-phonon-period compression of electron pulses for atomic diffraction," *Nature communications*, vol. 6, p. 8723, 2015.

[74] M. Walbran, A. Gliserin, K. Jung, J. Kim, and P. Baum, "5-femtosecond laser-electron synchronization for pump-probe crystallography and diffraction," *Phys. Rev. Applied*, vol. 4, p. 044013, Oct 2015.

[75] O. Zandi, K. J. Wilkin, Y. Xiong, and M. Centurion, "High current table-top setup for femtosecond gas electron diffraction," *Structural Dynamics*, vol. 4, no. 4, p. 044022, 2017.

[76] W. K. Panofsky and M. Phillips, *Classical electricity and magnetism*. Courier Corporation, 2005.

[77] P. Pasmans, G. B. van den Ham, S. F. P. D. Conte, S. B. van der Geer, and O. J. Luiten, "Microwave TM010 cavities as versatile 4D electron optical elements," *Ultramicroscopy*, vol. 127, pp. 19–24, 2013.

[78] D. M. Pozar, *Microwave engineering*. John Wiley & Sons, 2009.

[79] E. Rubiola, *Phase noise and frequency stability in oscillators*. Cambridge University Press, 2009.

[80] W. Robins, *Phase noise in signal sources: theory and applications*, vol. 9. IET, 1984.

[81] E. N. Ivanov, S. A. Diddams, and L. Hollberg, "Analysis of noise mechanisms limiting the frequency stability of microwave signals generated with a femtosecond laser," *IEEE Journal of Selected Topics in Quantum Electronics*, vol. 9, pp. 1059–1065, July 2003.

[82] J. Davila-Rodriguez, X. Xie, J. Zang, C. J. Long, T. M. Fortier, H. Leopardi, T. Nakamura, J. C. Campbell, S. A. Diddams, and F. Quinlan, "Optimizing the linearity in high-speed photodiodes," *Opt. Express*, vol. 26, pp. 30532–30545, Nov 2018.

[83] T. M. Fortier, F. Quinlan, A. Hati, C. Nelson, J. A. Taylor, Y. Fu, J. Campbell, and S. A. Diddams, "Photonic microwave generation with high-power photodiodes," *Opt. Lett.*, vol. 38, pp. 1712–1714, May 2013.

[84] R. Bouchand, D. Nicolodi, X. Xie, C. Alexandre, and Y. L. Coq, "Accurate control of optoelectronic amplitude to phase noise conversion in photodetection of ultra-fast optical pulses," *Opt. Express*, vol. 25, pp. 12268–12281, May 2017.

[85] M. Currie and I. Vurgaftman, "Microwave phase retardation in saturated InGaAs photodetectors," *IEEE Photonics Technology Letters*, vol. 18, pp. 1433–1435, July 2006.

[86] J. Taylor, S. Datta, A. Hati, C. Nelson, F. Quinlan, A. Joshi, and S. Diddams, "Characterization of power-to-phase conversion in high-speed p-i-n photodiodes," *IEEE Photonics J.*, vol. 3, p. 140, 2011.

[87] W. Zhang, T. Li, M. Lours, S. Seidelin, G. Santarelli, and Y. L. Coq, "Amplitude to phase conversion of ingaas pin photo-diodes for femtosecond lasers microwave signal generation," *Appl. Phys. B*, vol. 106, p. 301, 2012.

[88] Y. Hu, C. R. Menyuk, X. Xie, M. N. Hutchinson, V. J. Urick, J. C. Campbell, and K. J. Williams, "Computational study of amplitude-to-phase conversion in a modified unitraveling carrier photodetector," *IEEE Photonics Journal*, vol. 9, pp. 1–11, April 2017.

[89] X. Xie, R. Bouchand, D. Nicolodi, M. Giunta, W. Hänsel, M. Lezius, A. Joshi, S. Datta, C. Alexandre, M. Lours, *et al.*, "Photonic microwave signals with zeptosecond-level absolute timing noise," *nature photonics*, vol. 11, no. 1, p. 44, 2017.

[90] J. Kim, F. X. Kärtner, and F. Ludwig, "Balanced optical-microwave phase detectors for optoelectronic phase-locked loops," *Optics letters*, vol. 31, no. 24, pp. 3659–3661, 2006.

[91] M. Lessing, H. S. Margolis, C. T. A. Brown, P. Gill, and G. Marra, "Suppression of amplitude-to-phase noise conversion in balanced optical-microwave phase detectors," *Optics express*, vol. 21, no. 22, pp. 27057–27062, 2013.

[92] K. Jung, J. Shin, J. Kang, S. Hunziker, C.-K. Min, and J. Kim, "Frequency comb-based microwave transfer over fiber with 7× 10- 19 instability using fiber-loop optical-microwave phase detectors," *Optics letters*, vol. 39, no. 6, pp. 1577–1580, 2014.

[93] M. E. Fermann and I. Hartl, "Ultrafast fiber lasers," *Nature photonics*, vol. 7, no. 11, p. 868, 2013.

[94] F. Kiewiet, A. Kemper, O. Luiten, G. Brussaard, and M. van der Wiel, "Femtosecond synchronization of a 3 GHz RF oscillator to a mode-locked Ti:sapphire laser," *Nuclear Instruments and Methods in Physics Research Section A: Accelerators, Spectrometers, Detectors and Associated Equipment*, vol. 484, pp. 619–624, may 2002.

[95] F. J. Morin, "Oxides which show a metal-to-insulator transition at the Néel temperature," *Phys. Rev. Lett.*, vol. 3, pp. 34–36, Jul 1959.

[96] D. N. Basov, R. D. Averitt, D. van der Marel, M. Dressel, and K. Haule, "Electrodynamics of correlated electron materials," *Rev. Mod. Phys.*, vol. 83, pp. 471–541, Jun 2011.

[97] A. Cavalleri, C. Tóth, C. W. Siders, J. A. Squier, F. Ráksi, P. Forget, and J. C. Kieffer, "Femtosecond structural dynamics in VO_2 during an ultrafast solid-solid phase transition," *Phys. Rev. Lett.*, vol. 87, p. 237401, Nov 2001.

[98] P. Baum, D.-S. Yang, and A. H. Zewail, "4D visualization of transitional structures in phase transformations by electron diffraction," *Science*, vol. 318, no. 5851, pp. 788–792, 2007.

[99] C. Kübler, H. Ehrke, R. Huber, R. Lopez, A. Halabica, R. F. Haglund, and A. Leitenstorfer, "Coherent structural dynamics and electronic correlations during an ultrafast insulator-to-metal phase transition in VO_2," *Phys. Rev. Lett.*, vol. 99, p. 116401, Sep 2007.

[100] T. L. Cocker, L. V. Titova, S. Fourmaux, G. Holloway, H.-C. Bandulet, D. Brassard, J.-C. Kieffer, M. A. El Khakani, and F. A. Hegmann, "Phase diagram of the ultrafast photoinduced insulator-metal transition in vanadium dioxide," *Phys. Rev. B*, vol. 85, p. 155120, Apr 2012.

[101] A. Pashkin, C. Kübler, H. Ehrke, R. Lopez, A. Halabica, R. F. Haglund, R. Huber, and A. Leitenstorfer, "Ultrafast insulator-metal phase transition in VO_2 studied by multiterahertz spectroscopy," *Phys. Rev. B*, vol. 83, p. 195120, May 2011.

[102] S. Wall, D. Wegkamp, L. Foglia, K. Appavoo, J. Nag, R. Haglund Jr, J. Stähler, and M. Wolf, "Ultrafast changes in lattice symmetry probed by coherent phonons," *Nature Communications*, vol. 3, p. 721, 2012.

[103] S. Wall, L. Foglia, D. Wegkamp, K. Appavoo, J. Nag, R. F. Haglund, J. Stähler, and M. Wolf, "Tracking the evolution of electronic and structural properties of VO_2 during the ultrafast photoinduced insulator-metal transition," *Phys. Rev. B*, vol. 87, p. 115126, Mar 2013.

[104] D. Wegkamp, M. Herzog, L. Xian, M. Gatti, P. Cudazzo, C. L. McGahan, R. E. Marvel, R. F. Haglund, A. Rubio, M. Wolf, and J. Stähler, "Instantaneous band gap collapse in photoexcited monoclinic VO_2 due to photocarrier doping," *Phys. Rev. Lett.*, vol. 113, p. 216401, Nov 2014.

[105] M. M. Qazilbash, M. Brehm, B.-G. Chae, P.-C. Ho, G. O. Andreev, B.-J. Kim, S. J. Yun, A. V. Balatsky, M. B. Maple, F. Keilmann, H.-T. Kim, and D. N. Basov, "Mott Transition in VO_2 Revealed by Infrared Spectroscopy and Nano-Imaging," *Science*, vol. 318, no. 5857, pp. 1750–1753, 2007.

[106] M. Imada, A. Fujimori, and Y. Tokura, "Metal-insulator transitions," *Rev. Mod. Phys.*, vol. 70, pp. 1039–1263, Oct 1998.

[107] J. Zemann, "Crystal structures, 2nd edition. Vol. 1 by R. W. G. Wyckoff," *Acta Crystallographica*, vol. 18, no. 1, 1965.

[108] S. Westman, I. Lindqvist, B. Sparrman, G. B. Nielsen, H. Nord, and A. Jart, "Note on a phase transition in VO_2," *Acta Chemica Scandinavica (1989)*, vol. 15, 1 1961.

[109] J. B. Goodenough, "The two components of the crystallographic transition in VO_2," *Journal of Solid State Chemistry*, vol. 3, no. 4, pp. 490 – 500, 1971.

[110] N. F. Mott and L. Friedman, "Metal-insulator transitions in VO_2, Ti_2O_3 and $Ti_{2-x}V_xO_3$," *The Philosophical Magazine: A Journal of Theoretical Experimental and Applied Physics*, vol. 30, no. 2, pp. 389–402, 1974.

[111] A. Zylbersztejn and N. F. Mott, "Metal-insulator transition in vanadium dioxide," *Phys. Rev. B*, vol. 11, pp. 4383–4395, Jun 1975.

[112] R. M. Wentzcovitch, W. W. Schulz, and P. B. Allen, "vo_2: Peierls or mott-hubbard? a view from band theory," *Phys. Rev. Lett.*, vol. 72, pp. 3389–3392, May 1994.

[113] V. Eyert, "The metal-insulator transitions of VO_2: A band theoretical approach," *Annalen der Physik*, vol. 11, no. 9, pp. 650–704, 2002.

[114] S. Biermann, A. Poteryaev, A. I. Lichtenstein, and A. Georges, "Dynamical singlets and correlation-assisted peierls transition in VO_2," *Phys. Rev. Lett.*, vol. 94, p. 026404, Jan 2005.

[115] V. Eyert, "VO_2: A novel view from band theory," *Phys. Rev. Lett.*, vol. 107, p. 016401, Jun 2011.

[116] C. Weber, D. D. O'Regan, N. D. M. Hine, M. C. Payne, G. Kotliar, and P. B. Littlewood, "Vanadium dioxide: A Peierls-Mott insulator stable against disorder," *Phys. Rev. Lett.*, vol. 108, p. 256402, Jun 2012.

[117] W. H. Brito, M. C. O. Aguiar, K. Haule, and G. Kotliar, "Metal-insulator transition in VO_2: A DFT + DMFT perspective," *Phys. Rev. Lett.*, vol. 117, p. 056402, Jul 2016.

[118] R. E. Peierls, *Surprises in theoretical physics.* Princeton University Press, 1979.

[119] R. Peierls, "Zur theorie der elektrischen und thermischen leitfhigkeit von metallen," *Annalen der Physik*, vol. 396, no. 2, pp. 121–148, 1930.

[120] J. Hubbard and B. H. Flowers, "Electron correlations in narrow energy bands," *Proceedings of the Royal Society of London. Series A. Mathematical and Physical Sciences*, vol. 276, no. 1365, pp. 238–257, 1963.

[121] E. Pavarini, S. Biermann, A. Poteryaev, A. I. Lichtenstein, A. Georges, and O. K. Andersen, "Mott transition and suppression of orbital fluctuations in orthorhombic $3d^1$ perovskites," *Phys. Rev. Lett.*, vol. 92, p. 176403, Apr 2004.

[122] M. W. Haverkort, Z. Hu, A. Tanaka, W. Reichelt, S. V. Streltsov, M. A. Korotin, V. I. Anisimov, H. H. Hsieh, H.-J. Lin, C. T. Chen, D. I. Khomskii, and L. H. Tjeng, "Orbital-assisted metal-insulator transition in VO_2," *Phys. Rev. Lett.*, vol. 95, p. 196404, Nov 2005.

[123] M. F. Becker, A. B. Buckman, R. M. Walser, T. Lpine, P. Georges, and A. Brun, "Femtosecond laser excitation of the semiconductormetal phase transition in VO_2," *Applied Physics Letters*, vol. 65, no. 12, pp. 1507–1509, 1994.

[124] M. Hada, K. Okimura, and J. Matsuo, "Photo-induced lattice softening of excited-state VO_2," *Applied Physics Letters*, vol. 99, no. 5, p. 051903, 2011.

[125] Z. Tao, F. Zhou, T.-R. T. Han, D. Torres, T. Wang, N. Sepulveda, K. Chang, M. Young, R. R. Lunt, and C.-Y. Ruan, "The nature of photoinduced phase transition and metastable states in vanadium dioxide," *Scientific reports*, vol. 6, p. 38514, 2016.

[126] A. Cavalleri, M. Rini, H. H. W. Chong, S. Fourmaux, T. E. Glover, P. A. Heimann, J. C. Kieffer, and R. W. Schoenlein, "Band-selective measurements of electron dynamics in VO_2 using femtosecond near-edge x-ray absorption," *Phys. Rev. Lett.*, vol. 95, p. 067405, Aug 2005.

[127] A. Cavalleri, T. Dekorsy, H. H. W. Chong, J. C. Kieffer, and R. W. Schoenlein, "Evidence for a structurally-driven insulator-to-metal transition in VO_2: A view from the ultrafast timescale," *Phys. Rev. B*, vol. 70, p. 161102, Oct 2004.

[128] B. Mayer, C. Schmidt, A. Grupp, J. Bühler, J. Oelmann, R. E. Marvel, R. F. Haglund, T. Oka, D. Brida, A. Leitenstorfer, and A. Pashkin, "Tunneling breakdown of a strongly correlated insulating state in VO_2 induced by intense multiterahertz excitation," *Phys. Rev. B*, vol. 91, p. 235113, Jun 2015.

[129] M. F. Jager, C. Ott, P. M. Kraus, C. J. Kaplan, W. Pouse, R. E. Marvel, R. F. Haglund, D. M. Neumark, and S. R. Leone, "Tracking the insulator-to-metal phase transition in VO_2 with few-femtosecond extreme uv transient absorption spectroscopy," *Proceedings of the National Academy of Sciences*, vol. 114, no. 36, pp. 9558–9563, 2017.

[130] E. Abreu, S. N. Gilbert Corder, S. J. Yun, S. Wang, J. G. Ramírez, K. West, J. Zhang, S. Kittiwatanakul, I. K. Schuller, J. Lu, S. A. Wolf, H.-T. Kim, M. Liu, and R. D. Averitt, "Ultrafast electron-lattice coupling dynamics in VO_2 and V_2O_3 thin films," *Phys. Rev. B*, vol. 96, p. 094309, Sep 2017.

[131] M. F. Becker, A. B. Buckman, R. M. Walser, T. Lpine, P. Georges, and A. Brun, "Femtosecond laser excitation dynamics of the semiconductormetal phase transition in vo2," *Journal of Applied Physics*, vol. 79, no. 5, pp. 2404–2408, 1996.

[132] D. Wegkamp and J. Sthler, "Ultrafast dynamics during the photoinduced phase transition in vo2," *Progress in Surface Science*, vol. 90, no. 4, pp. 464 – 502, 2015.

[133] A. Hendaoui, N. Émond, M. Chaker, and Émile Haddad, "Highly tunable-emittance radiator based on semiconductor-metal transition of VO_2 thin films," *Applied Physics Letters*, vol. 102, no. 6, p. 061107, 2013.

[134] L. P. René de Cotret and B. J. Siwick, "A general method for baseline-removal in ultrafast electron powder diffraction data using the dual-tree complex wavelet transform," *Structural Dynamics*, vol. 4, no. 4, p. 044004, 2017.

[135] L. P. René de Cotret, M. R. Otto, M. J. Stern, and B. J. Siwick, "An open-source software ecosystem for the interactive exploration of ultrafast electron scattering data," *Advanced Structural and Chemical Imaging*, vol. 4, p. 11, Sep 2018.

[136] T. Elsaesser and M. Woerner, "Photoinduced structural dynamics of polar solids studied by femtosecond X-ray diffraction," *Acta Crystallogr. Sect. A Found. Crystallogr.*, vol. 66, pp. 168–178, 2010.

[137] D. A. Valverde-Chavez, C. S. Ponseca, C. C. Stoumpos, A. Yartsev, M. G. Kanatzidis, V. Sundstrom, and D. G. Cooke, "Intrinsic femtosecond charge generation dynamics in single crystal $CH_3NH_3PbI_3$," *Energy Environ. Sci.*, vol. 8, pp. 3700–3707, 2015.

[138] D. G. Cooke, F. C. Krebs, and P. U. Jepsen, "Direct observation of sub-100 fs mobile charge generation in a polymer-fullerene film," *Phys. Rev. Lett.*, vol. 108, p. 056603, Jan 2012.

[139] J. L. Tomaino, A. D. Jameson, J. W. Kevek, M. J. Paul, A. M. van der Zande, R. A. Barton, P. L. McEuen, E. D. Minot, and Y.-S. Lee, "Terahertz imaging and spectroscopy of large-area single-layer graphene," *Opt. Express*, vol. 19, pp. 141–146, Jan 2011.

[140] B. T. O'Callahan, A. C. Jones, J. H. Park, D. H. Cobden, J. M. Atkin, and M. B. Raschke, "Inhomogeneity of the ultrafast insulator-to-metal transition dynamics of VO_2," *Nature communications*, vol. 6, p. 6849, 2015.

[141] S. A. Dönges, O. Khatib, B. T. OCallahan, J. M. Atkin, J. H. Park, D. Cobden, and M. B. Raschke, "Ultrafast nanoimaging of the photoinduced phase transition dynamics in vo2," *Nano Letters*, vol. 16, no. 5, pp. 3029–3035, 2016.

[142] L. Vidas, C. M. Gunther, T. A. Miller, B. Pfau, D. Perez-Salinas, E. Martínez, M. Schneider, E. Guhrs, P. Gargiani, M. Valvidares, *et al.*, "Imaging nanometer phase coexistence at defects during the insulator–metal phase transformation in vo2 thin films by resonant soft x-ray holography," *Nano letters*, vol. 18, no. 6, pp. 3449–3453, 2018.

[143] H. Stinson, A. Sternbach, O. Najera, R. Jing, A. Mcleod, T. Slusar, A. Mueller, L. Anderegg, H. Kim, M. Rozenberg, *et al.*, "Imaging the nanoscale phase separation in vanadium dioxide thin films at terahertz frequencies," *Nature communications*, vol. 9, no. 1, p. 3604, 2018.

[144] S. Wall, S. Yang, L. Vidas, M. Chollet, J. M. Glownia, M. Kozina, T. Katayama, T. Henighan, M. Jiang, T. A. Miller, D. A. Reis, L. A. Boatner, O. Delaire, and M. Trigo, "Ultrafast disordering of vanadium dimers in photoexcited vo2," *Science*, vol. 362, no. 6414, pp. 572–576, 2018.

[145] R. Landauer, "Electrical conductivity in inhomogeneous media," *AIP Conference Proceedings*, vol. 40, no. 1, pp. 2–45, 1978.

[146] V. A. Lobastov, J. Weissenrieder, J. Tang, and A. H. Zewail, "Ultrafast electron microscopy (uem): Four-dimensional imaging and diffraction of nanostructures during phase transitions," *Nano letters*, vol. 7, no. 9, pp. 2552–2558, 2007.

[147] M. G. Evans and M. Polanyi, "Some applications of the transition state method to the calculation of reaction velocities, especially in solution," *Trans. Faraday Soc.*, vol. 31, pp. 875–894, 1935.

[148] S. G. Tomlin, "Optical reflection and transmission formulae for thin films," *Journal of Physics D: Applied Physics*, vol. 1, no. 12, p. 1667, 1968.

[149] Z. He and A. J. Millis, "Photoinduced phase transitions in narrow-gap mott insulators: The case of VO_2," *Phys. Rev. B*, vol. 93, p. 115126, Mar 2016.

[150] Q. H. Wang, K. Kalantar-Zadeh, A. Kis, J. N. Coleman, and M. S. Strano, "Electronics and optoelectronics of two-dimensional transition metal dichalcogenides," *Nature nanotechnology*, vol. 7, no. 11, p. 699, 2012.

[151] D. Jariwala, V. K. Sangwan, L. J. Lauhon, T. J. Marks, and M. C. Hersam, "Emerging device applications for semiconducting two-dimensional transition metal dichalcogenides," *ACS nano*, vol. 8, no. 2, pp. 1102–1120, 2014.

[152] K. F. Mak and J. Shan, "Photonics and optoelectronics of 2d semiconductor transition metal dichalcogenides," *Nature Photonics*, vol. 10, no. 4, p. 216, 2016.

[153] S. Manzeli, D. Ovchinnikov, D. Pasquier, O. V. Yazyev, and A. Kis, "2d transition metal dichalcogenides," *Nature Reviews Materials*, vol. 2, no. 8, p. 17033, 2017.

[154] T. C. Berkelbach and D. R. Reichman, "Optical and excitonic properties of atomically thin transition-metal dichalcogenides," *Annual Review of Condensed Matter Physics*, vol. 9, no. 1, pp. 379–396, 2018.

[155] G. Grüner, "The dynamics of charge-density waves," *Rev. Mod. Phys.*, vol. 60, pp. 1129–1181, Oct 1988.

[156] W. Kohn, "Image of the fermi surface in the vibration spectrum of a metal," *Phys. Rev. Lett.*, vol. 2, pp. 393–394, May 1959.

[157] F. Weber, S. Rosenkranz, J.-P. Castellan, R. Osborn, R. Hott, R. Heid, K.-P. Bohnen, T. Egami, A. H. Said, and D. Reznik, "Extended phonon collapse and the origin of the charge-density wave in $2h-\mathrm{nbse}_2$," *Phys. Rev. Lett.*, vol. 107, p. 107403, Sep 2011.

[158] M. Hoesch, A. Bosak, D. Chernyshov, H. Berger, and M. Krisch, "Giant kohn anomaly and the phase transition in charge density wave zrte$_3$," *Phys. Rev. Lett.*, vol. 102, p. 086402, Feb 2009.

[159] M. Maschek, S. Rosenkranz, R. Heid, A. H. Said, P. Giraldo-Gallo, I. R. Fisher, and F. Weber, "Wave-vector-dependent electron-phonon coupling and the charge-density-wave transition in TbTe$_3$," *Phys. Rev. B*, vol. 91, p. 235146, Jun 2015.

[160] D. DiCarlo, R. E. Thorne, E. Sweetland, M. Sutton, and J. D. Brock, "Charge-density-wave structure in $NbSe_2$," *Phys. Rev. B*, vol. 50, pp. 8288–8296, Sep 1994.

[161] M. Holt, P. Zschack, H. Hong, M. Y. Chou, and T.-C. Chiang, "X-ray studies of phonon softening in $TiSe_2$," *Phys. Rev. Lett.*, vol. 86, pp. 3799–3802, Apr 2001.

[162] N. Bonini, M. Lazzeri, N. Marzari, and F. Mauri, "Phonon anharmonicities in graphite and graphene," *Phys. Rev. Lett.*, vol. 99, p. 176802, Oct 2007.

[163] F. Weber, S. Rosenkranz, J.-P. Castellan, R. Osborn, G. Karapetrov, R. Hott, R. Heid, K.-P. Bohnen, and A. Alatas, "Electron-phonon coupling and the soft phonon mode in $TiSe_2$," *Phys. Rev. Lett.*, vol. 107, p. 266401, Dec 2011.

[164] M. D. Johannes and I. I. Mazin, "Fermi surface nesting and the origin of charge density waves in metals," *Phys. Rev. B*, vol. 77, p. 165135, Apr 2008.

[165] F. J. Di Salvo, D. E. Moncton, and J. V. Waszczak, "Electronic properties and superlattice formation in the semimetal $TiSe_2$," *Phys. Rev. B*, vol. 14, pp. 4321–4328, Nov 1976.

[166] A. Zunger and A. J. Freeman, "Band structure and lattice instability of $TiSe_2$," *Phys. Rev. B*, vol. 17, pp. 1839–1842, Feb 1978.

[167] C. Chen, B. Singh, H. Lin, and V. M. Pereira, "Reproduction of the charge density wave phase diagram in 1T-$TiSe_2$ exposes its excitonic character," *Phys. Rev. Lett.*, vol. 121, p. 226602, Nov 2018.

[168] T. Pillo, J. Hayoz, H. Berger, F. Lévy, L. Schlapbach, and P. Aebi, "Photoemission of bands above the fermi level: The excitonic insulator phase transition in 1T-$TiSe_2$," *Phys. Rev. B*, vol. 61, pp. 16213–16222, Jun 2000.

[169] T. E. Kidd, T. Miller, M. Y. Chou, and T.-C. Chiang, "Electron-hole coupling and the charge density wave transition in $TiSe_2$," *Phys. Rev. Lett.*, vol. 88, p. 226402, May 2002.

[170] K. Rossnagel, L. Kipp, and M. Skibowski, "Charge-density-wave phase transition in 1T-$TiSe_2$: Excitonic insulator versus band-type jahn-teller mechanism," *Phys. Rev. B*, vol. 65, p. 235101, May 2002.

[171] H. Cercellier, C. Monney, F. Clerc, C. Battaglia, L. Despont, M. G. Garnier, H. Beck, P. Aebi, L. Patthey, H. Berger, and L. Forró, "Evidence for an excitonic insulator phase in 1T-$TiSe_2$," *Phys. Rev. Lett.*, vol. 99, p. 146403, Oct 2007.

[172] C. Monney, C. Battaglia, H. Cercellier, P. Aebi, and H. Beck, "Exciton condensation driving the periodic lattice distortion of 1T-$TiSe_2$," *Phys. Rev. Lett.*, vol. 106, p. 106404, Mar 2011.

[173] A. Kogar, M. S. Rak, S. Vig, A. A. Husain, F. Flicker, Y. I. Joe, L. Venema, G. J. MacDougall, T. C. Chiang, E. Fradkin, *et al.*, "Signatures of exciton condensation in a transition metal dichalcogenide," *Science*, vol. 358, no. 6368, pp. 1314–1317, 2017.

[174] H. P. Hughes, "Structural distortion in $TiSe_2$ and related materials-a possible Jahn-Teller effect?," *Journal of Physics C: Solid State Physics*, vol. 10, pp. L319–L323, jun 1977.

[175] T. Rohwer, S. Hellmann, M. Wiesenmayer, C. Sohrt, A. Stange, B. Slomski, A. Carr, Y. Liu, L. M. Avila, M. Kalläne, *et al.*, "Collapse of long-range charge order tracked by time-resolved photoemission at high momenta," *Nature*, vol. 471, no. 7339, p. 490, 2011.

[176] S. Hellmann, T. Rohwer, M. Kalläne, K. Hanff, C. Sohrt, A. Stange, A. Carr, M. Murnane, H. Kapteyn, L. Kipp, *et al.*, "Time-domain classification of charge-density-wave insulators," *Nature communications*, vol. 3, p. 1069, 2012.

[177] M. Porer, U. Leierseder, J.-M. Ménard, H. Dachraoui, L. Mouchliadis, I. Perakis, U. Heinzmann, J. Demsar, K. Rossnagel, and R. Huber, "Non-thermal separation of electronic and structural orders in a persisting charge density wave," *Nature materials*, vol. 13, no. 9, p. 857, 2014.

[178] C. Monney, M. Puppin, C. W. Nicholson, M. Hoesch, R. T. Chapman, E. Springate, H. Berger, A. Magrez, C. Cacho, R. Ernstorfer, and M. Wolf, "Revealing the role of electrons and phonons in the ultrafast recovery of charge density wave correlations in 1T-$TiSe_2$," *Phys. Rev. B*, vol. 94, p. 165165, Oct 2016.

[179] J. Lindhard, "On the properties of a gas of charged particles," *Dan. Mat. Fys. Medd.*, vol. 28, no. 8, 1954.

[180] H. Haug and S. W. Koch, *Quantum Theory of the Optical and Electronic Properties of Semiconductors: Fivth Edition.* World Scientific Publishing Company, 2009.

[181] B. Mihaila, "Lindhard function of a d-dimensional Fermi gas," *arXiv preprint arXiv:1111.5337*, 2011.

[182] H. Fröhlich, "Electrons in lattice fields," *Advances in Physics*, vol. 3, no. 11, pp. 325–361, 1954.

[183] J. van Wezel, P. Nahai-Williamson, and S. S. Saxena, "Exciton-phonon-driven charge density wave in $TiSe_2$," *Phys. Rev. B*, vol. 81, p. 165109, Apr 2010.

[184] M. Calandra and F. Mauri, "Charge-density wave and superconducting dome in $TiSe_2$ from electron-phonon interaction," *Phys. Rev. Lett.*, vol. 106, p. 196406, May 2011.

[185] R. Bianco, M. Calandra, and F. Mauri, "Electronic and vibrational properties of $TiSe_2$ in the charge-density-wave phase from first principles," *Phys. Rev. B*, vol. 92, p. 094107, Sep 2015.

[186] D. L. Duong, M. Burghard, and J. C. Schön, "Ab initio computation of the transition temperature of the charge density wave transition in $TiSe_2$," *Phys. Rev. B*, vol. 92, p. 245131, Dec 2015.

[187] Z.-G. Fu, Z.-Y. Hu, Y. Yang, Y. Lu, F.-W. Zheng, and P. Zhang, "Modulation of doping and biaxial strain on the transition temperature of the charge density wave transition in 1T-$TiSe_2$," *RSC Adv.*, vol. 6, pp. 76972–76979, 2016.

[188] K. Persson, "Materials Data on $TiSe_2$ (SG:164) by Materials Project," 2 2016. An optional note.

[189] S. K. Chan and V. Heine, "Spin density wave and soft phonon mode from nesting fermi surfaces," *Journal of Physics F: Metal Physics*, vol. 3, pp. 795–809, apr 1973.

[190] T. E. Karam, J. Hu, and G. A. Blake, "Strongly Coupled ElectronPhonon Dynamics in Few-Layer $TiSe_2$ Exfoliates," *ACS Photonics*, vol. 5, no. 4, pp. 1228–1234, 2018.

[191] R. P. Chatelain, V. R. Morrison, B. L. Klarenaar, and B. J. Siwick, "Coherent and Incoherent Electron-Phonon Coupling in Graphite Observed with Radio-Frequency Compressed Ultrafast Electron Diffraction," *Physical Review Letters*, vol. 113, no. December, p. 235502, 2014.

[192] M. J. Stern, L. P. René de Cotret, M. R. Otto, R. P. Chatelain, J.-P. Boisvert, M. Sutton, and B. J. Siwick, "Mapping momentum-dependent electron-phonon coupling and nonequilibrium phonon dynamics with ultrafast electron diffuse scattering," *Phys. Rev. B*, vol. 97, p. 165416, Apr 2018.

[193] L. Waldecker, R. Bertoni, H. Hübener, T. Brumme, T. Vasileiadis, D. Zahn, A. Rubio, and R. Ernstorfer, "Momentum-resolved view of electron-phonon coupling in multilayer WSe_2," *Phys. Rev. Lett.*, vol. 119, p. 036803, Jul 2017.

[194] T. Chase, M. Trigo, A. H. Reid, R. Li, T. Vecchione, X. Shen, S. Weathersby, R. Coffee, N. Hartmann, D. A. Reis, X. J. Wang, and H. A. Dürr, "Ultrafast electron diffraction from non-equilibrium phonons in femtosecond laser heated Au films," *Applied Physics Letters*, vol. 108, p. 041909, 1 2016.

[195] J. F. O'Hanlon, *A user's guide to vacuum technology.* John Wiley & Sons, 2005.

American Physical Society
Reuse and Permissions License

12-Jun-2019

This license agreement between the American Physical Society ("APS") and Martin Otto ("You") consists of your license details and the terms and conditions provided by the American Physical Society and SciPris.

Licensed Content Information

License Number:	**RNP/19/JUN/015658**
License date:	12-Jun-2019
DOI:	10.1103/PhysRevLett.3.34
Title:	Oxides Which Show a Metal-to-Insulator Transition at the Neel Temperature
Author:	F. J. Morin
Publication:	Physical Review Letters
Publisher:	American Physical Society
Cost:	USD $ 0.00

Request Details

Does your reuse require significant modifications: No

Specify intended distribution locations:	Worldwide
Reuse Category:	Reuse in a thesis/dissertation
Requestor Type:	Student
Items for Reuse:	Figures/Tables
Number of Figure/Tables:	1
Figure/Tables Details:	Figure 1 only, not caption.
Format for Reuse:	Electronic

Information about New Publication:

University/Publisher:	McGill University
Title of dissertation/thesis:	Advancements in electron pulse compression technology applied to ultrafast electron scattering
Author(s):	Martin R. Otto
Expected completion date:	Sep. 2019

License Requestor Information

Name:	Martin Otto
Affiliation:	Individual
Email Id:	martin.otto@mail.mcgill.ca
Country:	Canada

American Physical Society
Reuse and Permissions License

TERMS AND CONDITIONS

The American Physical Society (APS) is pleased to grant the Requestor of this license a non-exclusive, non-transferable permission, limited to Electronic format, provided all criteria outlined below are followed.

1. You must also obtain permission from at least one of the lead authors for each separate work, if you haven't done so already. The author's name and affiliation can be found on the first page of the published Article.

2. For electronic format permissions, Requestor agrees to provide a hyperlink from the reprinted APS material using the source material's DOI on the web page where the work appears. The hyperlink should use the standard DOI resolution URL, http://dx.doi.org/{DOI}. The hyperlink may be embedded in the copyright credit line.

3. For print format permissions, Requestor agrees to print the required copyright credit line on the first page where the material appears: "Reprinted (abstract/excerpt/figure) with permission from [(FULL REFERENCE CITATION) as follows: Author's Names, APS Journal Title, Volume Number, Page Number and Year of Publication.] Copyright (YEAR) by the American Physical Society."

4. Permission granted in this license is for a one-time use and does not include permission for any future editions, updates, databases, formats or other matters. Permission must be sought for any additional use.

5. Use of the material does not and must not imply any endorsement by APS.

6. APS does not imply, purport or intend to grant permission to reuse materials to which it does not hold copyright. It is the requestor's sole responsibility to ensure the licensed material is original to APS and does not contain the copyright of another entity, and that the copyright notice of the figure, photograph, cover or table does not indicate it was reprinted by APS with permission from another source.

7. The permission granted herein is personal to the Requestor for the use specified and is not transferable or assignable without express written permission of APS. This license may not be amended except in writing by APS.

8. You may not alter, edit or modify the material in any manner.

9. You may translate the materials only when translation rights have been granted.

10. APS is not responsible for any errors or omissions due to translation.

11. You may not use the material for promotional, sales, advertising or marketing purposes.

12. The foregoing license shall not take effect unless and until APS or its agent, Aptara, receives payment in full in accordance with Aptara Billing and Payment Terms and Conditions, which are incorporated herein by reference.

13. Should the terms of this license be violated at any time, APS or Aptara may revoke the license with no refund to you and seek relief to the fullest extent of the laws of the USA. Official written notice will be made using the contact information provided with the permission request. Failure to receive such notice will not nullify revocation of the permission.

14. APS reserves all rights not specifically granted herein.

15. This document, including the Aptara Billing and Payment Terms and Conditions, shall be the entire agreement between the parties relating to the subject matter hereof.

American Physical Society
Reuse and Permissions License

10-Jul-2019

This license agreement between the American Physical Society ("APS") and Martin Otto ("You") consists of your license details and the terms and conditions provided by the American Physical Society and SciPris.

Licensed Content Information

License Number:	**RNP/19/JUL/016530**
License date:	10-Jul-2019
DOI:	10.1103/PhysRevLett.86.3799
Title:	X-Ray Studies of Phonon Softening in ${\mathrm{TiSe}}_{2}$
Author:	M. Holt et al.
Publication:	Physical Review Letters
Publisher:	American Physical Society
Cost:	USD $ 0.00

Request Details

Does your reuse require significant modifications: No

Specify intended distribution locations:	Worldwide
Reuse Category:	Reuse in a thesis/dissertation
Requestor Type:	Academic Institution
Items for Reuse:	Figures/Tables
Number of Figure/Tables:	1
Figure/Tables Details:	Figure 4 no caption
Format for Reuse:	Electronic

Information about New Publication:

University/Publisher:	McGill University
Title of dissertation/thesis:	Advancements in pulse compression technology applied to ultrafast electron scattering
Author(s):	Martin R. Otto
Expected completion date:	Sep. 2019

License Requestor Information

Name:	Martin Otto
Affiliation:	Individual
Email Id:	martin.otto@mail.mcgill.ca
Country:	Canada

American Physical Society
Reuse and Permissions License

TERMS AND CONDITIONS

The American Physical Society (APS) is pleased to grant the Requestor of this license a non-exclusive, non-transferable permission, limited to Electronic format, provided all criteria outlined below are followed.

1. You must also obtain permission from at least one of the lead authors for each separate work, if you haven't done so already. The author's name and affiliation can be found on the first page of the published Article.

2. For electronic format permissions, Requestor agrees to provide a hyperlink from the reprinted APS material using the source material's DOI on the web page where the work appears. The hyperlink should use the standard DOI resolution URL, http://dx.doi.org/{DOI}. The hyperlink may be embedded in the copyright credit line.

3. For print format permissions, Requestor agrees to print the required copyright credit line on the first page where the material appears: "Reprinted (abstract/excerpt/figure) with permission from [(FULL REFERENCE CITATION) as follows: Author's Names, APS Journal Title, Volume Number, Page Number and Year of Publication.] Copyright (YEAR) by the American Physical Society."

4. Permission granted in this license is for a one-time use and does not include permission for any future editions, updates, databases, formats or other matters. Permission must be sought for any additional use.

5. Use of the material does not and must not imply any endorsement by APS.

6. APS does not imply, purport or intend to grant permission to reuse materials to which it does not hold copyright. It is the requestor's sole responsibility to ensure the licensed material is original to APS and does not contain the copyright of another entity, and that the copyright notice of the figure, photograph, cover or table does not indicate it was reprinted by APS with permission from another source.

7. The permission granted herein is personal to the Requestor for the use specified and is not transferable or assignable without express written permission of APS. This license may not be amended except in writing by APS.

8. You may not alter, edit or modify the material in any manner.

9. You may translate the materials only when translation rights have been granted.

10. APS is not responsible for any errors or omissions due to translation.

11. You may not use the material for promotional, sales, advertising or marketing purposes.

12. The foregoing license shall not take effect unless and until APS or its agent, Aptara, receives payment in full in accordance with Aptara Billing and Payment Terms and Conditions, which are incorporated herein by reference.

13. Should the terms of this license be violated at any time, APS or Aptara may revoke the license with no refund to you and seek relief to the fullest extent of the laws of the USA. Official written notice will be made using the contact information provided with the permission request. Failure to receive such notice will not nullify revocation of the permission.

14. APS reserves all rights not specifically granted herein.

15. This document, including the Aptara Billing and Payment Terms and Conditions, shall be the entire agreement between the parties relating to the subject matter hereof.

American Physical Society
Reuse and Permissions License

10-Jul-2019

This license agreement between the American Physical Society ("APS") and Martin Otto ("You") consists of your license details and the terms and conditions provided by the American Physical Society and SciPris.

Licensed Content Information

License Number:	**RNP/19/JUL/016529**
License date:	10-Jul-2019
DOI:	10.1103/PhysRevLett.86.3799
Title:	X-Ray Studies of Phonon Softening in ${\mathrm{TiSe}}_{2}$
Author:	M. Holt et al.
Publication:	Physical Review Letters
Publisher:	American Physical Society
Cost:	USD $ 0.00

Request Details

Does your reuse require significant modifications: No

Specify intended distribution locations:	Worldwide
Reuse Category:	Reuse in a thesis/dissertation
Requestor Type:	Student
Items for Reuse:	Figures/Tables
Number of Figure/Tables:	1
Figure/Tables Details:	Figure 2 only, not caption
Format for Reuse:	Electronic

Information about New Publication:

University/Publisher:	McGill University
Title of dissertation/thesis:	Advancements in pulse compression technology applied to ultrafast electron scattering
Author(s):	Martin R. Otto
Expected completion date:	Sep. 2019

License Requestor Information

Name:	Martin Otto
Affiliation:	Individual
Email Id:	martin.otto@mail.mcgill.ca
Country:	Canada

American Physical Society
Reuse and Permissions License

TERMS AND CONDITIONS

The American Physical Society (APS) is pleased to grant the Requestor of this license a non-exclusive, non-transferable permission, limited to Electronic format, provided all criteria outlined below are followed.

1. You must also obtain permission from at least one of the lead authors for each separate work, if you haven't done so already. The author's name and affiliation can be found on the first page of the published Article.

2. For electronic format permissions, Requestor agrees to provide a hyperlink from the reprinted APS material using the source material's DOI on the web page where the work appears. The hyperlink should use the standard DOI resolution URL, http://dx.doi.org/{DOI}. The hyperlink may be embedded in the copyright credit line.

3. For print format permissions, Requestor agrees to print the required copyright credit line on the first page where the material appears: "Reprinted (abstract/excerpt/figure) with permission from [(FULL REFERENCE CITATION) as follows: Author's Names, APS Journal Title, Volume Number, Page Number and Year of Publication.] Copyright (YEAR) by the American Physical Society."

4. Permission granted in this license is for a one-time use and does not include permission for any future editions, updates, databases, formats or other matters. Permission must be sought for any additional use.

5. Use of the material does not and must not imply any endorsement by APS.

6. APS does not imply, purport or intend to grant permission to reuse materials to which it does not hold copyright. It is the requestor's sole responsibility to ensure the licensed material is original to APS and does not contain the copyright of another entity, and that the copyright notice of the figure, photograph, cover or table does not indicate it was reprinted by APS with permission from another source.

7. The permission granted herein is personal to the Requestor for the use specified and is not transferable or assignable without express written permission of APS. This license may not be amended except in writing by APS.

8. You may not alter, edit or modify the material in any manner.

9. You may translate the materials only when translation rights have been granted.

10. APS is not responsible for any errors or omissions due to translation.

11. You may not use the material for promotional, sales, advertising or marketing purposes.

12. The foregoing license shall not take effect unless and until APS or its agent, Aptara, receives payment in full in accordance with Aptara Billing and Payment Terms and Conditions, which are incorporated herein by reference.

13. Should the terms of this license be violated at any time, APS or Aptara may revoke the license with no refund to you and seek relief to the fullest extent of the laws of the USA. Official written notice will be made using the contact information provided with the permission request. Failure to receive such notice will not nullify revocation of the permission.

14. APS reserves all rights not specifically granted herein.

15. This document, including the Aptara Billing and Payment Terms and Conditions, shall be the entire agreement between the parties relating to the subject matter hereof.

American Physical Society
Reuse and Permissions License

04-Jul-2019

This license agreement between the American Physical Society ("APS") and Martin Otto ("You") consists of your license details and the terms and conditions provided by the American Physical Society and SciPris.

Licensed Content Information

License Number:	**RNP/19/JUL/016354**
License date:	04-Jul-2019
DOI:	10.1103/PhysRevB.92.245131
Title:	Ab initio
Author:	Dinh Loc Duong, Marko Burghard, and J. Christian Schön
Publication:	Physical Review B
Publisher:	American Physical Society
Cost:	USD $ 0.00

Request Details

Does your reuse require significant modifications: No

Specify intended distribution locations:	Worldwide
Reuse Category:	Reuse in a thesis/dissertation
Requestor Type:	Student
Items for Reuse:	Figures/Tables
Number of Figure/Tables:	1
Figure/Tables Details:	Figure 1, not including caption
Format for Reuse:	Electronic

Information about New Publication:

University/Publisher:	McGill University
Title of dissertation/thesis:	Advancements in pulse compression technology applied to ultrafast electron scattering
Author(s):	Martin Otto
Expected completion date:	Sep. 2019

License Requestor Information

Name:	Martin Otto
Affiliation:	Individual
Email Id:	martin.otto@mail.mcgill.ca
Country:	Canada

American Physical Society
Reuse and Permissions License

TERMS AND CONDITIONS

The American Physical Society (APS) is pleased to grant the Requestor of this license a non-exclusive, non-transferable permission, limited to Electronic format, provided all criteria outlined below are followed.

1. You must also obtain permission from at least one of the lead authors for each separate work, if you haven't done so already. The author's name and affiliation can be found on the first page of the published Article.

2. For electronic format permissions, Requestor agrees to provide a hyperlink from the reprinted APS material using the source material's DOI on the web page where the work appears. The hyperlink should use the standard DOI resolution URL, http://dx.doi.org/{DOI}. The hyperlink may be embedded in the copyright credit line.

3. For print format permissions, Requestor agrees to print the required copyright credit line on the first page where the material appears: "Reprinted (abstract/excerpt/figure) with permission from [(FULL REFERENCE CITATION) as follows: Author's Names, APS Journal Title, Volume Number, Page Number and Year of Publication.] Copyright (YEAR) by the American Physical Society."

4. Permission granted in this license is for a one-time use and does not include permission for any future editions, updates, databases, formats or other matters. Permission must be sought for any additional use.

5. Use of the material does not and must not imply any endorsement by APS.

6. APS does not imply, purport or intend to grant permission to reuse materials to which it does not hold copyright. It is the requestor's sole responsibility to ensure the licensed material is original to APS and does not contain the copyright of another entity, and that the copyright notice of the figure, photograph, cover or table does not indicate it was reprinted by APS with permission from another source.

7. The permission granted herein is personal to the Requestor for the use specified and is not transferable or assignable without express written permission of APS. This license may not be amended except in writing by APS.

8. You may not alter, edit or modify the material in any manner.

9. You may translate the materials only when translation rights have been granted.

10. APS is not responsible for any errors or omissions due to translation.

11. You may not use the material for promotional, sales, advertising or marketing purposes.

12. The foregoing license shall not take effect unless and until APS or its agent, Aptara, receives payment in full in accordance with Aptara Billing and Payment Terms and Conditions, which are incorporated herein by reference.

13. Should the terms of this license be violated at any time, APS or Aptara may revoke the license with no refund to you and seek relief to the fullest extent of the laws of the USA. Official written notice will be made using the contact information provided with the permission request. Failure to receive such notice will not nullify revocation of the permission.

14. APS reserves all rights not specifically granted herein.

15. This document, including the Aptara Billing and Payment Terms and Conditions, shall be the entire agreement between the parties relating to the subject matter hereof.